POLITECNICO DI MILANO
Doctoral Programme in Environmental and Infrastructure Engineering
Department of Civil and Environmental Engineering

Multi-source and Multi-scale Satellite Observations for Hydrological Modelling and Irrigation Water Management

Doctoral Dissertation of:
Nicola PACIOLLA

Supervisor:
Prof. Chiara Corbari

Tutor:
Prof. Marco Mancini

The Chair of the Doctoral Program:
Riccardo Barzaghi

Acknowledgements

The work here shown has been funded by numerous projects, notably: SIM (Water Joint Programming Initiative), DRAGON 4 (ESA-MOST China Programme), RET-SIF (Eranetmed, EU) and SMARTIES (PRIMA, Horizon 2020, EU).

More than three years of work in the SIA Section at Polimi would not have been at all possible without the kind and firm guidance of Chiara and Prof. Mancini, who helped me all the way and managed to get the best out of me. Special thanks also to Alessandro and Giovanni, for their expert support, and all the staff of the "Fantoli" laboratory, always helpful. Thanks also to all the staff of the DICA Department, always nice and open to discussion.

A special thanks goes to all the co-authors to the works I've published, for their useful suggestions and helpful work: Guangcheng Hu, Chaolei Zheng, Massimo Menenti, Li Jia, Ahmad Al Bitar, Yann Kerr, Imen Ben Charfi, Drazen Skokovic, José Sobrino, Mel Woods, Antonino Maltese and Giuseppe Ciraolo.

Abstract

Remote Sensing has known a consistent spread in use for agricultural purposes in recent years, although the relationship with in-situ correspondents and hydro-energetical modelling results is still being debated. Among the main variables in agricultural applications, **Evapotranspiration** (ET) plays a major role and its measuring complexity has prompted the development of numerous modelling formulations. This thesis work has focused on the improvement of **hydrological modelling** in **agricultural** applications, covering a wide variety of inter-connected themes, all linked to **spatial heterogeneity** and **data source multiplicity**.

Satellite Surface Soil Moisture (SSM) datasets have been analysed to determine their reliability in agricultural applications. A hydrological consistency algorithm has been developed, providing quite underwhelming results: on average, consistency was attained barely 60% of the time. The reason for these low values was explored, identifying generally-better performances during the irrigation season and with newer retrieval technologies. Extending the analysis to other satellite data, a high-density sensor network in a greatly heterogeneous agricultural area has been used as a reference to determine the reliability of satellite observations, with surface temperature (LST) and Leaf Area Index showing good correspondences. SSM data, on the other hand, has shown weak feasibility for use in irrigation schemes. Thus, the optimal solution for improving irrigation management and agricultural monitoring would be a merging of on-ground information and satellite data.

Hydrological modelling is a robust way to improve, characterise and exploit the full potential of input data (whether from satellite and on-ground measurements) and thus the second part of the thesis has focused on the FEST-EWB distributed energy-water balance model. Firstly, the model scale dependence has been investigated, with a multi-scale cross-analysis over a vineyard. Model accuracy with coarser data showed positive results, with a lower-than-one-third estimation error on ET, compared to ≈10% errors from the (benchmark) aggregated model outputs. Another source of model uncertainty is the energetical heterogeneity in mixed soil-vegetation systems. A two-source version of FEST-EWB (FEST-2-EWB) has been developed to the purpose, separating the energy balances for the two components of any given pixel. The new model was tested over a dedicated innovative laboratory setting where it was possible to extract the Transpiration component from the total ET. Global performances were similar across both models, whereas Transpiration was portrayed quite closely by FEST-2-EWB, while FEST-EWB saw a consistent overestimation. A similar comparison was also performed in two open field cases, obtaining comparable results. Finally, the role of Aerodynamic Temperature (T_O) in Sensible Heat formulation has been explored. A considerable dataset of EC measurements in a water-abundant and a quasi-arid location have been used to derive and compare T_O and LST. Notwithstanding temperature differences as high as 15-20°C, the integration of Aerodynamic Temperature into the model infrastructure yielded only small gains in terms of Sensible and Latent Heat estimation.

Contents

List of Figures

List of Tables

Chapter 1

Introduction

The use of Remote Sensing for agricultural purposes has seen a spike in recent years (Cracknell, 2018; Shanmugapriya et al., 2019) along with the new wave of available products. As a lot of satellite data sources are freely accessible and require little effort from the final user, they can be valid substitutes for in-situ data, which on the other hand may require extensive and time-consuming measuring campaigns to be gathered (Mishra and Coulibaly, 2009; Ochoa-Tocachi et al., 2018). Another perk of satellite data with respect to in-situ data relates to the spatial value of the information: for extensive fields, point-wise measurements can be of limited use, in particular in spatially heterogeneous crops, as they require the adoption of spatial interpolation techniques which add to the global uncertainty (Grayson and Blöschl, 2000). Furthermore, in-situ data gathered by different study groups may not follow one unique data gathering protocol (Dorigo et al., 2021) and be hard to harmonize (Jolivot et al., 2021). On the other hand, satellite information is already spatialized and can provide useful information without disregarding the natural crop variability in space (Ochsner et al., 2013). Of course, the use of satellite data has some drawbacks (Dubovik et al., 2021), with data availability sometimes limited by cloud cover or vegetation influence on the signal of interest (Ulaby et al., 1982). Furthermore, both spatial resolution and temporal frequency of the data can be unsuitable for some applications, e.g. low-resolution data for analysing highly-heterogeneous crops (Molero et al., 2018; Piles et al., 2014) or long revisit times (Bauer-Marschallinger et al., 2019). Finally, the accuracy of the variable-retrieving algorithms can be itself in question (Skokovic et al., 2017). As a result of these strengths and weaknesses on both parts, many studies have tried to use both types of products jointly (Joshi et al., 2016), for instance in irrigation management, to assess landscape heterogeneity (Foster et al., 2019) and in theoretical analyses about the relevance of the representation scale for agronomically-relevant hydrological variables (Anderson et al., 2004; Liang, 2000). One main application field for satellite-in-situ synergies is the calibration and/or validation of satellite data using in-situ counterparts (Czapla-Myers et al., 2015; Jackson et al., 2010). In Surface Soil Moisture (SSM) applications, this has produced somewhat mixed results (Brocca et al., 2011), also with multi-layer validation approaches such as triple allocation (Chen et al., 2018; Gruber et al., 2016). One main outlet for the data wealth that has invested the agricultural research world has been hydro-energetical field modelling (Gonzalez-Dugo et al., 2009; Hank et al., 2015; Hoefsloot et al., 2012; Huang et al., 2019). More than employing data as it is, the use of more or less complex modelling structures allows to identify data inconsistencies and errors, as is the case of the reanalyses (Bastola and Misra, 2014; Berg et al., 2018), and provides a general framework for the computation of non-measurable quantities that can

be of interest (Quintana-Seguí et al., 2020). Physically-based models can add theoretically-founded concepts to the table, enforcing a better understanding of the available data. These kinds of models usually require at least an energetical part, dealing with the energy fluxes between vegetation, soil-subsoil and lower atmosphere, as energy input from the sun is the main driver of plant development (Allen et al., 1998; Priestley and Taylor, 1972). Usually, a hydrological component is also present in the model, accounting for the amount of soil moisture available to the plant and its variation in time (Corbari et al., 2011).

The key variable to estimate in crop monitoring is Evapo-Transpiration (ET) (Monteith, 1965). It identifies the amount of water that is released into the atmosphere as a result of direct Evaporation, from soil and leaf surface, and plant-mediated Transpiration, a process driven by plant metabolism, making it a critical component of the organism development (Allen et al., 1998). The accuracy in its estimation has long been object of debate in the scientific community, as it is extremely complex to measure directly (requiring costly and a necessarily limited measuring apparatus) and thus it requires indirect estimation from oscillations of water vapour concentration in the air (Campbell and Norman, 1998). A huge variety of formulae exist to estimate ET, ranging from the simplest ones – employing only the air temperature, simply available from a meteorological station on site (Thornthwaite and Holzman, 1939) – up to complex structures that also account for micro-meteorological conditions and plant status – requiring not only meteorological data but also variables like temperature, soil moisture and vegetation indices (Penman, 1948). The numerous uncertainties (Ershadi et al., 2013; W. Kustas et al., 2004) in the computation of ET suggest that a good estimation approach could come from integrated modelling of the plant-environment interaction (Campbell and Norman, 1998), which can be all the more precise and continuous in time if it draws on all the available data – both gathered on-site and remotely-sensed (McCabe et al., 2016). In the plurality of existing models, different categories can be traced, according to the different possible distinction criteria. One is the application scale, with generally low-resolution models (e.g., Global Circulation Models) and higher-definition models, whose difference stands in the relative importance of the modelled phenomena, variable with the representation scale (Blöschl and Sivapalan, 1995). Another criterion is the structure of the intra-pixel energetical partition, with two main categories: single-source (Bastiaanssen et al., 1998; Su, 2002) and two-source models (P. Colaizzi et al., 2014; W. P. Kustas and Norman, 1999). Further differences emerge according to the way the energy balance closure is attained, with residual models computing one of the energy fluxes by enforcing the global balance (W. Kustas and Anderson, 2009) and others retaining physically based formulations for all fluxes and using other parameters to obtain energy balance closure (Corbari et al., 2011). Among these models, a special mention goes to the FEST-EWB (Corbari et al., 2011; Mancini, 1990) model, a distributed hydro-energetical model able to work with both satellite and on-ground data to reproduce all the components of the hydrological cycle at different scales. Its main perk is that the Land Surface Temperature (LST), which is required as an input in most models, is instead computed internally by coupling the energetical and water-mass balances and enforcing their closure. This main concept disengages the model from the LST availability, which for field applications is a great constraint (Sishodia et al., 2020): while point-wise LST data can be obtained continuously by inverting upwelling long-wave radiation measurements from a radiometer in a meteorological station, distributed data is necessarily subject to either private flights or publicly-available satellite overpasses (Heinemann et al., 2020). Although these latter range considerably in terms of temporal frequency and accuracy, they are available at most at daily frequency – and, in such a case, at relatively-low resolutions (Piles et al., 2014). This means that most models are able to work only sporadically, which can be incongruous with crop-monitoring necessities that require day-by-day – and even sub-daily – knowledge of the plant status (e.g., in

order to decide whether to enforce an irrigation event). FEST-EWB, on the other hand, can run seamlessly in time, using LST data only for calibration purposes and, thus, only when available. FEST-EWB has already performed in a wide variety of contexts, providing fairly positive results: snow cover estimation (Corbari et al., 2009); joint temperature-discharge model calibration (Corbari and Mancini, 2014a); high-resolution ET modelling (Corbari et al., 2020); smart irrigation forecast (Corbari et al., 2019).

The main focus of this PhD thesis work has been the improvement of hydrological modelling in agricultural applications. The first part covers a quality analysis on some kinds of satellite data that are usually employed in agricultural monitoring. This has been conceived as a premise, in order to provide more information about the quality and applicability of the data that are injected into hydro-energetical models and their possible detrimental effects. The second part focuses on the FEST-EWB model, analysing its relation with satellite information: first, a study on heterogeneity is performed, testing how the model reacts to data quality loss brought on by decreasing spatial resolution; then, a model development is discussed, in order to obtain a better representation of heterogeneous areas, operating a kind of disaggregation on satellite information; finally, a way to fully respect physically-based principles while using satellite data is explored, with the re-introduction of aerodynamic temperature – a variable long-overlooked because of its difficult measurability – within energetical modelling.

Part I

Materials and Methods

Chapter 2

Methodology

This chapter details all the approaches employed in this Thesis work. The first two Sections will deal mostly with satellite data analysis, while the others will focus more on model performance.

In Section 2.1, an algorithm to verify the hydrological consistency of satellite Surface Soil Moisture (SSM), by contrast with precipitation and irrigation data, is detailed. As satellite SSM data is widely-known to hold weak correlations with precipitation information (Dai et al., 1999; Sehler et al., 2019), a targeted analysis algorithm is presented in this Section, able to investigate these matters.

In Section 2.2, the overall comparison approach between a network of sensors for high-resolution crop monitoring and corresponding satellite measurements is traced. This is framed within a low-cost sensor citizen science project (Woods et al., 2019) aimed at improving the data quality and quantity from long-term hydrological monitoring networks. Data from different satellites will be contrasted with the on-ground measurements and their suitability to agricultural applications will be discussed.

Next, the main focus will shift towards the FEST-EWB distributed hydrological model, presented in detail in the following Section 2.3. It enjoys a long list of successful applications in the agricultural world and across all sorts of scales: from field to agricultural district (Corbari et al., 2013; Corbari et al., 2020; Ravazzani et al., 2017) and river basin scale (Corbari and Mancini, 2014a). FEST-EWB stands amongst other hydrological models for its scale flexibility and the joint enforcing of both the energy and water-mass balances for each pixel. Its main feature is probably the independence from Land Surface Temperature (LST) data availability, as the variable is computed internally to enforce the balances closure. This allows the model to perform continuous runs even during data scarce periods, preserving the evolution of basin system in terms of Soil Moisture dynamics.

In Section 2.4, the details of a scale analysis performed on the model are presented. This has been devised in order to understand the impact of input data spatial resolution on the model outputs, testing these responses in a heterogeneous, thus challenging from a resolution perspective, agricultural area. For this scale analysis, a combination of model runs and data aggregations has been employed, similarly to what performed by Ershadi et al. (2013) and Sharma et al. (2016) with the single-source SEBS model (Su, 2002). They both found much higher relative errors over latent heat estimation (>40%) when modelling with resolution-wise degraded data as opposed to the resolution degradation of model outputs (<30%) obtained using the original, high-resolution input data. A similar approach is taken on the FEST-EWB, to test its elasticity with changing

input data quality.

In Section 2.5, an extension for the FEST-EWB model is discussed, aimed at an improved modelling of heterogeneous areas. Most hydro-energetical models can be classified as either single-source (Bastiaanssen et al., 1998) or two-source (W. P. Kustas and Norman, 1999), depending on the formulation used for intra-pixel energy flux distinction. The former category treats the given pixel as homogeneous, while the latter differentiates the energy balance between the vegetated and non-vegetated internal fractions of the pixel. In this framework, FEST-EWB is something of an outsider, employing one single energy balance equation (as single-source models do) but partitioning the turbulent fluxes into a vegetated and a non-vegetated component (similarly to two-source formulations). This "hybrid" outlook provides an undoubtedly higher accuracy when dealing with relatively homogeneous areas, but can be less precise over heterogeneous ones. The structure of a two-source version of the model (called FEST-2-EWB) is discussed.

In Section 2.6, another possible extension to the FEST-EWB is discussed. A common assumption (P. D. Colaizzi et al., 2004) in Sensible Heat modelling is using the radiometric surface temperature as a surrogate of aerodynamic temperature, which should be the correct driving force of the process. This stems from a general belief that differences between the two are small, although many a study has shown this to be untrue, with absolute differences as high as 15°C (Choudhury et al., 1986; W. Kustas et al., 2007; Mahrt and Vickers, 2004). In this section, the methodology for the indirect estimation of aerodynamic temperature from sensible heat measurements is provided, together with possible ways to integrate it both "instantaneously" and continuously with the general FEST-EWB framework.

2.1 Hydrological Consistency Index

In this Section, an approach to contrast satellite with ground-retrieved data will be outlined. An algorithm has been developed to verify the hydrological consistency of satellite Surface Soil Moisture (SSM), by contrast with precipitation measurements. This originates from the fact that satellite SSM data is widely-known to provide weak correlations with precipitation information, with values as low as 0.11-0.26 in rural Kansas, U.S.A. (Dai et al., 1999) and 0.4 in Mediterranean Europe (Sehler et al., 2019). In order to identify possible underlying causes, some studies have adopted deeper analysis techniques. McCabe et al. (2008) worked on AMSR-E data in semi-arid Arizona, computing correlations between SSM anomalies and precipitation in the preceding hours, obtaining widely-ranging values (0.03-0.77). In the work by Meng et al. (2018), using ESA-CCI SSM data, it was shown that only 57% of the study area with non-null 24-h cumulative precipitation registered a positive SSM anomaly greater than 4%. For some reason, satellite SSM data seems to respond weakly to (on-ground measured) precipitation inputs, and little work has been done on similar situations involving irrigation.

The improved correlation index focuses on the physical consistency between the two mechanisms that regulate the water cycle in the superficial soil layer: water accretion (snow- and ice-melt, rainfall, or irrigation) and water depletion (evapotranspiration, surface runoff, or deep percolation).

The general algorithm of this Hydrological Consistency Index (HCI) is shown in Figure 2.1a. The algorithm evaluates the sign of the soil moisture variation "positively" or "negatively" according to the presence or absence of precipitation. In detail, for each soil moisture record in the dataset, the precedent soil moisture retrieval and the cumulated rainfall in the elapsed period are compared. A "positive agreement" (A+) is assigned for any day in which either (case a1) an increase in soil moisture corresponds to a non-null rainfall or (a2) a decrease in soil moisture is registered in the

absence of rainfall. On the other hand, a disagreement, or "negative agreement" (A–) is assigned if the opposite situations unfold, that is: either (b1) an increase in soil moisture is observed in absence of precipitation or (b2) a decrease in soil moisture is found even though a consistent amount of precipitation has been registered. As a further step, the case (b1) is classified differently if it verifies during an irrigation event, as the SSM increase can be explained by this artificial water input. In this case, the agreement is considered as "positive" and labelled as "irrigation-driven positive agreement" (IA+) as opposed to the cases (a1) and (a2), which can be seen as "rainfall-driven positive agreements".

An example application of the HCI over fictitious data is detailed in the right-hand panel of Figure 2.1. Each dot represents an SSM measurement, which is expressed in its SSM variation from the previous retrieval and the cumulated precipitation in between the two. The black lines represent the conceptual divides between the different scenarios. The vertical one (ΔSSM = 0 m^3 m^{-3}) is corrected to the dashed grey lines (ΔSSM = $\pm\xi$) to comply with the declared measurement error of the datasets. In this first application, a standard value (0.04 m^3 m^{-3} in volumetric ratio, 4.5% in corresponding saturation ratio) has been chosen for ξ, following the declared accuracy target for SMAP and SMOS data (Y. H. Kerr et al., 2010), also found to be quite correct in real-world applications (Wanders et al., 2012). When comparing datasets with a widely varying spatio-temporal resolution, this parameter can be tailored to each dataset characteristics. The horizonal black line in Figure 2.1b ($P_{CUM} = \zeta$) is set slightly higher than zero to prevent equating small precipitation amounts, generated by the spatial interpolation process, to full precipitation events. This threshold has been set to 0.5 mm for this first analysis, but different climates may require a different parameterization.

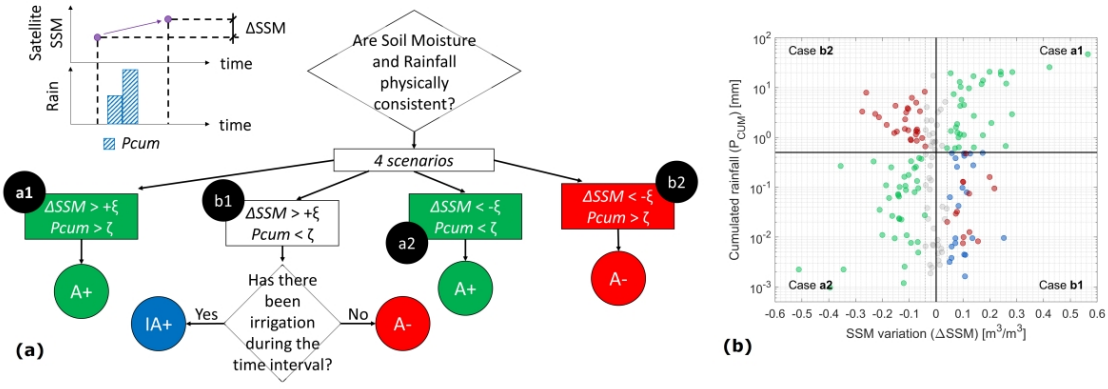

Figure 2.1: Flux diagram of the Hydrological Consistency Index (HCI) (a) and example application with fictitious data (b).

An ideal soil moisture dataset would display only positive agreements (either rainfall- or irrigation-driven). The amount of negative agreements recorded for a given soil moisture dataset can be seen as an indirect, application-oriented estimate of its error. The results of the developed methodology are also compared with Pearson and Spearman correlations, common simple statistical correlation indexes, to verify the improvements in discerning the relationship between SSM and precipitation and irrigation.

2.2 Ground sensor network for crop monitoring

This Section is devoted to the sensor network data analysis which will be detailed in the later Chapter 5. The employed sensors are able to collect solar illuminance, air temperature and soil moisture information. Two different Irrigation Water Needs (IWN) are formulated in Section 2.2.2, which will be used to exploit the data from the sensors to obtain some practically-oriented indicators to help in agricultural management. In the Sections 2.2.3 and 2.2.4, ancillary information about the pre-processing of illuminance data from the sensors and the steps required to derive Leaf Area Index are detailed.

2.2.1 Actual and potential evapotranspiration

Actual and Potential ET are useful parameters to determine the plant activity and will be used in the computation of the irrigation-oriented indexes.

The Potential Evapotranspiration (PET) is computed according to the general micro-meteorological conditions of the area, adopting Priestley-Taylor (Priestley and Taylor, 1972) equation (useful because of its lower data requirements with respect to the Penman-Monteith formulation) and using, as a preliminary approximation, a unitary crop coefficient (K_c):

$$PET = K_c \cdot 1.26 \frac{\Delta}{\Delta + \gamma} S_{IN} \tag{2.1}$$

$$\Delta = \frac{\mathrm{d}e_{SAT}}{\mathrm{d}T} \tag{2.2}$$

$$e_{SAT}(T) = e^*(T) = 0.6108 \cdot \exp\left(\frac{17.27 \cdot T}{T + 237.3}\right) \tag{2.3}$$

Where Δ is the local slope of the curve (Equation 2.2) relating Saturated Water Vapor Pressure (e_{SAT}, Pa) to Air Temperature (T, °C), γ (Pa K^{-1}) is the psychrometric constant, S_{IN} is the incoming short-wave radiation (W m^{-2}).

The Actual Evapotranspiration (ET) is then obtained by constraining the PET (Equation 2.1) with the soil moisture availability of each single field. ET is computed by multiplying the PET by a reduction coefficient: the α (Parlange et al., 1999) and β (Kutílek and Nielsen, 1994) functions, respectively for bare soil and vegetated fields.

$$\alpha = 0.082 \cdot SM + 9.173 \cdot SM^2 - 9.815 \cdot SM^3 \tag{2.4}$$

$$\beta = \begin{cases} 0 & SM \leq WP \\ \frac{SM - WP}{FC - WP} & WP \leq SM \leq FC \\ 1 & SM \geq FC \end{cases} \tag{2.5}$$

In particular, the β function is based on the concept that when the soil moisture value is lower than the field capacity (FC, the soil moisture amount right after superficial water is drained away), the vegetation stomata begin to close and transpiration decreases significantly, following the soil moisture dynamic and until it stops completely for soil moisture values less than or equal to the wilting point (WP, minimum soil moisture at which plant roots can still extract water from the soil).

2.2.2 Irrigation water needs

The sensors data have been used to power two distinct indicators, called Irrigation Water Needs (IWN), which have been designed for the purpose with the aim of assessing instantaneous crop irrigation needs. The first one, Evapotranspiration-based (IWN_{ET}) is defined as the amount of water required by the plants to transpire at full potential (i.e., without being limited by water availability), and is indirectly obtained by evaluating the difference between Potential (i.e., water-abundant, Equation 2.1) and Actual Evapotranspiration:

$$IWN_{ET} = PET - ET \tag{2.6}$$

Alternatively, the Soil-Moisture-based IWN (IWN_{SM}) has been defined as the amount of water the near-plant soil needs in order to achieve field capacity. This indicator follows the principle of triggering irrigation if the plant is in "stressful" conditions, where this state is defined by the Soil Moisture Crop Stress Threshold (CST), as detailed in Allen et al. (1998). The threshold is defined by:

$$CST = FC - p \cdot (FC - WP) \tag{2.7}$$

$$p = p_{stand} + 0.04 \cdot (5 - ET_c) \tag{2.8}$$

where p is the fraction of the Total Available Soil Water (TAW) that can be depleted from the root zone before moisture stress occurs, and depends on the specific crop and climatic parameters (represented by the Evapotranspiration under standard conditions, ET_c, computed following Allen et al. (1998). A reference value for p (p_{stand}) is proposed by Allen et al. (1998) for several crops. The p factor normally varies from 0.30 (70% of the FC–WP range provides stressful conditions for the plants) for shallow-rooted plants at high PET rates (> 8 mm d^{-1}) to 0.70 for deep-rooted plants at low ET rates (< 3 mm d^{-1}). The final SM-based IWN is thus computed as:

$$IWN_{SM} = \begin{cases} 0 & \text{if SM} > \text{FC} \\ (FC - SM) \cdot z & \text{if SM} < \text{FC} \end{cases} \tag{2.9}$$

Where z identifies the crop-specific root zone depth. By formulation, the IWN_{SM} assumes that every irrigation event is aimed at restoring the SM status to field capacity conditions, avoiding water losses by superficial runoff.

2.2.3 Radiation-Illuminance conversion

In order to elaborate the computations detailed above, some pre-processing steps need to be performed on the data gathered by the sensors. Each sensor provides the amount of solar radiation it receives in the form of illuminance, which is the total luminous flux incident on the sensor surface per unit area. Thus, it is an areal average of the luminous energy emitted in space by a luminous source. The measurement unit is the lux (lx), related to other luminosity units by Equation 2.2.3:

$$Illuminance\,[lx] = \frac{Luminous\ Energy}{Area}\left[\frac{lm}{m^2}\right] = \frac{Luminous\ Intensity}{Area}\left[\frac{cd \cdot sr}{m^2}\right] \tag{2.10}$$

The transition from luminosity variables to radiative ones is mediated by the luminosity function $y(\lambda)$ (Michael et al., 2020). This stems from the fact that the intrinsic meaning of luminosity

variables is to "translate" energetical inputs to effects on the human eye. The luminosity function is a wavelength-weighted relation between Watts and Lumens that accounts for the human eye sensibility to different energy wavelengths. In particular, the human eye is most sensitive to monochromatic radiation at 555 nm, and is unable to perceive energy outside the visible bounds of the electromagnetic spectrum (380–400 nm up to 700–780 nm). This means that the Lumen–to–Watt (Lux–to–Watt/m^2 in this case) conversion is not "stable" across all the wavelengths of the visible spectrum, but shows a peak at 555 nm (where 1 Watt = 683 Lumens) and has proportionally-lower values for other wavelengths. The data used in this thesis is the one provided in 2006 (last update) by the *Commission Internationale de l'Eclariage* (CIE) (Sliney, 2007). This means that the Lumen–to–Watt conversion factor (χ) is obtained as follows:

$$\chi = \phi \cdot \int_0^\infty y(\lambda)\,\Gamma(\lambda)\,d\lambda \tag{2.11}$$

Where ϕ is the peak-sensitivity conversion coefficient (683 lm/W) and $\Gamma(\lambda)$ is the relative solar radiative spectrum, normalized over the whole shortwave energy. The standard solar spectrum set by the American Society for Testing of Materials (ASTM) in its Air Mass (AM1.5) G173 Global Tilt data can be used to solve the integral. The integral computation yields a value of 0.1688, meaning that the final conversion factor is equal to 116 lx to 1 W m^{-2}. This procedure follows the guidelines set by Michael, et al. (2020).

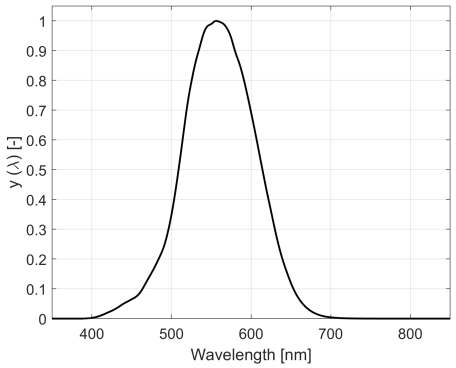

Figure 2.2: Luminosity function $y(\lambda)$.

2.2.4 Leaf Area Index

One major interest with radiation data is their conversion to Leaf Area Index (LAI). This parameter represents the total green leaf area normalized over the pixel area, it is globally associated with vegetation density and growth and is a major driver in photosynthesis and plant respiration processes (Watson, 1947). Apart from direct (and leaf-destructive) measurement (Breda, 2003), LAI can be obtained as a canopy gap fraction from Beer-Lambert law (Nilson, 1971). As the vegetation shadow reduces the incoming radiation, the resulting radiation dampening ratio is strictly correlated to the dampening medium (the canopy density), which is in turn related to LAI (Campbell and Norman, 1998) (Equation 2.2.4).

$$LAI = -\ln \frac{\left(\frac{S_{sens}}{S_{sun}}\right)}{K(\psi)} \tag{2.12}$$

$$K(\psi) = \frac{\sqrt{x^2 + \tan\psi^2}}{x + 1.774 \cdot (x + 1.182)^{-0.733}} \tag{2.13}$$

Where S_{sens} (W m^{-2}) identifies the radiation reading of a sensor placed in a vegetated field, while S_{sun} (W m^{-2}) is the unperturbed solar radiation reaching the ground (it can be obtained both

from an independent radiometer or from sensors placed in bare soil areas). The (nondimensional) beam extinction coefficient K depends on the solar zenith angle (ψ) and the leaf spatial distribution index (x). This latter is a parameter accounting for the presence of any preferential direction for the leaves spatial distribution, with a unitary value identifying a spherical (isotropic) distribution.

2.3 FEST-EWB

The FEST-EWB (Flash–flood Event–based Spatially–distributed rainfall–runoff Transformation Energy-Water Balance) model is a distributed hydrological energy-water balance model (Corbari et al., 2011; Mancini, 1990). It structure prescribes a pixel-by-pixel joint solution of the energy and water mass balance equations (Eq. 2.14) at each calculation step. The two equations are linked by the Latent Heat / Evapotranspiration correspondence (Eq. 2.15), and the solution to this system is found iteratively by searching for the surface temperature that ensures the closure of both balances. Thus, this surface temperature is, mathematically speaking, the result of an equilibrium (hence its name, Representative Equilibrium Temperature, or RET), quite akin to its real-world correspondent, the Land Surface Temperature (LST), itself the final result of a thermodynamic equilibrium in the superficial soil layer. The list of variables used by the model is detailed in Table 2.1, while the general model structure is provided in Figure 2.3.

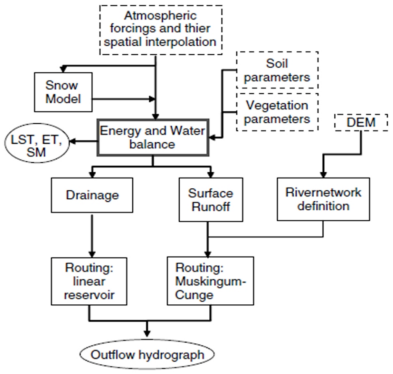

Figure 2.3: FEST-EWB diagram.

$$\begin{cases} Rn - G - (H_S + H_C) - (LE_S + LE_C) = \Delta W/\Delta t \\ \Delta SM/\Delta t = (P - R - PE - ET)/z \end{cases} \tag{2.14}$$

$$LE = LE_S + LE_C = \lambda_w \rho_w ET \tag{2.15}$$

where the first equation refers to the water mass balance and the second to the energy balance, with the "s" and "c" subscripts identifying the "soil" and "canopy" components of the fluxes, respectively. The mathematical stability of this system of equations is generally guaranteed by the assumption of negligible storage terms ($\Delta W/\Delta t$), usually safe at low spatial resolutions (Meyers and Hollinger, 2004). In the following subsections, the single energetical fluxes will be shown in detail.

Table 2.1: List of symbols and variables employed by FEST-EWB.

Parameter	Meaning	Unit
c_P	Specific heat of humid air	J kg^{-1} K^{-1}
d	Zero-plane displacement height	m
$e^* = e_{SAT}$	Saturation vapour pressure	kPa
e_A	Air vapour pressure	kPa
ET	Evapotranspiration	mm
FC	Field Capacity	m^3 m^{-3}
f_V	Vegetation Fraction	–
G	Soil Heat Flux	W m^{-2}
g_{th}	Soil Thermal Conductivity	W m^{-1} K^{-1}
H	Sensible Heat Flux	W m^{-2}
L	Monin-Obukhov length	m
LE	Latent Heat Flux	W m^{-2}
LAI	Leaf Area Index	m^2 m^{-2}
P	Precipitation rate	mm
PE	Drainage flux	mm
R	Runoff flux	mm
R_A, R_{ABS}	Vegetation and Bare-Soil Aerodynamic resistance	s m^{-1}
R_C	Canopy / Crop resistance	s m^{-1}
RET	Representative Equilibrium Temperature	K
RH	Air humidity	-
R_{LD}	Longwave downwelling radiation	W m^{-2}
Rn	Net Radiation	W m^{-2}
R_S	Soil resistance	s m^{-1}
$R_{S,min}$	Minimum stomatal resistance	s m^{-1}
R_{soil}	Wet-soil resistance	s m^{-1}
S_{IN}	Shortwave downwelling radiation	W m^{-2}
SM	Soil Moisture	m^3 m^{-3}
SM_{SAT}	Saturation Soil Moisture	m^3 m^{-3}
T_{AIR}	Air Temperature	°C
T_{zero}	Temperature below the first soil layer	°C
w	Horizontal wind velocity	s m^{-1}
WP	Wilting Point	m^3 m^{-3}
z	Depth of the first soil layer	m
Z_{oh}	Roughness length governing heat and vapour transfer	m
Z_h	Height of humidity measurements	m
Z_{om}	Roughness length governing momentum transfer	m
Z_m	Height of wind measurements	m
α_{ALB}	Albedo	-
γ	Psychrometric constant	kPa °C^{-1}
$\Delta W/\Delta t$	Energy storage terms	W m^{-2}
ε_{atm}, ε_{soil}	Atmosphere and Soil emissivity	-
κ	Von Karman constant	-
λ_w	Latent Heat of Vaporization for water	J kg^{-1}
ρ_a	Air density	kg m^{-3}
ρ_w	Water density	kg m^{-3}
σ	Stefan-Boltzmann constant	W m^{-2} K^{-4}
Ψ_H	Atmospheric stability function for heat and vapour transfer	-
Ψ_M	Atmospheric stability function for momentum transfer	-

2.3.1 Net Radiation

Net Radiation is the global resultant of four distinct radiative fluxes, each of which can be characterized as incoming or outgoing and as short- or long-wave. These components are displayed in Equation 2.16:

$$Rn = S_{IN}(1 - \alpha_{ALB}) + \varepsilon_{atm}\sigma T_{AIR}^4 - \varepsilon_{soil}\sigma RET^4 \tag{2.16}$$

The first element identifies the net shortwave radiation (Rn), featuring the incoming amount (a meteorological input to the model) and the surface albedo (α_{ALB}, a vegetation-related input either chosen according to literature or obtained from satellite observations). The last two elements of the equation represent the longwave radiation fluxes, respectively incoming from the lower atmosphere and outgoing as thermal emission of the surface. The atmosphere emissivity (ε_{atm}) is usually obtained from models that account for cloud cover fraction (Sedlar and Hock, 2009).

2.3.2 Soil Heat Flux

The Soil Heat Flux (G) identifies the energy transferred from the superficial soil layer down to the lower soil strata via conduction, and has a linear relation with RET (Eq. 2.17):

$$G = \frac{g_{th}}{z}(RET - T_{zero}) \tag{2.17}$$

Where the soil thermal conductivity is parametrized on soil water tension, i.e., a combination of soil texture and soil moisture conditions, through the McCumber-Pielke equation (1981).

2.3.3 Sensible Heat Flux

Sensible Heat encompasses the energy transfers between surface and lower atmosphere, driven by a temperature gradient between the two. In the model, it is formulated as two separate components, accounting for soil and canopy contributions (Eq. 2.18):

$$H = H_S + H_C = (1 - f_V)\rho_A c_P \frac{RET - T_{AIR}}{R_{ABS}} + f_V \rho_A c_P \frac{RET - T_{AIR}}{R_A} \tag{2.18}$$

The aerodynamic resistance for the canopy is obtained as follows (Thom, 1975):

$$R_A = \frac{1}{\kappa^2 w}\left[\ln\frac{Z_m - d}{Z_{om}} - \Psi_M\left(\frac{Z_m - d}{L}\right)\right]\left[\ln\frac{Z_h - d}{Z_{oh}} - \Psi_H\left(\frac{Z_h - d}{L}\right)\right] \tag{2.19}$$

$$R_{ABS} = \frac{1}{\kappa^2 w}\left[\ln\frac{Z_m - d(Z_{low})}{Z_{om}(Z_{low})} - \Psi_M\left(\frac{Z_m - d(Z_{low})}{L}\right)\right]\left[\ln\frac{Z_m - d(Z_{low})}{Z_{oh}(Z_{low})} - \Psi_H\left(\frac{Z_m - d(Z_{low})}{L}\right)\right] \tag{2.20}$$

It depends on a series of roughness lengths, related to the vegetation height, and on the wind intensity: low wind speeds and jagged surfaces create slow-moving air pockets which decrease the water evaporation rate, while the opposite situation enhances the turbulent air mixing and energy exchanges. The equivalent resistance for bare soil conditions (R_{ABS}) shares the same formulation but with a close-to-null ($Z_{low} = 0.1$ m) vegetation height (Eq. 2.20).

According to strict theoretical formulations, the temperature gradient driving the sensible heat flux is established by the aerodynamic temperature. However, for most of the FEST-EWB applications, and in line with common practices in literature, the aerodynamic temperature has been assumed equal to the surface temperature (P. D. Colaizzi et al., 2004).

2.3.4 Latent Heat Flux

This component describes the amount of heat released in the atmosphere as a result of the Evapotranspiration process (Eq. 2.15). Its computation is performed through the Penman-Monteith formulation (Monteith, 1965; Penman, 1948), with the addition of a differentiated formulation (Eq. 2.21) for the bare soil and canopy contributions:

$$LE = LE_S + LEc = (1 - f_V)\frac{\rho_A c_P}{\gamma}\frac{e^* - e_A}{R_{ABS} + R_S} + f_V\frac{\rho_A c_P}{\gamma}\frac{e^* - e_A}{R_A + R_C} \tag{2.21}$$

Both components feature the saturation vapour pressure, function of the surface temperature and the actual vapour pressure, determined by the air temperature and relative humidity (Campbell and Norman, 1998). The canopy and soil resistances are detailed in Equations 2.22 and 2.23, and feature a dependence on soil moisture conditions, together with components accounting for vegetation characteristics (R_{Smin}) and density (LAI) (Jarvis, 1976).

$$R_C = \frac{R_{Smin}}{LAI}\frac{FC - WP}{SM–WP} \tag{2.22}$$

$$R_S = 3.5\left(\frac{SM_{SAT}}{SM}\right)^{2.3} + R_{Soil} \tag{2.23}$$

2.3.5 Parameters

More or less explicitly, all the terms in Equations 2.14–2.23 are functions of the input soil and vegetation parameters. These can be either stationary or time-varying. Soil and terrain parameters belong to the former category and include descriptors of the soil water motion (e.g., hydraulic conductivity, pore-size index, bubbling pressure, residual and saturation water contents, active soil depth) and geo-morphological characteristic of the basin (e.g., aspect, elevation, slope). Vegetation (e.g., plant height, vegetation fraction and leaf area index) and meteorological (e.g., rainfall, incoming shortwave radiation, air temperature and relative humidity) parameters, on the other hand, mostly belong to the "time-varying" category. Minimum stomatal resistance (depending on the specific plant) and wet-soil resistance to evaporation (depending on the soil type) are generally assumed to be fixed with time. Finally, all input data can be provided either as single-valued or with their own spatial distribution, depending on data availability.

2.3.6 Calibration and Validation procedure

The traditional calibration procedure for hydrological models features point-wise measurements of the calibration variable, like river discharge (e.g. for flood management purposes) or soil moisture (e.g. for agricultural applications) collected at specific points, which are limited in number and only represent a part of the basin hydrological cycle. The FEST-EWB hydrological model, on the other hand, allows a pixel-by-pixel calibration, particularizing the calibration parameters with a spatial heterogeneity derived from the calibration variable patterns (Corbari and Mancini, 2014a; Corbari and Mancini, 2014b; Paciolla, Corbari, Hu, et al., 2021).

The calibration of the FEST-EWB distributed hydrological model is performed by means of a pixel-by-pixel comparison between the modelled Representative Equilibrium Temperature (RET) and the remotely-sensed Land Surface Temperature (LST). The calibration process is regulated by

the pixel-by-pixel minimization of the average model error, defined as the objective function O (Eq. 2.24).

$$O = \frac{1}{n}\sum_{i=1}^{n}(RET_i – LST_i) \tag{2.24}$$

Where n stands for the total number of calibration data available. The pixel-by-pixel approach of the calibration process allows to refine the spatial heterogeneity of the calibration parameters involved.

In previous applications of the model (Corbari and Mancini, 2014b), five main parameters have been found to be critical for the calibration process: the Brooks-Corey (or pore-size distribution) index, the saturated hydraulic conductivity, the soil depth, the minimum stomatal resistance and the wet-soil resistance to evaporation. Of these, the first three are mainly related to water geodynamics, while the last two are more closely connected to the ET process.

As the model can use LST information for the calibration phase and does not need flux tower data as an input, energy fluxes can be used for the validation. Moreover, since model inputs and energy fluxes measurements originate from independent sources, a given the integrated nature of the model, which simulates the entire water cycle, calibration and validation can be performed over the same time window, without the need of identifying a calibration-only and a validation-only period.

2.4 Scale analysis

For the Rapitalà case study (which will be described in Section 3.3), proximal-sensing data of land surface temperature and vegetation indices was available from airplane flight at the spatial resolution of 1.7 m (vegetation indices were resampled to this resolution from their native 0.7 m for uniformity reasons), relatively high in the field of agricultural applications (Mikhail et al., 2001). This has allowed to test the importance of data resolution on the FEST-EWB, by means of a scale analysis (Figure 2.4). Firstly, the model outputs (Latent and Sensible Heats, Soil Moisture and Representative Equilibrium Temperature) have been upscaled to some specific spatial resolutions. Then, the input data have been aggregated to the same scales and fed to the model, which is calibrated anew for each spatial resolution employing the same calibration function of the highest-resolution calibration. The model results, either originated from the upscaling of the native-resolution results or after the model calibration employing upscaled input data, have then been compared.

The scales chosen for the analysis have been selected by similarity with those of some common satellite products: 10 m for Sentinel 2; 30 m for Landsat (multispectral); 250 m for MODIS Visible and 1000 m for MODIS Thermal. To avoid reprojections that could alter the original data, the target scales are picked among the multiples of the native scale (1.7 m): 10.2 m for similarity with Sentinel, 30.6 m with Landsat, 244.8 m for MODIS Visible and 734.4 m (the total extension of the area) for MODIS Thermal.

The upscaling has been performed through simple averaging of the original data to the target resolutions. The process is detailed in the following, as an example, for the production of the 10.2 m upscaled product. The ratio (6:1) between the target (10.2 m) and native (1.7 m) spatial resolutions indicates that any target pixel covers 36 (6x6) native pixels. The value to be assigned to the target pixel is obtained as the average of the 36-pixel sample. For each sample, also the

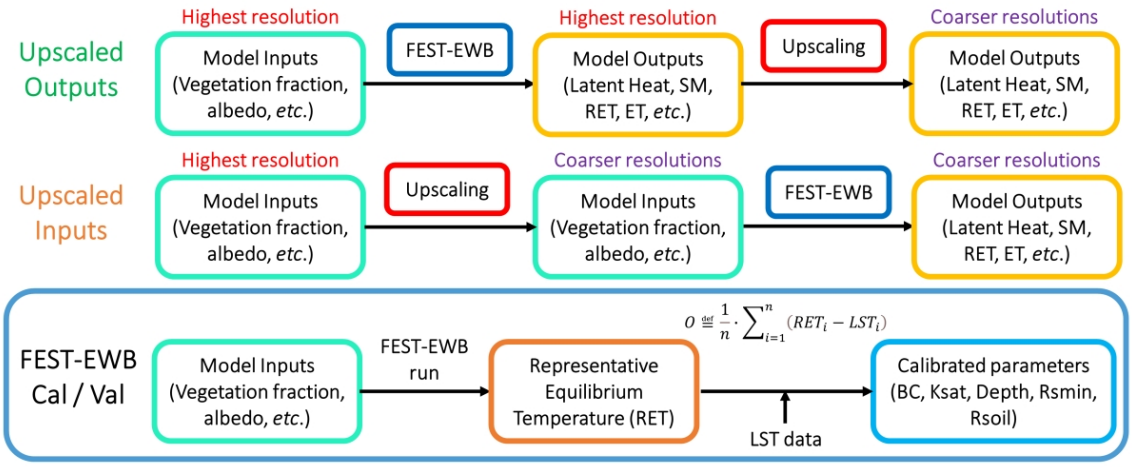

Figure 2.4: Flowchart of the two approaches compared in the scale analysis. The calibration/validation process for the FEST-EWB model is also detailed in the lowermost box.

standard deviation is retained as an indirect measure of the pixel heterogeneity. Thus, for each final product, both an average and a standard deviation map are stored. The process is repeated, always starting from the native 1.7 m spatial resolution, for all the scales involved in the analysis.

2.5 FEST-2-EWB

In this section, the FEST-2-EWB (Flash–flood Event–based Spatially–distributed rainfall–runoff Transformation 2-source Energy-Water Balance) model is presented, as an extension to the original, hybrid-structured, FEST-EWB model described in Section 2.3. The main assumption is that each pixel can be split into a vegetated and a non-vegetated fraction, according to its vegetation fraction parameter (f_V). As a step forward from the original model, each pixel sub-area is assumed in independent thermal equilibrium with its own subsoil and atmosphere surface layer. This means that the superficial temperatures at which these equilibria are reached are separate for the two sub-areas, and are identified as the Soil Temperature (T_{SOIL}) and the Crop Temperature (T_{CROP}). The original system of equation (Eq. 2.14) is thus split into Equations 2.25–2.34.

$$Rn_{SOIL} - G_{SOIL} = LE_{SOIL} + H_{SOIL} \tag{2.25}$$

$$Rn_{SOIL} = S_{IN}(1 - \alpha_{ALB,S}) + R_{LD} - \varepsilon_S \sigma T_{K,soil}^4 \tag{2.26}$$

$$G_{SOIL} = \frac{g_{th}}{z}(T_{soil} - T_{zero}) \tag{2.27}$$

$$LE_{SOIL} = \frac{\rho_A c_P}{\gamma} \frac{e^*(T_{soil}) - e_A}{R_{ABS} + R_S} \tag{2.28}$$

$$H_{SOIL} = \rho_A c_P \frac{T_{soil} - T_{air}}{R_{ABS}} \tag{2.29}$$

$$Rn_{CROP} - G_{CROP} = LE_{CROP} + H_{CROP} \tag{2.30}$$

$$Rn_{CROP} = S_{IN}(1 - \alpha_{ALB,C}) + R_{LD} - \varepsilon_C \sigma T_{K,crop}^4 \tag{2.31}$$

$$G_{CROP} = \frac{g_{th}}{z}(T_{crop} - T_{zero}) \tag{2.32}$$

$$LE_{CROP} = \frac{\rho_A c_P}{\gamma} \frac{e^*(T_{crop}) - e_A}{R_A + R_C} \tag{2.33}$$

$$H_{CROP} = \rho_A c_P \frac{T_{crop} - T_{air}}{R_A} \tag{2.34}$$

With respect to the original equations, the only addition concerns a slightly differentiated emissivity for soil (ε_S) and canopy (ε_C) for longwave emitted radiation, with two distinct values instead of the global one employed in Equation 2.16.

The energy balances structure is organized such that their closure is performed both at subpixel and global pixel level, by computing these latter as shown with a generic quantity X in the following Equation 2.35.

$$X_{pixel} = (1 - f_V) \cdot X_{SOIL} + f_V \cdot X_{CROP} \tag{2.35}$$

Finally, as is usual practice for two-source energetical models (W. Kustas and Anderson, 2009; Norman et al., 1995), a pixel-level "global" representative temperature is obtained from the two subpixel temperatures. This equivalent pixel-level temperature, which is necessary for model output interaction with outsourced satellite data, is obtained from the longwave upwelling radiation balance (Eqs. 2.36–2.37):

$$R_{L,UP}{}^{(pix.)} = (1 - f_V) \cdot R_{L,UP}{}^{(S)} + f_V \cdot R_{L,UP}{}^{(C)} \tag{2.36}$$

$$RET^4 \approx (1 - f_V) \cdot T_{SOIL}^4 + f_V \cdot T_{CROP}^4 \tag{2.37}$$

The overall pixel temperature is identified with the acronym RET, which stands (again) for Representative Equilibrium Temperature, by usage similarity with the RET from FEST-EWB. However, the two critically differ from a conceptual point of view: the FEST-EWB RET is the temperature that closes the energy balance for the overall pixel, whereas the FEST-2-EWB RET is the representative radiative temperature for the pixel, which joins the two fraction-level temperatures that actually close the single energy balances for their respective pixel sub-areas.

The calibration/validation procedure is the same as for FEST-EWB. The calibration involves the comparison between the modelled surface temperature (RET) and the estimated one (LST), with five main calibration parameters: active soil depth, hydraulic conductivity at saturation, Brooks-Corey (pore size) index, minimum stomatal resistance and wet-soil evaporation resistance.

With respect to the original FEST-EWB structure, this expansion allows to compute two additional outputs (T_{SOIL} and T_{CROP}), provided the same input data required by FEST-EWB. More than gaining two extra outputs, the main rationale for working on this extension has come from the necessity of differentiating the contributions to the energy balance in heterogeneous areas. Crop temperatures have been found to be generally lower than soil temperatures in heterogeneous scenarios (Bian et al., 2017; Nieto et al., 2019), and this holds even for more homogeneous crops, although with a heavier dependency on the amount of incoming radiation (P. D. Colaizzi et al., 2012). This means that, when assuming one single temperature for a heterogeneous pixel (e.g., for single-source models), this temperature is actually somewhere in between a cooler canopy temperature (which powers plant transpiration) and a warmer soil temperature (which determines water evaporation

from the soil). By estimating total Evapotranspiration with just one global temperature (Eq. 2.14), FEST-EWB is expected to overestimate the canopy contribution and underestimate the soil one. For agricultural applications, since ET is a major indicator of plant water consumption, this potential overestimation could lead to erroneous amplification of crop yield or irrigation requirements, with consequent produce prevision error or water resource waste. By setting two distinct temperatures in regulating the energetical balances of soil and vegetation, a more accurate modelling is expected to be obtained in all vegetation conditions, with the more remarkable difference expected in the most heterogeneous scenarios (vegetation fraction around half of the pixel). The activities detailed in the following Chapter 7 are aimed at proving these expected results.

2.6 FEST-AeroT

The aerodynamic temperature (T_{AERO}) identifies an extrapolated value associated with an "effective depth" within the canopy, which is the origin of the Sensible Heat Flux (Boulet et al., 2012; W. Kustas et al., 2007). This makes this temperature the primary driver of Sensible Heat transmission, instead of the more commonly used radiometric temperature. However, numerous studies have shown how the two may differ considerably, leading to potentially large errors in evapotranspiration estimates (Choudhury et al., 1986; Verhoef et al., 1997). Focusing only on the sign of the temperature divergence (LST–T_{AERO}), Mahrt and Vickers (2004) obtained mixed results in an arboreal environment, as did Colaizzi et al. (2004), while both Chebbouni et al. (1996) and Kustas et al. (2007) found more univocal relations, with the radiometric temperature consistently the highest, in some cases with big margins (by up to 20-25°C). While no clear direction was found for the divergence, some of these studies tried to link it to its boundary conditions, both meteorological and vegetation-related. Mahrt and Vickers (2004) found a non-negligible positive dependency of the temperature divergence on incoming solar radiation (S_{IN}), also testing dependencies on Leaf Area Index (LAI) and Soil Moisture (SM) with less conclusive results. They also proposed a linear relation based on S_{IN}, which was also employed by Kustas et al. (2007), who however found much higher differences between the two temperatures and a non-negligible range of variation of the relation results on SM. A more recent use of T_{AERO} can be seen in the work of Mallick et al. (2015) and following, where T_{AERO} reprises its role as main driver of the Sensible Heat exchange, although it is seldom employed as an explicit variable. In the following subsections, the analysis main points will be detailed:

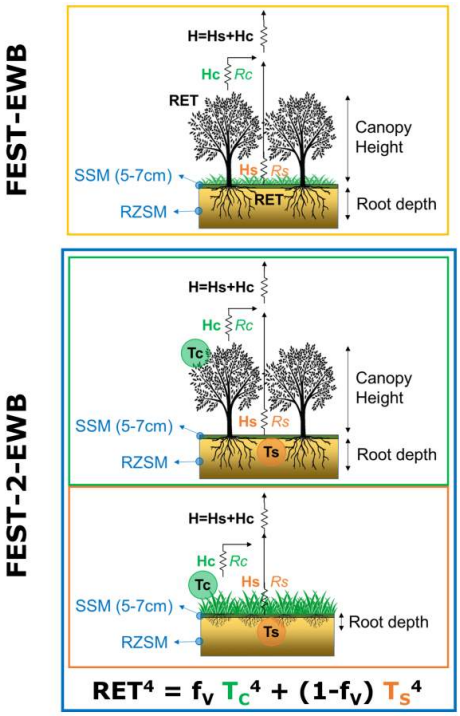

Figure 2.5: Models schematic fluxes

1. the aerodynamic resistance parametrization necessary for the estimation of T_{AERO} from Sen-

sible Heat measurements;

2. the preliminary models employed to assess the effect of T_{AERO} on Latent Heat;
3. the parametrization of T_{AERO} for continuous usage within the model
4. the final model form encapsulating T_{AERO}

This analysis paradigm is detailed in Figure 2.6.

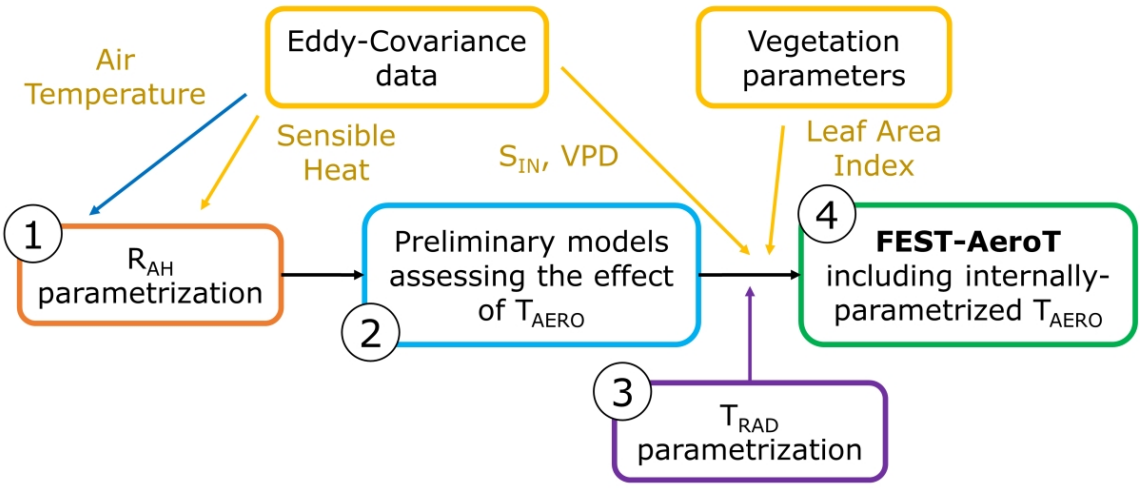

Figure 2.6: Aerodynamic Temperature analysis flowchart

2.6.1 Resistance parametrization

The accurate definition of Sensible Heat Flux, as opposed to commonly-known formulations such as the one employed in FEST-EWB (Eq. 2.18) is the following:

$$H = \rho_A c_P \frac{T_{AERO} - T_{AIR}}{R_A} \tag{2.38}$$

Thus, it is possible to obtain T_{AERO} estimations indirectly, starting from Sensible Heat measurements (together with air temperature ones), and through a modelling of the aerodynamic resistance. Indeed, a wide variety of formulae exist for this parameter, changing wildly in characteristics and range of application. In order to identify the formulation of R_A best suited to the integration in FEST-EWB, nine different formulae have been compared, similarly to the work by Liu et al. (2007), listed in Table 2.2.

In the table, "MOST" identifies the verification of the Monin-Obukhov Similarity Theory (Foken, 2006; Monin and Obukhov, 1954), that is the theoretical structure of logarithmic integral gradient of the wind and temperature profiles over the surface layer. This features the stability parameters, which correspond to the normalization over the Monin-Obukhov length (L) of the wind and temperature measurement height (ζ), and the momentum (ζ_m) and temperature (ζ_h)

Table 2.2: Aerodynamic resistance parametrizations.

Source	Formulation	Assumption
Thom, 1975	$R_A = \frac{1}{\kappa^2 w}\left[\ln\left(\frac{Z_m-d}{Z_{om}}\right) - \Psi_M(\zeta)\right]\left[\ln\left(\frac{Z_h-d}{Z_{oh}}\right) - \Psi_H(\zeta)\right]$	MOST $Z_{om} \neq Z_{oh}$
Thom (simpl.)	$R_A = \frac{1}{\kappa^2 w}\ln\left(\frac{Z_m-d}{Z_{om}}\right)\ln\left(\frac{Z_h-d}{Z_{oh}}\right)$	MOST $Z_{om} \neq Z_{oh}$
Yang et al., 2001	$R_A = \frac{1}{\kappa^2 w}\left[\ln\left(\frac{Z}{Z_{om}}\right) - \Psi_M{}^{(Y)}(\zeta,\zeta_m)\right]\left[\ln\left(\frac{Z}{Z_{oh}}\right) - \Psi_H{}^{(Y)}(\zeta,\zeta_h)\right]$ $\zeta = \left[R_I \frac{[\ln(\frac{Z}{Z_{om}})]^2}{\ln(\frac{Z}{Z_{oh}})}\frac{Z}{Z_{om}}\right] \div \left[1 - 2R_I\frac{1-Z_{om}/Z}{1-Z_{oh}/Z}\cdot P_Y\right]$ $P_Y \approx \sum c_{ijk}[\ln(-R_I)]^i\left[\ln\left(\ln\frac{Z}{Z_{om}}\right)\right]^j\left[\ln\left(\ln\frac{Z}{Z_{oh}}\right)\right]^k$	MOST $Z_{om} \neq Z_{oh}$
Choudhury et al., 1986	$R_A = \frac{1}{\kappa^2 w}\left[\ln\left(\frac{Z-d}{Z_{om}}\right)\right]\left[\ln\left(\frac{Z-d}{Z_{oh}}\right)\right](1-\beta\, R_I)^{-3/4}$	Semi-empirical $Z_{om} \neq Z_{oh}$
Viney, 1991	$R_A = \frac{1}{\kappa^2 w}\left[\ln\left(\frac{Z-d}{Z_{om}}\right)\right]\left[\ln\left(\frac{Z-d}{Z_{oh}}\right)\right][a + b(-R_I)^c]^{-1}$ With a, b, c empirical relations on Z	Semi-empirical $Z_{om} \neq Z_{oh}$
Verma et al., 1976	$R_A = \frac{1}{\kappa^2 w}\left[\ln\left(\frac{Z-d}{Z_{om}}\right)\right]^2(1-16\, R_I)^{-1/4}$	Empirical $Z_{om} = Z_{oh}$
Hatfield et al., 1983	$R_A = \frac{1}{\kappa^2 w}\left[\ln\left(\frac{Z-d}{Z_{om}}\right)\right]^2(1+\beta\, R_I)$	Empirical $Z_{om} = Z_{oh}$
Mahrt and Ek, 1984	$R_A = \frac{1}{\kappa^2 w}\left[\ln\left(\frac{Z-d}{Z_{om}}\right)\right]^2\left[\frac{1+c\sqrt{-R_I}}{1+c\sqrt{-R_I}-15R_I}\right]$ with $c = \left[75\kappa^2\sqrt{\frac{Z+Z_{om}}{Z_{om}}}\right] \div \left[\ln\left(\frac{Z+Z_{om}}{Z_{om}}\right)\right]^2$	Empirical $Z_{om} = Z_{oh}$
Xie, 1988	$R_A = \frac{1}{\kappa^2 w}\left[\ln\left(\frac{Z-d}{Z_{om}}\right)\right]\left[\ln\left(\frac{Z-d}{Z_{oh}}\right)\right]\left[1 + \frac{\left[1-16R_I\ln\frac{Z-d}{Z_{om}}\right]^{-1/2}}{\ln\left(\frac{Z-d}{Z_{om}}\right)}\right]$	Empirical $Z_{om} = Z_{oh}$

sink heights, respectively. The Monin-Obukhov length, together with the Richardson number (R_I, J. Hunt, 1998), are abstract quantities that are widely employed in the assessment of atmospheric stability. Their equations are:

$$L = \frac{-\rho_A c_P w_{sh}^3 T_{AIR}}{\kappa g H} \tag{2.39}$$

$$R_I = \frac{g}{T_{AIR}}\frac{(T_{AIR} - T_{SURF})(Z-d)}{w^2} \tag{2.40}$$

While the Monin-Obukhov length is a characteristic scale of surface layer turbulence, the Richardson number accounts for the influence of atmospheric stability on the flux-gradient relationship in the surface layer.

Among these formulae, the Thom formulation is widely employed in literature, mainly because of its low parameter requirements and its computational simplicity. It is employed also in the classic FEST-EWB model, most of the times in its simplified, neutral-conditions version, neglecting the instability components (Ψ_M, Ψ_H).

2.6.2 Test models

In order to assess possible effects of employing T_{AERO} over Latent Heat estimation, two test versions of FEST-EWB have been developed. Both start from the assumption that the Sensible Heat measurement from EC stations is acquired as a model input, so that H is not simulated by the model and is considered a constant in the energy water balance. This shifts all the focus on the Latent Heat, trying to shed light on what happens to the energy balance when one flux (the Sensible Heat) is "captured" perfectly by the model. The first model ("Test Model 1") uses the classical FEST-EWB formulation (Eq. 2.21) for Latent Heat, with the following energy balance equation:

$$Rn - G - H^{(const.)} - LE = 0 \tag{2.41}$$

The second model ("Test Model 2") highlights the role of the aerodynamic temperature in the latent heat transmission. This is done by acknowledging (Mallick et al., 2015) that the transpiration water flux can be split into two successive phases: (a) a motion from the inner leaf stoma to the leaf surface and (b) the transition from the leaf surface to the external atmosphere. The starting conditions can be assumed as an environment with 100% relative humidity (saturation conditions) and temperature equal to the radiant temperature of the leaf (T_{RAD} or, in the model framework, RET). The leaf surface can be assumed at an almost-saturated relative humidity, and the exchange with the outer atmosphere at source-sink height temperature (that is, T_{AERO}). Finally, the external atmosphere is characterized by ever-changing relative humidity and air temperature, constantly obtained in input from the model. This transition can be summed up in the following equation:

$$LE^{(int.)} = \frac{\rho_A c_P}{\gamma} \frac{{e_O}^* - e_O}{R_C} = \frac{\rho_A c_P}{\gamma} \frac{e_O - e_A}{R_A} = LE^{(ext.)} \tag{2.42}$$

$$LE = \frac{\rho_A c_P}{\gamma} \frac{{e_O}^* - e_A}{R_A + R_C} = LE^{(int.)} = LE^{(ext.)} \tag{2.43}$$

Injecting this concept into the model formulation of Latent Heat yields the revised energy balance:

$$Rn - G - H^{(const.)} - LE^{(int.)} = 0 \tag{2.44}$$

2.6.3 T_{AERO} Parametrization

The previous steps were aimed at assessing the effect of indirectly-measured T_{AERO} over other components of the energy balance, meaning that the comparison were possible only when sensible heat measurement were available. In order to achieve a continuous and full presence of To within the model, and following in the footsteps of Mahrt and Vickers (2004) and Kustas et al. (2007), in this section the parametrization of T_{AERO} against surface temperature is explored. The parametrization formula they propose defines the temperature difference as function of incoming shortwave radiation and Leaf Area Index:

$$T_{RAD} - T_{AERO} = C[S_{IN} - C_S(LAI - LAI_{REF})] \cdot \nu \tag{2.45}$$

Where C, C_S and LAI_{REF} are empirical parameters and ν is a correction factor accounting for border-line radiation conditions (S $<$ 100 W m^{-2}). From previous applications (W. Kustas et al., 2007), values of 0.0087, 850 and 1 can be used in a first instance, provided that – in particular on C_S – different crops and climates can determine a non-negligible variability. Following some

considerations on the formula structure, another alternative formulation is proposed (Eq. 2.46), differing from Equation 2.45 in two main aspects: (a) the negative value of the C coefficient and (b) the addition of Vapour Pressure Deficit (VPD) as a further parameter. The first edit is due to the consideration that, in the original formula, the proportionality between aerodynamic temperature and leaf area index was direct. This may result in contrast with the turbulent fluxes partition: when LAI increases, the turbulent energy flux tends to shift towards its Latent Heat component, and the decrease in Sensible Heat should be mirrored by a decrease of its main driver, aerodynamic temperature. The second consideration is due to the fact that aerodynamic temperature, being a result of the turbulent fluxes equilibrium, is influenced also by the main drivers of Latent Heat exchange: energy inputs in the system (already accounted for in the original formula through the presence of radiation) and air saturation conditions, which can be summarized in the VPD parameter, described in Equation 2.47.

$$T_{RAD} - T_{AERO} = -\{C[S_{IN} - C_S(LAI - LAI_{REF})] + \eta VPD\} \cdot \nu \tag{2.46}$$

$$VPD = (1 - RH)\, e^*(T_{AIR}) \tag{2.47}$$

VPD identifies the pressure difference between the saturation conditions for the particular air temperature and the actual conditions. The lower the VPD, the closer the air is to its saturation conditions, the more difficult (i.e., "more energy-consuming") the evapotranspiration process. Such an influence over turbulent energy partition is worth the effort of including VPD within the proposed parameters, provided that its effective bearing on the parametrization is regulated by the calibration of its weight coefficient (η).

2.6.4 FEST-AeroT continuous model

Once the parametrization is tested and verified, the final version of the model (FEST-AeroT) is obtained by its integration within the Sensible Heat formulation, as detailed in the new energy balance equation (Eq. 2.48).

$$Rn - G = \left[\rho_A c_P \left(\frac{f_V}{R_A} + \frac{1 - f_V}{R_{ABS}}\right)[RET + [C(S_{IN} - C_S(LAI - LAI_{REF})) + \eta VPD] \cdot \nu - T_{AIR}]\right] + LE \tag{2.48}$$

In Equations 2.41, 2.44 and 2.48 the fluxes symbols, when not detailed, retain the same meaning as already shown in Table 2.1 and Equations 2.14–2.23.

2.7 General statistical indices and errors

In this section, some useful statistical indexes and error estimators will be recalled, provided their frequent use in the following pages.

2.7.1 Correlation coefficients

The Pearson Correlation coefficient (ρ) is a measure of linear correlation between two datasets (Pearson, 1896). It is defined as the ratio between the covariance of the two datasets and the product of their standard deviations. It ranges between the values of –1 (perfect inverse correlation) and +1 (perfect direct correlation), with a null value identifying uncorrelated data.

$$\rho = \frac{\mathrm{Cov}(A, B)}{\sigma_A \cdot \sigma_B} \tag{2.49}$$

The Spearman Correlation coefficient (ρ_S) is a measure of rank correlation (Kendall, 1938). It is defined as the Pearson correlation between the ranks of two datasets. Its main perk with respect to Pearson's correlation is that it is able to go beyond linear relations between variables, describing in general all monotonic relationships. In this case, the extreme ± 1 values identify two variables which are perfect monotone functions of each other.

$$\rho_S = \frac{\mathrm{Cov}(r_A, r_B)}{\sigma_{r_A} \cdot \sigma_{r_B}} \tag{2.50}$$

Where r_X identifies the rank function, assigning to each element x in a dataset its position in the ordered dataset.

2.7.2 Error estimators

The Coefficient of Determination (R^2) identifies the proportion of the variation in the dependent variable that can be explained by the independent variable. Generally, when dealing with model interpretation of measured data, it provides an evaluation of how well the model manages to replicate the data. In linear interpolation scenarios, it also provides a measure of how clustered the interpolated observations are with respect to the main interpolation line. It is computed as:

$$R^2 = 1 - \frac{\sum_i (m_i - o_i)^2}{\sum_i (o_i - \mu_{obs})^2} \tag{2.51}$$

Where m_i identifies a model estimation, o_i its corresponding data observation and μ_{obs} the observation average.

The average bias – also Average Error (AE) – is computed as the average of all the errors between model and observation. Closely related to AE are also the absolute bias – or Mean Absolute Error (MAE) – which accounts only for absolute deviations from the observed data, and the relative bias – or Mean Absolute Percentage Error (MAPE) – which normalizes model-to-data deviation over the actual data value. Their formulations are summed up below, with n being the data sample numerosity.

$$AE = \frac{1}{n} \sum_{i=1}^{n} (m_i - o_i) \tag{2.52}$$

$$MAE = \frac{1}{n} \sum_{i=1}^{n} |m_i - o_i| \tag{2.53}$$

$$MAPE = \frac{100\%}{n} \sum_{i=1}^{n} \frac{|m_i - o_i|}{o_i} \tag{2.54}$$

Root-Mean Square Error (RMSE) or Deviation (RMSD) is the square root of the second sample moment of the differences between modelled and observed values. One key characteristic of RMSE is that it is scale-dependent, being a dimensional quantity. Its computation is shown in Equation 2.55.

$$RMSD = \sqrt{\left[\sum_{i=1}^{n} (m_i - o_i)^2\right] / n} \tag{2.55}$$

2.7.3 Taylor diagrams

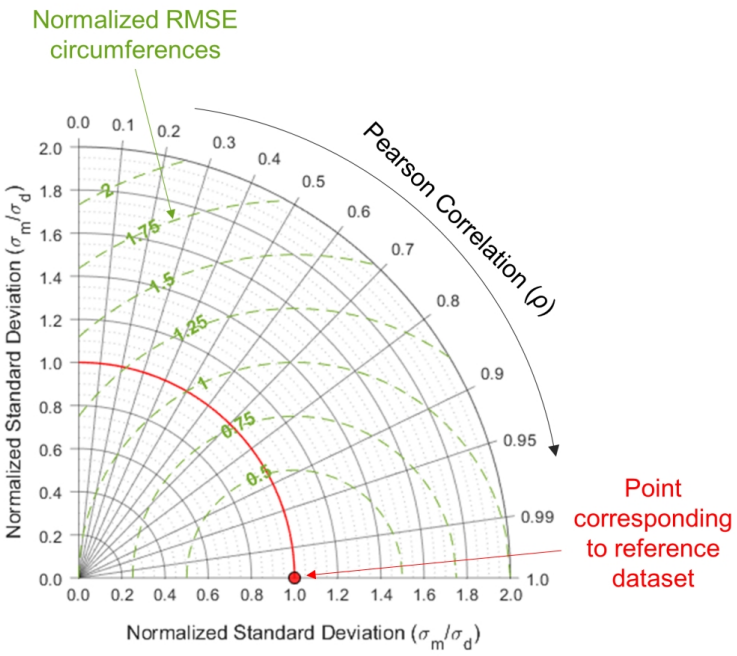

Figure 2.7: Elements composing a Taylor diagram

Taylor diagrams (also *plots*) have been designed to provide at the same time multiple indicators about model representation of measured data (Taylor, 2001). These are the Pearson correlation coefficient, the RMSE and the standard deviation. The empty Taylor field is shown in Figure 2.7. In it, each model performance can be displayed with a single dot, whose position is linked to its performance indexes: the cosine of its angle with the axes origin and the horizontal identifies the Pearson correlation coefficient; the radial polar coordinate represents its standard deviation; the distance from the low red point (representing the observed data, or a "perfect" model) is equal to its RMSE.

In particular when comparing different modelled variables, the model standard deviation (σ_m) and RMSD parameters in the diagram can be normalized with the observed data standard deviation in order to obtain non-dimensional quantities. Finally, Taylor (2001) also provided a scoring system that condensed the three model representativity indicators into one single number, ranging in a scale from 0 to 100:

$$TS = \frac{4(1+\rho)}{(\sigma_m/\sigma_o + \sigma_o/\sigma_m)^2(1+\rho_{max})} \tag{2.56}$$

Where ρ_{max} identifies the maximum correlation attainable, lower than 1 if external constraints limit the model representation of observed data.

Chapter 3

Case Studies

In this part, the details about the wide-ranging case studies involved in this thesis work will be presented. Figure 3.1 collects them all, with further information provided in Table 3.1. In terms of areal extension, they range and, thus, reference scale, they range from the hundreds of square kilometres down to the small lysimeter environment. This far-reaching abundance helps to provide a wide outlook to the whole analysis, showing how, at different scales, different processes acquire relevance in the scientific analysis.

Figure 3.1: Case studies

Table 3.1: List of analysed case studies.

Case study	Location	Climate[1]	Crop(s)	Year(s)	Area
Capitanata Irrigation Consortium	Foggia, Italy	Humid subtropical	Vegetables, Fruit trees	2015-2019	986 km^2
Chiese Irrigation Consortium	Mantova, Italy	Humid subtropical	Maize	2015-2018	200 km^2
Barrax area	Albacete, Spain	Cold Semi-Arid	Vegetables, Fruit trees, Flowers	2012	1200 ha
Rapitalà farm	Palermo, Italy	Hot-Summer Mediterranean	Vine	2012	54 ha
Landriano	Pavia, Italy	Humid subtropical	Maize	2006, 2010, 2011	10 ha
Livraga	Lodi, Italy	Humid subtropical	Maize	2010-2013	12 ha
Lysimeter	Milan, Italy	*Artificially controlled*	Grass	2021	2.25 m^2

3.1 Capitanata Irrigation Consortium

The Capitanata Irrigation Consortium[2] is located in Southern Italy, in the Puglia region, in a plain area delimited by the Apennines on the west and the Gargano Promontory on the east. It covers an area of about 98 600 ha, 45% of which is irrigated through the Consortium water distribution network, while the remaining areas are irrigated with private wells. The role of irrigation is crucial: the mean irrigation volume in the irrigation season (from April to October) is about 600 mm, while the seasonal rainfall amount is about 150 mm. Daily irrigation volumes measured in the main aqueduct are available from 2013 to 2018. During the different years, the irrigation amounts range between 21 and 60 hm^3. The Sud Fortore district within the Consortium is an intensively cultivated area mainly devoted to durum wheat (*T. durum*) and tomatoes (*S. lycopersicum*) during the spring–summer season and fresh vegetables in the autumn-winter period (sown in late summer and harvested October–February). Two major soil classes can be found: silty clay and gravel sandy soil.

3.1.1 Meteorological data

Weather data are obtained via spatial interpolation of information from 21 stations managed by the regional government (ARPA Puglia). Furthermore, three more stations managed directly by Politecnico di Milano were installed on site during the monitoring period. All meteorological data

[2] www.consorzio.fg.it

was gathered continuously at 5 minutes temporal resolution. The meteorological stations are Davis Vantage Pro2 Plus[3], equipped to measure the following variables: air temperature (SAT, °C), with 0.1°C accuracy; relative air humidity (RH, %); rainfall (P, mm), with 0.2 mm accuracy; incoming shortwave solar radiation (S_{IN}, W m^{-2}), with 1 W m^{-2} accuracy.

For the purposes of the activities detailed in Section 3.6, coarse-pixel precipitation information is obtained with a high-resolution precipitation field, computed through quadratic inverse distance interpolation of the data from the rain gauges, followed by low-resolution averaging of the data up to the position and resolution of the SSM pixels. Temporally, data were grouped to compute one single value for each 24-h period preceding a satellite overpass.

3.1.2 Eddy Covariance data

Two Eddy Covariance (EC) stations have been installed in the area and moved in time with the different crop development periods (Corbari et al., 2020). Both are placed in the territory of the city of Foggia: one in the "Incoronata" area, within the territory of the "Agricola Guzzetti s.r.l." farm, and the other in the "Onoranza" area, in the fields of the "Futuragri Società Cooperativa Agricola" farm. Henceforth, these stations will be named "Foggia-Incoronata" (FIN) and "Foggia-Onoranza" (FON), respectively.

These stations provide all the components of the energy balance, measuring Net Radiation through a multi-component radiometer and Soil Heat Flux through a heat flux plate. For the turbulent fluxes (Latent and Sensible Heats), measured data is retrieved at high frequency (20 Hz) in order to capture the slightest oscillations in temperature and water vapour concentration in the air, following the formulae (Campbell and Norman, 1998):

$$H = \rho_a c_P \overline{w'T'} \tag{3.1}$$

$$LE = \lambda_w \rho_a \overline{w'[H_2O]'} \tag{3.2}$$

Where w' is the oscillation around the average value of the vertical component of the wind and T' and $[H_2O]'$ are the contemporary oscillations registered in air temperature and water vapour concentration, respectively. The raw data requires a series of well-established (Foken et al., 2006) pre-processing steps that average its final temporal frequency to 30 minutes. For the Polimi stations, the correction is performed using the PEC software (Polimi Eddy Covariance) (Corbari et al., 2012). Other steps in the pre-processing comprise a series of physical and instrumental corrections, in particular for the turbulent fluxes. Generally, the EC station method registers an underestimation of the available energy, determining an energy balance error ω:

$$\omega = Rn - G - (H + LE) \tag{3.3}$$

The correction procedure (Twine et al., 2000) is regulated by the preservation of the Bowen ratio (β_B):

$$\beta_B = \frac{H}{LE} \tag{3.4}$$

$$H_{(corr.)} = H + \frac{\beta_B}{\beta_B + 1}\omega \tag{3.5}$$

[3]https://www.davisinstruments.com/

$$LE_{(corr.)} = LE + \frac{1}{\beta_B + 1}\omega \tag{3.6}$$

Finally, due to the physics itself at the core of the EC measurement technique, the resulting turbulent data are never referred to the single point in space in which the instrument is placed (as, for example, radiometer measurements are), but are influenced by the aerodynamic conditions of the atmosphere bottom layer in the neighbouring area. An approximate analytical model has been developed (Hsieh et al., 2000), to simulate the relative importance of a certain pixel over the EC measurement in given atmospheric conditions (Eq. 3.7). This model has then been expanded in a bidimensional formulation (F. Li et al., 2008) to compute the areal footprint of the eddy-covariance measurement (Eq. 3.8).

$$f(x, z_m) = \frac{1}{\kappa^2 x^2} D {z_u}^P |L|^{1-P} \exp - \left(\frac{D {z_u}^P |L|^{1-P}}{\kappa^2 x} \right) \tag{3.7}$$

$$g(x, y, z_m) = \frac{1}{\sigma_y \sqrt{2\pi}} \exp \left[-\frac{1}{2} \left(\frac{y}{\sigma_y} \right)^2 \right] f(x, z_m) \tag{3.8}$$

where x identifies the fetch in the upwind direction, D and P are similarity constants (depending on the atmospheric stability) and z_u a length scale dependent on the measurement height. In Equation 3.8, the transversal coordinate y is added, together the the cross-directional standard deviation (σ_y) of the footprint area.

The stations, together with energy fluxes, measure also soil moisture, employing TDR (Time Domain Reflectometer) sensors (CS616, Campbell Sci., UT, USA), mainly working at the depth of 15 cm, which for most crops is close to the main root water uptake depth.

3.1.3 Chiese Irrigation Consortium

The Chiese river basin closed at the confluence with the Oglio river has a total area of 1 270 km^2, including Lake Idro. Partially included in the river basin is the Chiese Irrigation Consortium[4], covering an area of 20 000 ha, powered by the Chiese river downstream Lake Idro, just downstream of the Gavardo station. In the Lombardy region, one of the most urbanized and industrialized regions of Italy, water management is critical during summer, when multiple and conflicting usages (i.e., civil, industrial, agriculture, and hydroelectric) can reduce water availability for irrigation. The area is intensively cultivated with summer crops (i.e., corn, forage), which are highly irrigated, and winter wheat, which cover about 68% and 8% of the agricultural land, respectively. The irrigation practice is based on fixed irrigation turns of 7-8 days, defined a priori before the beginning of the irrigation season for each sub district. The irrigation is provided to each field with a channel network of 1 400 km covering an area of 18 000 ha, with additional wells (more than 10 000) providing for the remaining 2 000 ha. Irrigation water is mainly provided by surface flood irrigation. Mean rainfall in the crop season is 250 mm, while the irrigation contribution is around 1 200 mm.

As for the Capitanata Irrigation Consortium, weather data are gathered from a series of stations managed by the regional government (ARPA Lombardia). The regional data is also integrated with the measurements obtained from the Meteonetwork[5] association, joining the private meteorological stations of single citizens. Coarse-pixel precipitation information is obtained with a joint quadratic

[4] www.consorziodibonificachiese.it
[5] www.meteonetwork.it

inverse distance interpolation of the rain gauges data and a successive upscaling to the position and resolution of the SSM pixels, as already detailed in Section 3.1.1.

In the Chiese Consortium, one EC station has been installed (Corbari et al., 2020) in the same maize field for three consecutive years (2016 through 2018). The maize field is located in the "Campagnoli sera" area, within the town of Montichiari (Brescia), and will thus be identified as "Montichiari" (MON). The measurement principle and raw data corrections are the same already shown in Section 3.1.2, with meteorological information collected in continuous and soil moisture information retrieved by TDR sensors placed at a depth of 35 cm. The higher depth with respect to the Capitanata EC stations is due to the different structure of maize (Lundstrom and Stegman, 1988) root systems as opposed to those of the tomatoes.

3.2 Parrot sensors

Across the Capitanata case study, a large number (456) of low-cost sensors have been deployed, in order to build a comparison between this high-density sensor network and corresponding satellite measurements. This data analysis is framed within a low-cost sensor citizen science project (Woods et al., 2019) aimed at improving the data quality and quantity from long-term hydrological monitoring networks, notoriously expensive both in terms of actual instrumentations and maintenance (Mishra and Coulibaly, 2009). The employed Parrot sensors, characterized by low costs and a lay-user-friendly interface and data transmission protocol, are extremely valuable for satellite data analysis, given their high distribution density (456 sensors spread over an area 584 ha wide) in a heterogeneous, multi-scope (thus, ideal) agricultural area.

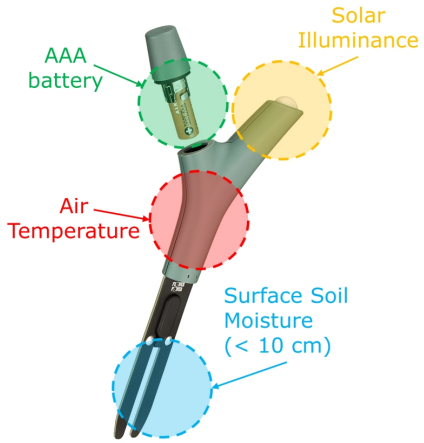

Figure 3.2: Parrot sensor

The sensors, named "Flower Power", are produced by the French company Parrot SA[6], and are able to measure time series data collected at 15-minute intervals: soil moisture (SM), at a maximum depth of 5 cm, air temperature (AT), few centimetres above ground surface and solar illuminance (ILL), measured in proximity of the air temperature sensor (Fig. 3.2). The sensors characteristics are reported in details in Table 3.2. In particular, soil moisture is measured with a capacitance probe made of two rods of 10 cm, which allows measuring the dielectric permittivity that is influenced by SM. Soil moisture accuracy has been tested through laboratory experiments by Xaver, et al. (2020) showing a good sensor accuracy, except for dry conditions of silty clay soils. Illuminance is measured by a sensor in the wavelength spectrum between 400 and 700 nm. The data are stored on the Flower Power sensors and then downloaded by smartphones App via Bluetooth.

[6]https://support.parrot.com/us/support/products/parrot-flower-power

Table 3.2: Flower Power measured variables and specifics.

Variable	Units	Range	Accuracy
Air Temperature (AT)	°C	-5to +50 °C	1.5 °C
Solar Illuminance (ILL)	Lux	0.1 to 200 lux	15 %
Soil Moisture (SM)	Vol.%	0 to 50%	3 %

3.2.1 Sensor placement

The sensors have been deployed mainly in the two areas already presented in Section 3.1, the "Incoronata" and the "Onoranza" areas. Different fields have been chosen, either with Bare Soil (BS) or vegetation-covered: mainly Tomatoes (TOM) and Asparagus (ASP), but also Cabbage (CAB), Celery (CEL), Fennel (FEN), Pak-Choi (PCH), Salad (SAL) and Spinach (SPI). In Figure 3.3 the locations of the sensors are shown in the different fields and farms, along with the October 2019 land cover status. The monitoring covered the period between 22nd July and 20th October 2019 (91 days). In occasion of these two dates, two surveys have been conducted to classify the fields in which the sensors had been placed. The distribution of the sensors across the different land cover categories is detailed in the alluvial plot of Figure 3.4. The predominance of bare-soil fields is testified by the high amount of Bare Soil sensors in the July classification. Most of these, however, were part of a vegetated field by October. Tomato sensors, on the other hand, were the only group to shift from a vegetated field to a bare-soil one during Summer, because of the tomato harvest in August.

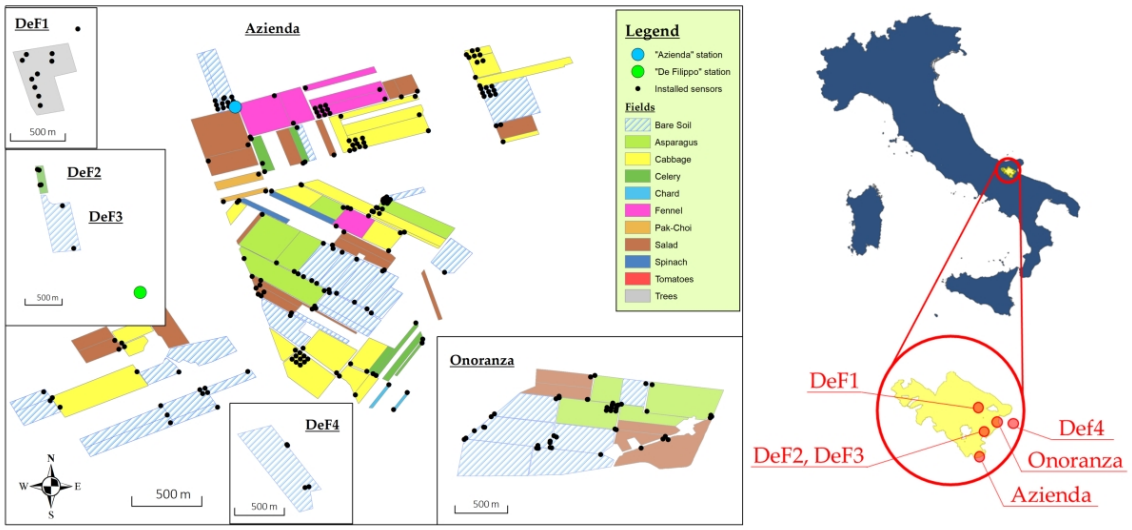

Figure 3.3: Parrot sensor displacement, with field land use relative to Oct 2019

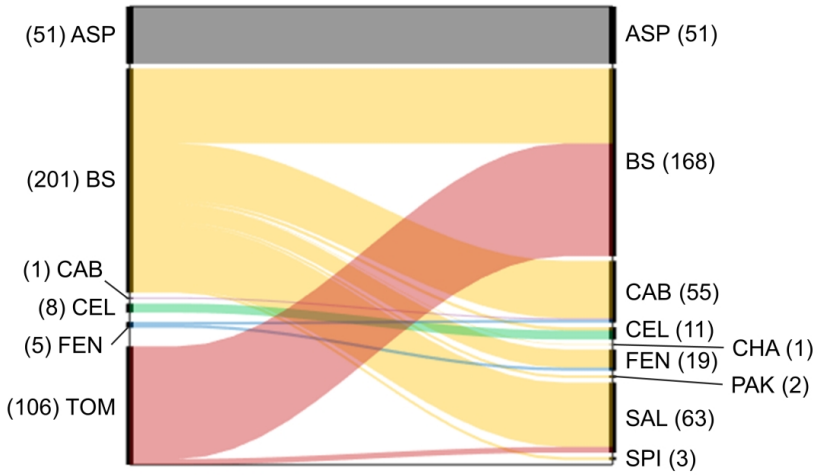

Figure 3.4: Alluvial plot of land use in the area: on the left, land uses for July 2019; on the right, land uses for October 2019

3.3 Rapitalà

The "Tenute Rapitalà" farm in the territory of Camporeale (Sicily, Italy) is a vineyard farm encompassing different vine cultivars, which has been object of different studies over time (Maltese et al., 2011). All its related data has been collected during the June-September 2008 "Digitalizzazione della Filiera Agro-Alimentare" (DIFA) field campaign (Ciraolo et al., 2012).

The Rapitalà area is shown in Figure 3.5, with the cyan square identifying the global modelling zone and the central yellow-bordered area highlighting the main experimental field, composed by four sectors separated by two cross-positioned paths. This main area hosts in its midst the eddy-covariance station and is thus the main focus for the turbulent fluxes comparisons. The vineyards are organized in rows 2.4 m apart; in each row, the single plants are positioned every 0.95 m, resulting in a global plant density of 4386 plants per hectare. The terrain has mild slope (<10%), oriented towards S-SW. The soil texture is classified as loam (20% clay, 29% silt and 51% sand), with 1.7% organic content. Residual Soil Moisture is estimated at 0.04 m^3 m^{-3}, whereas Saturation Soil Moisture at 0.45 m^3 m^{-3} (Ciraolo et al., 2012). Drip irrigation is the main irrigation practice for the area.

During the DIFA campaign (summer 2008), five proximal sensing acquisitions have been carried out, using the airborne platform SKY ARROW 650 TC/TCNS with sampling height around 1000 m above ground level. A multispectral Duncantech MS4100 camera operating in the 767–832, 650–690 and 530–570 nm bands has been used to retrieve the visible (VIS) and near-infrared (NIR) images; a Flir SC500/A40M camera, working in the 7 500–13 000 nm band, provided the thermal infrared (TIR) images. This distinction resulted in a different nominal pixel resolution for the VIS/NIR data (0.7 m) and the TIR data (1.7 m). The original data have been aggregated at 1.7 m using a pixel aggregate method. Thus, the 1.7 m spatial resolution is assumed as reference resolution for scale effects analyses.

The flights days are 11th June (DOY 163), 3rd (185) and 22nd (204) July, 22nd August (235)

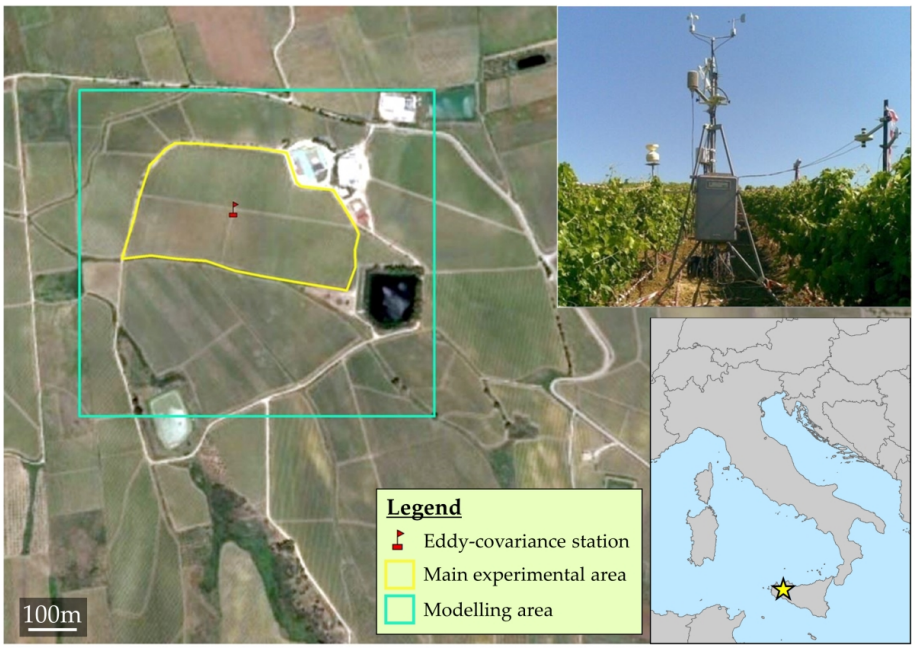

Figure 3.5: Rapitalà area

and 3rd September (247). These days were all characterized by optimal meteorological conditions to improve the quality of the data collection process.

The images acquired by the Duncantech camera were affected by radiometric inhomogeneity including vignetting (DiStasio Jr. and Resmini, 2010; Karpouzli and Malthus, 2003) and additional distortions due to the combined effects of the optical prism and the coating treatment on the faces, besides the sensitivity and response of the sensor. Radiometric correction factors for the three spectral bands were determined by carrying out laboratory measurements with an integrating sphere, an Extended Range Lamp (EKE-ER) and an ASD Hi-Res Fieldspec spectroradiometer.

A flux tower was located at the centre of the experimental field for the entire duration of the monitoring period. The station is equipped to measure also air temperature and humidity with a sensor placed at 2.75 m above ground and a pluviometer, with 0.2 mm accuracy, installed at 2 m above ground. The eddy-covariance setup included a CSAT3 sonic anemometer and an open-path LICOR-7500 IR Gas analyser operating at 3.40 m above ground and with 20 Hz measurement frequency. Final data is provided with 30-mins time step.

Figure 3.6 shows the available energy underestimation (Foken et al., 2006) for four of the flight dates. Data from 22nd August refers only to the 09:30–21:30 (local time) period, as data for the rest of the day was unavailable due to a malfunctioning of the instrument. As already described in Section 3.1.2, the data have been corrected by distributing the error among the turbulent fluxes according to the Bowen ratio to force the closure of the energy balance (Twine et al., 2000).

Flux tower footprint location is accounted for by following the guidelines set by Hsieh et al. (2000) and Li et al. (2008). In this particular case, average day-time conditions determine that 90% of the eddy footprint area falls within 10 ha of the EC tower. According to the analysis spatial resolution, these numbers can mean that a footprint computation may or may not be required to

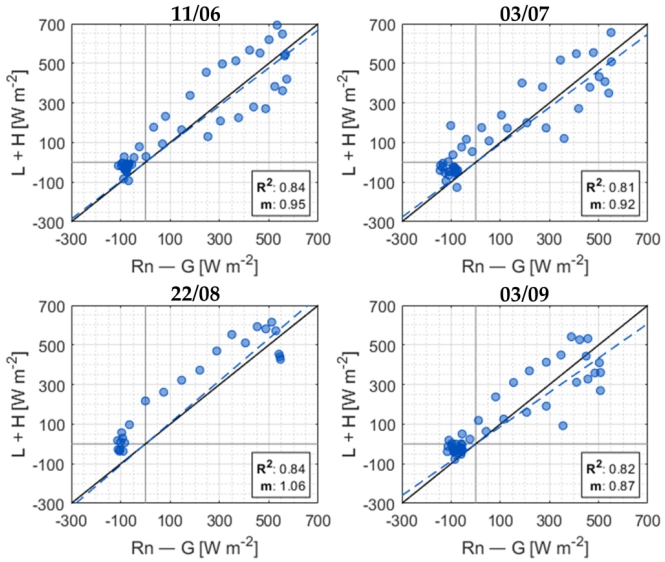

Figure 3.6: Energy balance closure check for the eddy-covariance data on the four available dates. Turbulent energy (L + H) against Available energy (Rn – G).

aptly simulate the measurement performed by the instrument. Lower resolutions, covering with only one pixel most of the footprint, do not require any specific footprint computation, and the simple pixel value is enough for the comparison with the EC station measurements. The global available data are summed up in Table 3.3.

Table 3.3: Overview of available data.

Test days	11th Jun	3rd Jul	22nd Jul	22nd Aug	3rd Sep
DOYs (year 2008)	163	185	204	235	247
Meteorological data	Yes	Yes	Yes	Partial	Yes
Energy Fluxes	Yes	Yes	No	Partial	Yes
Flight time (local, UTC+2)	10:45	08:15	08:45	09:15	08:45
Land Surface Temperature	Yes	Yes	Yes	Yes	Yes
Calibration date	Yes	No	Yes	No	Yes
Validation date	Yes	Yes	No	Yes	Yes

Energy fluxes information was unavailable for 22nd July, making it unfeasible for the validation step. Meteorological and energy fluxes data for 22nd August were available only for the 10:00–21:30 time range, implying that the conditions at the time of the flight overpass (09:15) could not be simulated using FEST-EWB. This means that this date could not be included in the calibration. Finally, also data from 3rd July have been excluded from the calibration step, because of incongruencies in the reported flight time with usual registered LSTs. Turbulent fluxes data, on the other hand, are employed in the validation process. Being meteorological data available only for the single flight dates, no continuous model run could be performed. Instead, single daily simulations

were executed.

3.4 Barrax

The Barrax agricultural area (Fig. 3.7a) is located in the centre of Spain (39°03' N, 02°06' W) and is characterized by an extensive variety of land uses. Some pivot-irrigation areas are devoted to mainly homogeneous crops such as corn, alfalfa, sunflower and barley. Other areas are mostly bare (either pasture or fallow land), while three high-stem vegetation zones can be identified: an orchard, a forest nursery area (also identified as "Reforestation") and a vineyard. Overall, the area offers a wide variety of crop patterns, offering a heterogeneous scenario for model application. The data from this case study have been collected during the Regional Experiments For Land-atmosphere Exchanges (REFLEX) field campaign (Timmermans et al., 2015), in the period 16th–28th July 2012. Airborne multi- and hyper-spectral data have been collected, with three separate flux towers recording meteorological and flux data in three different areas of the site: (a) a vineyard, (b) a reforestation and (c) a camelina zone (a mostly-bare area). These have been highlighted in the land cover classification map for 25th July 2012 (Fig. 3.7b), where it is also possible to identify some crops that had already been harvested, while others were in the process during the field campaign.

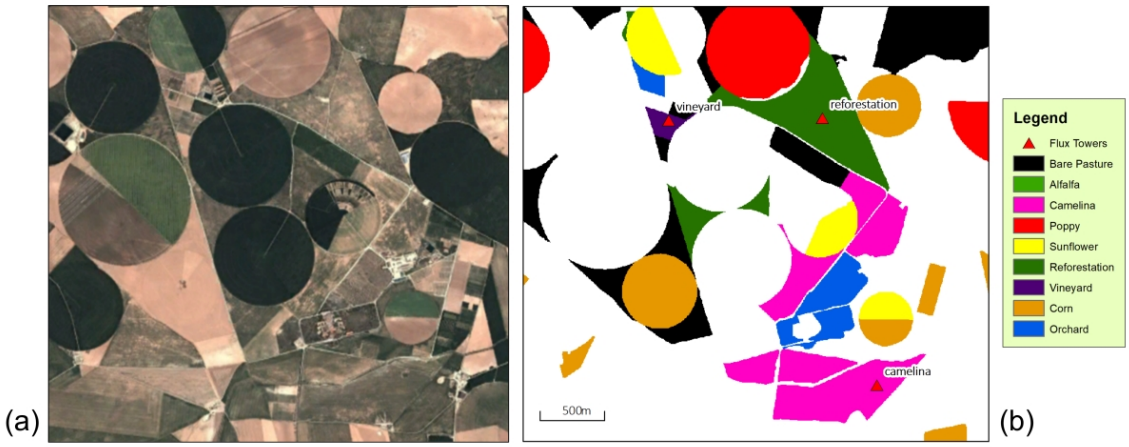

Figure 3.7: Barrax agricultural area: satellite image (11/5/12) and land use for the analysis period

3.5 Landriano and Livraga

In this Section, the information about two EC stations, managed by Politecnico di Milano and placed in maize fields, is provided. The stations are named after the towns in which they are placed: Landriano (Pavia) and Livraga (Lodi), which are roughly 25 km apart in the medium Po Valley. They are presented together, provided their similarity in characteristics.

The Landriano EC station ("LAN") has been monitored in 2006, 2010 and 2011 (Masseroni et al., 2014). The soil is mainly sandy loam and the irrigation is performed with the border method (100–200 mm per irrigation event), with 1–2 seasonal irrigations. This extremely low irrigation

frequency is motivated by the extremely shallow water table, which guarantees natural feeding to the roots (Facchi et al., 2013). The station is located in a 10 ha field, and is equipped with a four-component radiometer (CNR–1, Kipp & Zonen, Netherlands), and infrared gas analyser (LI–7500, LICOR, NE, USA) and a 3D sonic anemometer (RM–81000V, Young, MI, USA), positioned at 4.80 m above ground level. The radiometer was installed at a slightly lower height (4.30 m) but at the end of a 3-m long pole, in order to minimize disturbances from the main tower pole, and southward-oriented, in order to optimize solar input reception. The station footprint for turbulent flux measurement has been computed to extend between 30 and 120 m from the main tower pole, according to wind and vegetation conditions. Soil Moisture measurements are gathered with TDR probes.

The Livraga EC station ("LIV") has provided data in the 2010–2013 period (Corbari et al., 2020). It is in a clay loam soil maize fields, located within the "Muzza Bassa Lodigiana" Irrigation Consortium, covering an area of 740 km^2. Numerous irrigation canals feed the area, with an average irrigation volume of 100 mm per irrigation event, through flooding (Ceppi et al., 2013). Irrigations are scheduled every 2 weeks, provided the higher water table depth than for the Landriano test case and the annual rainfall rates, totalling 1 000 mm in the northern consortium area and degrading down to 800 mm in the southernmost reaches. The instrumentational set-up is in all aspects similar to that already described for the Landriano EC station.

3.6 Laboratory Lysimeter

A lysimeter is a device employed to perform high-accuracy measurements of the soil water fluxes. It consists of a volume of soil isolated from its surroundings through a (usually metallic) container and placed over a weighing scale, able to assess the global weight variations continuously in time. The main concept is that all water fluxes are measurable: precipitation or irrigation are known quantities, deep percolation can be obtained by measuring the flux through a dedicated outlet at the bottom of the lysimeter and evapotranspiration can be gathered through the weight change in time. With the necessary precautions, a lysimeter can also be installed directly in field, in order to work in a scenario as close as possible to real-life applications. Otherwise, laboratory set-ups can be organized, which leads to highly-controlled (albeit less realistic) boundary conditions. For this thesis work, a similar set-up has been employed to gather useful data for the validation of the FEST-2-EWB model presented in Section 2.5.

3.6.1 Instrumentation

The activity detailed in this thesis has been developed using the laboratory lysimeter located in the "Gaudenzio Fantoli" laboratory at Politecnico di Milano. The lysimeter (Fig. 3.8) has a 1.5 m $\times$ 1.5 m basal area and is 1 m high; the boundary conditions are enforced by the following tools:

- A set of four halogen lights, each with 400 W nominal power
- One infrared and ultraviolet lamp, with 300 W nominal power and able to convey that part of the solar radiation not provided by the halogen lights
- A drip irrigation set-up

All the measurements are provided by the following instruments, with the letter corresponding to the labels in Figure 3.8:

(a) A pluviometer, used to measure deep percolation and connected to the lower outlet, where percolation water is conveyed by the basal shape of the external casing

(b) The main weighing scale, providing continuous measurements of the total weight

(c) Eight soil moisture sensors, distributed over all the lysimeter at a depth around 10 cm

(d) A Soil Heat Plate, which uses a thermopile to measure the soil temperature gradient over its surface

(e) A four-component radiometer, capable of measuring both the short- and long-wave components of the radiance, both downwelling from the lamps and upwelling from the lysimeter

(f) A thermo-hygrometer, providing both air relative humidity and temperature

(g) A smaller weighing scale, employed for the smaller box weight variations

(h) A thermal camera, bound to a wooden pole positioned at 1.2 m height above the lysimeter, which is used to mimic flight or satellite overpasses and retrieves both visible (RGB) and thermal (TIR) data

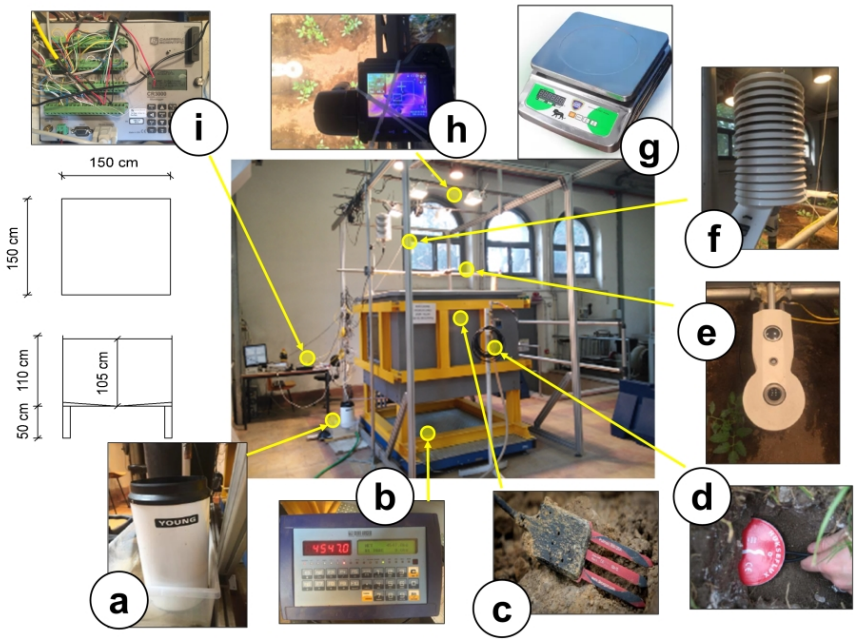

Figure 3.8: Laboratory Lysimeter and instrumentation

The instruments characteristics have been summed up in Table 3.4.

All instruments, except the weighing scales and the thermal camera are connected with a datalogger (Fig. 3.8i, Campbell Scientific CR3000), which continuously receives the incoming data at their varying sampling frequency (ranging from milliseconds to minutes) and provides 10-minutes

Table 3.4: Measuring instruments and their accuracy.

Instrument	Model	Measured variable	Units	Accuracy
Pluviometer	Young 52202	Deep percolation	mm	2%
Weighing Scale	DiniArgeo	Weight	kg	0.5 kg (0.22 mm_{H2O})
Soil Moisture probes	Decagon 5Tm	Soil moisture and temperature	m^3 m^{-3}	$\pm$0.03 m^3 m^{-3}
Plate	Hukseflux HFP01	Soil Heat Flux	W m^{-2}	$\pm$3%
Radiometer	Kipp&Zonen CNR4	Net Radiation budget	W m^{-2}	$\pm$5%
Hygrometer	Campbell Scien– ific HMP155A-L	Air Relative Humidity Air Temperature	% °C	$\pm$0.8%
Small Weighing scale	*n/a*	Box Weight	g	2 g (0.02 mm_{H2O})
Thermal camera	FLIR T450sc	Surface temperature RGB images	°C *none*	0.1°C (1.20 mm spatial res.) n/a (0.39 mm spatial res.)

averages as an output. This overall sampling time step has been suggested by past experience (Mantovani, 2016; Rozzoni, 2017) with the lysimeter, as a good compromise between good representation of rapid variations in the measured variables and practical data management.

The data sampling is theoretically continuous in time, even at night and during the weekends. However, some issues (e.g., power outages, datalogger or single sensor failures) have caused the loss of some of the data (in particular with soil moisture sensors). Only when the data gap was sufficiently small (a few time steps) and within relatively stable boundary conditions (with lights off, far from any irrigation instance), it was filled in by way of simple linear interpolation.

3.6.2 Soil data

The soil used in the lysimeter belongs to the silty-clay category, after removal of most of the coarser grains (> 5 mm in diameter). In preceding studies (Mantovani, 2016), the hydraulic properties of the soil detailed in Table 3.5 were determined.

Table 3.5: Lysimeter soil data.

Property	Symbol	Value
Saturation soil moisture	SM_{SAT}	0.440 m^3 m^{-3}
Field capacity	FC	0.260 m^3 m^{-3}
Wilting Point	WP	0.167 m^3 m^{-3}
Residual soil moisture	SM_{RES}	0.040 m^3 m^{-3}
Permeability at saturation	K_{SAT}	2.0 10^{-6} m s^{-1}
Brooks-Corey Index	BCI	0.206

3.6.3 Experimental outline

An overhead view of the experimental set-up is shown in Figure 3.9, with the lysimeter surface split into two distinct sectors. Firstly, Sector 1 is organized into seven rows (each 15 cm wide), three vegetated and four non-vegetated: the former (Zone 1) are sown with grass and a drip irrigation line is arranged in order to provide water just to this specific area; the latter (Zone 2) are left unsown and unirrigated, weeding out possible crop growth brought on by stray seeds. The main weighing scale provides the weight variations of the lysimeter as a whole, without distinguishing between the two sub areas. To this aim, in Sector 2 two plastic boxes have been positioned, measuring 400 $\times$ 300 $\times$ 120 mm^3 (364 $\times$ 264 $\times$ 115 mm^3 internally). These two correspond to the categories in Sector 1 – one being fully vegetated (Box 1), the other bare (Box 2) – and can be temporarily moved from the lysimeter to be weighted separately using a smaller weighing scale. This allows to measure the distinct ET from crop and bare soil. If a sound proportionality can be established between each box and the corresponding Zone in Sector 2, the ET measured for the whole lysimeter can be disaggregated into its crop- and soil-related components.

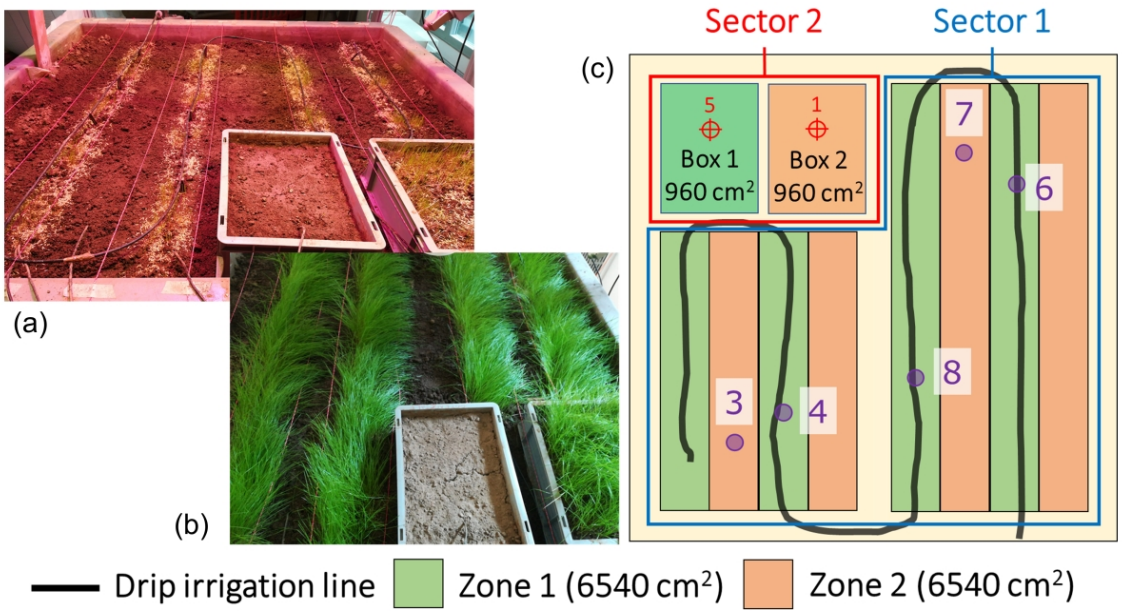

Figure 3.9: Lysimeter after sowing (a) and with full growth (b). On the right, the scheme with the different areas and SM probes.

3.6.4 Experimental routine

The instruments already detailed in Section 3.6.1 record continuously the micro-meteorological data required for the model runs. Further data, both for the model runs and their validation, are obtained in "instantaneous" data-gathering routines, with expected temporal frequency of two times a week. These routines allow to gather the following: (a) weights of the plastic boxes, (b) lysimeter total

weight, (c) surface temperature data and (d) irrigation, when performed. This last step is generally variable with the crop growth stage: at the beginning, a few heavy irrigations are required to prepare the soil for the seed development; once the first plants have started development, a more regular regime can be enforced, generally maintaining the soil moisture above the FAO-provided CST (Eq. 2.7); finally, when the plants reach a full growth and their water demand increases, irrigations can be performed more frequently and/or with higher amounts, to avoid stressful situations for the plants.

3.6.5 Box-Lysimeter correspondence

In order to validate the use of the boxes to obtain the differentiated crop and soil ETs, two approaches will be explored, with the more accurate one to be employed in the box-lysimeter conversion. The conceptual diagrams for the approaches are outlined in Figure 3.10.

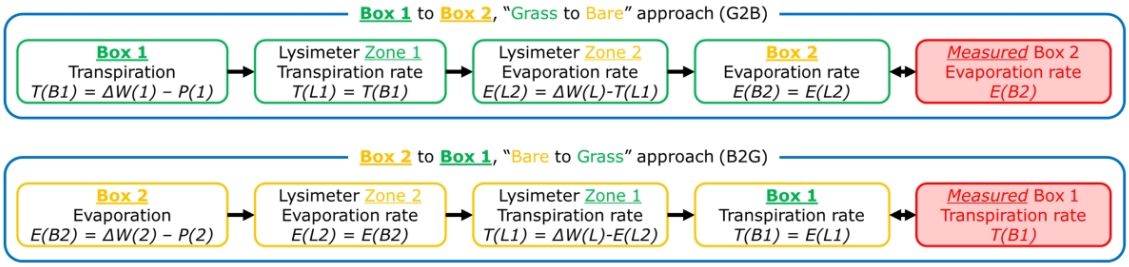

Figure 3.10: Lysimeter ET disaggregation approaches

For the first one ("Grass to Bare", G2B), the starting point will be the vegetated box (Box 1) weightings. For any given time interval (Δt) between two successive weightings (obtained at times t_A and t_B), the SM evolution is used in determining the total percolated volume, by use of Brooks-Corey formula (1964):

$$K_{unsat} = K_{sat} \left(\frac{SM - SM_{res}}{SM_{sat} - SM_{res}} \right)^{\frac{2}{BCI}+3} \tag{3.9}$$

$$PE = \int_{t_A}^{t_B} K_{unsat} dT \tag{3.10}$$

Where K_{unsat} is the unsaturated soil hydraulic conductivity, dependent on SM. Its integration over the whole observation period provides the total specific percolated volume. Following the mass conservation principle, subtracting this volume to the weightings difference provides the vegetated box ET. The main assumption here is that the evapotranspiration rate is the same in both Box 1 and Zone 1, and also for Box 2 and Zone 2. Using the same ET rate for Zone 1 provides, residually from the lysimeter weightings difference, the ET for Zone 2, which in turn can be associated to Box 2. This value can also be independently computed by subtracting its percolation volume (obtained again with Eqs. 3.9 and 3.10) from the weightings difference. The comparison between these two Box 2 ETs, ideally equal, can be used as an estimate of the scaling process error.

The second approach ("Bare to Grass", B2G) is composed of the same exact equations, but arranged in reverse order, starting from Box 2 ET, upscaling to Zone 2 ET, then residually com-

puting Zone 1 ET and finally downgrading back to Box 1 ET, to be compared with the same value obtained by box weightings difference.

3.7 Satellite data

In this section, an overview is provided about some EO data which will be employed throughout the whole thesis work. These are mainly organised into three categories: SSM datasets (Section 3.7.1), Vegetation Indices (VIs, Section 3.7.2) and thermal information (Section 3.7.3).

3.7.1 Satellite SSM datasets

The Soil Moisture Ocean Salinity (SMOS) Earth Explorer is the European Space Agency (ESA) mission aimed at providing global SSM over land and ocean salinity (Y. H. Kerr et al., 2010). Launched in November 2009, it is the first mission to provide global multi-angular and full-polarization L-band (1.4 GHz) microwave observations using 2D interferometry. The main advantage of the use of L-Band frequency is that the SSM-related surface emittance is higher in this frequency than in higher frequencies, and also both cloud and canopy cover affect less the measurement. In addition, passive microwave sensing technology is generally less impacted by clouds and vegetation (Ulaby et al., 1982) than active technology. The volumetric soil moisture is retrieved at coarse resolution (roughly 15 or 25 km), with an accuracy mission goal higher than 0.04 m^3 m_{-3}. Two overpasses are available, one in the ascending orbit (06:00 local time) (SMOS Asc.) and the other in the descending one (18:00 local time) (SMOS Desc.)[7]. The MIR_CLF31 Level3 product v4 used for this study (Al Bitar et al., 2017) was downloaded from the *Centre Aval de Traitement des Données SMOS* (CATDS) processing centre.

The Soil Moisture Active Passive (SMAP) mission is the National Aeronautics and Space Administration (NASA) project aimed at studying the surface soil water. Launched in 2014, it featured both a radar (an active instrument) and a radiometer (a passive one), operating in the L-band (1.41 GHz) of the microwave spectrum with a mesh antenna. SMAP featured also an onboard RFI processor. The SMAP acquisitions are at a fixed angle (40°) in dual polarization with a 40 km resolution. While the radiometer provides "passive" estimates with its coarse spatial resolution, the radar analyses the "active" backscatter obtained from a Synthetic Aperture Radar (SAR) technology at 3 km spatial resolution. Unfortunately, the SAR stopped operations 3 months after launch due to failure. The combination of the two datasets creates the final product, joining the penetrating capacity of the "passive" technology with the high spatial resolution of the "active" one (Entekhabi et al., 2010). SMAP level3 (release 16) soil moisture from passive sensor at 36km (SMAP_L3_SM_P) was downloaded from the NASA Earthdata portal.

The dataset from the ESA Climate Change Initiative (CCI) (Gruber et al., 2019) is not the result of a direct observation but is the result of the merging of multiple datasets. The main goal was standardizing different SSM observations throughout the years to obtain a unique database. First, data from active SSM sensors (AMI-WS, ASCAT-A and ASCAT-B) and passive ones (SMMR, SSM/I, TMI, AMSR-E, Windsat, SMOS, AMSR2) are joined in two separate datasets, ESA-CCI Active and ESA-CCI Passive, respectively. Thus, the homogeneity of the retrieval technology is preserved. Employing this wide range of instruments allows reducing the no-data days, as opposed to the single products, effectively decreasing the virtual revisit time of the dataset. Active products are obtained through the Water Retrieval Package (WARP) algorithm (Naeimi et al., 2009), which

[7] https://earth.esa.int/documents/10174/1854519/SMOS_L2_SM_ATBD

is a change-detection approach that retrieves soil moisture in the form of saturation degree, referring to the historically lowest and highest observed values. On the other hand, passive products are obtained through the Land Parameter Retrieval Model (LPRM) algorithm and are provided in volumetric ratio units (m^3 m^{-3}). In order to join data from different missions in one unique dataset, all the products are harmonized to a common reference, chosen because of expected higher accuracy and most recent operative period: ASCAT for the active group and AMSR-E for the passive one (Y. Liu et al., 2012). In order to join the two global datasets, both active and passive product are re-scaled against Global Land Data Assimilation System (GLDAS) Noah soil moisture simulations. Finally, the combined hybrid dataset is obtained through an algorithm that merges the two datasets according to the estimated reliability of each. The resulting dataset (ESA-CCI Combined) is thus an aggregate dataset, containing information from a wide variety of active and passive sensors (Dorigo et al., 2017; Gruber et al., 2017).

The Copernicus Surface Soil Moisture 1km Version 1 product (SSM1km) is obtained from Sentinel-1 C-band SAR backscatter after geo-correction and radiometric calibration. The output product is an index in percent of saturation, with 1°/112 nominal resolution (around 1 km at European latitudes). Overpasses from the Sentinel-1 are programmed every day, but the revisit time over a single spot on the Earth surface is longer: in the Capitanata case study, for example, the actual revisit time is slightly higher than 4 days (Bauer-Marschallinger et al., 2018). In order to achieve a valuable comparison with the other (coarse-resolution) datasets, this data have been upscaled (Copernicus Upscaled dataset) by employing a simple average of all the pixels contained within each dataset footprint. The resulting fictitious pixel covers a large area (ca. 1 100 km^2 for the Capitanata irrigation consortium, ca. 1 000 km^2 for the Chiese one) that can be assimilated to a 30 km pixel, which is in line with the other coarse-resolution datasets. On the other hand, this data can also be employed at its original high resolution, as is the case for the comparison with the data from the Parrot sensors (detailed in Section 5.5). For that specific activity, a total number of 26 images have been selected within the study period (20^{th} July to 20^{th} October 2019).

The Advanced Microwave Scanning Radiometer 2 (AMSR2) is the successor of AMSR-E, operating since 2012. It is part of the Global Change Observation Mission (GCOM) by the Japan Aerospace Exploration Agency (JAXA). In its orbit around the Earth, it guarantees two overpasses, one in the Ascending path (13:30 local time) (AMSR2 Asc.) and the other in the Descending one (01:30 local time) (AMSR2 Desc.) (de Jeu and Owe, 2008). Data from AMSR2 are featured within the ESA-CCI Passive product, in some cases making up most of the source data for the product. In the Chiese case study, ESA-CCI Passive data is obtained only from this dataset, so in this case using either dataset amounts to the same result. On the other hand, for the Capitanata case study, ESA-CCI Passive data is not available on the area of interest because of geographical reprojection issues. In its stead, the AMSR2 at its source has been analysed. Among the many sources of the AMSR2 dataset, the one chosen for this study is the LPRM_AMSR2_DS_D_SOILM3 surface soil moisture (de Jeu and Owe, 2008), which is also the one employed for the ESA-CCI product.

An overview of all employed datasets is available in Table 3.6.

Figure 3.11 provides a map of the satellite SSM pixel footprints over the Capitanata and Chiese Irrigation Consortia, where the analysis will take place. The rain gauges used for precipitation interpolation are also shown.

3.7.2 Vegetation indices

Vegetation indices (VIs) were obtained in Corbari et al. (2020) from the Visible (VIS), Near-Infrared (NIR) and Shortwave Infrared (sIR) bands of Landsat-8 and Sentinel-2 satellites. In particular, the

Table 3.6: Specifics of the different Surface Soil Moisture (SSM) dataset employed in the study.

Dataset	Product	Ref. Time	Retrieval Technology	E.M. Spectrum	Revisit Time	Sensor Grid	Product Grid
SMOS	Ascending Descending	06:00 18:00	Passive	L band	1-2 days	40 km	25 km
SMAP	Descending	18:00	Passive	L band	2.2 days	40 km	36 km
ESA-CCI	Active Passive Combined	00:00	Active Passive Hybrid	Various bands	1.2 days	Variable	0.25°
Copernicus (Sentinel1)	Original Upscaled	00:00	Active	C band	4.1 days	10 m	1°/112 30 km
AMSR-2	Ascending Descending	13:00 01:00	Passive	C band	1.5 days	50 × 70 m	10 km

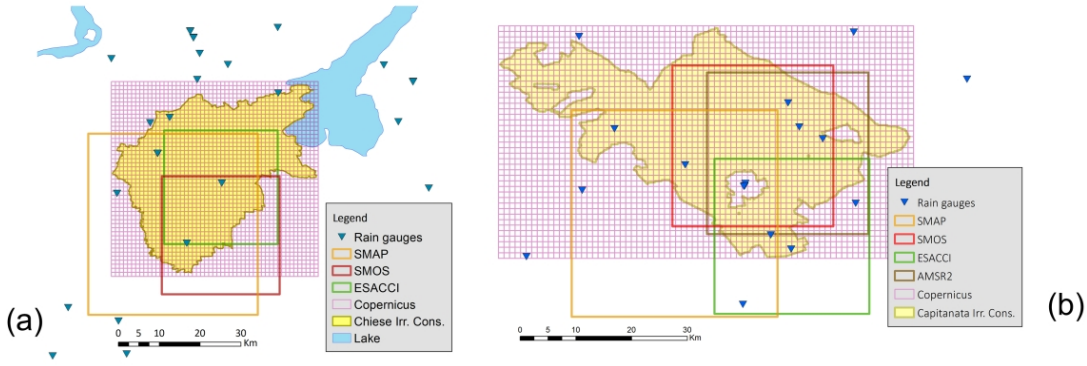

Figure 3.11: Chiese (a) and Capitanata (b) Irrigation Consortia with SSM datasets footprints

bands around 660 nm and 850 nm were used for vegetation index estimation and those around 1 600 nm and 850 nm were used for vegetation water content. All bands were atmospherically corrected by the use of 6S software (Vermote et al., 1997) in order to account for the surface reflectance.

A quite common index is the Normalized Difference Vegetation Index (NDVI), which is directly linked to the amount of vegetation present on ground. It is computed from the remotely-sensed reflectances in the Near InfraRed (NIR) and Red bands, as live green plants appear relatively dark in the Photosynthetically Active Radiation (PAR, covering the Red bands) and relatively bright in the NIR (Gutman and Ignatov, 1998).

$$NDVI = \frac{NIR - Red}{NIR + Red} \tag{3.11}$$

The Vegetation Fraction (f_V) identifies the fraction of the total pixel area which is covered by vegetation and it can be estimated through from the NDVI, by selecting an area wide enough to cover both fully-vegetated (NDVIv) and completely bare (NDVIs) pixels:

$$f_V = \frac{NDVI - NDVI_S}{NDVI_V - NDVI_S} \tag{3.12}$$

The values for NDVIv and NDVIs can also be chosen from literature, as is the case for the

applications in this thesis (0.90 and 0.15, respectively). Once obtained the f_V, Leaf Area Index (LAI) can be calculated in a way similar to that already employed for LAI data from Parrot, adopting the formulation:

$$LAI = -\frac{\ln(1 - f_V)}{K(\psi)} \tag{3.13}$$

where $K(\psi)$ is the beam extinction coefficient for a given solar zenith angle (ψ). In this case, the beam extinction coefficient is set to a general value of 0.5.

The Soil Adjusted Vegetation Index (SAVI) is an alternative to NDVI, which can be computed in order to reduce the soil background effect (Huete, 1988).

$$SAVI = \frac{(1 + L_{can})(NIR - Red)}{NIR + Red + L_{can}} \tag{3.14}$$

where L_{can} accounts for first-order soil background variations, and in this case is computed as the average vegetation cover of the image, varying from 1 (image fully covered by vegetation pixels) to 0 (image completely bare). Moisture Stress Index (MSI) and Normalized Difference Water Index (NDWI) are two basic indices for the estimation of vegetation water content. Equations for both are:

$$MSI = \frac{\rho_{1600}}{\rho_{850}} \tag{3.15}$$

$$NDWI = \frac{\rho_{850} - \rho_{1600}}{\rho_{850} + \rho_{1600}} \tag{3.16}$$

The 1 600 nm wavelength (sIR) corresponds to a peak in radiation absorption from vegetation, which increases with high leaf water contents. On the other hand, at 850 nm (NIR) the absorption is practically undisturbed by water content changes, and thus this reflectance can be used as a reference. By its structure, the MSI has an opposed trend with respect to other indexes: as absorption at 1 600 nm increases with water content, low ρ_{1600} values – and, thus, low MSI values – are associated with water stress conditions (E. R. Hunt and Rock, 1989). The same band reflectances are employed by NDWI, which also accounts for the light scattering from vegetation canopies, which influences reflectance around 1 600 nm (Gao, 1996).

3.7.3 Land surface temperature

LST can be calculated through different techniques, which require the use of one, two or more thermal bands of one sensor. This section provides the data elaboration performed in Corbari et al. (2020) Two techniques were employed: Single Channel (SC) algorithm and Split Window (SW) algorithm, which were applied to Landsat-7 Enhanced Thematic Mapper Plus (ETM+) and Landsat-8 Thermal InfraRed Sensor (TIRS). For ETM+ and TIRS, LST was retrieved following the procedure explained in Skokovic et al. (2017) for SC algorithm and Jimenez-Muñoz et al. (2014) for SW algorithm, respectively. The SC equation is:

$$LST = \frac{{T_{sen}}^2}{b_\gamma L_{sen}} \left[\frac{\Psi_1 L_{sen} + \Psi_2}{\varepsilon} + \Psi_3 \right] + T_{sen} - \frac{T_{sen}^2}{b_\gamma} \tag{3.17}$$

where T_{sen} is the at-sensor brightness temperature, ε is the emissivity, b_γ is a constant (1 277 K), and Ψ_1, Ψ_2 and Ψ_3 are functions of the atmospheric parameters of transmissivity and upwelling and downwelling radiances. The SW equation used for TIRS bands is presented as:

$$LST(i,j) = T_i + a_0 - a_1(T_i - T_j) + a_2(T_i - T_j)^2 + (a_3 + a_4 awc)(1-\epsilon) + (a_5 + a_6 awc)\Delta\varepsilon \quad (3.18)$$

where T_i and T_j are the at-sensor brightness temperatures at the SW bands i and j, ε is the average emissivity across both bands, $\Delta\varepsilon$ is the corresponding difference, awc is the total atmospheric water vapor content (g cm^{-2}) and a_0, a_1, a_2, a_3, a_4, a_5 and a_6 are the SW coefficients with values of 16.40, -0.268, 1.378, 0.183, 54.30, -2.238 and -129.20, respectively.

For both equations, the atmospheric parameters and water vapor content inputs were computed using the MODTRAN 5.0 radiative transfer code, employing a forecasted atmospheric profile from the European Centre for Medium-Range Weather Forecasts (ECMWF), included in the Sentinel-3 data. For the emissivity inputs, the NDVI Thresholds Method (NDVI-ThM) was applied, following the original equations presented in Sobrino et al. (2008). Finally, in order to disaggregate the ETM+ and TIRS pixels from their original spatial resolution of 60 m and 100 m, respectively, to a resolution of 30 m, the Nearest Neighbour Temperature Sharpening (NNTS) methodology was used as described in Skokovic (2017). More complete information about the whole procedure of LST retrieval at 30-m spatial resolution is available at Corbari et al. (2020).

Part II

Satellite data analysis

Chapter 4

Hydrological Consistency Index

In this section, the different SSM satellite datasets have been analysed through the newly-developed Hydrological Consistency Index (HCI, Paciolla et al., 2020) described in Section 2.1. Firstly, a more classical analysis based on common correlation indexes is detailed. Then, the potentialities of the HCI are explored, analysing the differences between the datasets and the case studies, verifying also some potential weak points of the algorithm.

4.1 Correlation Between SSM and Precipitation

Before adopting the newly-formulated algorithm, a simpler way to investigate the relationship between SSM and the precipitation occurred in the preceding 24 hours is adopted. Two commonly-used correlation indices have been employed: Pearson and Spearman. Although the former requires an assumption of normality for the distribution of the involved variables, which is rarely the case for precipitation, it has nonetheless been used in numerous studies on SSM precipitation comparison (Dai et al., 1999; Sehler et al., 2019). On the other hand, Spearman correlation does not require an assumption of normality and helps to provide some information about their possible relationship. As shown in Table 4.1, low-to-negligible Pearson and Spearman correlations were found for all datasets. The lowest correlation values around 0.03 and 0.05 are obtained for SMOS Desc. data for Capitanata and Chiese, respectively; while higher values are found for SMOS Asc. (0.24). The highest overall values were obtained for the Copernicus dataset (0.45 in Capitanata area), as would be expected from the comparison between a precipitation field obtained by the spatial interpolation of rain gauge measurements and (relatively) high resolution SSM data. This suggests a strong link between spatial resolution of the SSM product and physical correspondence of the rainfall-SSM duality. Data from ESA-CCI Passive are not featured for the Capitanata area because of a lack of data over the main Consortium area. Data from AMSR2 are not featured for Chiese, as they are already contained within the ESA-CCI passive dataset.

In similar scenarios, a number of other studies found wide-ranging results. Middle-to-high correlations (0.64—0.81) for ASCAT and middle-to-low (0.21—0.64) for AMSR-E were registered by Brocca et al. (2011), while in a multi-product analysis, Cui et al. (2017) found the best correlations with on-site data when employing L-band products (SMOS and SMAP). This is consistent with the deeper depth gauged by these frequencies and their low susceptibility to vegetation and atmosphere influences. Kerr et al. (2016) found middle-to-high correlation values for SMOS on Australian,

Table 4.1: Pearson and Spearman correlations among different SSM dataset estimates and the rainfall occurred in the preceding 24 h.

Dataset	Capitanata		Chiese	
	Pearson	Spearman	Pearson	Spearman
ESA-CCI Active	0.1644	0.278	0.212	0.304
ESA-CCI Passive	n/a	n/a	0.085	0.108
ESA-CCI Combined	0.131	0.308	0.106	0.205
Copernicus	0.381	0.417	0.298	0.304
Copernicus Upscaled	0.417	0.450	0.341	0.363
SMOS Asc.	0.240	0.293	0.119	0.145
SMOS Desc.	0.038	0.067	0.055	0.092
SMAP	0.393	0.427	0.177	0.249
AMSR-2 Asc.	0.119	0.120	n/a	n/a
AMSR-2 Desc.	0.102	0.122	n/a	n/a

African, and, mainly, U.S. test sites, while El Hadjj et al. (2018) identified correlation values in the range 0.4–0.6 for SMAP, ASCAT, and SMOS in Southern France. Moreover, results from a triple (and even quadruple, using both active and passive sensors independently) collocation analysis on a global scale indicate that SMAP is the best-performing dataset globally (achieving a cross-correlation of 0.76, against 0.66 for SMOS and 0.63 for ASCAT) (Chen et al., 2018). Finally, low correlation values have been found by other studies, 0.11–0.26 measured in Kansas, USA (Dai et al., 1999) and 0.4 in Mediterranean Europe (Sehler et al., 2019). These numbers pointed out the scarce feasibility of this mathematical tool to analyse the SSM–precipitation relationship.

4.2 Consistency for Capitanata Irrigation Consortium

The newly-defined consistency procedure is applied to all the datasets over the Capitanata irrigation consortium. Figure 4.1 shows an example application on the SMOS descending dataset, with further examples shown in Appendix A. First, an algorithm run is performed without taking irrigation into account. Then, the same data are analysed considering irrigation, in order to highlight its contribution to the analysis process. In the first panel (Fig. 4.1a), the SSM time-series along year 2015 has been displayed. The yellow background identifies irrigation days, while the blue one is associated with the non-irrigation ones. Each SSM estimation is labelled green if a positive agreement (A+) is recorded for that instance, red if a negative one (A–) is found, white if the variation from the previous SSM estimation is below the measurement error threshold (in this case, the algorithm is not applied at all and that SSM instance is discarded from the final computation). In the middle panel (Fig. 4.1b), the algorithm is applied, taking into account the presence of irrigation: some SSM retrievals, which were red (A–) in the first panel, have now been coloured blue to represent the irrigation-driven positive agreements (IA+). In the third and lower panel (Fig. 4.1c), the aggregated precipitation field over the SSM pixel is shown.

The first take-away from the no-irrigation algorithm run (Fig. 4.1a) is that the dataset does not show a clear positive trend: of over 145 records in year 2015, 62 (43%) show some incongruence when compared with the registered rainfall. However, when looking at these results split by irrigation regime, a higher proportion of positive agreements is recorded in the irrigation period (61%-29%

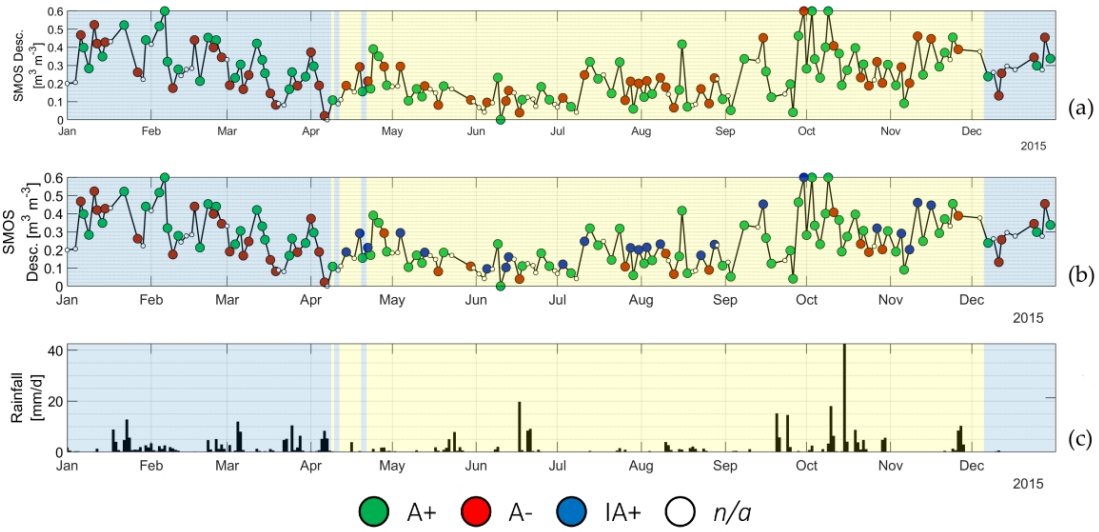

Figure 4.1: Distribution of positive (A+), negative (A–) and irrigation-driven positive (IA+) agreements for a SMOS descending pixel in the Capitanata test case. Results before (a) and after (b) taking irrigation volumes into consideration. The corresponding precipitation time series is shown in the lower panel (c).

against 51%-49% for the non-irrigation period).

The results from the complete algorithm are detailed in Figure 4.1b and the right-hand half of Table 4.2. Of the 37 negative agreements (A–) recorded during the irrigation season, 24 are found to be explainable with the knowledge about the irrigation regime (IA+). This leaves out 13 "unexplainable" negative agreements between the SSM dataset and precipitation. Thus, the performance of the SMOS dataset, for the year 2015 and over the Capitanata Irrigation Consortium, can be considered "mild" in the non-irrigation period (49% of negative agreements) but quite positive in the irrigation one (only 14%).

Table 4.2: Number of SSM retrievals classified for each consistency category (relative weight in parentheses), as displayed in Figure 4.1

Irrigation Regime	Simple HCI (No Irrigation)		Complete HCI (With Irrigation)	
Non-Irrigation period	A+	26 (51%)	A+	26 (51%)
	A–	25 (49%)	A–	25 (49%)
Irrigation period	A+	57 (61%)	A+	57 (61%)
	A–	37 (29%)	A–	13 (14%)
			IA+	24 (26%)

This same analysis has been carried out for all datasets and all years. An example image corresponding to year 2016 is shown in Figure 4.2. SMAP data (Fig. 4.2c) show smoother variability than SMOS data (a lower standard deviation throughout the year) and in general show a higher positive agreement irrespective of the irrigation information. Data from the ESA-CCI are quite

heterogeneous, starting from the units: the active dataset (Fig. 4.2d) is a saturation ratio dataset, while the passive one is a volumetric ratio. The combined dataset (Fig. 4.2e), although showing a much higher data density (approximately 1 SSM estimate every day against the 2 days of the single active and passive datasets), displays little variation from one estimate to the next. Most (73% in 2016) of the combined SSM values vary from their respective previous ones by less than 0.04 m^3 m^{-3}, which results in a much smaller number of recorded SSM–precipitation couples used in the evaluation of the agreement. Upscaled Copernicus data are visible in Figure 4.2f, showing the lower data density of this dataset with respect to the others, with one SSM estimate on average every 4 days. AMSR-2 data (Figs. 4.2g,h) show an important oscillation around the average and a low degree of seasonality, almost retaining the same average value all year long, which can be explained by the impact of the vegetation cover on the retrievals when using C and X-Band microwave (Njoku and Chan, 2006).

The original, 1km-resolution Copernicus data allow the algorithm to be applied on each and every one of the 1 353 pixels covering the Consortium, every year. Therefore, the global result is presented in terms of maps, adding a further level (possible spatial heterogeneities) in the description of the SSM dataset (Fig. 4.3).

The summarized results over the different datasets for the four test years (2015-2018) are detailed in Table 4.3 for the non-irrigation period and Table 4.4 for the irrigation season. For each year and product, the number of the SSM-precipitation couples, or "occurrences" (n), the proportions of positive (A+), negative (A–), and irrigation-driven positive (IA+) agreements are provided. For every SSM dataset except Copernicus SSM1km, the table data refer to the single pixel chosen for the evaluation; for the Copernicus SSM1km, the average values from all the pixels covering the irrigation consortium are provided. Overall, negative agreements occur on average 40% of the times in the non-irrigation period. The ESA-CCI datasets tend to score lower results than the passive datasets (SMOS and AMSR2, for example). When shifting to the irrigation period, the negative agreements fall, on average, to 14%. Some datasets feature very sharp decreases (e.g., SMOS descending from 57% down to 17% in 2017), while some register a moderate increase (e.g., SMOS descending from 25% up to 31% in 2018). The decrease in registered negative agreements is only partly justified by a connected increase in positive agreements. Irrigation-driven positive agreements are usually recorded between 15% and 30%, with an average value of 23%.

Globally, not much difference can be found between the datasets. For any given year, the agreements tend to cluster around a common value, with relatively low variation coefficients (10%-20%), notwithstanding the depicted differences between the datasets.

The averaged Copernicus data are presented in Table 4.3 and 4.4, with results in line with those of the other datasets. However, the dataset shows a much more heterogeneous behaviour, as can be seen in Figure 4.3: very low positive agreements (less than 30%) can be registered in the north-western area of the consortium. The irrigation-driven positive agreement shows a highly heterogeneous pattern, probably reflecting the distribution of the most irrigated fields within the consortium. This may be explained by the combined impact of surface roughness and vegetation biomass on the retrieved soil moisture (Qiu et al., 2019).

4.3 Consistency for Chiese Irrigation Consortium

The same analysis has been carried out over the Chiese test case. Results are displayed, dataset by dataset, in Figure 4.4 (example run for 2016 with all datasets except Copernicus) and 4.5 (2016 run for Copernicus). Numerical results are detailed in Table 4.5 and 4.6. In many aspects, the results

Table 4.3: HCI results for the non-irrigation period over Capitanata: number of SSM–precipitation couples (n), proportion of positive (A+) and negative (A–) agreements.

Dataset	2015			2016			2017			2018		
	n	A+	A–	n	A+	A–	n	A+	A–	n	A+	A–
Active	49	71%	29%	45	64%	36%	65	75%	25%	36	83%	17%
Combined	26	69%	31%	19	58%	42%	32	72%	28%	21	90%	10%
Copernicus	18.5	59%	41%	18.1	50%	50%	37.3	62%	38%	36.0	58%	42%
Up. Copernicus	17	59%	41%	16	44%	56%	34	65%	35%	35	60%	40%
SMOS Asc.	46	50%	50%	36	50%	50%	19	63%	37%	22	68%	32%
SMOS Desc.	50	50%	50%	34	56%	44%	41	44%	56%	16	75%	25%
SMAP	-	-	-	24	79%	21%	-	-	-	-	-	-
AMSR2 Asc.	48	60%	40%	57	53%	47%	92	50%	50%	97	48%	52%
AMSR2 Desc.	71	48%	52%	60	53%	47%	103	52%	48%	105	59%	41%

Table 4.4: HCI results for the irrigation period over Capitanata: number of SSM–precipitation couples (n), proportion of positive (A+), negative (A–), and irrigation-driven positive (IA+) agreements

Dataset	2015				2016				2017				2018			
	n	A+	A–	IA+	n	A+	A–	IA+	n	A+	A–	IA+	n	A+	A–	IA+
Active	61	75%	7%	18%	94	70%	14%	16%	43	70%	9%	21%	33	67%	12%	21%
Combined	40	65%	8%	28%	63	71%	10%	19%	29	76%	-%	24%	30	63%	13%	23%
Copernicus	31.4	65%	23%	12%	25	51%	31%	18%	26	62%	17%	21%	22	63%	23%	14%
Up. Copernicus	32	69%	22%	9%	29	59%	24%	17%	25	60%	16%	24%	23	74%	17%	9%
SMOS Asc.	102	56%	16%	28%	76	61%	22%	17%	58	71%	10%	19%	26	62%	15%	23%
SMOS Desc.	95	59%	16%	25%	72	49%	25%	26%	53	53%	19%	28%	35	31%	31%	37%
SMAP	-	-	-	-	44	64%	30%	7%	-	-	-	-	-	-	-	-
AMSR2 Asc.	105	55%	13%	31%	112	46%	22%	31%	94	54%	13%	33%	90	49%	17%	34%
AMSR2 Desc.	116	55%	16%	29%	107	56%	19%	25%	95	59%	12%	29%	108	57%	12%	31%

about the Chiese irrigation consortium resemble the ones about the more southern case study. For any given year, the performances of the different datasets do not differ much, in particular in the non-irrigation period. However, overall, positive agreements (A+) are higher than the Capitanata test case: values as high as 84% are attained, with frequent instances of overpassing the 70% mark. On the other hand, the irrigation-driven positive agreements (IA+) register low values; they are higher than 20% only a few times.

4.4 Capitanata–Chiese Comparison

When comparing the results of the methodology over the two cases studies, it is important to keep in mind the differences between them. The Capitanata consortium is located in a considerably dry area (540 mm/year on average), with a vital need for artificial irrigation. On the other hand, the area around Lake Garda, where the Chiese irrigation consortium is located, is much wetter (760 mm/year). This means that for this second test case, the increases in soil moisture should be mainly linked to the presence of precipitation, and so the "irrigation-driven positive agreements" should be less important. In fact, the higher amount of rainy days (206 days/year in the 2015-2018 period, against 158 days/year for the Capitanata in the same period) reduces the possibility of recording SSM variations without the presence of precipitation. Thus, from a purely methodological point of view, the possibility of registering IA+ cases decreases with the amount of rainy days in a year.

Table 4.5: HCI results for the non-irrigation period over Chiese: number of SSM–precipitation couples (n), proportion of positive (A+) and negative (A–) agreements.

Dataset	2015			2016			2017			2018		
	n	A+	A–	n	A+	A–	n	A+	A–	n	A+	A–
Active	49	71%	29%	45	64%	36%	65	75%	25%	36	83%	17%
Combined	26	69%	31%	19	58%	42%	32	72%	28%	21	90%	10%
Copernicus	18.5	59%	41%	18.1	50%	50%	37.3	62%	38%	36.0	58%	42%
Up. Copernicus	17	59%	41%	16	44%	56%	34	65%	35%	35	60%	40%
SMOS Asc.	46	50%	50%	36	50%	50%	19	63%	37%	22	68%	32%
SMOS Desc.	50	50%	50%	34	56%	44%	41	44%	56%	16	75%	25%
SMAP	-	-	-	24	79%	21%	-	-	-	-	-	-
AMSR2 Asc.	48	60%	40%	57	53%	47%	92	50%	50%	97	48%	52%
AMSR2 Desc.	71	48%	52%	60	53%	47%	103	52%	48%	105	59%	41%

Table 4.6: HCI results for the irrigation period over Chiese: number of SSM–precipitation couples (n), proportion of positive (A+), negative (A–), and irrigation-driven positive (IA+) agreements

Dataset	2015				2016				2017				2018			
	n	A+	A–	IA+	n	A+	A–	IA+	n	A+	A–	IA+	n	A+	A–	IA+
Active	36	67%	22%	11%	70	60%	30%	10%	65	59%	26%	15%	47	51%	43%	6%
Passive	91	74%	12%	14%	94	70%	18%	12%	77	75%	10%	14%	39	72%	15%	13%
Combined	42	84%	2%	14%	61	84%	5%	11%	58	79%	12%	9%	34	77%	18%	5%
Copernicus	33.9	57%	38%	5%	26.0	64%	29%	7%	60.3	70%	23%	7%	53.9	57%	39%	4%
Up. Copernicus	33	58%	42%	-%	30	67%	33%	-%	63	78%	17%	5%	53	55%	43%	2%
SMOS Asc.	100	65%	14%	21%	104	66%	18%	16%	82	56%	23%	21%	60	50%	37%	13%
SMOS Desc.	100	62%	22%	16%	101	55%	24%	21%	69	61%	23%	16%	62	58%	36%	6%
SMAP	-	-	-	-	34	77%	23%	-%	-	-	-	-	-	-	-	-

The results comparison is detailed in Table 4.7.

Table 4.7: Averaged HCI results (SMAP results refer only to 2016).

Case Study	Capitanata					Chiese				
Period	Non-Irrigation		Irrigation			Non-Irrigation		Irrigation		
Dataset	A+	A–	A+	A–	IA+	A+	A–	A+	A–	IA+
Active	73%	27%	71%	11%	18%	68%	32%	59%	30%	11%
Passive	-	-	-	-	-	64%	36%	73%	14%	13%
Combined	75%	25%	75%	4%	21%	64%	36%	81%	9%	10%
Copernicus	58%	42%	60%	24%	16%	55%	45%	63%	32%	5%
Up. Copernicus	59%	41%	65%	20%	15%	56%	44%	65%	32%	2%
SMOS Asc.	55%	45%	62%	15%	23%	54%	46%	61%	21%	18%
SMOS Desc.	52%	48%	54%	19%	28%	47%	53%	59%	25%	16%
SMAP*	79%	21%	70%	23%	7%	69%	31%	77%	24%	-%
AMSR2 Asc.	54%	46%	61%	11%	29%	-	-	-	-	-
AMSR2 Desc.	52%	48%	55%	12%	33%	-	-	-	-	-

Neither of the test cases features a very high incidence of positive agreements in the non-

irrigation period. The highest recorded values are both from the ESA-CCI datasets: the combined (75%) for Capitanata and the active (64%) for Chiese, apart from SMAP, whose data refer to one year alone. All the other datasets cluster not much further than the 50% threshold, with SMOS Desc. (over Chiese) not even attaining that value.

When shifting to the irrigation period, all datasets present a reduction of the negative agreements: for the Capitanata case study, the irrigation negative agreements are at least halved, being on average reduced by a factor higher than 3; for the Chiese case study, this reduction is less important, around a factor of 2. This improvement in the dataset performance is found also in the increase of the A+ cases, which grow by a much smaller factor of 1.05 for Capitanata and 1.13 for Chiese, with little variation among datasets. Thus, the main factor determining the better performances of the SSM products in the irrigation period is the identification of irrigation-driven positive agreements. These are mainly restricted at less than 20% of the total records in the irrigation period but contribute to reduce the unexplainable negative agreements.

The IA+ cases are quite homogeneous for the Capitanata case study, averaging at about 23% for all datasets and with a low variation coefficient (28%). On the other hand, in the Chiese area, the average value falls to 11% with a much wider dispersion between the different datasets (the coefficient of variation is 51%).

4.5 Retrieval Technology and Algorithm Comparison

Averaging the data according to the retrieval technology, as detailed in Table 4.8, eventual differences due to the active/passive dualism can be detected. A slightly better non-irrigation performance from active instruments is registered with respect to passive ones, scoring better results in the Capitanata test case (+10%) as opposed to the Chiese one (+5%). When shifting to the irrigation period, the increase in registered A+ orbits around 5%-10%. On the other hand, hybrid products (mainly the ESA-CCI combined) outperform the others scoring on average much more A+ cases (+15%) with respect to the other instruments both in irrigation and non-irrigation periods.

Table 4.8: HCI results averaged by retrieval technology class.

Dataset	Capitanata					Chiese				
Period	Non-Irrigation		Irrigation			Non-Irrigation		Irrigation		
Class	A+	A–	A+	A–	IA+	A+	A–	A+	A–	IA+
Active	63%	37%	65%	18%	16%	60%	40%	62%	31%	6%
Passive	53%	47%	58%	14%	28%	55%	45%	64%	20%	16%
Hybrid	75%	25%	74%	4%	21%	64%	37%	81%	9%	10%

It is worth noting also the comparison between SMOS, SMAP, and AMSR2 results, non-hybrid products of passive retrieval technology, and similar spatial resolutions. The different choice of auxiliary data and parameters involved in the pre-processing of the estimation contributes to the heavily different HCI results.

4.6 Spatial Resolution Differences with Copernicus

The Copernicus product, being the only high-resolution dataset in this analysis, can be evaluated both in its original and its upscaled version. This allows assimilating the product to the macro-

scale of the other datasets, allowing a more coherent comparison. Furthermore, by contrasting two datasets that share every characteristic apart from their spatial resolution, some conclusions could be drawn about the influence of spatial scales in the dataset performance.

Comparing the year-by-year results over both Capitanata and Chiese, no clear difference emerges between the two datasets performances. This means that in a global, averaged analysis, the consistency of the Copernicus SSM with precipitation does not improve the results obtained by coarser-resolution datasets. However, as the maps in Figures 4.3 and 4.5 point out, higher (and lower) consistencies can be attained locally. This may be due to the high heterogeneity characteristic of an Irrigation Consortium made up of a wide variety of farms with different crops and irrigation practices.

This means that the high-resolution Copernicus SSM product possesses, on average, a mild consistency with precipitation, with results that can vary greatly on a local basis. It is important to add that these results do not account for the percentage of irrigated areas in the coarse scale pixel.

4.7 Incidence of Yearly Rainfall and Data Density

As part of the analysis, two "heterogeneity factors" have been investigated: data density and basin wetness. As each dataset has a different sampling frequency, when comparing the relative number of agreements expressed as percentages, the data pool from which these percentages are computed could affect the final results. Smaller data pools could favour more erratic results. On the other hand, the wetness of any given year could have an impact on the results, as wetter years may reduce the chances of recording negative agreements.

When looking at the positive agreements sorted by the number of SSM–precipitation couplings or "occurrences" (Fig. 4.6), a slightly higher data dispersion emerges for datasets with a low number of occurrences. Around 100 yearly occurrences, data tend to cluster around a common value, independently of the year or the dataset. This behaviour is more evident in the Capitanata example (Figs. 4.6a,b) than the Chiese one (Figs. 4.6c,d), and it seems to be amplified when shifting from the non-irrigation period (Figs. 4.6a,c) to the irrigation one (Figs. 4.6b,d).

The same positive agreements can be classified by the year wetness (Fig. 4.7). However, no clear decreasing or increasing trend with the cumulated rainfall emerges. The Capitanata results (Figs. 4.7a,b), which referred to dry conditions (annual rainfall between 350 and 500 mm/year), are more densely grouped than the Chiese results (Figs. 4.7c,d), which are recorded in wetter meteorological conditions (annual rainfall between 700 and 1 100 mm/year). This may descend from the relative importance that artificial irrigation invests in the Capitanata Irrigation Consortium. Relying on rainfall and irrigation, which is a steadier water resource than simple precipitation, it is reasonable that the performances, across all years and datasets, do not differ much.

4.8 Hit Rate and False Positives Check

The procedure detailed in this work could be inaccurate in situations in which irrigation data are unknown or imprecise, as the introduction of irrigation may increase the probability of registering consistency. Hydrologically speaking, increases in SSM in the absence of precipitation should occur only when another water input, such as irrigation, is present. If there is an absence of information about irrigation, any SSM increase without precipitation is classified as irrigation-driven (IA+),

and the final consistency result can be polluted by a number of "false positives", i.e., SSM increases without precipitation and happening outside of the irrigation period.

In order to ascertain the incidence of these false positives in the total IA+ count, a reference run of the algorithm has been performed. In this scenario, any increase in SSM with no recorded rainfall has been assumed to happen in an irrigation regime, irrespectively of whether any actual irrigation took place. Thus, these results show what would happen if the procedure was performed without any *a priori* knowledge of the actual irrigation.

The resulting fraction of IA+ cases recorded during actual irrigation periods can be seen as a Hit Rate (HR) of the HCI. For example, a HR of 60% would mean that out of 100 SSM increases recorded by the given dataset in an absence of precipitation, only 60 happen during the irrigation period and contribute to a good hydrological consistency of the dataset. An ideal result would be HR = 100%, meaning that the only cases in which SSM increases without precipitation are the ones in which artificial irrigation is involved. On the other hand, a lower HR could be an application-oriented estimate of the quality of the dataset with respect to water accretion phenomena in the water cycle.

The results of this analysis are provided in Figure 4.8 for the Capitanata (Fig. 4.8a) and Chiese (Fig. 4.8b) test cases. For each SSM dataset, the total number of IA+ cases is shown. The yellow bar represents the fraction of these cases that are recorded when irrigation is being performed. The complementary blue bar identifies the similar cases (increase in SSM without any recorded rainfall) that are recorded when the area is not being irrigated. Thus, if we had applied this algorithm without having any information about irrigation, the blue bars would represent the amount of "false positives" among all the IA+ recorded cases, and the yellow bars would represent the algorithm Hit Rate.

Apart from SMAP (having just one year of data, it is less representative than the other datasets), all the datasets cluster around the average hit rate of 65% for Capitanata and 38% for Chiese. In the Capitanata case, the high-resolution Copernicus records a value below the 60% mark, while in the Chiese, the ESA-CCI combined is the only dataset attaining a HR higher than 60%, with ESA-CCI passive barely reaching the 50% threshold.

One possible explanation for these different results between the two test cases can lie in the different climate between the two datasets. On average, rainy days in the Apr–Sep period for the Chiese dataset are similar to those in the Oct–Mar period (41 and 40, respectively). On the other hand, in the Capitanata test case, the irrigation period is much drier (26 rainy days against 40 in the non-irrigation period). This climatic distinction provides an important difference in the relevance of irrigation for the agricultural practice. Finally, the amount of private, unregistered wells in the Chiese test case is quite important, affecting the correct use of irrigation data in the HCI.

4.9 Final take-aways

Overall, the main finding is that no soil moisture product among the tested ones shows a systematic and definitive hydrological coherence with the rainfall data. This is particularly evident in the non-irrigation season, with some datasets that show consistency with precipitation only about half of the time. On the other hand, during irrigation seasons, this consistency increases, partly because of an increase in rainfall-driven positive agreements (A+, increasing around 5%) and partly because of artificial irrigation and irrigation-driven positive agreements (IA+, averaging 15%–20%). Not many studies approached this paper's object from the same approach, but some indications can be gathered from McCabe et al. (2008) and Meng et al. (2018). These focused on SSM anomalies

and comparison with the presence of precipitation in the 24 hours preceding the satellite overpass. In some cases, 47% of the studied area showed an SSM anomaly being registered in the absence of precipitation; in others, only 57% of the area with precipitation registered in the preceding 24 hours subsequently shows a positive anomaly in SSM. The results of this study agree with these previous findings in testifying the moderate consistence of the SSM and rainfall datasets.

The results breakdown across dataset characteristics show that: (i) active and passive measurements do not show major performance differences, while hybrid estimates perform better, relying less on irrigation to achieve hydrological consistency (IA+ averaging 10% for hybrid, against 17% and 22% for active and passive, respectively); (ii) no noticeable difference is found between the two high- and coarse-resolution version of the same dataset (Copernicus SSM), although high-resolution data would be needed to better interpret the results; (iii) no clear trends were found in separating the results by yearly rainfall; (iv) low data densities (less frequent satellite overpasses) were found to be associated to a higher result dispersion , although no clear trend (e.g., better/worse results with less available data) was detected.

These results could have a number of explanations other than the natural error within the SSM product itself, which could point to possible improvements to the HCI algorithm:

1. Information about irrigation may not be complete: unregistered irrigation volumes (e.g., those related to unrecorded private wells) can provide explanation for increasing SSM values in absence of precipitation even outside of the "official" irrigation season. The integration of this kind of data would have immediate effect in improving the HR seen in Section 4.8;

2. The algorithm does not take into account daily evapotranspiration: especially in the warmer months of the year, sometimes, the actual evapotranspiration can be high enough that even though some rainfall has been registered, the overall water balance in the soil results negative, implying an SSM decrease;

3. The presence of vegetation can alter the SSM retrieval process for non-L-band satellites: although no clear difference has emerged between L-band (i.e., SMOS and SMAP) and C-band (i.e., Copernicus and AMSR2) datasets, it is reasonable to assume that vegetation contributes to the hydrological inconsistencies found in our analysis. For example, the fact that the Chiese case is more vegetated than the Capitanata one may be part of the reason for a higher average inconsistency in Chiese (22%) than in Capitanata (15%).

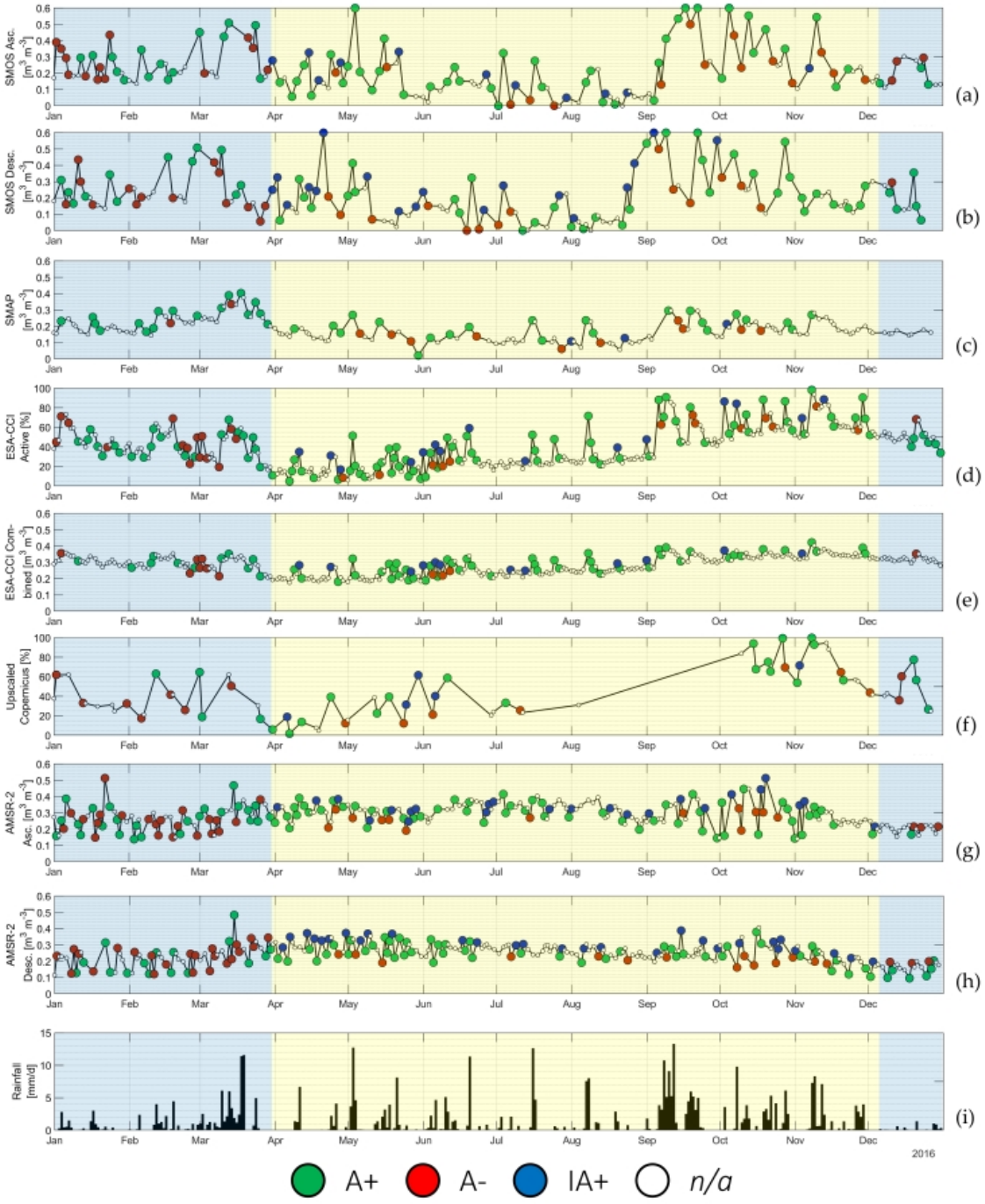

Figure 4.2: HCI data for 8 datasets for the Capitanata test case in 2016: SMOS Asc. (a) and Desc. (b), SMAP (c), ESA-CCI Active (d) and Combined (e) products, Up. Copernicus (h), AMSR2 Asc. (g) and Desc. (h). Rainfall data also provided (i).

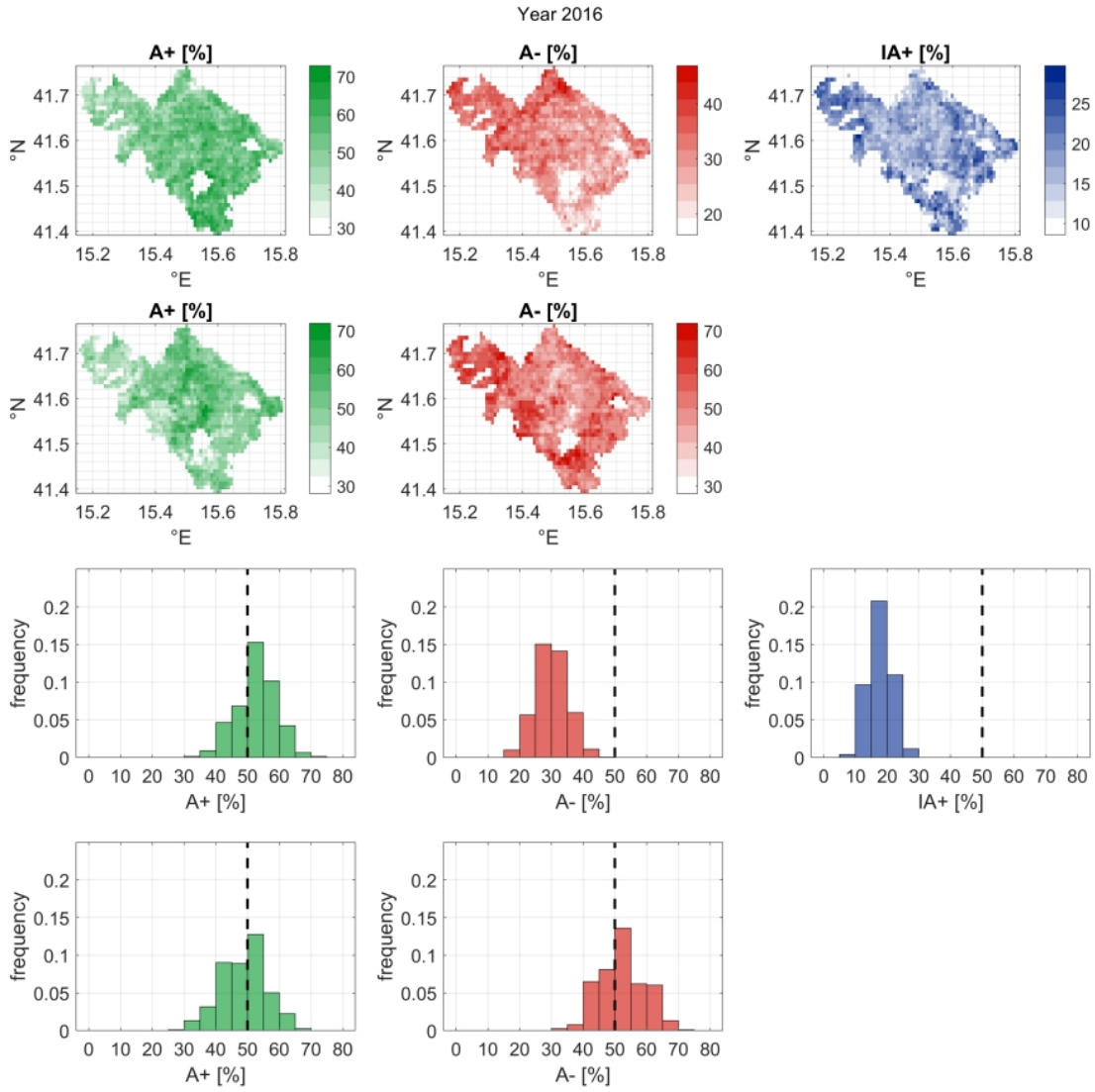

Figure 4.3: HCI results for the Capitanata case study, year 2016, with the Copernicus dataset. The first row details the HCI for the irrigation period: positive (A+), negative (A–) and irrigation-driven positive (IA+) agreements. The second row refers the HCI for the non-irrigation period: positive (A+) and negative (A–) agreements.

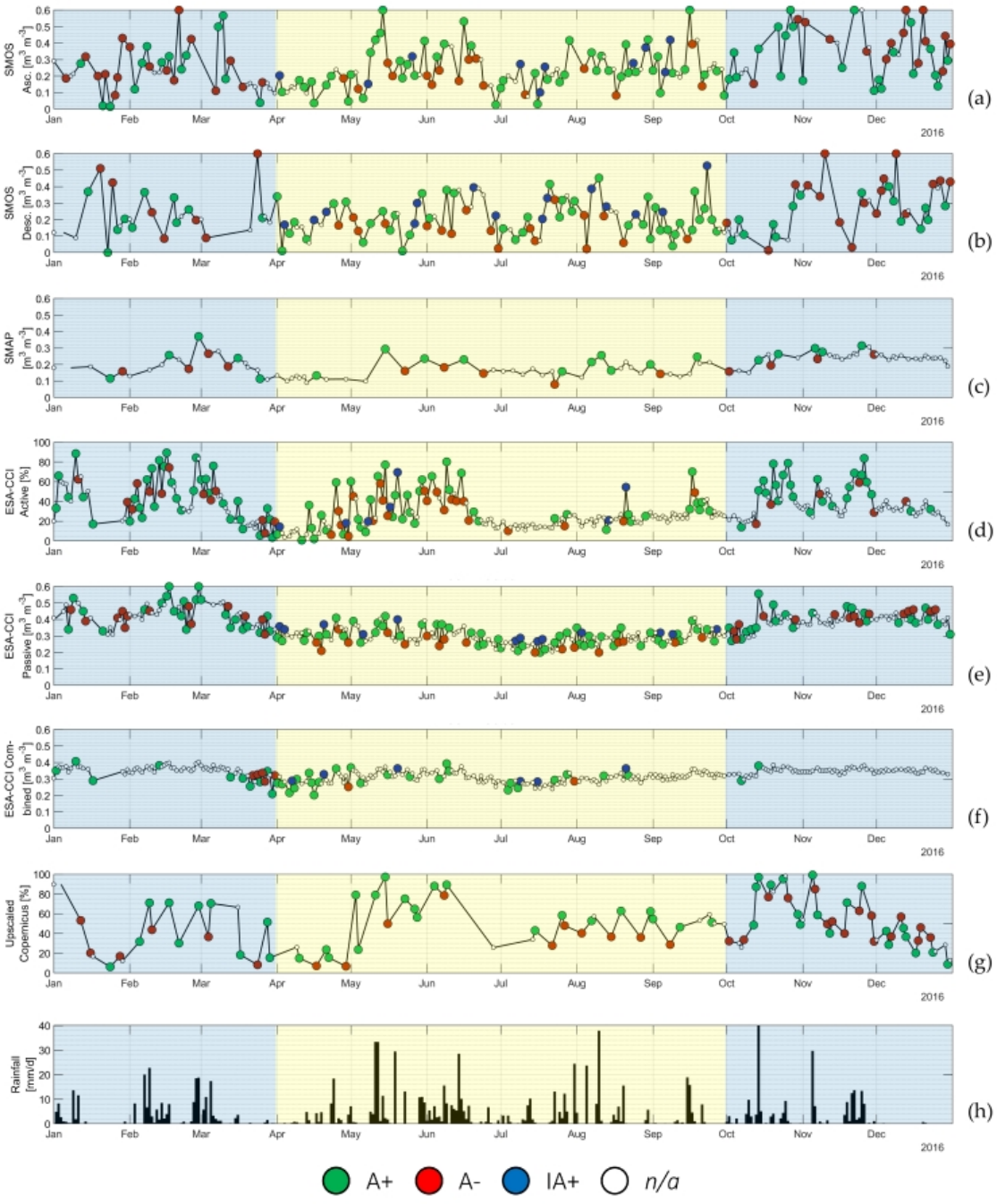

Figure 4.4: HCI data of 7 datasets for the Chiese test case in 2016: SMOS Asc. (a) and Desc. (b), SMAP (c), ESA-CCI Active (d), Passive (e) and Combined (f) products, Up. Copernicus (g). Rainfall data also provided (h).

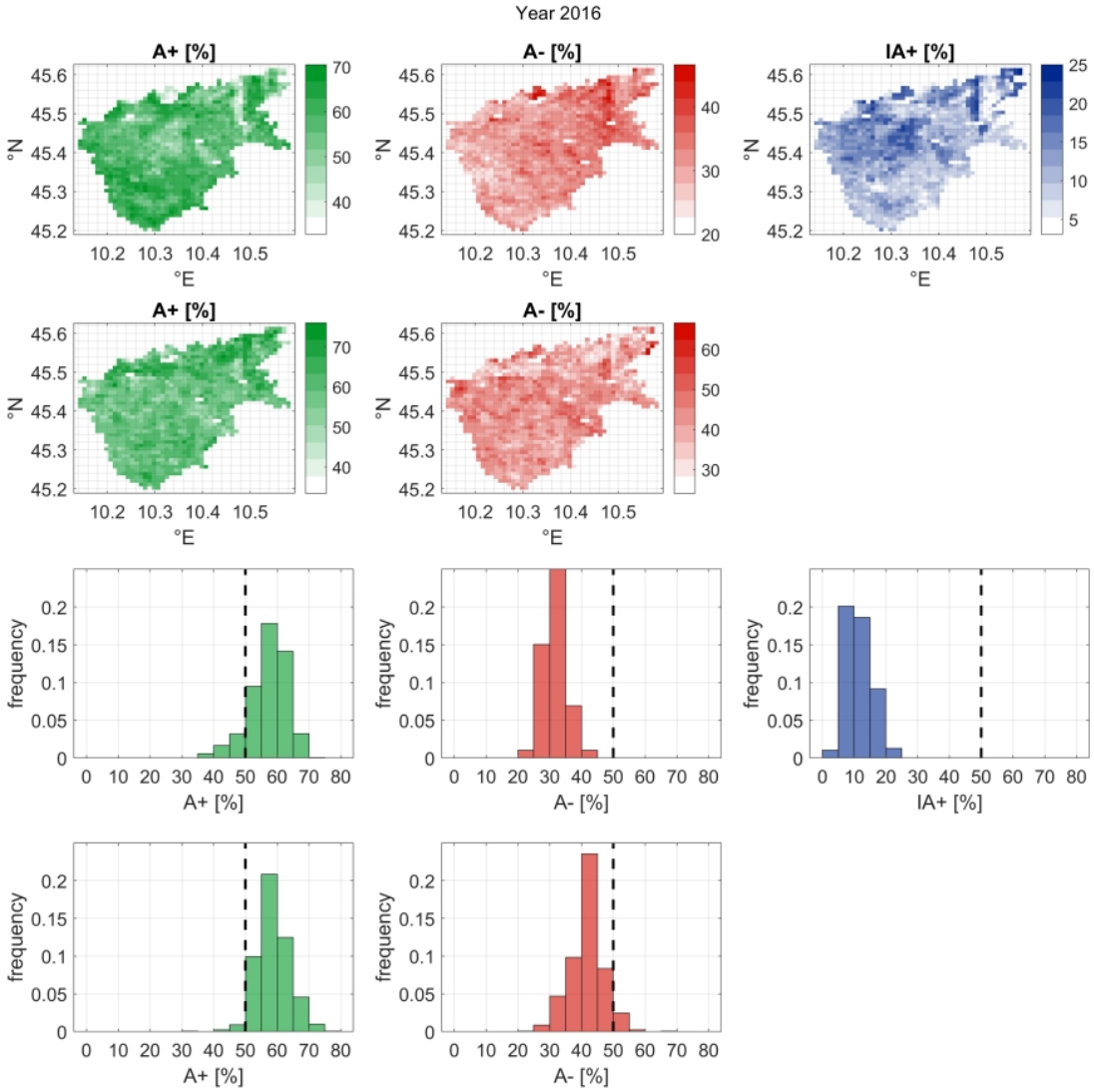

Figure 4.5: HCI data for the Chiese case study, year 2016, for the Copernicus dataset. The first row details the HCI for the irrigation period: positive (A+), negative (A–), and irrigation-driven positive (IA+) agreements. The second row refers the HCI for the non-irrigation period: positive (A+) and negative (A–) agreements.

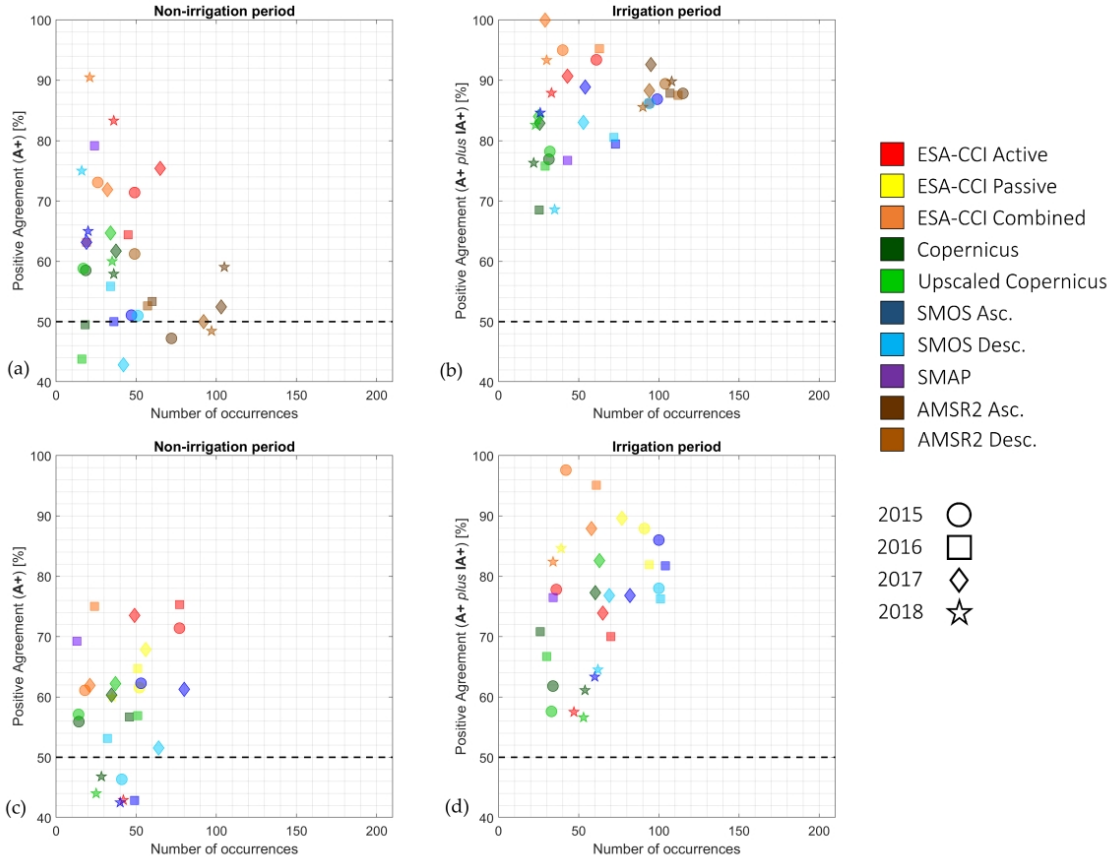

Figure 4.6: Positive agreements, either "A+" cases for the non-irrigation period (a, c), or "A+" and "IA+" cases for the irrigation period (b, d), sorted by the number of occurrences (SSM–rainfall couplings) for the Capitanata (a, b) and Chiese (c, d) case studies.

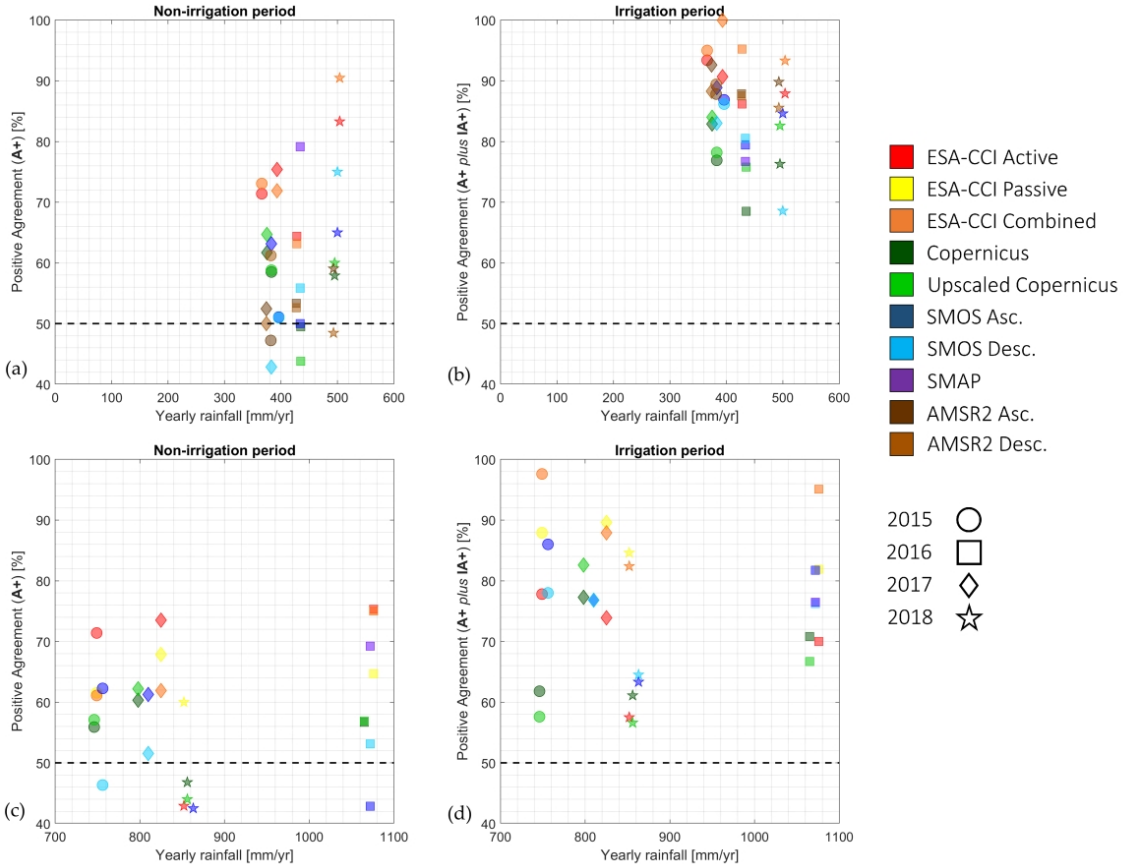

Figure 4.7: Positive agreements, either "A+" cases for the non-irrigation period (a, c) or "A+" plus "IA+" cases for the irrigation period (b, d), sorted by cumulated yearly rainfall for the Capitanata (a, b) and Chiese (c, d) case studies.

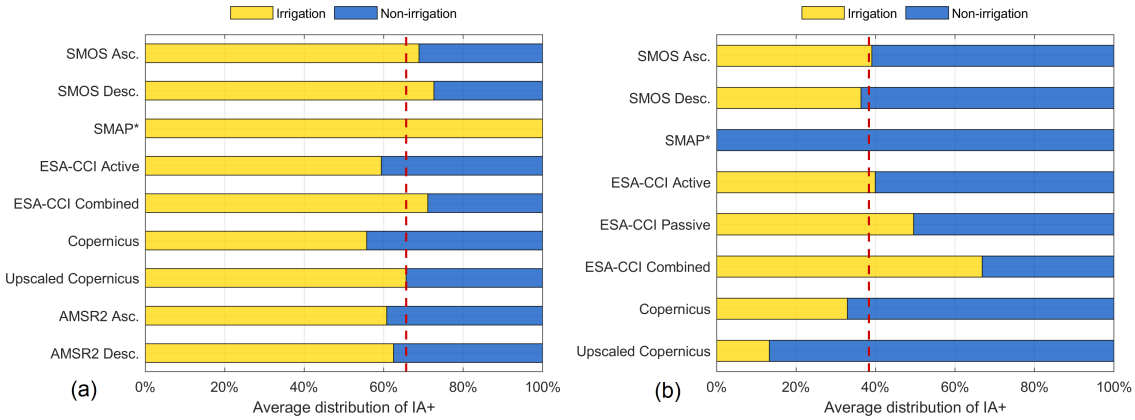

Figure 4.8: Distribution of potential irrigation-driven (IA+) cases among irrigation (yellow bars) and non-irrigation (blue bars) periods for the Capitanata (a) and Chiese (b) test cases. The red dotted line identifies the average hit rate (65% for Capitanata and 38% for Chiese).

Chapter 5

High-resolution crop monitoring

In this chapter, the data gathered from a high-density sensor network has been contrasted with corresponding retrievals from satellite, in order to determine their reciprocal validity. First (Section 5.1), the reliability of the sensors presented in Section 3.2 is discussed. Then, the monitoring of four main geophysical variables are detailed: Air Temperature (Section 5.2), Radiation (Section 5.3), LAI (Section 5.4) and SSM (Section 5.5). After these raw-data comparisons with the corresponding EO data, two irrigation management indexes, formulated in Section 2.2.2, have been put to the test, and their results are used to evaluate in an operative fashion the presented data.

5.1 Sensor performance

Among the 387 active sensors during the 91-days monitoring period, the data collection was intermittent. Two major periods without any data can be identified, in early August and in the first half of September, as detailed in Fig. 5.1a. For the other days, the average number of sensors collecting data was 102. Evaluating the data wealth for each sensor (Fig. 5.1b), the average number of days with data for a given sensor was 18. A non-negligible number of sensors (76, or 20% of the monitored ones) provided data for only one day, and a considerable group (158, 41%) provided at most 20 days with data. The most prolific sensor was D363, placed in a Celery field, with 61 days-worth of data.

5.2 Air temperature

The air temperature measurements collected by the sensors have been compared with those of the nearest Davis station. An example is shown in Figure 5.2. Sensor G222 (Fig.5.2a) is placed in a permanently-bare soil field. The Parrot air temperature (PAT), although similar to the Davis station air temperature (DAT) in the nocturnal hours, attains much higher values during the day, reaching temperatures 10-15°C warmer. The main reason for this may be the measurement height: while PAT is collected a few centimetres above ground, DAT is measured 2 metres above ground. This means that, although conceptually different, PAT has much in common with satellite Land Surface Temperature – also displayed in Figure 5.2 – even though displaying higher values especially in the summer. Another issue could be the overheating of the plastic cover of the sensor, as pointed out by Xaver et al. (2020). Other three sensors are displayed, with different behaviours. Sensor

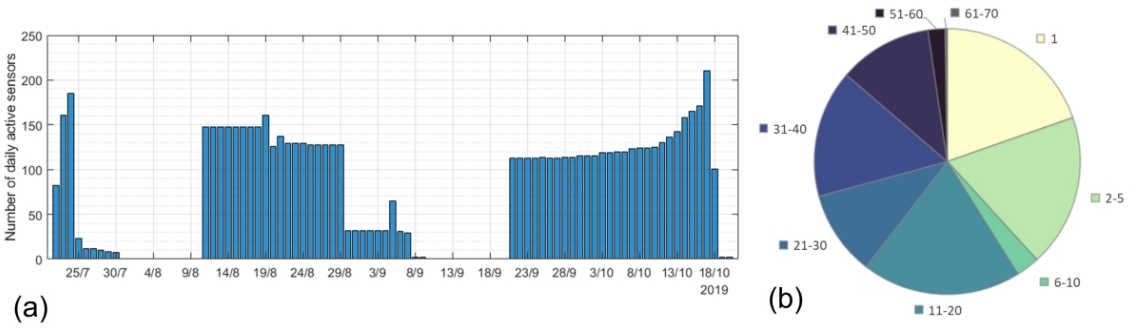

Figure 5.1: Number of active sensors for each day of the monitoring period (a). Sensors classified by number of days with data (b).

GO190 (Fig. 5.2b) is in a Tomato (TOM) field: the shadow from the plants causes the PAT to be much closer to the DAT during August; after the harvest, the PAT measured in the now-bare field grows again higher than DAT. Sensor D363 (Fig. 5.2c) displays an opposite trend. Placed in a Celery (CEL) field, the PAT values display the bare-soil trend during summer, when the crop is still virtually non-existent; as it grows, PAT converges to DAT under the influence of vegetation. Finally, Sensor G150 (Fig. 5.2d), placed in an Asparagus (ASP) field, shows a more regular trend, similar to that of the Bare-Soil (BS) sensor (Fig. 5.2a). This can be motivated by the scarce vegetation density of the Asparagus crop, which poorly affects the downwelling radiation.

To understand the general behaviour, all the sensors data are compared with both the Davis station air temperature (Fig. 5.3a) and the high-resolution (30 m) LST data retrieved from Landsat 7 and 8 (Fig. 5.3b). The comparison is done considering data every 15 minutes, with the Davis stations data are averaged at this temporal frequency from their original sampling time of 5 minutes. This provides a high number of PAT-DAT couples (402 487) and, for a better representation, a density plot is provided. The PAT overestimation already discussed for Figure 5.2 is clearly visible in the right-hand side of the density plot.

Figure 5.3b identifies the comparison between PATs and satellite LST. In this case, the satellite overpass time (around 11:25 a.m.) is a major constraint, reducing the number of PAT-LST couples to 1 017. There appears to be a certain correlation between the two datasets, as shown by the close-to-one slope coefficient of the interpolation (m=1.02). However, the data seems poorly clustered around the interpolation line, as testified by the moderate R^2 value (0.44). One possible reason for such a behaviour is the heterogeneity that can be associated to each pixel, notwithstanding its (relatively) high spatial resolution. In a given pixel – roughly 900 m^2 wide – warmer and cooler sensors may be found, belonging to fields with different destination. The data dispersion can be considered as an indirect estimate of the pixels own heterogeneity.

To try and discern the specifics of this comparison, sensors are clustered by land cover type, with each sensor-to-satellite group statistics detailed in Table 5.1. As a reference, the sample dimension (number of sensor-to-satellite couplings) is also shown. Focusing on the most populated land cover types, Bare Soil, Celery and Tomatoes provide, on average, a negative sensor-to-satellite bias, while Asparagus, Fennel and Trees show a positive bias. However, as the determination coefficients show, sensor data never manages to explain more than 50% of the satellite data variance.

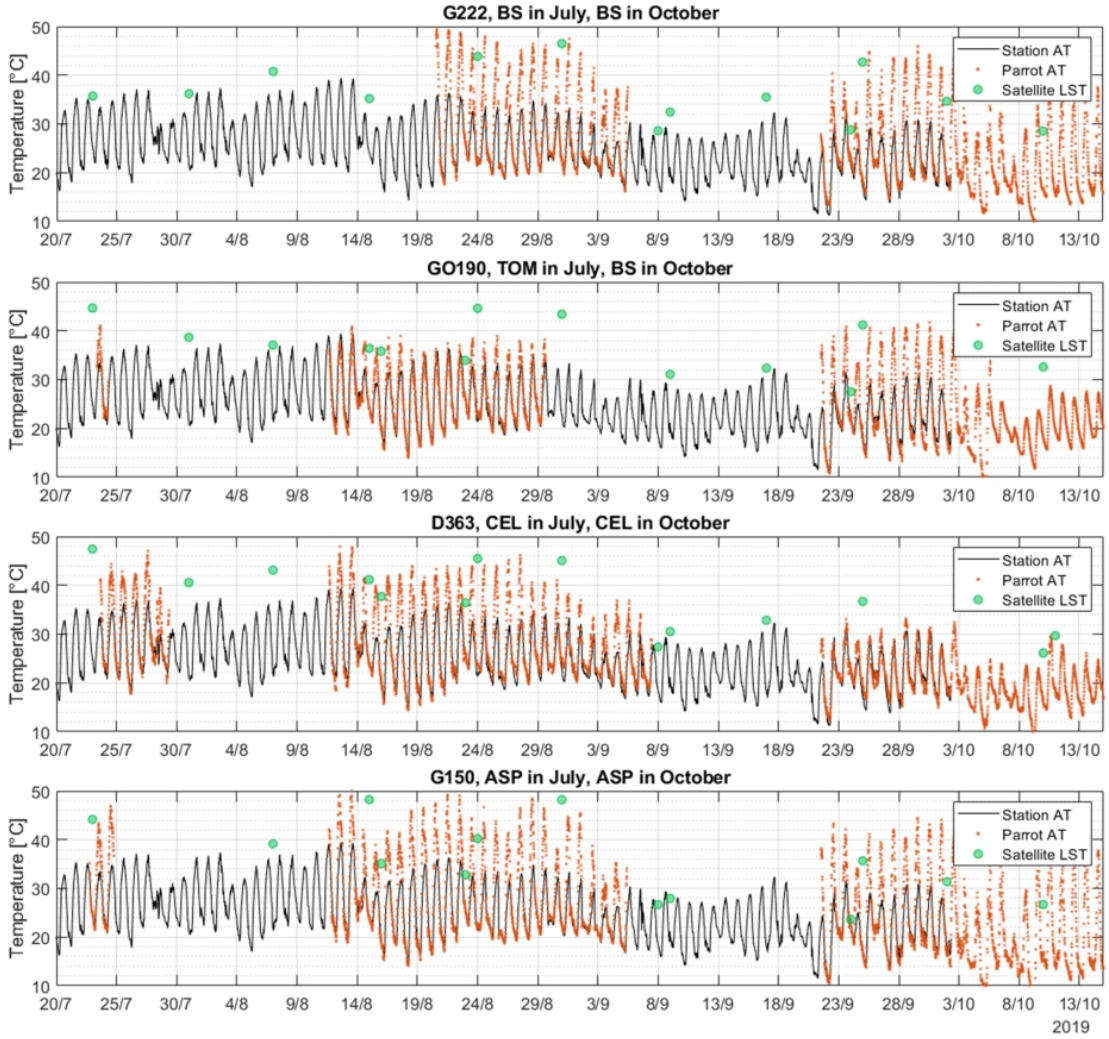

Figure 5.2: Time series of air temperature from Parrot sensors (orange dots) and Davis station (black line), together with land surface temperature from Landsat 7 and 8 satellites (green circles).

Table 5.1: Correlation information for the sensor-to-satellite couplings sorted by land cover type

Crop	Couples	R^2	Avg. Bias	Crop	Couples	R^2	Avg. Bias
All sensors	**1 017**	**0.44**	**-0.7°C**	Celery	60	0.46	-1.4°C
Bare Soil	551	0.45	-0.4°C	Fennel	24	0.48	+0.1°C
Asparagus	165	0.44	+1.1°C	Tomato	179	0.39	-3.4°C
Cabbage	7	0.20	-0.9°C	Trees	15	0.32	+1.4°C

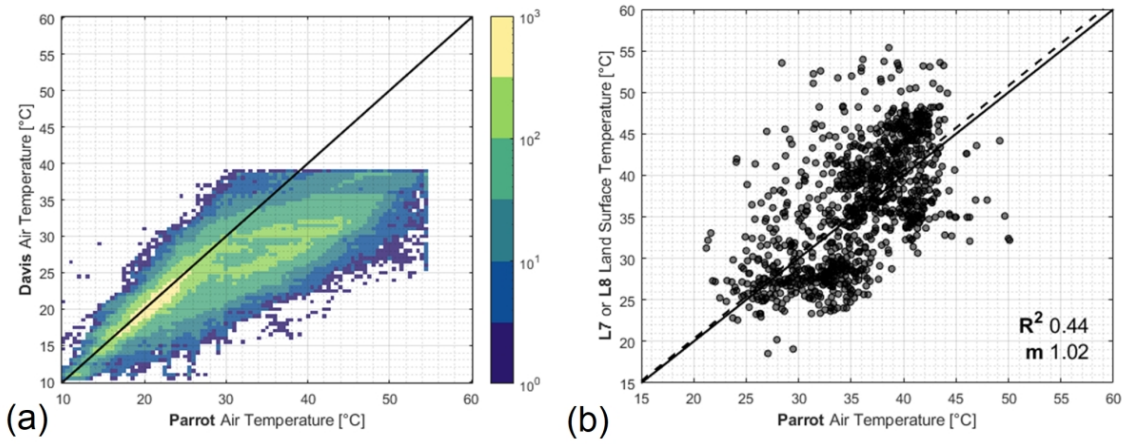

Figure 5.3: Comparison between Parrot air temperature (PAT) and station air temperature (SAT) (a) or Landsat 7/8 land surface temperature (LST) (b)

5.3 Radiation

In the comparison of Parrot illuminance to the shortwave radiation from the Davis Station, two "problematic" data categories have been weeded out: cloudy days data and nocturnal data. Notwithstanding this, the Lumen-to-Watt (or Lux-to-Watt-per-square-metre) theoretically-based conversion (116 lux to 1 W m^{-2}) detailed in Section 2.2.3 has not been found in the actually measured data. As an example, data for Sensor G67, placed in a bare-soil field, are shown in Figure 5.4. The empirical conversion coefficient (m=5.69), obtained with a strong accuracy (R^2=0.96) is quite far from what expected from theoretical conversion. Repeating the comparison with other sensors, similar values are found, although each specific to its own sensor.

The wide variety of illuminance-to-radiation couplings is mapped in Figure 5.4b. First, a consistent group can be noticed on the left-hand side of the plot, with very low illuminance values corresponding to high radiation values collected by the station. These couplings are mainly referred to sensors in vegetated fields, where the dampening effect invalidates the illuminance reading for this kind of comparison. Excluding these sensors, the remaining ones providing suitable data (numbering 110) show an average radiation-illuminance ratio of 5.41:1 (0.185 "lux" to 1 W m^{-2}), with a low variation coefficient (6.4%). In order to motivate this empirically-found number, and going back to Equation 2.2.3, the following steps can be taken:

$$ILL\ [\mathrm{lx}] = \chi\ [\mathrm{lm/W}] \cdot 0.1688 \cdot S_{IN}\ [\mathrm{W/m^2}] \tag{5.1}$$

$$ILL^* = ILL/\chi\ [\mathrm{W/m^2}] = 0.1688 \cdot S_{IN}\ [\mathrm{W/m^2}] \tag{5.2}$$

$$S_{IN}\ [\mathrm{W/m^2}] = 5.92 \cdot ILL^*\ [\mathrm{W/m^2}] \tag{5.3}$$

In this new form, the conversion coefficient is strikingly close to the one found empirically. This suggests that the "illuminance" provided by the sensors is rather a "sensitivity-peak converted" illuminance (ILL^*), obtained converting the radiation with the sensitivity-peak conversion factor (χ) and disregarding the luminosity function correction, as detailed in Section 2.2.3 and Micheal et al. (2020). For the rest of the analysis, the simpler – and safer – empirical conversion will be employed.

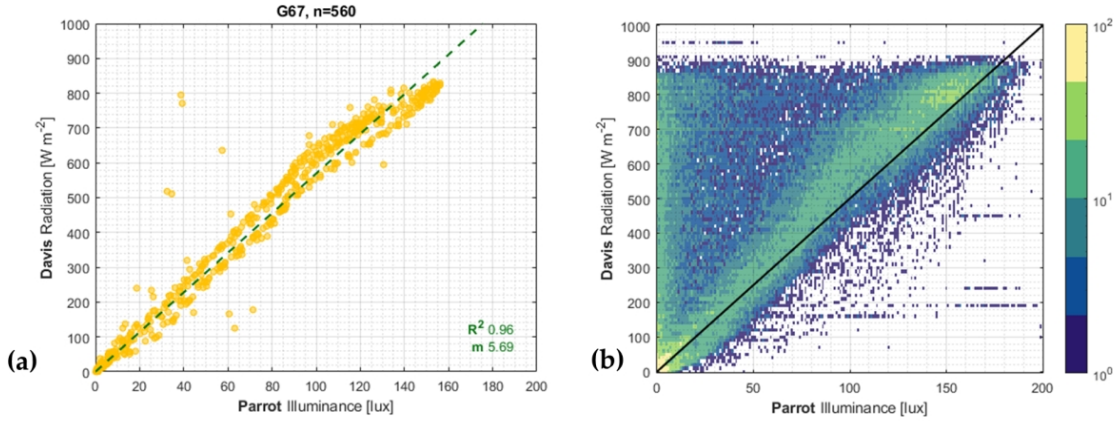

Figure 5.4: Sensor-to-Station comparison between illuminance and radiation. Example on a bare soil sensor (a) and global density plot for all the sensors (b).

5.4 Leaf Area Index estimates

Provided the findings in the previous section, the procedure detailed in Section 2.2.4 to obtain Leaf Area Index has been slightly modified. As sensor-specific conversion factors where not always obtainable for sensors in vegetated fields – as not necessarily there were collected data obtained in vegetation-free conditions – the radiation dampening ratio was replaced with the illuminance dampening ratio. For any vegetation-dampened illuminance, an average was taken of contemporary illuminance measurements from other, vegetation-free sensors.

The results have been compared against estimates (Section 3.7.2) from Sentinel 2 satellite data, with mixed results. Figure 5.5a shows a good correlation with a positive trend, as the field is shifting from an empty bare soil to a vegetated pattern (cabbage). This evolution is evident both in the sensor and satellite retrievals, and just as clearly in general trend and in actual LAI values. An opposite trend is shown in Figure 5.5b, where sensor GO186 placed in an asparagus field, records a reduction of the vegetation density in the monitoring period. The general decreasing satellite LAI trend and its actual values result again well-interpreted by the sensor.

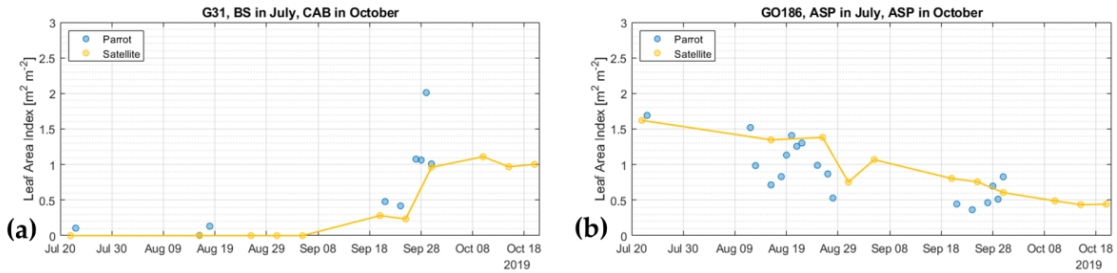

Figure 5.5: Two examples of successful comparison between sensor-computed LAI and data gathered from satellite.

On the other hand, Figure 5.6 displays two examples of the satellite-sensor comparison with a low correlation. Figure 5.6a involves another sensor (G71) placed in an asparagus field: while the sensor registers LAI values around 1 m^2 m^{-2}, its corresponding satellite pixel features practically null values (0.02 m^2 m^{-2} at most). Looking more in details the LAI satellite image (Fig. 5.6b), it clearly appears how the Parrot sensor placement, in the angle of the asparagus field, creates a conflict with its covering pixel. In fact, the sensor shares the pixel space with the neighbouring, mainly bare soil area, affecting the overall LAI value. As a reference, the neighbouring pixel (just 9 m west of the sensor) has been added in green to Figure 5.6a, showing a LAI series much more in tune with that obtained from the sensor. The same concept applies for sensor G122 (Fig. 5.6c), placed in an originally bare soil field, later cultivated with celery. Also in this case, the sensor-to-satellite divergence is due to the fact that the sensor has been placed to the corner of the crop field and, once again, the neighbouring satellite pixel shows a LAI time series more in line with what the sensor perceives.

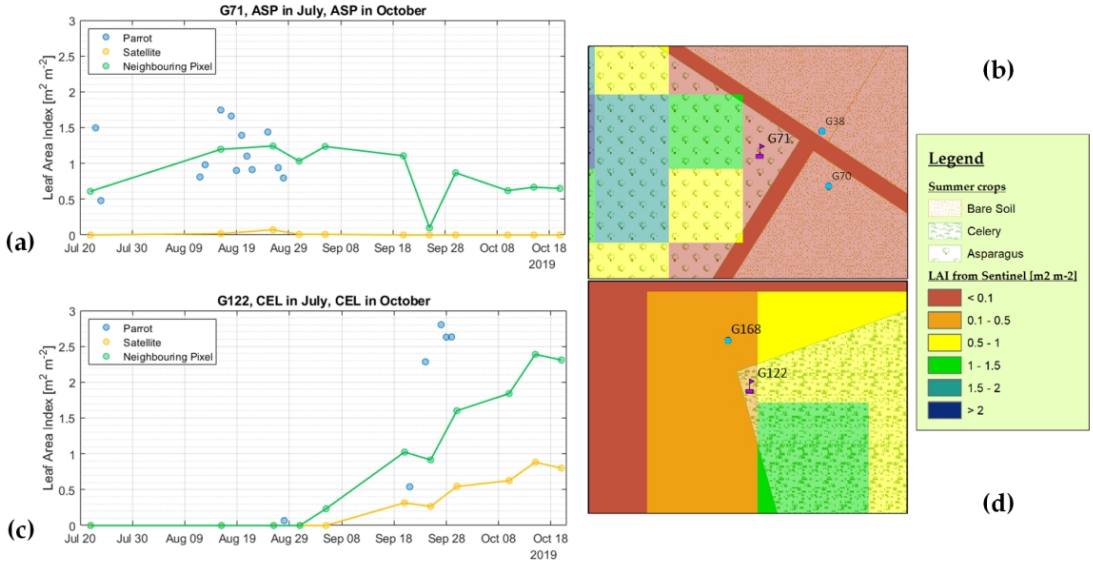

Figure 5.6: Two examples of problematic comparison between sensor-computed LAI and data gathered from satellite.

5.5 Soil moisture measurements

5.5.1 Comparison with SM satellite data

Each sensor in the Parrot SM dataset is compared against satellite data from the corresponding Copernicus SSM1km product pixel, nominally 1 km^2 large. The complete data are provided in Appendix B. Copernicus data, provided in the form of saturation percentage, are converted to volumetric ratio (same unit as the Parrot SM) employing the known saturation and residual water contents for the area (Section 3.1). In the first panel of Figure 5.7, the overall scatterplot, involving

all sensors, is shown. Although the interpolation slope is not far from unity (m=0.75), it is clear how the heterogeneity of each Copernicus cells clashes with the degree of detail provided by the Parrot sensors. In the other panels of Figure 5.7, the same data is provided filtered out by land cover, starting from the bare soil category and covering all crops found in the area. The correspondence varies a lot from category to category with m values ranging between 0.84 for the bare soil field to 0.50 for chard, confirming the difficulties of microwave radar data in retrieving soil moisture in highly vegetated fields (Giacomelli et al., 1995). Low values of R^2, never higher than 0.31, are also obtained for the fields.

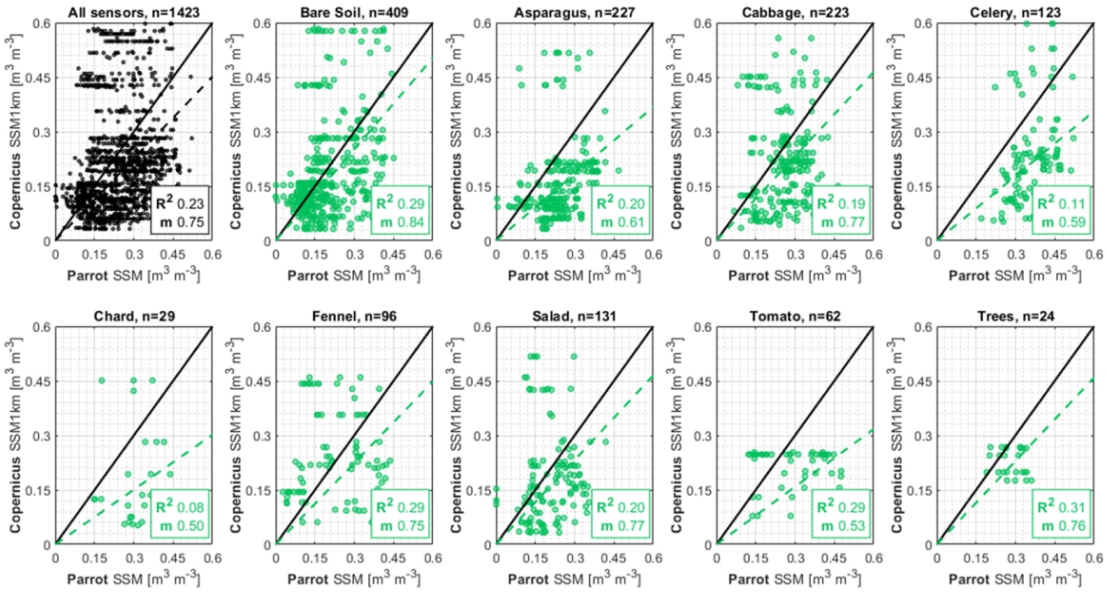

Figure 5.7: Parrot to Copernicus soil moisture comparison for different crops categories. Number of couples (n), determination coefficient (R^2) and interpolation slope (m) are provided for each plot.

To better understand also the spatial resolution issue of the satellite images, in Figure 5.8 one of the Copernicus SSM1km pixels has been selected for a focus, as it covers 56 different Parrot sensors over the total period of observation. The time series of Copernicus SM, completed by the dataset uncertainty in the shaded area, is shown in Figure 5.8a together with the SM distribution of all the active Parrot sensors in the same pixel. A similar behaviour in the overall trend is observable among the two datasets detecting the SM increases around DOY 240, while high differences in the extreme values are detected, with sensor data generally compact. In terms of error statistics, satellite data shows a RMSE of 0.116 m^3 m^{-3}, an interpolation slope of 0.76 and a determination coefficient of 0.12. These discouraging values may be explained by the different land cover conditions of the considered satellite pixel (July, Figure 5.8b and October, Figure 5.8c) of the observation period, which describe a particularly bare pixel. Such a pixel would be expected to show generally low SM values, with peaks only for precipitation events, involving the whole area without differentiation.

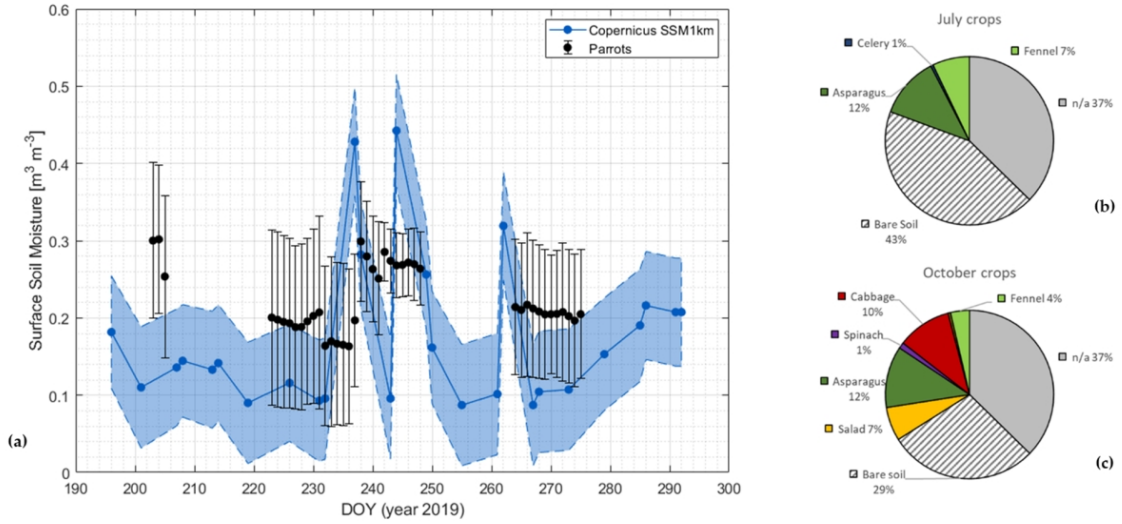

Figure 5.8: SM time series example for a Copernicus SSM1km pixel, with its uncertainty (shaded area) and the SM distribution of the Parrot sensors located within the pixel. July (b) and October (c) field type distribution is also detailed.

5.5.2 Comparison with satellite water stress indices

Parrot soil moisture data were compared to some satellite-derived vegetation indices (described in Section 3.7.2) to detect their sensibility to soil moisture variations. The employed indexes are FV, MSAVI, MSI, NDVI and NDWI, obtained from Sentinel 2 and Landsat 8 satellite images. These indices evolve with the crop, as shown for a small area in Figure 5.9. This area is mainly composed of asparagus fields in Summer; during August, other crops are planted (mainly cabbage), progressively increasing the vegetation presence. The comparison between sensors and vegetation indices is detailed for three different sensors in Figure 5.9. Sensor 8360 (Fig. 5.9a), located in a celery field, registers high SM values during Summer, corresponding to soil preparation before planting. All the VIs show equally increasing trends but remain quite clustered around similar values. The same happens with an asparagus sensor (F070, Fig. 5.9b) and a tomato one (849E, Fig. 5.9c). The VIs do not show particularly sharp changes in low-SSM phases, corresponding to stress conditions for the crop. Generally, low temporal frequency in the VIs data is poorly compatible with the temporal scales of water stress and irrigation for most crops, as appears clearly for the celery and tomato sensors.

A global overview of the SM-VIs link is performed through a cross-correlation between the different datasets, as shown in Table 5.2, across all the Parrot sensors. The close relation between the VIs is witnesses by the high (absolute) correlation values, whereas their weak link with on-ground SM is quantified in the extremely low corresponding correlations.

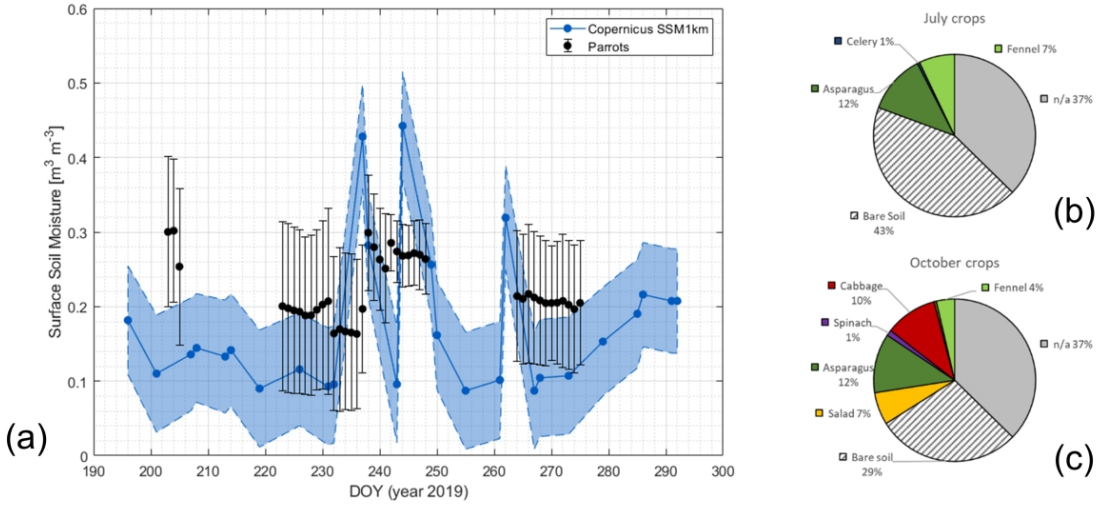

Figure 5.9: F_{cover}, MSAVI, MSI, NDVI and NDWI evolution for selected dates within the observation period. Parrot soil moisture (upper half) and vegetation indices (VIs, lower half) for some selected sensors in the plots on the right.

Table 5.2: Correlation coefficients between SM and the vegetation indices

	SM				
Fcover	-0.03	Fcover			
MSAVI	-0.07	0.96	MSAVI		
MSI	-0.08	-0.84	-0.79	MSI	
NDVI	-0.09	0.91	0.88	-0.80	NDVI
NDWI	-0.07	0.83	0.83	0.97	0.84

5.5.3 Effective and potential evapotranspiration

Employing Equation 2.1, a Potential Evapotranspiration (PET) can be computed for each sensor, using its own illuminance (converted into radiation) and air temperature data. Across all sensors, relatively similar PET values are found, with a small standard deviation of 1.1 mm/day. This consistency in PET estimate is also detailed in Figure 5.10, where a boxplot relates the daily ETP variability across all available sensors. Some of the outliers could be explained by the sensor-specific radiance-illuminance conversion adopted method, whose uncertainties were detailed in full in Section 5.3. A general impression of a decreasing trend in PET, as summer transitions into autumn, is quite visible, with values as high as 10 mm/day in August shrinking to 6 mm/day by the first half of October.

In order to compute effective evapotranspiration (ET), soil moisture data from the sensors is factored in (Eqs. 2.4 and 2.5), increasing dataset variability as a direct consequence of the spatial heterogeneity in precipitation and irrigation instances. ET and PET temporal dynamics are detailed in Figure 5.11 for some sensors, together with the respective soil moisture information. The upper panel (Fig. 5.11a) identifies a sensor placed in a bare soil field during the whole analysed period

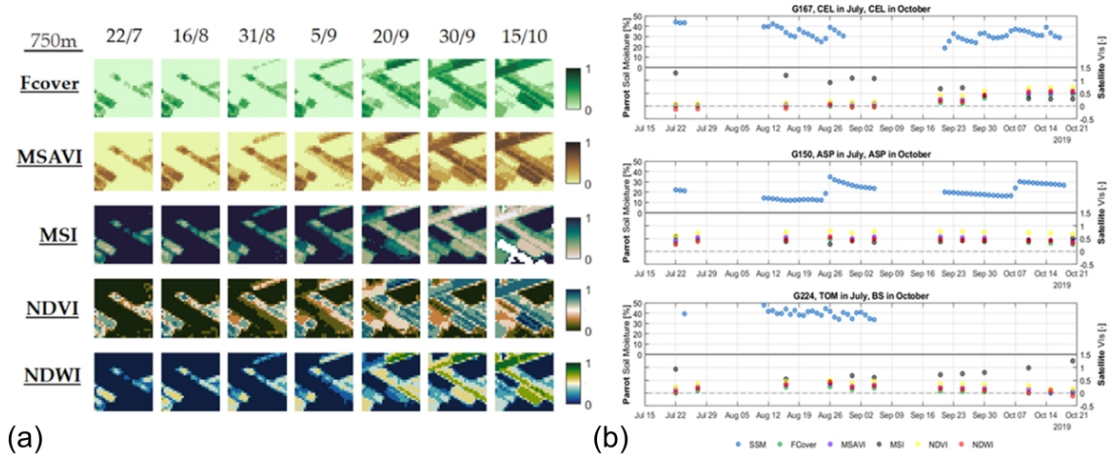

Figure 5.10: Box plot of the potential evapotranspiration for all the available sensors for each date.

from July to October. Soil moisture is constantly very low, and as a consequence ET is almost equal to zero. A similar behaviour is observable in (Fig. 5.11b), with a sensor located in field initially bare (July) before being sowed with celery and developing a full crop by October. Contemporary SM dynamics reflect an initially-empty field (SM values below wilting point at mid-August) being prepared for cultivation with insistent irrigation, and finally transpiring at high potential (SM well above the Field Capacity) by October. The third panel (Fig. 5.11c) identifies a celery field which undergoes harvesting during the monitoring period. ET is constantly up to PET during cultivation, with SM well above field capacity. After harvesting, the field is left unattended, and a monotonical decrease in SM ensues. Finally, (Fig. 5.11d) refers to a sensor placed in an Asparagus field. The oscillating pattern of the SM is reflected in the time behaviour of ET, which fluctuates in a similar fashion in the vicinity of PET.

5.6 Irrigation water needs

In this last part, two operational products have been developed for irrigation management purposes, called Irrigation Water Needs (IWNs) and feeding on data collected by the Parrot sensors.

5.6.1 Evapotranspiration-based IWN

The first IWN is based on evapotranspiration computation (thus, IWN_{ET}), and is simply identified with being the difference between PET and ET. This indicator is computed sensor-by-sensor, and can be described as a phytologically-oriented product helping to define the distance of plant transpiration from full-potential conditions. The daily IWN_{ET} values are shown for the entire dataset in Figure 5.12 in boxplot fashion. During August, since many fields are quite dry, a higher deficit is observable, while during October the IWN_{ET} values are generally smaller, mainly due to lower-PET conditions and near-field-capacity SM values as a consequence of autumnal precipitations and more intense irrigation. Irrigation events determine also a wider same-daily variability.

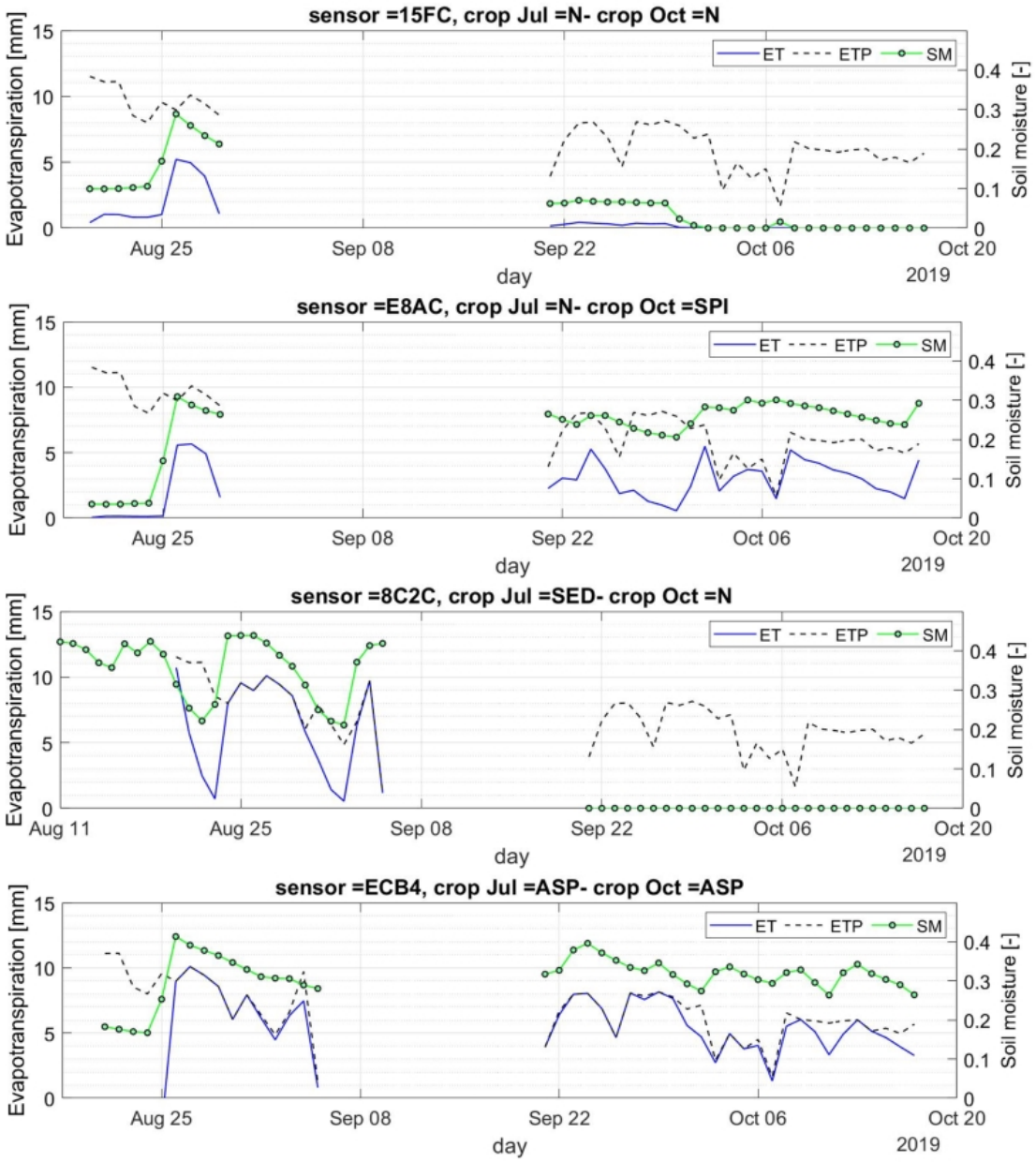

Figure 5.11: Four example computations of the ET and PET linked to the soil moisture dynamic: a fully bare-soil field (a), a bare-soil plot being planted (b), a vegetated plot being harvested (c), a continuously-cultivated field (d).

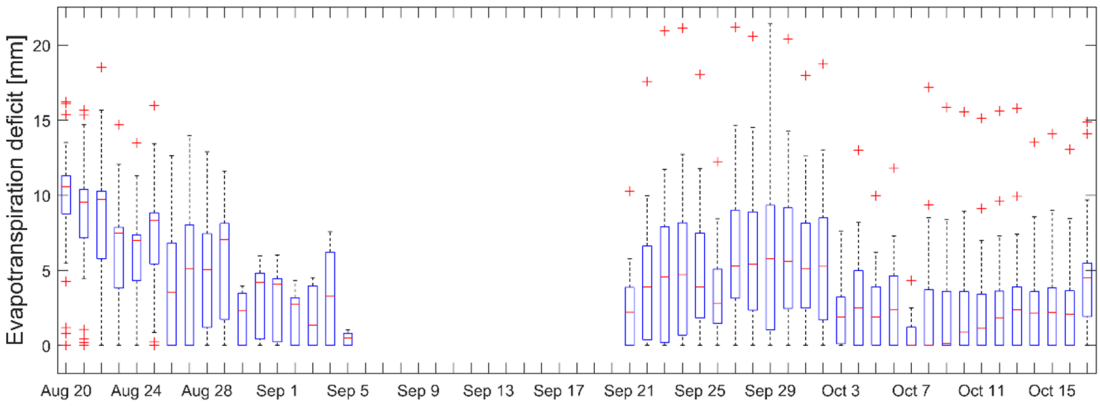

Figure 5.12: Boxplots of $\mathrm{IWN_{ET}}$ for all available dates.

5.6.2 Soil-moisture-based IWN

The second operative product for irrigation management is directly derived from the Parrot soil moisture data (thus, $\mathrm{IWN_{SM}}$), comparing them against the crop-dependent stress threshold and the field capacity (Fig. 5.13). In the upper panel (Fig. 5.13a), a bare soil field with almost no soil water is then planted with cabbages in the beginning of September. A typical soil moisture dynamic of an irrigated field becomes observable, with values seesawing between the stress threshold and well above field capacity, with an average irrigation frequency of about 5 days. This SM excess over field capacity indicates that a certain amount of water is lost to surface runoff, meaning that a non-optimal irrigation volume was used. Similarly, but with an opposite timing, the second panel (Fig. 5.13b) shows sensor 8C2C data, referring to a celery field during August. On the other hand, a more accurate irrigation amount is observable in an asparagus field (sensor EBA6, Fig. 5.13c) with SM never overpassing field capacity during its 4-day period fluctuations. Finally, the lower panel (Fig. 5.13d) portrays a bare-soil field where soil moisture remains well below wilting point.

For the focus date of 20$^{\mathrm{th}}$ August 2019, the SM data from the Parrot sensors have been compared with the corresponding Copernicus SSM1km data, together with the corresponding $\mathrm{IWN_{SM}}$, computed both using sensor data and satellite retrievals. Generally, the satellite pixel footprint is much bigger than the average field in the area, meaning that for a single satellite SSM value, numerous sensor SSM data are available. To this end, two distinct satellite pixels have been selected, one covering the main Incoronata ("Guzzetti" farm) area (featuring 54 active sensors in that date, Figure 5.14a,b) and the other in the Onoranza area (with 11 active sensors, Figure 5.14c,d). The analysed sensors have been classified in two categories: those pertaining to irrigated areas (consisting of about 15% of the total pixel area for that date) and those to non-irrigated areas. The former includes all sensors associated with crops that are detected as "irrigated" from the sensors themselves. This means that the Parrot sensors located in the asparagus fields belong to the "non-irrigated" category, since the sub-superficial (at a depth of 20 cm) irrigation in place for that crop is practically undetectable to both the Parrot sensors (which have a sensing depth of roughly 7 cm) and the Copernicus SSM (around 5 cm). For each sensor category, the average SM value is indicated with the bold red horizontal line, and an additional dashed line identified the single Crop Stress Threshold (Eq. 2.7) for the irrigated-areas sensors. The behavioural difference among the

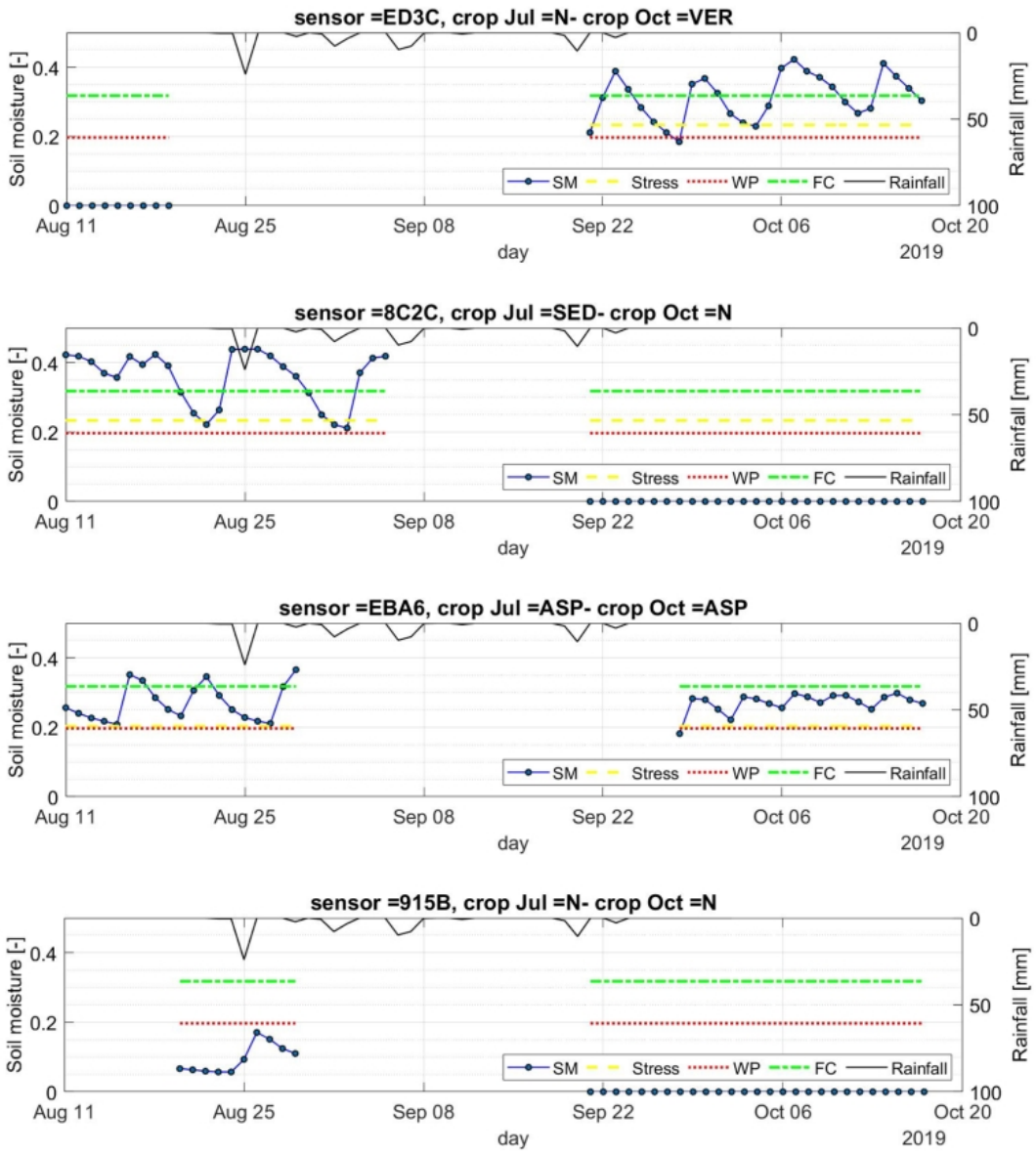

Figure 5.13: Four examples of soil moisture dynamic: a bare-soil plot being planted (a), a vegetated plot being harvested (b), a continuously-cultivated field (c) a fully bare-soil field (d).

sensors is quite clear. For both the Incoronata and the Onoranza pixels, the low amount of irrigated areas (15% and 26%, respectively) mean that the Copernicus SSM is generally closer to the data from "non-irrigated" areas, with values close to the wilting point. In terms of IWN_{SM} values, as for both cases the average "irrigated"-areas sensor SM is above field capacity, no irrigation is required;

on the other hand, using Copernicus SSM would prompt important irrigation volumes (around 10 mm) (Figs. 5.14b,d).

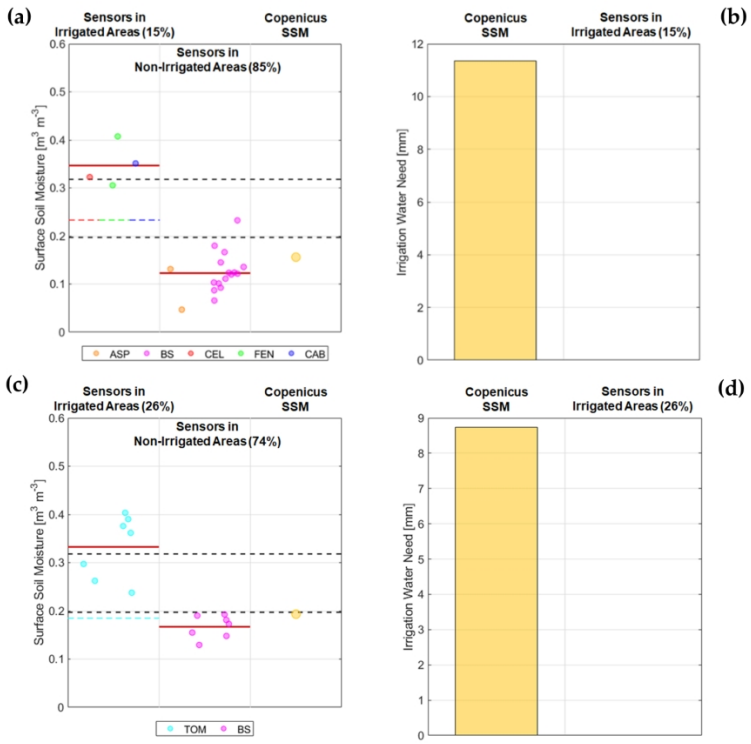

Figure 5.14: Soil moisture values from Parrot sensors and Copernicus SSM for the Incoronata (a) and the Onoranza (c) selected pixels, for the 20$^{\text{th}}$ August 2019. Corresponding IWN_{SM} are also shown: respectively, (b) and (d).

5.7 Final take-aways

As a general result, the Flower Parrot sensors have proved to be a valid alternative to traditional instruments, providing accurate measurements which can be highly dense in space. Parrot air temperature has been found to be in agreement with professional air temperature data especially during the night, while during the daytime hours and especially over bare soil fields higher discrepancies are obtained mainly due to the PAT measurement height of 5 cm. Actually, daytime PAT has been proved to be better correlated with satellite LST.

A strong correlation has been obtained among the Flower Parrot sensors illuminance data and the incoming shortwave radiation data for all sensors, although not respecting the expected conversion factor.

Similar good results have been obtained between the LAI estimated from the ground sensors and the remote sensing data, excluding the situations in which the sensor is located in a satellite

pixel straddling several fields with different coverages.

A higher variability is instead obtained when the sensors' SM is compared with the Copernicus SSM1km data, probably because of low spatial resolution not being able to capture the variability detected by the ground measurements. This is consistent with the findings of Zappa et al. (2019), proving that low-cost sensors are valuable for satellite SM data validation over homogenous areas. As opposed with satellite SM information, the high spatial density of Parrot SM retrievals can be quite useful in improving the knowledge of soil moisture spatial heterogeneity, quite undetectable with traditional sensors (Bogena et al., 2010).

Through the computation of operative irrigation monitoring indicators, the accuracy of such data has been shown to overcome that of satellite-derived information, weakly responsive to SM spatial heterogeneity. On the other hand, the single use of Parrot SM data might be more useful for satellite SM validation than for actual agricultural uses (Zappa et al., 2019), as their measurement depth is limited to few centimetres, which is similar to most microwave SM data but potentially irrelevant to farmers, as the water root uptake zone is usually much deeper.

Another issue with extensive use of low-cost sensor networks is their reliability. In this case, out of 456 sensors, only 107 (23%) provided meaningful data (covering more than a couple of days) and even for these 107 sensors, many data gaps were recorded. Notably, no data was stored for the 31st July – 10th August and 8th September – 20th September periods due to sensor acquisition issues. Some sensors have also been lost during the end of August harvest operations.

A proper merging of the information from a dense ground low-cost network with satellite information could be a good solution for improving irrigation management and agricultural monitoring activities.

Part III

Model enhancement

Chapter 6

Scale analysis

The scale analysis detailed in this Chapter is organized around the FEST-EWB model performance over the Rapitalà vineyard (Paciolla, Corbari, Maltese, et al., 2021). The case study considerable underlying heterogeneity is a major factor in creating adverse conditions for the modelling, as single-energy-balance models (all single-source models and the hybrid FEST-EWB) work on the main presumption that the given pixel either is or can be assumed to be homogeneous. A preliminary calibration and validation of the model is presented in Section 6.1, while the two main analyses directions are detailed in Sections 6.2 and 6.3. Finally, global results are analysed in Section 6.4.

6.1 FEST-EWB calibration and validation

6.1.1 Calibration

As the data available for the Rapitalà test case spans five separate days in summer 2008, the FEST-EWB simulations will consist of five distinct runs, each modelling a single day. Such short daily simulations, without any precipitation nor irrigation, do not allow the possibility for the model to capture the water dynamics influenced by the soil calibration parameters. Hence, the calibration has been restricted to the two parameters linked to the evapotranspiration process: the minimum stomatal resistance ($R_{S,min}$) and the wet-soil surface resistance (R_{Soil}). These parameters have been corrected across numerous simulations with the aim of minimizing the temperature error, as detailed in Section 2.3.6. The results of this calibration are detailed in Table 6.1. Originally, wet-soil surface resistance was set to 500 s/m for all the pixels; minimum stomatal resistance, on the other hand, was set to 200 s/m for highly-vegetated pixels and to 50 s/m for the remaining pixels, based on well-established literature values for vineyards and grass patches, respectively (Allen et al., 1998).

The comparison between modelled RET and estimated LST is shown in Figure 6.1 for the three calibration dates. Results show a good correspondence, especially in the distinction between warmer bare-soil areas and cooler vegetated patches. Some areas have been blanked out, as not pertinent to the analysis (artificial basins, tarmac, and buildings).

Model biases (difference between modelled RET and estimated LST) are plotted in detail in Figure 6.2, both in map and histogram formats. Model errors are generally distributed around their average value, with most of the pixels (61%, 59% and 78% for each date, respectively) displaying

Table 6.1: Parameter statistics before and after the calibration process.

Parameter	Before Calibration		After Calibration	
	Average	Min–Max	Average	Min–Max
$R_{S,min}$	128 s/m	50–200 s/m	606 s/m	50–1920 s/m
R_S	500 s/m	–	603 s/m	0–1920 s/m

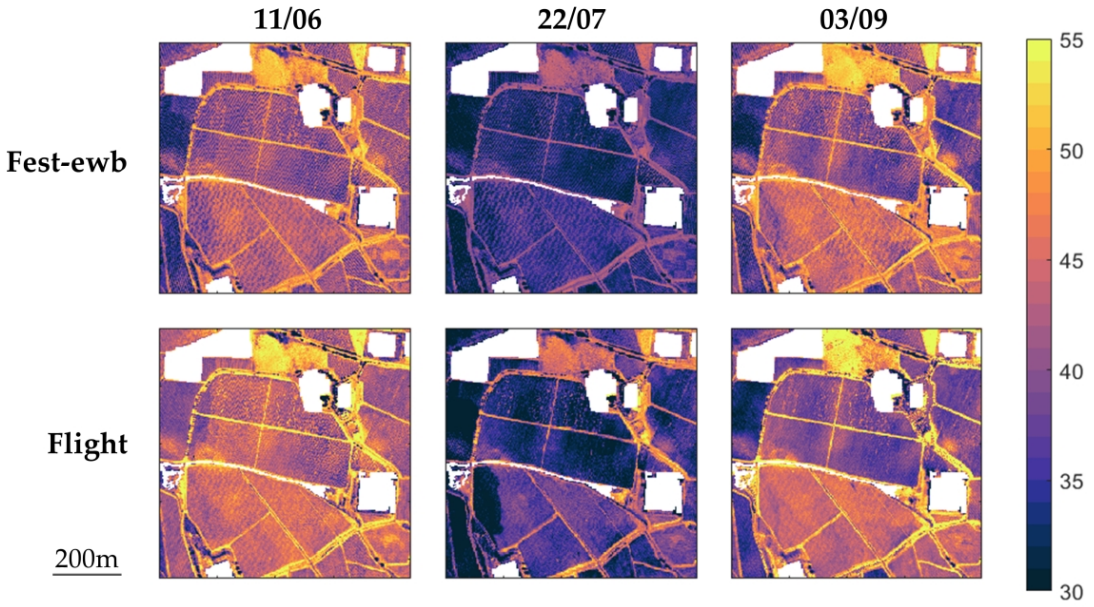

Figure 6.1: Comparison between FEST-EWB generated RET (upper row) and proximally-sensed LST (lower row) for the three calibration dates.

an error within ±3°C of the target LST. For what concerns the spatial distribution of the error, different trends are visible for each date. While 11th June seems to have a uniform error distribution, 22nd July shows important underestimation-errors in the non-vegetated areas, and 3rd September displays a diffused overestimation in the vegetated part. In all three dates, however, some "spot"-like errors are present, mostly found in the western part of the image. For these "spot"-like areas, the model error seems to be distinguished from that of the nearby area: on 11th June the model is much cooler than the LST in that area with respect to the central part of the test site, and on 22nd July a sudden change in model trend (from a sharp overestimation to a mild underestimation) is clearly visible. These problems may be due to the nature of the LST images employed, which are the result of a composition of different passages of the same airborne instrument over the area. Thus, some areas, although geographically close, can be sensed by the instrument in similar, but different, time intervals; a cloud temporarily obscuring the sun can then be enough to produce a sharp temperature difference between relatively close areas. The extent of these areas can be assessed in the original LST images from Figure 6.1. On the other hand, some discontinuities in the RET distribution can also be detected for 11th Jun and 3rd Sep. These may be linked to similar

image composition problems in the input vegetation data.

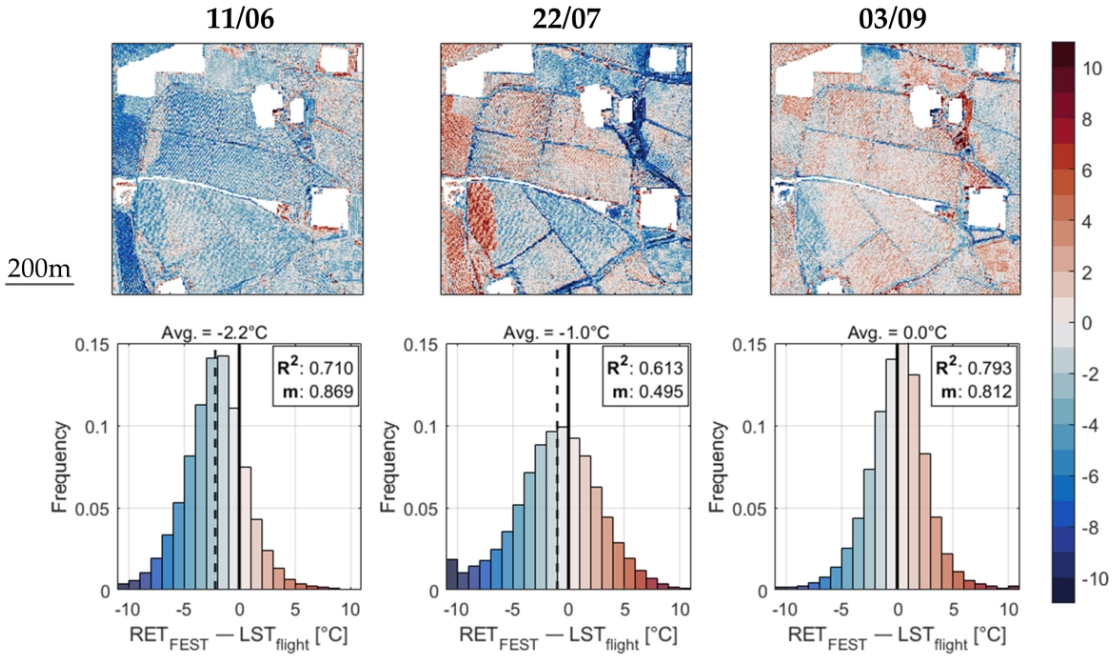

Figure 6.2: Temperature differences (RET–LST) for the three calibration dates: spatial distributions (upper row) and histograms (lower row).

The adaptation statistics for the calibration process are detailed in Table 6.2. On the left-hand side of the Table, classic adaptation statistics are displayed: model-to-data bias (AE), slope of the linear regression (m) and determination coefficient (R^2). On the right-hand side, the surface temperature error (expressed in terms of Root Mean Square Error, RMSE) is sorted by vegetation degree (in terms of Leaf Area Index, LAI) of the relative pixel. Generally, lower errors are found for medium-to-high vegetation levels, although the 11th June test date shows a less definite trend.

Table 6.2: Calibration statistics: Bias (AE), linear interpolation slope (m) and determination coefficient (R^2) on a global level. Root-Mean-Square-Error (RMSE) global and sorted by Leaf Area Index (LAI).

Date	AE	m	R^2	RMSE [°C] by LAI [m^2 m^{-2}] (Pixel Num.)					Global RMSE
				<0.5	0.5–1	1–1.5	1.5–2	>2	
11th Jun	–2.2°C	0.87	0.710	3.5 (18%)	2.8 (27%)	3.0 (22%)	3.8 (15%)	4.5 (17%)	3.5°C
22nd Jul	–1.0°C	0.50	0.613	5.6 (13%)	4.4 (13%)	3.7 (16%)	3.4 (15%)	3.3 (42%)	3.9°C
3rd Sep	+0.0°C	0.81	0.793	3.8 (25%)	2.7 (18%)	2.3 (20%)	2.0 (16%)	2.2 (22%)	2.8°C

6.1.2 Validation results

Among the FEST-EWB results, components of the energy balance for each pixel are available. These outputs can be compared with the quantities measured by the eddy-covariance instruments, as detailed in Figure 6.3. For the modelled turbulent fluxes (LE and H), both information extracted for the eddy footprint area and data from the station pixel itself are provided. For the purpose of validation, both original (black line) and Bowen-corrected (red line) eddy covariance data are shown for both Latent and Sensible Heat. The corrected ones in some instances appear out-of-phase with the others, as a result of some issues with longwave radiation components. In compliance with energy-budget-closure principles (Twine et al., 2000), the corrected data have been employed for the validation statistics detailed below, but original ones have been preserved in Figure 6.3 all the same.

In the lower panels of Figure 6.3, Net Radiation (Rn) and Soil Heat Flux (G) are compared, with positive results, although a slight out-of-phase relation between modelled and measured fluxes is noticeable, in particular for the Soil Heat Flux. This, however, is consistent with the slight shift observed in the eddy station data, as mentioned earlier in Section 3.3, and can be blamed to some reference data inconsistencies. In the upper panels, Latent and Sensible Heats are displayed. The green line details the flux modelled in the station pixel; the yellow line depicts the average flux in the station footprint area. As detailed in Section 3.1.2, the physics of the turbulent flux measurement requires the knowledge of a certain footprint area, highly dependent on the meteorological conditions, such as wind intensity and direction and atmospheric temperature. The presence of a consistent bare-soil area around the station is evident in the higher values of the Sensible Heat as opposed to the Latent Heat registered by the station. These dynamics are all well-captured by the model interpretation.

The visual adaptation shown in Figure 6.3 is detailed in Table 6.3 with some common statistics. Linear interpolation slope (m), determination coefficient (R^2) and Nash-Sutcliffe Efficiency (NSE) are provided for all the curves displayed in Figure 6.3. A comprehensive average column has been added to the right of the Table. The turbulent fluxes are overall well-interpreted by the model (NSE ¿ 0.5) when referred to the station pixel. As footprint filtration is introduced, model performances generally decrease (only the Latent Heat for 11^{th} June presents a performance increase when employing the footprint). This may be attributed to the extremely heterogeneous conditions of the vineyard crop structure, that constrain the flux tower measurements to its immediate vicinity by hindering water vapor (for latent heat) and heat (sensible heat) horizontal motion across the field.

6.1.3 Evapotranspiration output

Modelled evapotranspiration for the global experimental vineyard area is also evaluated. The modelled ET is presented for the main experimental area, in form of histograms and spatial distributions, in Figure 6.4. Bare-soil paths are clearly visible in every date, together with an alternance between high- and low-ET pixels in the vine rows area.

The averaged values have been compared with others, as reported in Figure 6.5. First, the Flux Tower estimated ET, which is relative only to the flux footprint area. Then, the global area ET (as shown in Figure 6.4) estimated by two energy-balance models already employed in the comparison in Ciraolo et al. (2012): the single-source SEBAL and the two-source TSEB. The modelled results seem quite in-line with those of the other energy-balance models. This may be explained by the presence of vegetation (low grass) in the vines interrow, which participates to the

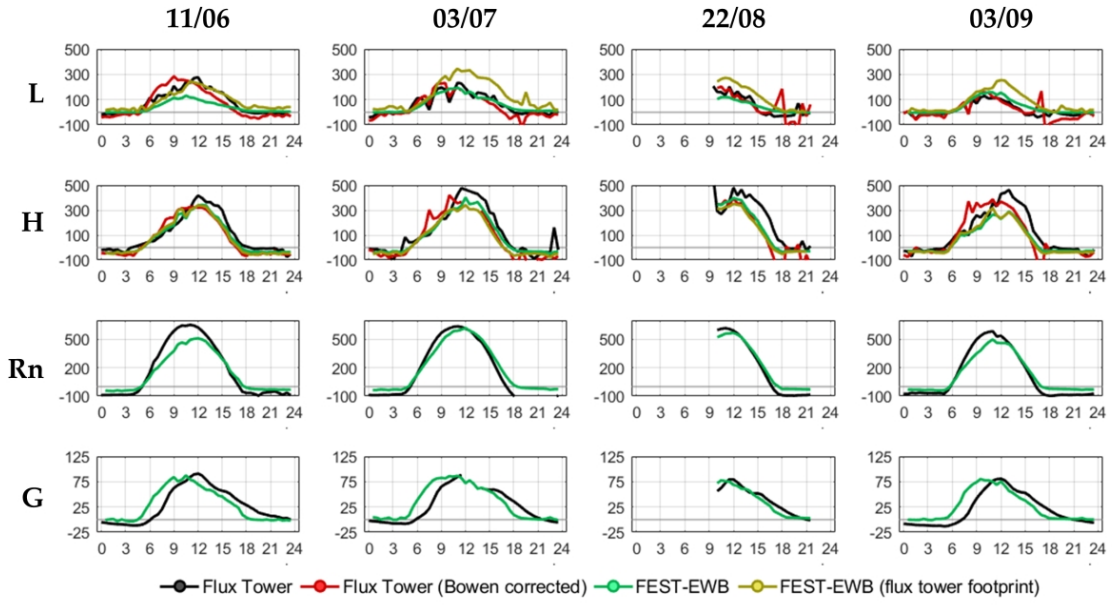

Figure 6.3: Daily evolution of the energy fluxes, expressed in W m^{-2} against the hours in each day. Fluxes are grouped in each row ("L" = Latent Heat, "H" = Sensible Heat, "Rn" = Net Radiation, "G" = Soil Heat Flux), while different validation dates are organized in each column.

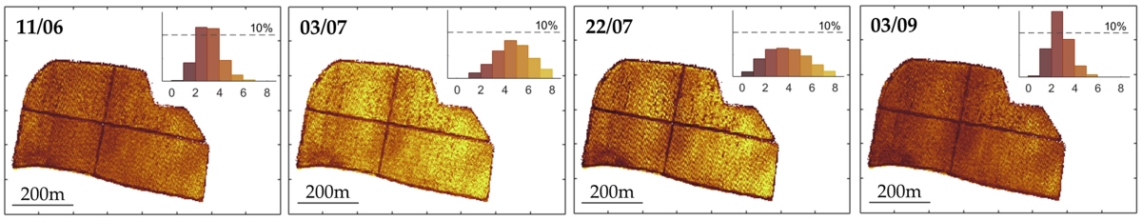

Figure 6.4: Daily evapotranspiration (in mm d^{-1}) maps and histograms for the main experimental area.

overall evapotranspiration. The overall area, although not homogeneous, results less heterogeneous and can thus be portrayed with comparable accuracy by models with approaches both "extreme" to one another (SEBAL and TSEB) and "hybrid" between the two (FEST-EWB). Flux Tower results are quite low, with respect to the modelled ones, for the 3rd Jul and 3rd Sep dates. This is because, in those days, the dominant wind direction is WNW, partially aligned with the main bare path, reducing the overall measured daily ET.

Table 6.3: Validation statistics by energy flux: linear interpolation slope (m), determination coefficient (R2) and Nash-Sutcliffe Efficiency (NSE) for the four validation dates together with their average (Avg.).

Energy Flux	Stat.	11th Jun	3rd Jul	22nd Aug	3rd Sep	**Avg.**
Latent Heat	m	0.41	0.74	0.49	1.06	**0.68**
	R^2	0.85	0.80	0.85	0.86	**0.84**
	NSE	0.446	0.790	0.776	0.573	**0.646**
Latent Heat (flux tower footprint)	m	0.74	1.3	1.1	1.4	**1.14**
	R^2	0.93	0.80	0.85	0.81	**0.85**
	NSE	0.880	-0.371	0.544	-1.09	**-0.009**
Sensible Heat	m	0.86	0.79	0.81	0.63	**0.77**
	R^2	0.87	0.89	0.73	0.86	**0.84**
	NSE	0.846	0.849	0.811	0.693	**0.800**
Sensible Heat (flux tower footprint)	m	0.87	0.72	0.73	0.65	**0.74**
	R^2	0.80	0.78	0.69	0.79	**0.77**
	NSE	0.761	0.695	0.743	0.653	**0.713**
Net Radiation	m	0.75	0.92	0.94	0.82	**0.86**
	R^2	0.97	0.94	0.97	0.96	**0.96**
	NSE	0.897	0.940	0.967	0.929	**0.933**
Soil Heat Flux	m	5.5	6.4	6.9	5.7	**6.13**
	R^2	0.84	0.81	0.78	0.82	**0.81**
	NSE	0.699	0.647	0.888	0.650	**0.721**

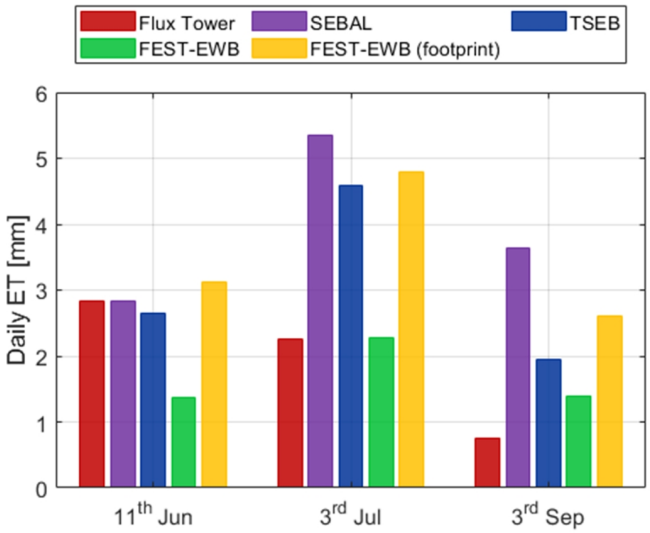

Figure 6.5: Average daily evapotranspiration for the main experimental area computed from the eddy-covariance measurements (Flux Tower), the SEBAL, TSEB and FEST-EWB models.

6.2 Upscaled Outputs (UO)

The aggregated maps employed in the scale analysis are shown in Figure 6.6. In the example 11th June date (11:00 local time): airborne-sensed Land Surface Temperature (LST), Latent Heat (LE), Sensible Heat (H), Soil Moisture (SM) and Representative Equilibrium Temperature (RET) are shown. Results of the Upscaled Outputs approach are displayed in the left-hand side of the image. It appears clearly that some surface heterogeneity features (e.g., bare-soil paths) are preserved in the first step (10.2 m) and still distinguishable in the second (30.6 m), where the scale ratio is 18:1. From the third step (244.8 m) all heterogeneity is lost. The information degradation process that follows the aggregation is also visible when comparing the LST and RET evolution. Although the colours suggest slightly different values, the obliteration of the fields characterizing features is definitely similar.

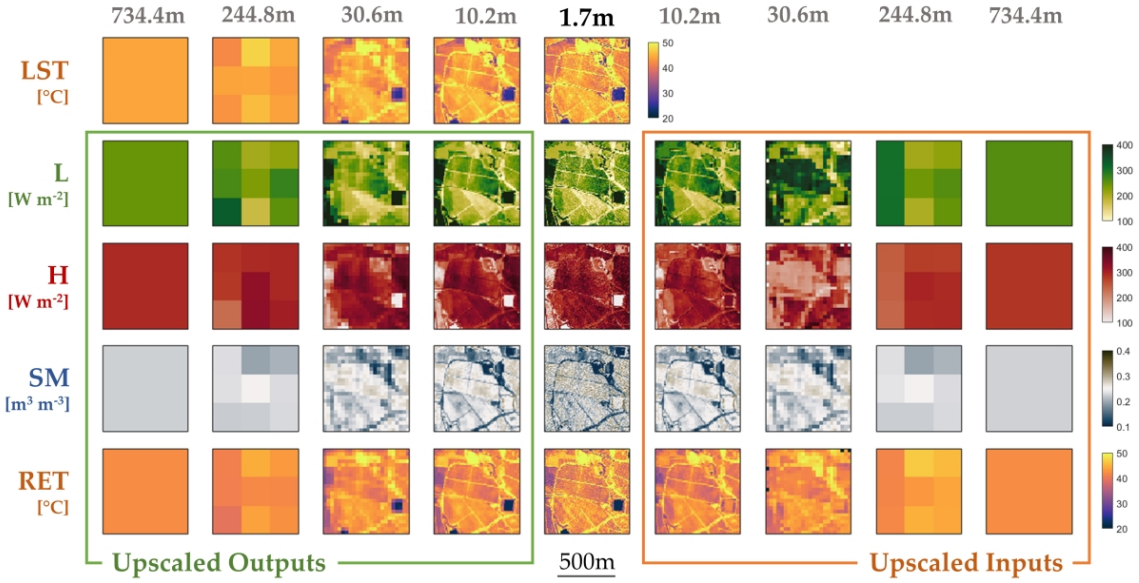

Figure 6.6: Overview of Land Surface Temperature (LST) and four FEST-EWB outputs across the selected scales and the two aggregation approaches: Latent Heat (L), Sensible Heat (H), Soil Moisture (SM) and Representative Equilibrium Temperature (RET).

6.2.1 Data variance across scales

In Figure 6.7 the evolution of the frequency distribution for the same data displayed in Figure 6.6 for 11th June (11:00) across the different scales is detailed. The first row displays the Upscaled Outputs results. FEST-EWB RET and flight-gathered LST (Figure 11a), modelled Latent and Sensible Heats (Figure 6.7b) and modelled soil moisture (Figure 6.7c) are shown. For each plot, the darkened area identifies the one-standard-deviation-range ($\pm\sigma$) around the average value. As scales progress, the overall data average is unaffected, whereas fewer pixels covering the same area determine a decreasing heterogeneity of the data. Being the 734.4 m step made up of just one pixel, all standard deviations are null at that stage.

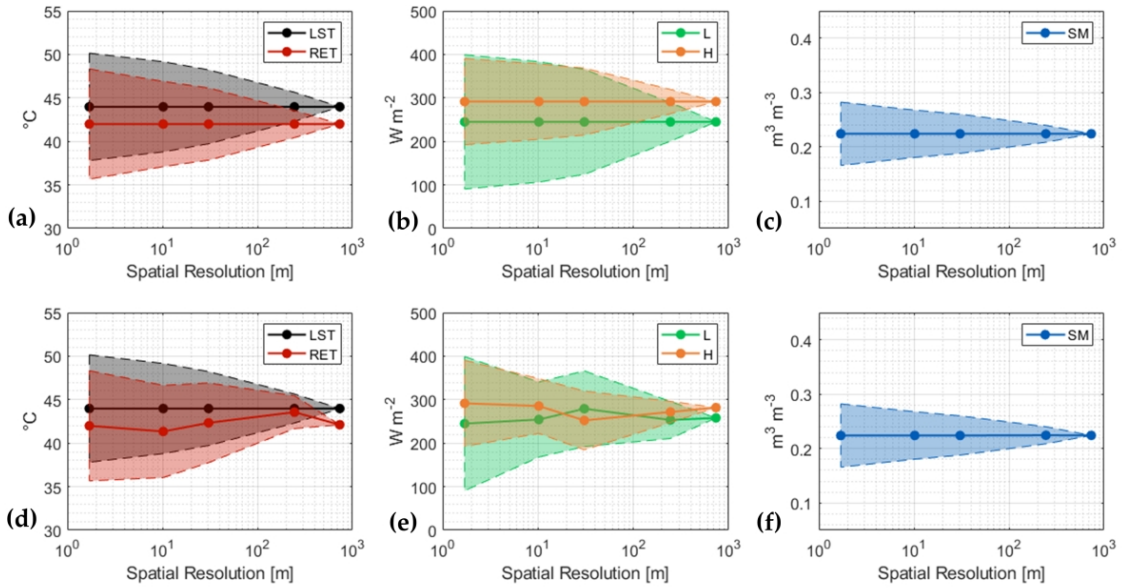

Figure 6.7: Average (solid line) and Standard Deviation (shaded area) of the remotely-sensed Land Surface Temperature (LST) some FEST-EWB outputs: Representative Equilibrium Temperature (RET), Latent Heat (L), Sensible heat (H) and Soil Moisture (SM). Data from the Upscaled Outputs approach (upper row) and the Upscaled Inputs approach (lower row).

In Figure 6.7a, the positive model interpretation of the LST transpires from the similar shape of the two plots. The bias that separates them at the native resolution, detailed in Table 6.2, is preserved along the aggregation process. In Figure 6.7b, it can be observed how Latent Heat tends to be more widely distributed than Sensible Heat. This distinction holds until the 30.6 m threshold, with the two fluxes gaining similar heterogeneity by the 244.8 m step. This is consistent with what observed in Figure 6.6, where the heterogeneity features are shown to hold until the 30.6 m upscaling step. The entity of these heterogeneity shifts is detailed in Table 6.4. For each product and each scale, the variation coefficient (standard deviation normalized with the average value) is shown, progressively decreasing with the increase of the spatial resolution.

Table 6.4: Variation coefficient for the variables shown in Figure 6.7 across all the tested scales. Data for the 734.4 m scale not included, since the value is, by definition, 0%. Model results described both from the Upscaled Outputs (UO) and Upscaled Inputs (UI) approaches.

Dataset	LST	RET		LE		H		SM	
		UO	UI	UO	UI	UO	UI	UO	UI
1.7 m	14%	15%		63%		34%		26%	
10.2 m	12%	12%	13%	57%	34%	30%	22%	20%	19%
30.6 m	10%	10%	11%	49%	31%	26%	27%	16%	16%
244.8 m	4%	4%	4%	18%	17%	10%	9%	7%	7%

6.3 Upscaled Inputs (UI)

In the second part of the scale analysis, data inputs have been upscaled to the different target scales before being employed in the model. Thus, after calibration, the model results are produced directly at the target scale, simulating the functioning of the model at coarser resolutions for the same data set. In order to identify the heterogeneity loss with spatial resolution of the model inputs, some of them are described in Table 6.5. Heterogeneity information is presented in terms of Variation Coefficient for all scales except the coarser (744.8 m), for which only one pixel is available. Since the aggregation is performed with the simple averaging approach, the average value of each parameter is preserved, just like the UO results. Variation coefficients decrease to about one fourth of their highest-resolution value by the last scale step, indicating a quite uniform data levelling for the model input.

Table 6.5: Variation coefficient for selected FEST-EWB model inputs across the selected scales.

Parameter	1.7 m	10.2 m	30.6 m	244.8 m
Albedo	27%	24%	21%	8%
Vegetation Fraction	51%	38%	31%	13%
Leaf Area Index	65%	45%	37%	15%
Vegetation Height	43%	32%	27%	12%

A similar effect is visible on the calibration parameters, and is detailed in Table 6.6 for all the calibration steps. The Variation Coefficient stays high (above 50%) until the 30.6 m step, before plummeting to the 25% value of the 244.8 m scale. The calibration functions employed for the two parameters are practically the same, except for overestimated values. This distinction brings about different calibrated datasets until the 10.2 m step. By the 30.6 scale, the most extreme overestimations have been smoothed out, and the two parameters converge to similar distributions.

Table 6.6: Average and variation coefficient for the calibration parameters of the different steps in the scale analysis

Parameter	$R_{S,min}$		R_S	
	Average	Var. Coeff.	Average	Var. Coeff.
Original	127 s/m	59%	500 s/m	-
Calibrated, 1.7 m	579 s/m	63%	603 s/m	63%
Calibrated, 10.2 m	410 s/m	51%	407 s/m	52%
Calibrated, 30.6 m	355 s/m	58%	355 s/m	58%
Calibrated, 244.8 m	399 s/m	25%	399 s/m	25%
Calibrated, 734.4 m	310 s/m	-	310 s/m	-

The scale evolutions for LST, RET, Latent Heat, Sensible Heat and Soil Moisture are portrayed in Figure 6.6 (lower row) for 11th June, 11:00 local time, with the relative variation coefficients detailed in Table 6.4. Turbulent fluxes (Fig. 6.6e) show similar behaviours to those of the upscaled outputs (Fig. 6.6b), with smaller variation coefficients, in particular in the Latent Heat and the higher-resolution steps. This may be attributed to the loss in spatial heterogeneity caused by the upscaling process: working on less heterogeneous input data, the model provides less heterogeneous outputs. Analysing the values in Table 6.5 and those in Table 6.4, it can be observed that, for the

10.2 m and 30.6 m scales, UI Latent Heat presents six-tenths of the diversity shown by its UO counterpart. However, the former is originated from input data with six-to-seven-tenths of the heterogeneity of the UO one.

These concepts are less visible for the Soil Moisture, as evident by the similarity be-tween Figure 11c and Figure 6.6f. The difference is minimal, being slightly perceptible only in the numbers in Table 6.4, because of the reduced soil moisture dynamics due to the brevity of the simulated period. Most pixels retain values very close to those of the starting condition, which is obviously uninfluenced by the upscaling approach.

6.4 Approaches comparison

6.4.1 Temperature biases

Figure 6.8 displays the summed-up surface temperature results for the two upscaling approaches. Green dots identify the average temperature biases (model RET against flight LST) obtained by upscaling the model outputs. The green area highlights the one-standard-deviation-range around the mean value ($\pm\sigma$). As already discussed, the averaging process preserves the global mean. On the other hand, the orange dots provide the average temperature biases for the upscaled-input model results, with the orange areas identifying the standard deviation range as above. The independent calibrations that produce the upscaled-input results, although completely unrelated to the upscaled-output data, provide quite similar temperature biases. For high resolutions (10.2 m and 30.6 m), the average biases are particularly similar to the upscaled-output results. Coarser resolutions lose some of that similarity (in particular on 3rd September), but the overall comparison of the two datasets remains remarkable. Generally, low (absolute) biases can be attained with either of the upscaling approaches, as in both the error-minimization calibration rationale is employed.

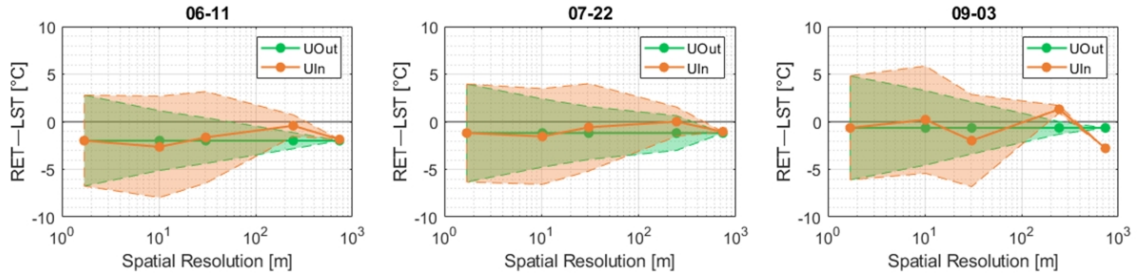

Figure 6.8: Evolution of the model temperature bias (RET–LST) across different scales: average value (solid line) and standard deviation range (shaded area).

6.4.2 Global evapotranspiration

The comparison between the two approaches is investigated also in terms of daily evapotranspiration, focusing on the main vineyard area. Figure 6.9 provides the absolute-value results of this comparison in the left-hand column. The golden bar identifies the calibrated-model ET result for the native resolution; the green bar identifies the up-scaled-outputs approach result, whereas the orange one the upscaled-inputs result. The UO and UI results are never equal, but they are

fundamentally never far from each other. Varying on the days, the differences can be more or less marked, but the overall value is similar, with no clear over-estimation of one over the other. Furthermore, both values are generally in the vicinity of the daily ET computed at the highest resolution (the golden bar). This aspect is further investigated in the right-hand column of Figure 6.9, which dis-plays the Relative Error (RE), for both approaches, between the ET valued at the coarser scale and the highest-resolution ET, assumed to be the most accurate. The green line identifies again the UO approach, and shows an error increasing monotonously, coherently with the simple averaging method at its origin. The line for the 3rd July, although seemingly constant at the null value, presents non-null errors, poorly distinguishable as always below 1%. The orange line represents the UI results, with a more erratic scale evolution, as already seen in Figure 6.8 for the independent calibrations. The RE data is useful because of the limited variability of the ET values, which hinders clear understanding of the possible error. The results shown confirm this assumption, as non-negligible errors – as high as ±30% – can be detected. Generally, UI errors are higher than those of UO but, being subject to calibration, can be even lower (as is the case for the 734.4 m scale in the 11th Jun and 3rd Sep dates). While UO, by construction of the simple averaging methods, is monotonically increasing, UI has no pre-defined behaviour.

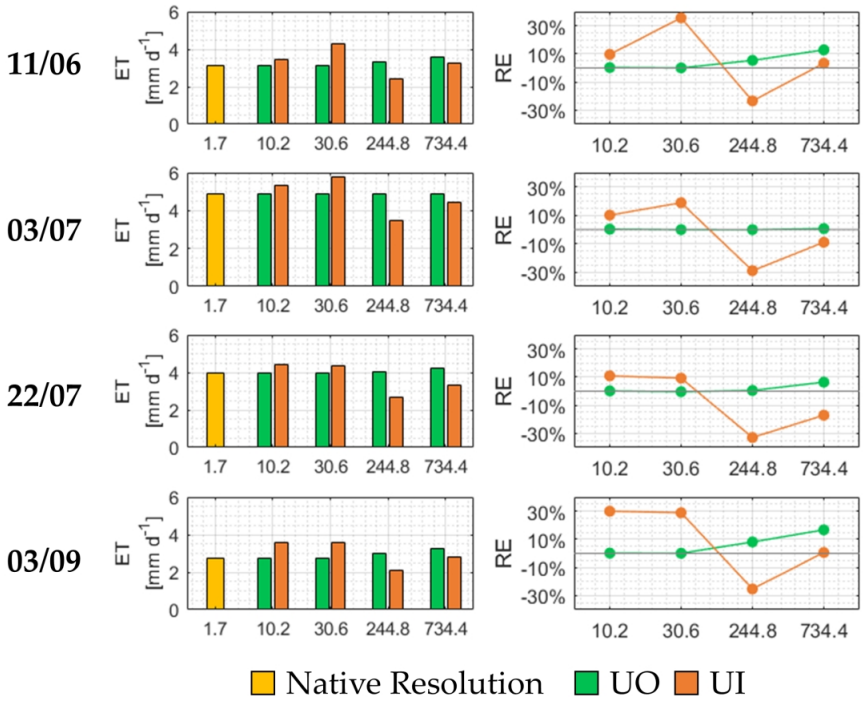

Figure 6.9: Average daily ET of the main experimental area for some of the test days. In the left-hand column, absolute-value comparisons between the upscaling approaches and the native-resolution value. In the right-hand column, Relative Errors (RE) with respect to the highest-resolution ET.

Given the nature of the scale analysis, a further insight into the effects of spatial resolution over

model application can be obtained by analysing the spatial distribution, in-stead of the average value, of ET. Figure 6.10 shows the different ET spatial distributions across the four scales of our analysis, for the example date of 11th June and comparing both scaling approaches. For the 10.2 m scale step, little differences can be detected, in line with the average value featured in Figure 6.9. The pattern of slightly higher ET in the eastern half of the vineyard is visible in both approaches, while the western half shows some discrepancies between the two. In the shift towards the 30.6 m step, the different calibration of the UI approach is quite evident (as foretold by the higher average value in Figure 6.9), although spatial patterns start to fade out. The low-ET roads surrounding the vineyard are clearly distinguishable in both approaches, as the empty fields are directly north and south of the main vineyard area. Finally, in the 244.8 m step, both approaches seem to converge to similar values for the pixels involving the main vineyard area, as the lumped nature of pixels at this coarse spatial resolution flattens out most singularities in the target area.

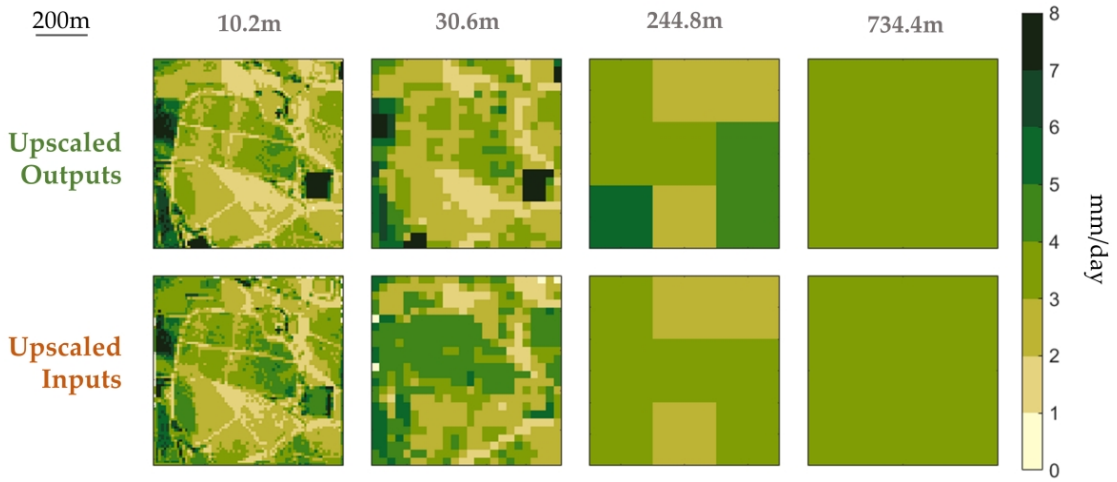

Figure 6.10: Spatial distribution of ET across the different scales (columns) and both scaling approaches (UO for the upper row and UI for the lower). Data about the example date of 11th June.

6.5 Final take-aways

Numerous doubts regarding the scale issues with energy fluxes involve the common assumption of pixel homogeneity in most surface energy balance models (Ershadi et al., 2013). These concerns revolve around the modelling non-linearities, which do not cope well with the (often) linear aggregation processes, non-linearities all the more evident for heterogeneous pixels. Again, Ershadi et al. (2013) focused on the dependency of modelling roughness lengths (used to compute aerodynamic resistances) on spatial resolution, postulating that all models following the Monin-Obukhov Similarity Theory (MOST) face this challenge.

The scale analysis shown in this study aims at testing the FEST-EWB sensitivity to modelling

non-linearities across common spatial resolutions for remote sensing product. Two approaches are contrasted: aggregating model results obtained at high resolution (Upscaled Outputs approach, or "UO"); aggregating model inputs before calibrating the model anew (Upscaled Inputs approach, or "UI"). Faced with this double approach, the FEST-EWB model has shown consistent results.

In the calibration phase (Figure 6.8), the temperatures are comparable between the two approaches. The calibration process, employing the same calibration functions for both approaches, demonstrated to be only slightly hampered by the spatial resolution. This is all the more impressive provided the loss in spatial information brought on by the upscaling process, both in the actual results for UO and in the input data for UI, as testified by Table 6.5. Although data inputs become up to three-fourths less diverse, the model still manages, with the appropriate calibration, to provide low temperature biases. The aggregated fluxes (Figure 6.7) reflect this decreased data diversity with less heterogeneous UI Latent and Sensible Heats with respect to their UO counterparts.

To provide an operative estimate for the model performance in coarser-resolution scenarios, ET global estimates for the vineyard area are computed with both approaches and compared to their high-resolution counterparts. This adaptation is detailed in Figure 6.9, with the two different scale evolutions for the UO and UI results. While the simple averaging approach provides a monotonous relative error increase in the UO scenario, the independent calibrations set a more erratic error distribution for the UI approach. Clearly, the UI errors appear overall higher than the UO ones, in agreement with Sharma et al. (2016). They found that ET was better preserved with output upscaling than with input upscaling, as in the former case the coarser-scale ET relative error reached, at most, 28%, whereas in the latter it stretched just above 40%. The results of input upscaling for their work was obtained for a model (SEBS) which did not require calibration; probably for this reason, the up-scaled-input ET showed a monotonously increasing error which is not the case for this study, as shown in Figure 6.9. The overall error values are however in tune with what was found in this study.

Some further considerations are due for the UI results shown in Figure 6.9. Being the model subject to a new calibration for each scale, low errors are theoretically possible even for coarse resolution, which is not the case of the UO results. However, as scales progress, fewer and fewer pixels cover the same area; in this case, only 1 pixel for the 734.4 m scale and 9 for the 244.8 m one. Fewer available pixels dramatically hinder the perks of employing a distributed hydrological model, as less parameter values can be tuned during the calibration process. Thus, while low relative errors are theoretically possible for coarse scales in the UI approach – as for the 11^{th} Jun and 3^{rd} Sep dates in this case, for the 734.4 m scale – the calibration process can provide worse results, as is the case for the 244.8 m scale.

Finally, some positive insights of high resolutions data can be gathered by the ET spatial patterns shown in Figure 6.10. The differences between the two scaling approaches seem quite in line with those of the averaged values discussed above. This is particularly true for the highest resolution of the scale analysis (10.2 m), the closest to the native resolution. As scales progress, some discrepancies emerge between the approaches, in particular for the medium-range spatial resolution (30.6 m), while coarser resolutions seem less affected. This is in line with the fact that 30.6 m is a critical resolution value, not high enough to encompass large field portions (like 244.8 m), not low enough to clearly distinguish the main features of the field (such as the bare-soil paths within the vineyard area, clearly visible at 10.2 m). In such mid-range resolutions, the model does seem to struggle in capturing the heterogeneity of the different contributions to the global ET.

Chapter 7

FEST-2-EWB

In this chapter, the robustness of the two-source version of the FEST-EWB model (FEST-2-EWB) will be explored, first in a controlled laboratory environment (Section 7.1), then over two field test cases (Section 7.2).

7.1 Lysimeter

The laboratory experiment with the lysimeter will be detailed in this section, first covering the data pre-processing steps (Section 7.1.1–7.1.6), that have been necessary for then evaluating the FEST-2-EWB model calibration and validation (Section 7.1.7–7.1.9).

7.1.1 Thermal infrared camera pre-processing

A total of 13 proximal sensing "flights" have been completed during the monitoring period with a thermal camera. Each acquisition provided both RGB and thermal infrared data, at different resolutions. At the camera height above lysimeter level (1.20 m), these amount to 0.39 mm and 1.2 mm, respectively. With the experimental configuration, the area covered by one image is roughly 1 200 cm^2 (around 5% of the whole lysimeter surface). This means that a minimum of 19 images are required to fully cover the whole lysimeter. However, for georeferentiation and mutual correction purposes, some overlapping areas had to be maintained among all images. The final acquisition scheme has involved four distinct stripes, each made up of 5-6 acquisitions, for a total of 20-24 acquisitions for each global lysimeter image. These images have then been geolocated and mosaiced to form two global data matrices for each sampling instance, one for land surface temperature (LST) (Figure 7.1a) and the other with RGB values (Figure 7.1b). In order to obtain thermal infrared data, the camera inverts Stefan-Boltmann law from its longwave radiation measurements, after an assumption a priori for the surface emissivity. From the final user perspective, these data need only to be patched together to be used in the calibration phase, while the RGB data needs a further post-processing step. As the final aim is determining the fractional vegetation cover, the following algorithm has been used over each pixel RGB triplet:

1. If the Green reflectance is higher than both the Red and the Blue ones, the pixel is classified as vegetated

2. If the highest reflectance is in the Red band, the pixel is classified as vegetated only if the Green reflectance is not much smaller than the Red one (a threshold Green/Red ratio of 0.75 has been chosen after some analyses)

3. In all other cases, the pixel is classified as non-vegetated

This follows in the steps of other works which were able to retrieve vegetation data from RGB images (Marcial-Pablo et al., 2019). This work is performed at the high resolution of RGB images (0.39 mm), so that the assumption of obtaining only fully-vegetated and completely-bare pixels can be considered safe, as this spatial resolution is comparable with the reference scale of the final object. An example of vegetation distribution is visible in Figure 7.1c.

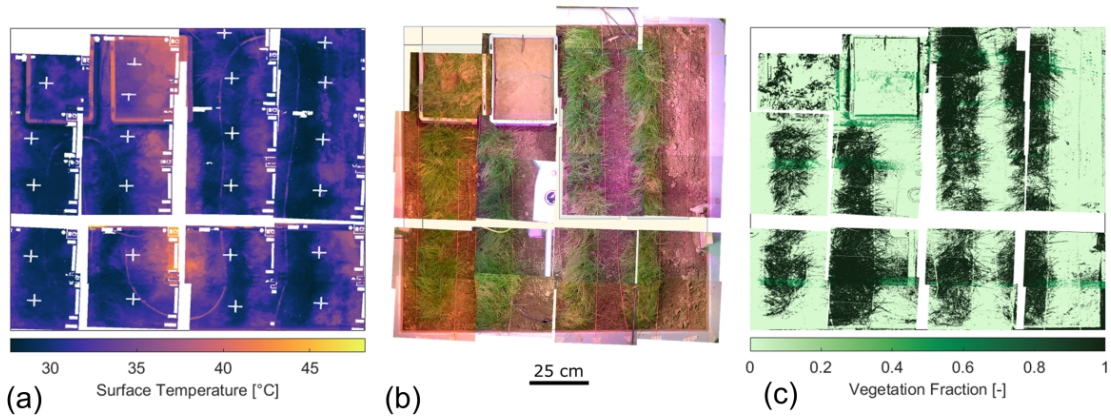

Figure 7.1: Data gathered from camera on 7th July: surface temperature composite (a), RGB data composite (b) and fine-scale vegetation fraction (c).

7.1.2 Spatial resolution resampling

All distributed data have been resampled through simple spatial averages to a 10 cm resolution from their native scale, before being fed to the model. This allows to achieve various levels of vegetation-soil mixing within each pixel, thus creating optimal heterogeneity conditions. In Figure 7.2 an example of final, pre-processed vegetation map is provided, for the example date of July 10th. The darker pixels are those that result better-aligned with the main vegetated row (Section 3.6.3), while the lighter ones cover mostly bare soil. The histogram in Figure 7.2b shows how no pixel has a definite 0 or 1 vegetation fraction, with a good portion (exactly one fifth) falling close ($\pm$10%) of the 50% mark that represents ideal heterogeneity conditions for the models comparison.

7.1.3 Meteorological data

While some meteorological data (air relative humidity and temperature) have been assumed as constant over the whole lysimeter area, radiation distribution has required some clarifications. The distance between lysimeter surface and lamp set-up is quite small (1.20 m), in order to optimize the energy distribution by having the lysimeter occupy most of the set-up field of view. However, this

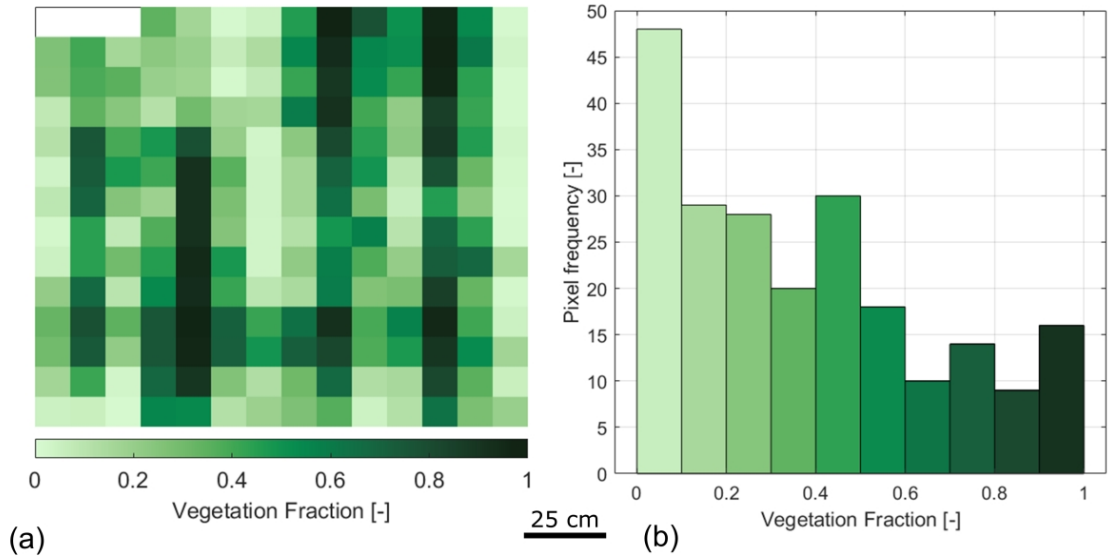

Figure 7.2: Spatial distribution (a) and histogram (b) for the vegetation fraction data of 7$^{\text{th}}$ July.

proximity implies that energy transmission cannot be assumed as cylindrical (as is the generally-assumed case with considerably distant sources, e.g., the Sun in open field), and effects of its conical distribution cannot be neglected. This means that an uneven short-wave energy distribution is in place, although the radiometer only provides one single value per time step. This energy distribution heterogeneity is further heightened by the effect of the nearby widows, which allow in natural light unevenly over the lysimeter surface. In order to identify the energy distribution, the data from one of the earliest thermal infrared camera overpasses (May 31$^{\text{st}}$) have been employed, since no vegetation had yet developed and, at that moment, the soil was overall dry after being exposed to the set of lights for some days without any spatially-differentiated irrigation. This means that the surface soil could be assumed as quite homogeneous, both in moisture and temperature. In this scenario, the temperature of each soil parcel would be a direct result of the thermodynamic equilibrium enforced by the amount of radiation it received, since no compositional or water-related gradients were present over the lysimeter surface at that time. For this reason, a proportionality has been imposed, based on equal Net Radiation across all pixels. This means that, for any given pixel x, the following will hold:

$$R_S(x) : {T_K}^4(x) = R_S(\text{rad}) : {T_K}^4(\text{rad}) \tag{7.1}$$

$$\varsigma = \frac{R_S(x)}{R_S(\text{rad})} = \left[\frac{T_K(x)}{T_K(\text{rad})}\right]^4 \tag{7.2}$$

Where $R_S(x)$ identifies the shortwave radiation received by the given pixel, $R_S(\text{rad})$ is the radiometer measurement, $T_K(x)$ the absolute pixel temperature and $T_K(\text{rad})$ the absolute temperature obtained by the radiometer from the longwave upwelling radiation measurement. The ς ratio allows to refer any pixel back to the radiometer. In this way, any value of incoming shortwave radiation can easily be distributed in space by applying the matrix ς, shown in Figure 7.3b. In

the image, a coarsely-concentric pattern emerges, with a decreasing radiation amount as distance from the radiometer nadir point increases. A darker area is also visible right in the middle of the lysimeter, which can be associated to the shadow provided by the radiometer itself.

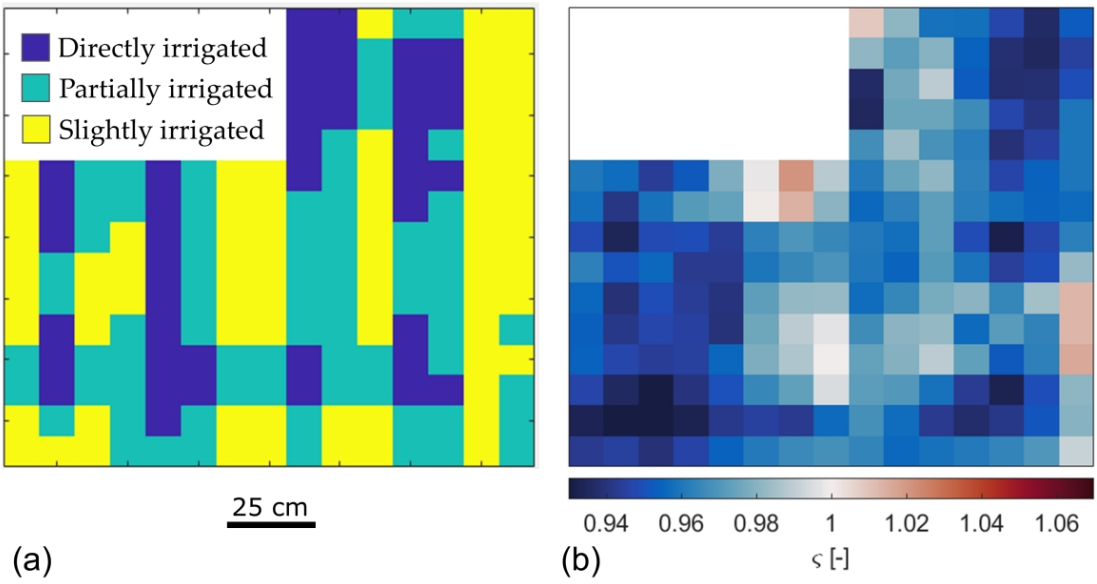

Figure 7.3: Irrigation (a) and radiation (b) modelled distributions.

7.1.4 Irrigation distribution

Irrigation distribution should have been quite straightforward to model, starting from the geometrical outline of the seeded (Zone 1) and unseeded (Zone 2) areas (as described in the experimental outline in Section 3.6.3). However, a combination of factors complicated the final pattern. Firstly, the structural pattern of the drip irrigation line was so that not all outlets were positioned within Zone 1 areas; blocking with tape the outlets located in Zone 2 was only partially effective, as some water reached Zone 2 nonetheless (clearly visible in the focus in Figure 7.3a). Another cause for Zone 2 pixels receiving some irrigation water was the partial unevenness of the lysimeter surface: small roughness patches caused some of the water accumulated during irrigation to flow towards Zone 2 pixels (also visible in Figure 7.3b). Finally, even for drip outlets located within Zone 1, horizontal soil water transmission caused the actual irrigated footprint to reach, in particular for the heavier irrigations, areas within Zone 2. In order to account for all these issues, the irrigation map has been extracted *a posteriori* from the last vegetation data, attributing more water to the highly-vegetated areas (Figure 7.3a).

7.1.5 Soil moisture probes calibration

A calibration step is always needed for the soil moisture probes due to the different soil types with respect to the manufactured one. Firstly, with the soil in very dry conditions, one soil undisturbed

Figure 7.4: Lysimeter view from above after full grass growth (a) and focus on the tape used to avoid irrigation of bare-soil areas (b).

sample was collected in the vicinity of each soil moisture probe, using metallic cylinders. The Sensor Output (SO) values from the SM probes during the sampling were also recorded, and the cylinders were weighted both at that moment and after 24 hours in an oven at 100°C. This assured that all the moisture was removed and the weight difference allowed to determine both the soil dry mass and the Actual Water Content (AWC) at sampling, following Equations 7.3–7.4:

$$AWA = W_{wet} - W_{dry} \tag{7.3}$$

$$AWC = \frac{\rho_w \, AWA}{\rho_s \, W_{dry}} \tag{7.4}$$

Where AWA is the Actual Water Amount (g) in the soil sample, W_{wet} (g) and W_{dry} (g) are the sample weights before and after oven desiccation (respectively) and ρ_w and ρ_s represent the water and soil densities, respectively equal to 1 g cm^{-3} and 1.3 g cm^{-3} – this value being obtained in precedent tests (Mantovani, 2016). A second sampling was taken after heavy irrigation, obtaining for each probe another SO–AWC couple. The result of this data collection is detailed in Figure 7.5a. SM as perceived from the probes results weakly perceptive of extreme (either very dry or very wet) water contents. Thus, a linear correction (quite similar in parameters across all soil moisture probes, with the exception of SM probe 5) was enforced for the successive steps. In Figure 7.5b, the final soil moisture profiles are displayed. The peaks corresponding to the irrigation events (also detailed in the figure) are quite visible, together with different decreasing curves, with the steeper ones associated to lights-on periods, and the milder ones mainly to the weekends.

7.1.6 Evaporation and Transpiration extraction and comparison

A total of 16 weightings were performed during the observation period (3rd June – 15th July 2021, 42 days), marking start and endings of 15 Monitoring Intervals (MIs). In the first part of the experiment, the weightings were performed twice a week, with MIs lasting 3-4 days. In the last part, a denser data collection schedule was enforced, and the average MI duration decreased to 1-2

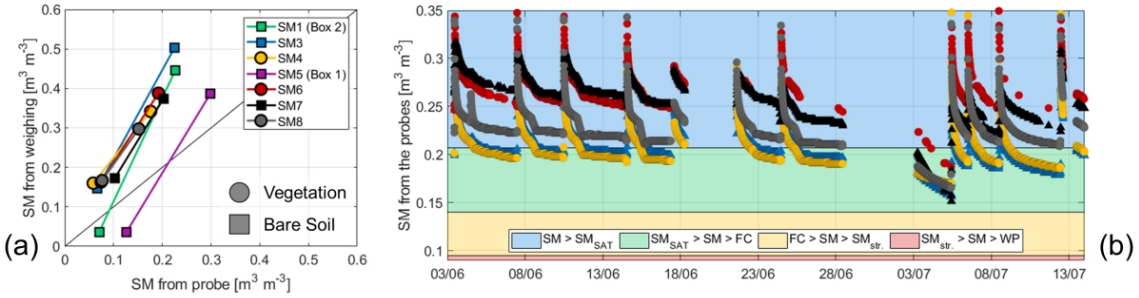

Figure 7.5: Data points obtained for SM probes correction (a) and SM data time series for the probes in the lysimeter (b).

days. Overall, the global average interval is 2.78 days. All the information about the performed weightings is detailed in Table 7.1.

Table 7.1: Boxes SM data availability for each MI

MI	Start	End	SM(P)	SM(N)	MI	Start	End	SM(P)	SM(N)
1	3/6	7/6			9	30/6	5/7	xxx	xxx
2	7/6	10/6			10	5/7	6/7	xxx	
3	10/6	14/6			11	6/7	7/7	xxx	
4	14/6	17/6			12	7/7	8/7		
5	17/6	21/6			13	8/7	12/7		
6	21/6	24/6			14	12/7	14/7		xxx
7	24/6	28/6		xxx	15	14/7	15/7	xxx	xxx
8	28/6	30/6	xxx	xxx					

Some MIs for each Box had to be discarded from the analysis as they lacked contemporary SM data (needed to compute percolation) because of SM probes malfunction. For all valid MIs, the weight difference was contrasted to the contemporary percolation (computed using Equation 3.10) and irrigation (when present) to determine the box ET inverting the box mass balance equation:

$$W_{end} - W_{start} = \Delta W = Irr - PE - ET \tag{7.5}$$

At this point, two controls have been performed: (i) a check on the consistence between the independent water loss measurements – from successive weightings and from SM probes outputs – and (ii) the relative partition of the water loss between Percolation and ET.

For the first control, Figure 7.6 provides the differences between weighting-obtained water loss and probes-obtained water loss, for both boxes. These differences are averaged over 24-hours periods to homogenize the different time intervals occurred during the experiment. The reciprocal errors shown by the measurements are relatively contained, falling most of the time within $\pm$ 0.5 mm/d. In general, Box 1 seems to provide better harmony between the two independent data sources, with an average absolute error of 0.57 mm/d against the 0.91 mm/d of Box 2. In panel (c), Figure 7.6 provides also the SM evolution for the two boxes, highlighting the temporal location of the valid weightings and the box irrigations performed.

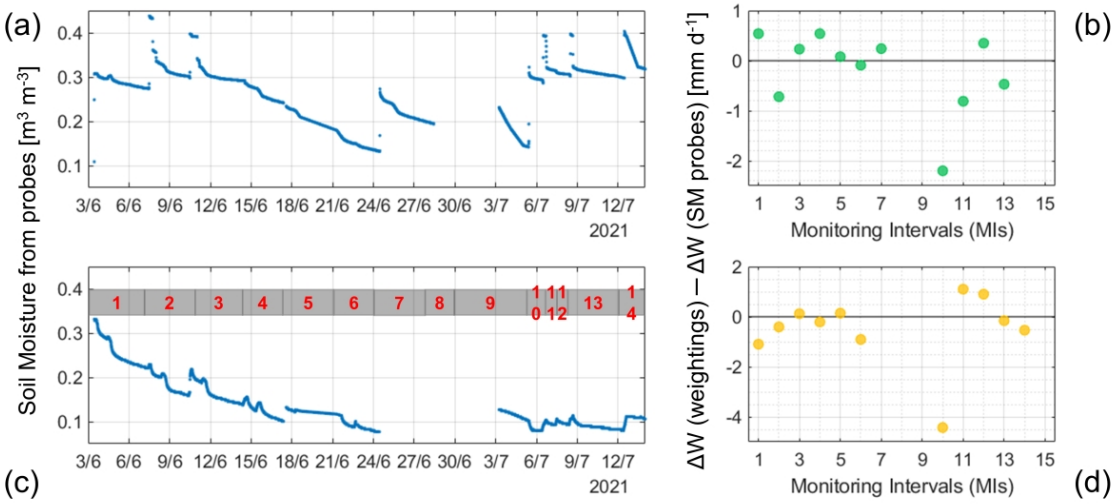

Figure 7.6: Soil Moisture time series for the Box 1 (a) and Box 2 (c) probes, together with the corresponding water loss errors: (b) for Box 1 and (d) for Box 2. Monitoring Intervals (MIs) are also highlighted in plot (c).

The second control concerns the partition of the water loss between percolation and ET. In Figure 7.7, for each box and each valid MI, the irrigation registered amounts, the (modelled) Percolation and (estimated) ET fluxes are provided. It can be observed how the low SM values in Box 2 (Figure 7.7a) mean that close to no percolation is possible, while for Box 1 consistent irrigation events imply that a non-negligible percolation phenomenon is active for the following period.

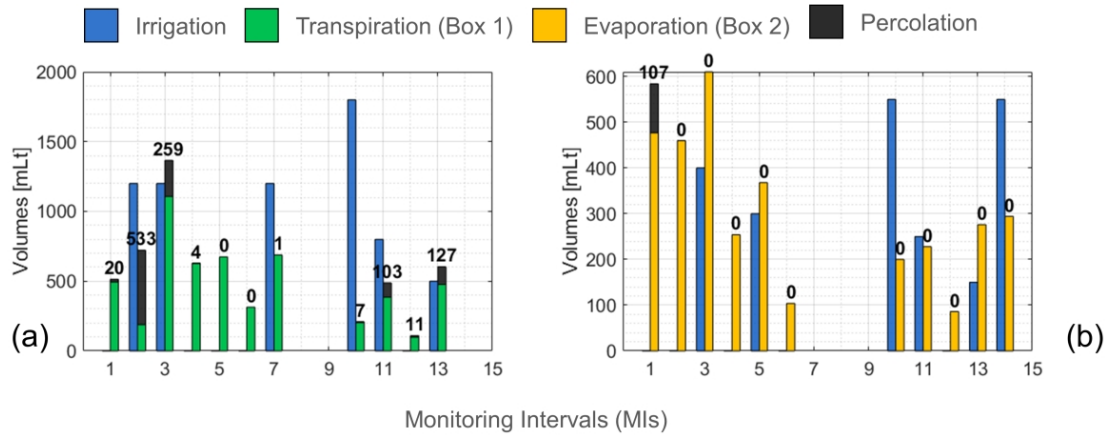

Figure 7.7: Water fluxes balances for Box 1 (a) and Box 2 (b).

The results of the disaggregation approaches detailed in Section 3.6.5 are shown in Figure 7.8. Dashed black lines highlight the global measurement error propagated in the final error estimate as a result of the disaggregation algorithm (±0.12 mm/d). Both disaggregation approaches seem to provide non-negligible uncertainties. Although the mean absolute errors are contained, with 0.56 mm/d for the "Grass-to-Bare" (G2B) approach (–0.20 mm/d average error) and 1.16 mm/d for the "Bare-to-Grass" (B2G) approach (–0.42 mm/d), their variability is quite large, with instances in which both approaches surpass the ±1 mm/d threshold and peak errors worse than –3 mm/d (B2G). In most cases, these uncertainties exceed the measurement error propagation within the algorithms, meaning that some external uncertainties play a role. One possible explanation would be the SM dynamics in both Boxes and general lysimeter, which were not always similar, damaging to the assumption of equal E and T rate at the bases of both disaggregation approaches (Section 3.6.5).

An error propagation procedure has also been applied, adopting the measurement uncertainties shown in Table 3.4.

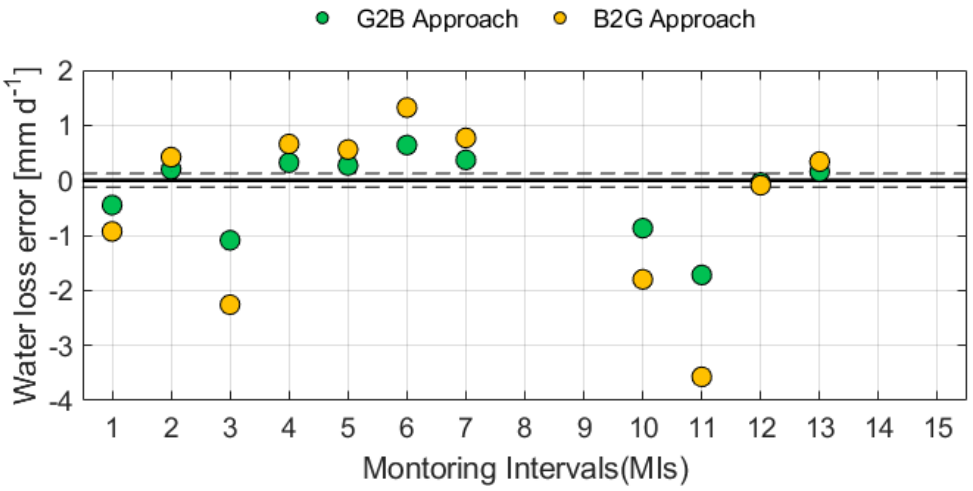

Figure 7.8: Water loss errors for both tested approaches.

Looking at underlying uncertainties in water loss computation (already shown in Figure 7.6), they seem to bare little weight on the errors in Figure 7.8, as shown by the cross-correlation contingency table (Table 7.2). In particular, roughly 36% of the mass balance error of both approaches can be explained with the underlying water loss error in Box 1, while the coarser errors shown by Box 2 are practically uncorrelated to the uncertainties in both approaches. As a result of this check, G2B is chosen for the disaggregation process.

7.1.7 Model calibration

Both FEST-EWB and FEST-2-EWB models are run for the lysimeter. By following the same approach detailed in Section 2.3.6, the optimization of the model error function was used for the calibration of both models. The results are detailed in Figure 7.9, both in form of day-by-day lumped bias and of average error distribution. The overall model errors are quite similar across

Table 7.2: Water and Mass balance errors correlations

		Mass balance error	
		G2B Approach	B2G Approach
Water loss error	Box 1	0.359	0.358
	Box 2	0.028	0.026

both models, both in terms of Average Error (1.80±1.9°C for FEST-EWB and 1.76±1.9°C for FEST-2-EWB) and pixel-wise RMSE (2.87°C for both FEST-EWB and FEST-2-EWB). In terms of spatial distribution, some inconsistencies seem to emerge with the radiation distribution, as a quasi-radial symmetry can be detected, with a temperature underestimation in the central part of the image. However, this estimation errors again seem similar for both models.

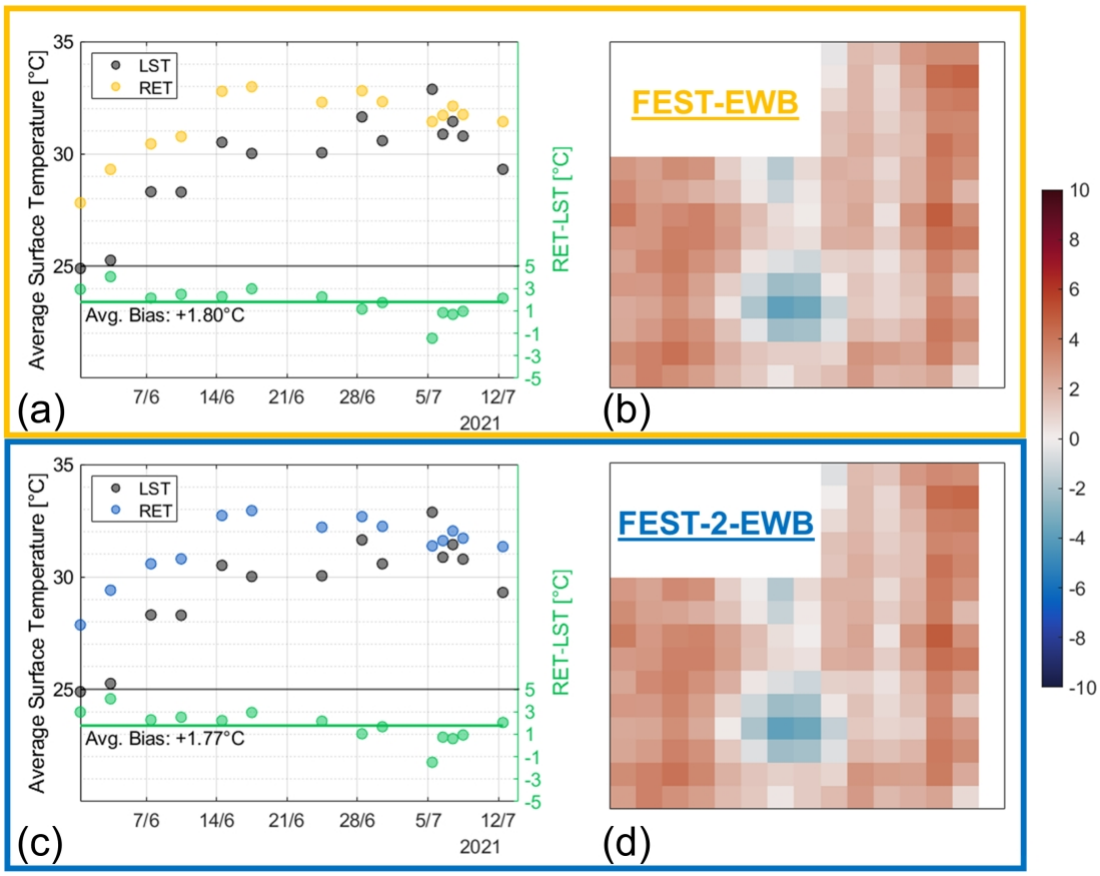

Figure 7.9: Average surface temperatures and biases (a-c) and temperature error distributions (in °C, b-d) for FEST-EWB (a-b) and FEST-2-EWB (c-d).

7.1.8 SM profiles

One of the main distinctive features of the FEST-EWB model structure is that Soil Moisture is continuously modelled starting from an initial condition, by maintaining the energy and water mass balances closure. This allows to preserve, in the long term, the SM dynamics, providing physical consistence to the different ET estimations. In Figure 7.3, the SM comparison between the corrected probes data in the lysimeter and the two models outputs in the corresponding cells is shown. Overall, FEST-EWB seems to identify better the measured SM dynamics, in particular for SM probes 7 (bare soil) and 8 (vegetation). Bias and RMSE values for each model are provided in Table 7.3, confirming how FEST-2-EWB provides worse SM results across all probes. However, the model performances are not too far apart from each other, in particular for SM probes 3, 4 and 6, as confirmed from the mild RMSE increased values, all below +0.04 m^3 m^{-3} (a value frequently associated with satellite SSM accuracy). One main concept to retain when looking at these data is that, although each SM probe is specifically assigned to one land cover (either completely bare or fully vegetated), the model pixels, with their 10 cm spatial resolution, are much more mixed, meaning that their values will inevitably be influenced by different land cover types from the one associated to the given SM probe. This is consistent with the fact that the amount of SM overestimation is not directly linked to the SM probe land cover, with different performances both from the two bare-soil probes (SM probe 3 registering an average RMSE of 0.104 m^3 m^{-3} against the much lower value from SM probe 7, 0.058 m^3 m^{-3}) and the three fully-vegetated probes ($RMSE^{(avg)}_{SM4}$ = 0.121 m^3 m^{-3}, roughly doubling the values for SM probe 6 – 0.067 m^3 m^{-3} – and SM probe 8 – 0.082 m^3 m^{-3}). Another useful information can be gathered analysing the temporal evolution of the model errors, by computing the variation of RMSE over time. On average, the RMSE daily variation values are shown in the last columns of Table 7.3. Across both models, a negative majority can be identified, meaning that, as time goes by, the model comes closer and closer to the observed data. This is particularly evident with FEST-2-EWB (four SM probes out of five show a negative trend, with values as high as 0.0011 m^3 m^{-3} improvement in RMSE per day), but also with FEST-EWB. Indeed, the ability to maintain a continuous SM simulation provides both models with the possibility of improving their estimates with the simulation time.

Table 7.3: Bias, RMSE and RMSE time variation for each SM probe. FEST-EWB identified with "1S", FEST-2-EWB with "2S"

	Bias [m^3 m^{-3}]		RMSE [m^3 m^{-3}]		RMSE time var. [m^3 m^{-3} d^{-1}]	
	1S	2S	1S	2S	1S	2S
SM3	0.085	0.121	0.086	0.122	-0.0001	-0.0011
SM4	0.106	0.134	0.106	0.135	+0.0003	-0.0006
SM6	0.046	0.082	0.049	0.085	+0.0005	-0.0002
SM7	0.024	0.088	0.026	0.089	-0.0001	+0.0012
SM8	0.046	0.111	0.052	0.112	-0.0020	-0.0006

7.1.9 Lysimeter ET partition

The final result of the experiment is detailed in Figure 7.11. In the first plot, the total ET rate is shown for the nine weighting instances in which box SM data were available. This condition is necessary as, following the procedure detailed in Section 3.6.5, percolation modelling is required to

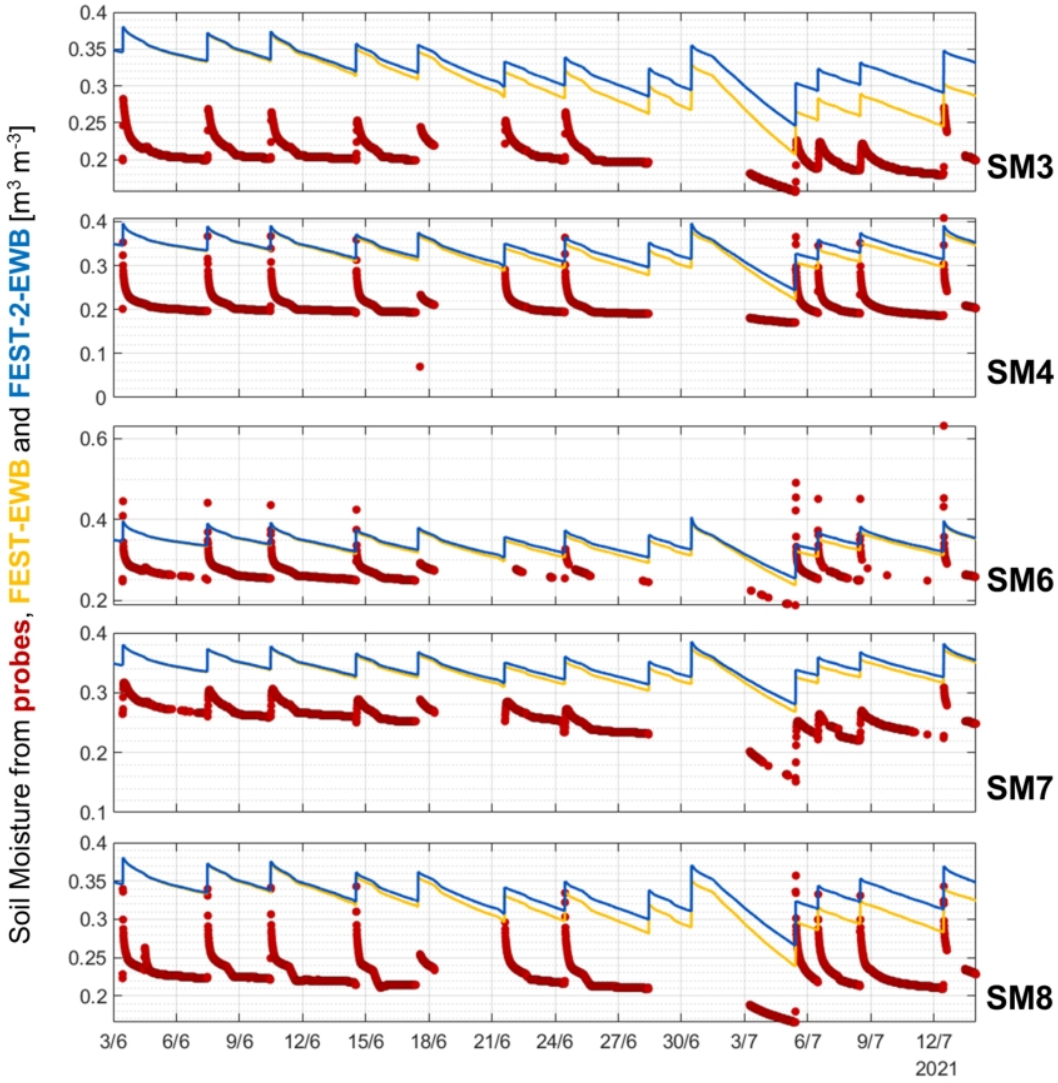

Figure 7.10: Lysimeter SM probes profiles together with model estimations from FEST-EWB (yellow) and FEST-2-EWB (blue).

extract actual ET from total weighting difference. Together with measured values, corresponding models simulations are shown, with both models performing equally good. This is consistent with the similar temperature biases shown above. In the second panel of Figure 7.11, the lysimeter transpiration rates are detailed. The lysimeter values are obtained following G2B Approach in Section 3.6.5, and can be higher than the contemporary ET values as they refer to "rates", i.e. water evaporation "intensities" per unit area. By looking at the model outputs, a distinguishable difference now emerges between the two, with FEST-EWB always exceeding FEST-2-EWB. This

is an expected result, as the former's transpiration is regulated by RET and the latter's by T_{CROP}, which is by construction lower than RET, as explained in Section 2.5. The important result is that – especially in the second part of the experiment (MIs E through I), when vegetation was denser and pixel heterogeneity at its maximum – lysimeter data seem to agree more with FEST-2-EWB, confirming how a two-source approach is more suitable in this kind of heterogeneous scenario. Focusing on the last five MIs, the average absolute error with FEST-2-EWB is 0.16 mm/d, while the single-source model performs a slightly worse 0.54 mm/d. In terms of water volumes difference, the average FEST-2-EWB error amounts to 0.5 Lt, less than one third of the single-source model's (1.8 Lt). To provide an idea of how much this impacts in the overall water volume economics of our system, FEST-EWB errs daily by roughly 20% of the ordinary irrigation volume (FEST-2-EWB own error skims 5%).

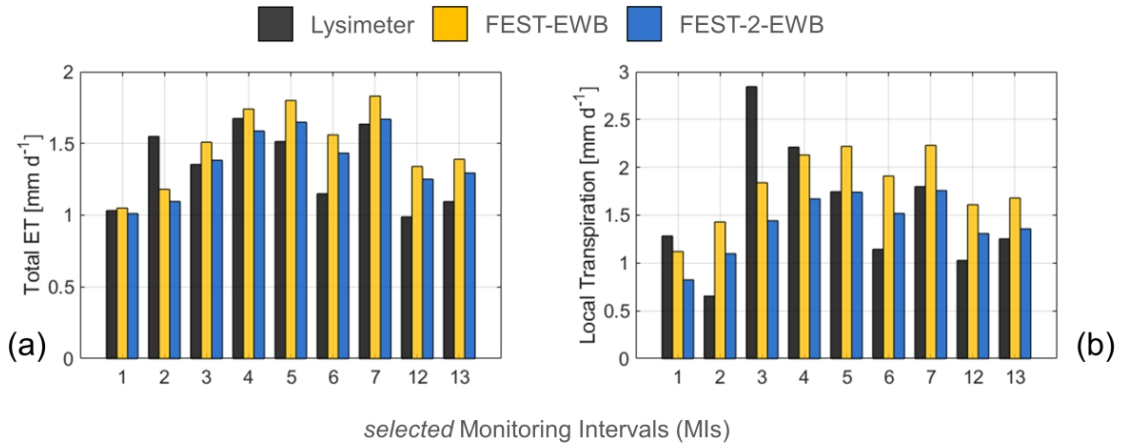

Figure 7.11: Measured and modelled total lysimeter ET (a) and partitioned Transpiration (b).

7.2 Field environment (Rapitalà and Barrax)

In order to extend the FEST-2-EWB results obtained in laboratory to real-world field conditions, an approach similar to that described in the previous section has been taken over two agricultural test cases, the Rapitalà vineyard (already modelled in single-source in Chapter 6) and the heterogeneous agricultural area of Barrax.

7.2.1 Models calibrations

In Figure 7.12, the calibration maps for the Rapitalà case study are shown, for both FEST-EWB (upper row) and FEST-2-EWB (lower row). Modelled RET versus sensed LST data are shown also in histogram format, with representation limits set at ±5°C. On a global analysis, there are not areas with a clear one-way behaviour (either over- or under-estimation of the temperatures). Generally, a quite mixed error distribution is found, irrespective of the calibration date. No link seems to be present with the regular vine-interrow patterns of the actual vineyard. Furthermore, some spot-like areas are visible (e.g., in 11th June, first column) in which the errors are markedly

different from the neighbouring area. Both characteristics may arise from a common origin: the calibration data presents some segmentation issue from the pre-processing phase. In Table 7.4, some calibration statistics are summed up, in terms of error bias and global RMSE. Small differences emerge between the two models.

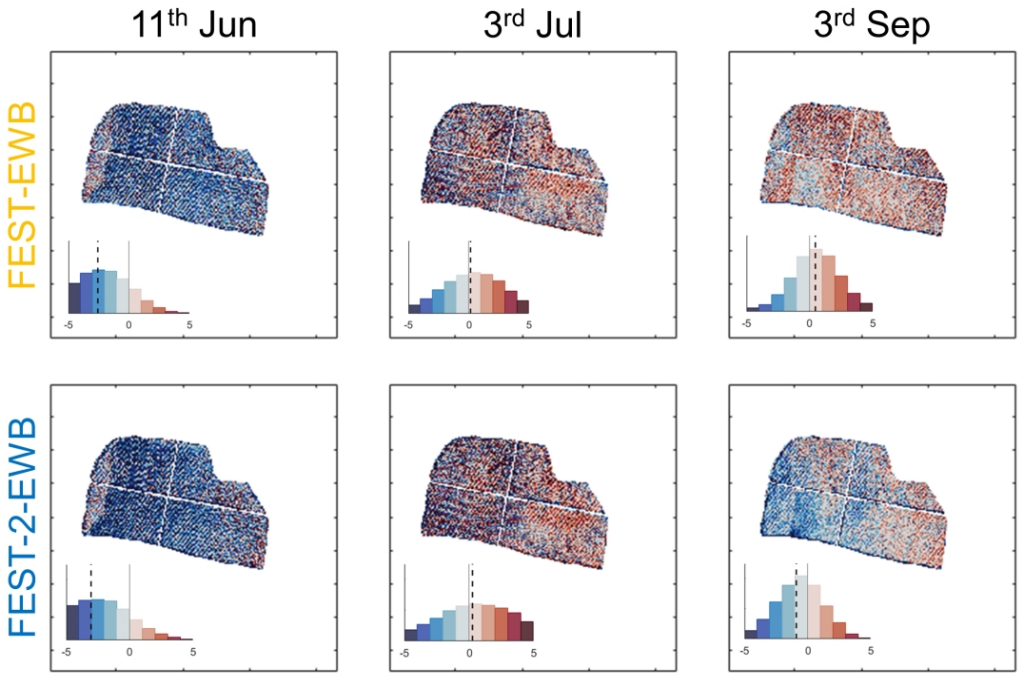

Figure 7.12: FEST-EWB (upper row) and FEST-2-EWB (lower row) temperature biases for the Rapitalà test case, both in map and histogram formats.

For the Barrax case study, Figure 7.13 shows the global superficial temperature bias maps from FEST-EWB (upper row) and FEST-2-EWB (lower row) for three selected flights. The FEST-EWB model was calibrated by Corbari et al. (2015). The flight tracks are clearly visible in the latter two columns, with some missing data. Both models reproduce positively the actual surface temperature. Some areas mismodelled by both approaches can be identified in the central upper pivot (a poppy field with harvesting operations in process during the observation period), where the harvested area is actually warmer than the modelling, and in some sparsely-cultivated areas (both an alfalfa field next to the poppy pivot and another pivot in the south-eastern corner of the area) where the vegetation is probably denser than the input data assume. Specific adaptations statistics are shown in the second part of Table 7.4 for all calibration flights. The quite similar RMSE values for the two models speak clearly about the models similar performances.

7.2.2 Barrax focus: vegetation degree and density

In this section, a specific close-up will be done on the Barrax case study, provided its wide range of different crop systems (Section 3.4). Two main distinctions can be made, in terms of vegeta-

Table 7.4: Calibration statistics

		FEST-EWB		FEST-2-EWB	
		Bias [°C]	RMSE [°C]	Bias [°C]	RMSE [°C]
Rapitalà	11/6	–2.57	3.69	–3.04	4.24
	3/7	+0.16	3.03	+0.27	3.45
	3/9	+0.46	2.14	–0.89	2.43
	Average	**–0.65**	**2.95**	**–1.22**	**3.37**
Barrax	25/7 8:43	–0.83	2.62	–2.53	3.58
	25/7 8:51	–0.53	3.30	–2.06	3.70
	25/7 9:02	1.78	3.27	0.34	2.52
	25/7 9:10	2.12	3.28	0.69	2.46
	25/7 9:19	1.37	3.11	–0.06	2.69
	25/7 9:28	0.81	2.83	–0.58	2.81
	25/7 9:38	0.21	3.22	–1.15	3.26
	25/7 9:46	1.00	3.14	–0.30	3.12
	26/7 8:43	–3.15	4.07	–4.40	5.21
	26/7 9:09	2.00	3.23	0.81	2.51
	26/7 9:19	0.69	2.52	–0.50	2.63
	26/7 9:27	0.74	2.75	–0.42	2.61
	26/7 9:40	–4.51	5.78	–5.68	6.71
	Average	**0.13**	**3.32**	**–1.22**	**3.37**

tion degree (drawing up two classifications: vegetated and non-vegetated) and density (other two classifications: homogeneous and heterogeneous). The assignment of each land cover category to its classification is performed based on personal knowledge of the site. This explains why fields with similar vegetation fractions (as Camelina and Reforestation, both with an average vegetation fraction of 9%) have been assigned to different classifications (Homogeneously non-vegetated and Heterogeneously vegetated areas, respectively) according to different intra-pixel vegetation patterns, not distinguishable by the simple vegetation fraction number alone.

Both models calibration results from Figure 7.13 have been broken down across these land cover categories, in order to identify possible trends within each classification (Fig. 7.14). This distinction is brought on by the precise research interest of trying to obtain similar findings for Homogeneous classifications and detect the improvements brought on by FEST-2-EWB over Heterogeneously Vegetated areas. In terms of surface temperature, however, although both models show equally good temperature interpretations for Homogeneous classifications (both Vegetated and Non-vegetated), no clear trend separates them in the Heterogeneously Vegetated classification.

7.2.3 Calibration parameters

In Table 7.5, the pre- and post-calibration statistics of the calibration parameters are shown. The selected calibration parameters, as already detailed in Section 2.3.6, involve mainly the Evaporation and Transpiration mechanisms, as the small time frames do not allow major groundwater dynamics to develop. The wider parameter range in the Barrax case study is easily explainable with the much larger crop heterogeneity of that agricultural area. Both from the Table and the Figure, a close similarity of the two models performances emerges clearly. For the Rapitalà test case, a narrower

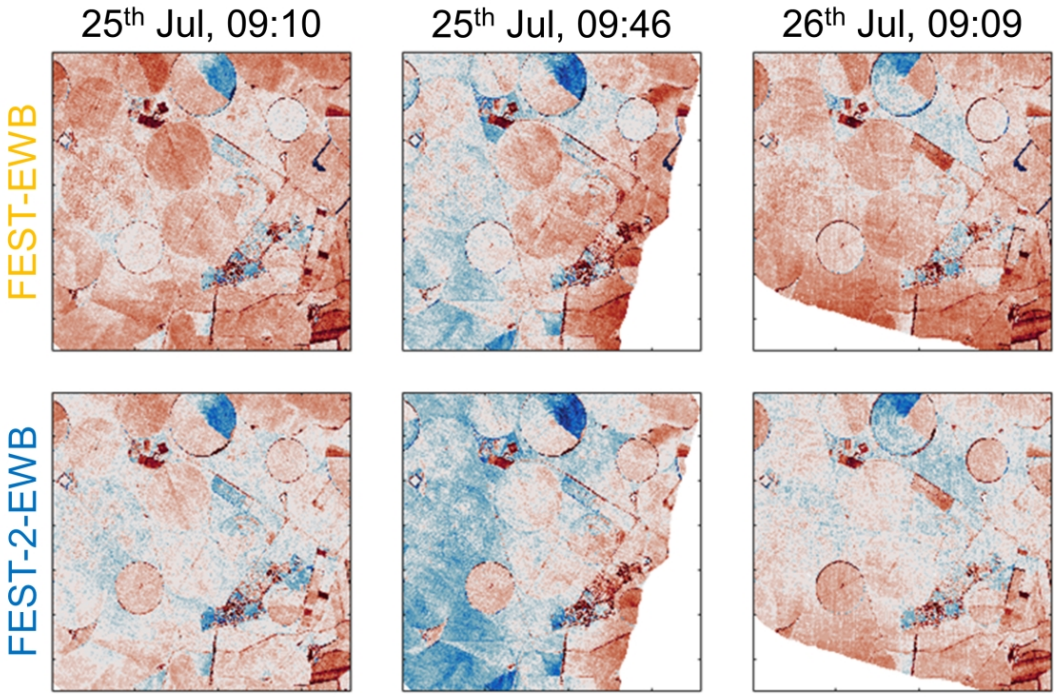

Figure 7.13: FEST-EWB (upper row) and FEST-2-EWB (lower row) temperature biases for the Barrax case study.

parameter range seems to be associated with the FEST-2-EWB model, with $R_{S,min}$ values after calibration much closer to the value suggested by the literature for vineyards (200 s/m), as opposed to the higher dispersion found with FEST-EWB.

Table 7.5: Calibration statistics for both models and both case studies.

Case study	Model	R_S range (avg.) [s/m]	$R_{S,min}$ range (avg.) [s/m]
Rapitalà	FEST-EWB	0 – 1920 (528)	50 -1920 (529)
	FEST-2-EWB	250 – 750 (580)	35 – 275 (184)
Barrax	FEST-EWB	500 – 2000 (1931)	54 – 2800 (220)
	FEST-2-EWB	500 – 2000 (1925)	54 – 2600 (210)

7.2.4 Models validations

The validation results for both models over the Rapitalà case study are shown in Figure 7.15. The comparison is limited to the turbulent fluxes for a more operational-oriented analysis (adaptation statistical indexes are nonetheless provided for all fluxes in Table 7.6). The behaviour of the two models seems specular: while FEST-EWB captures more closely the Sensible Heat and tends to

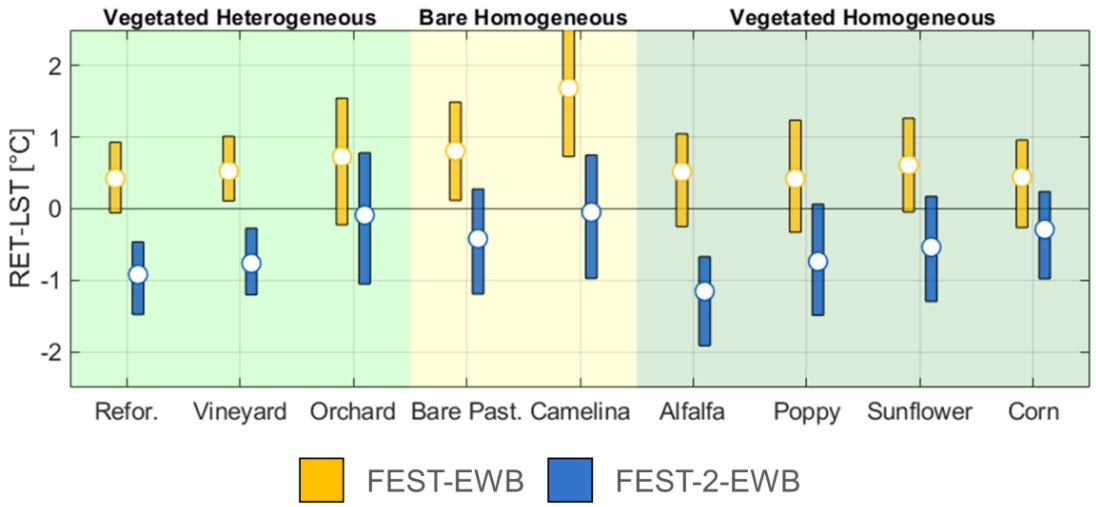

Figure 7.14: Temperature biases from FEST-EWB and FEST-2-EWB, sorted by vegetation density classes, for the Barrax test case

underestimate the Latent Heat, FEST-2-EWB does the opposite, well interpreting and sometimes overestimating the Latent Heat and falling short of describing adequately the Sensible Heat.

This difference in fluxes representation is all the more relevant when compared to the closeness in terms of land surface temperature bias shown by both models in Figure 7.12. Although maintaining a similar global temperature, and thus not affecting the overall thermodynamic equilibrium of the pixel, FEST-2-EWB manages to provide more accurate representations of Latent Heat by transferring the computation to its two internally-obtained surface temperatures, closer to the actual real-world values. Table 7.6 collects some adaptation statistics for the case study. The better interpretation of Latent Heat from the FEST-2-EWB is evident in the decrease of the related RMSE. Model interpretation statistics for the other fluxes are quite similar across both models, except for Sensible Heat, where the FEST-2-EWB underperformance with respect to FEST-EWB, already visible in Figure 7.12, is confirmed by a consistent increase in RMSE.

For what concerns the Barrax test case (Figure 7.16), the limited time window of data availability is compensated by the presence of three distinct flux towers, located in critically different areas. Looking at the Latent Heat data (left-hand side of the figure), different results depend on the land cover of the flux tower footprint. The first two rows show fluxes from heterogeneously vegetated areas (Reforestation and Vineyard), with three visible peaks. For the Reforestation site, two peaks out of three are clearly better interpreted by the FEST-2-EWB, while in the Vineyard site the distinction is less marked. The last row shows the Camelina results, with moderate Latent Heat peaks, easily interpreted by both models. This is consistent with the (relative) homogeneity of the Camelina area, over which both models are expected to converge.

On the other hand, the Sensible Heat comparisons show much more similar values across the two models, with a consistent overestimation in the vegetated categories. Generally, the FEST-2-EWB seems to perform slightly better, as shown in Table 7.6. A clear distinction emerges between the models interpretation of Latent and Sensible Heats. While the modelled Sensible Heats are

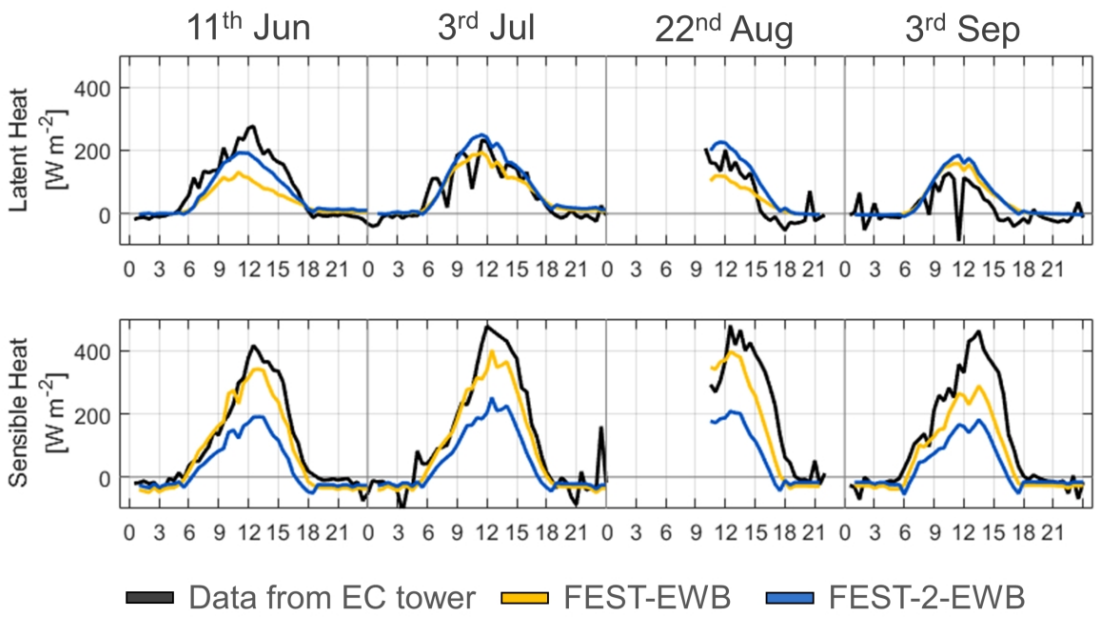

Figure 7.15: FEST-EWB and FEST-2-EWB Validation results for the Rapitalà test case

fundamentally similar, the Latent Heats show a definite difference between the models. Overall, the FEST-EWB model tends to overestimate the Latent Heat (with positive biases), while the FEST-2-EWB is more inclined to provide underestimations. Among both interpretations, the RMSE suggests that the FEST-2-EWB provides better flux modelling, with much lower values than those of FEST-EWB.

Table 7.6: Validation statistics for both models and both case studies. FEST-EWB identified with "1S", FEST-2-EWB with "2S", "Bias" and "RMSE" expressed in W m^{-2}

Case study		Rapitalà		Barrax					
Crop		Vineyard		Vineyard		Reforestation		Camelina	
Model		1s	2S	1S	2S	1S	2S	1S	2S
Latent Heat	Bias	-4.0	+14.5	-6.7	-5.6	+12.1	-0.2	-0.3	-0.7
	RMSE	51.6	47.2	30.3	29.9	23.2	16.9	13.4	13.5
Sensible Heat	Bias	-40.0	-87.9	+57.7	+35.0	+7.5	-6.9	+9.4	-7.7
	RMSE	69.6	130.7	119.4	90.1	69.7	59.2	53.6	44.3
Net Radiation	Bias	+5.3	-19.4	-1.3	-34.0	-49.7	-86.1	+6.5	-25.8
	RMSE	67.0	96.6	62.5	68.3	78.2	111.8	81.5	94.7
Soil Heat Flux	Bias	+3.6	-0.05	-52.3	-63.4	-69.3	-79.0	-7.8	-22.6
	RMSE	23.5	22.7	79.3	87.8	95.3	102.4	61.2	70.9

Latent Heat is a key variable in the energy balance, quite important in agriculture because of its direct link to the water vapour output of the crop. In Figure 7.17, model performances in both case

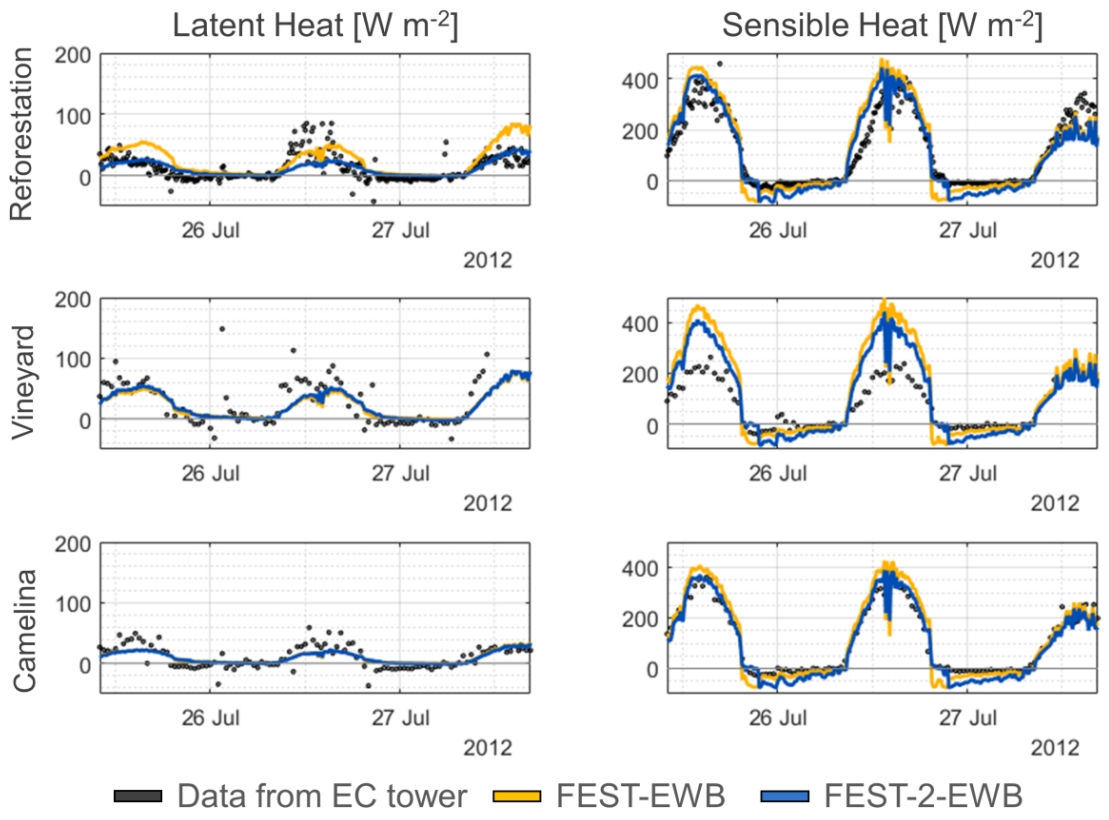

Figure 7.16: Validation results for the Barrax test case for the FEST-EWB and FEST-2-EWB models

studies are shown in a Taylor plot, focusing on the vineyard crops in order to have a uniform analysis. In both cases, a better performance (even if slightly so, as is the case of Rapitalà) is provided by the FEST-2-EWB. Correlations are relatively high for both models (the lowest values being just short of 0.7), but only the FEST-2-EWB Latent Heat for the Rapitalà case manages to almost fall below the 0.5 threshold value for the normalized Root-Mean Squared Difference (RMSD), considered as indicative of a good model interpretation (Taylor, 2001). Provided that both models manage to accurately capture the surface temperature (as seen in Section 7.2.1), the better performance of FEST-2-EWB in terms of Latent Heat can be seen as a step forward in evapotranspiration modelling without detectable losses to the thermodynamic equilibrium simulation.

7.2.5 Global vineyard ET

Similarly to what shown for the lysimeter in Section 7.1.9, the global ET amount and its partitioned Transpiration component are shown (Figure 7.18) for the vineyard from the Barrax case study. Similarly to what was found for the lysimeter, ET amounts (Figure 7.18a) are close among the two models, whereas the modelled Transpirations (Figure 7.18b) are quite distinct, with FEST-2-EWB

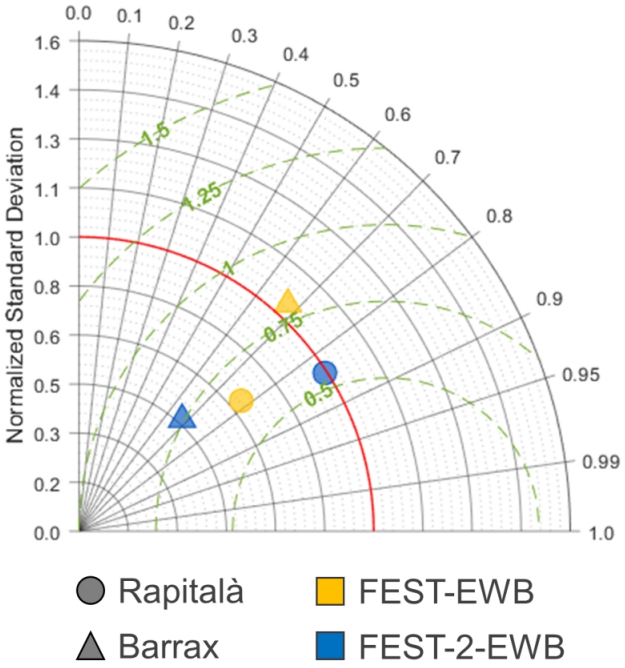

Figure 7.17: Taylor plot for the Latent Heat results over the vineyard areas.

providing lower values. This difference in Transpired volume is roughly correspondent to half of the Transpiration from FEST-EWB, cumulated over a period of almost two and a half days.

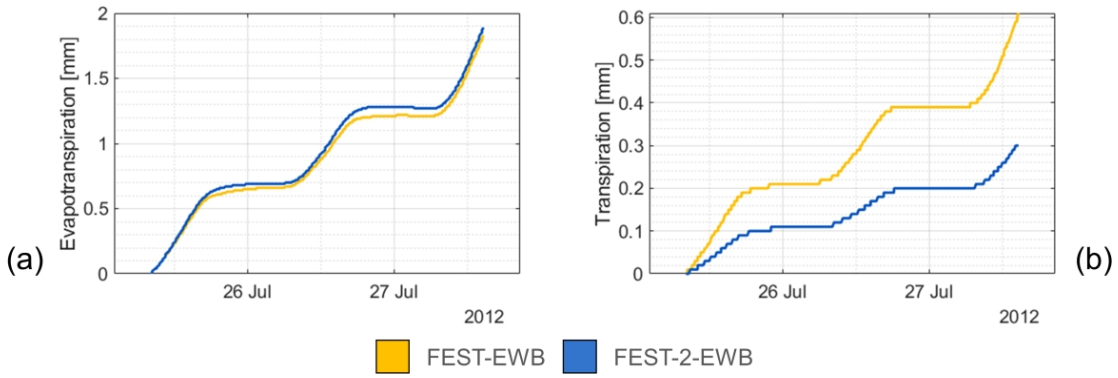

Figure 7.18: Cumulated total Evapotranspiration (a) and partitioned Transpiration (b) from both models over the Barrax vineyard.

In order to better understand these results, two main caveats need to be addressed. Firstly, in

this open-field application, as in most similar cases, accurate Transpiration data are not available. In order to create a comparison with the model results, field lysimeters would have been required, which are seldom available in real-world applications. Other approaches, which are in early testing phase, try to extract the ET sub-components directly from EC measurements by employing oscillations in CO_2 concentration (Zahn et al., 2022). Secondly, the short simulation time means that cumulated ET and T volumes are quite low, as compared to normal seasonal irrigation amounts. However, an extrapolation over a whole irrigation season could be imagined, to infer the potential impact of the use of FEST-2-EWB in agricultural management.

7.3 Final take-aways

In this chapter the potentialities of a two-source extension of the FEST-EWB distributed hydrological model have been explored. In heterogeneous areas (e.g., fruit tree crops), the assumption at the core of single-equation energy balances – pixel temperature can be assumed homogeneous over the whole pixel area – is unsound. By employing a single temperature for the whole pixel, and provided an unbiased model temperature, an underestimation of the ET from the non-vegetated area and an overestimation of the ET from the vegetated area can be expected. The main scientific reason for creating the novel FEST-2-EWB model was that, in agricultural applications, such ET overestimations could mean both plant growth overestimation (with consequent erroneous yield predictions) and irrigation excess (with consequent waste of the water resource).

The first part of the chapter has detailed an experiment conducted at the "Fantoli" laboratory at Politecnico di Milano, where a lysimeter was used to obtain disaggregated ET estimates from a grass crop planted in rows, imitating heterogeneous scenarios that can be frequently found in field (practically all fruit trees crops). The experiment results have been obtained with a contained error margin, and have been compared to the ET and T estimates from both FEST-EWB and FEST-2-EWB, which had been run over the lysimeter. With similar surface temperature outputs, both models show a good interpretation of the global lysimeter ET but differ when extracting the Transpiration component. FEST-EWB, in line with the theoretical expectations, produces Transpiration estimates higher than those from FEST-2-EWB, which are much more in line with the disaggregated estimates from the lysimeter. Provided the complexity of retrieving such disaggregated data in most model performance studies, this experiment is especially valuable, as it demonstrates the need for distinguishing intra-pixel heterogeneity when dealing with mixed land covers.

The second part of the chapter extends these consideration to two real-world cases, with open-field data available for the modelling over a vineyard (Rapitalà) and a complex agricultural area, featuring both non-vegetated and vegetated (with different densities) fields (Barrax). Such complex scenarios have provided some higher differences between the models in surface temperature estimations, although with both providing acceptable errors. The validation process has seen a generally better estimation of Latent Heat from FEST-2-EWB in both cases. A close up on the Barrax vineyard has shown how, while model-retrieved ET are similar, the corresponding Transpirations differ, with FEST-2-EWB providing estimates lower by approximately a half. This last finding is strikingly similar to that obtained over the lysimeter, although in this scenario field data to validate such a result were not available, as is the case for most E-T disaggregated fluxes in open field cases.

Numerous studies have successfully employed two-source modelling structures in more or less heterogeneous scenarios, starting from the TSEB model (W. Kustas and Anderson, 2009) and its numerous applications (Cammalleri et al., 2010, 2012; P. Colaizzi et al., 2014; P. D. Colaizzi et al.,

2012; Y. Li et al., 2019; Nieto et al., 2019).

Khan et al., 2021 devised a LAI-based methodology to develop a two-source version of the single-source SEBS model (Su, 2002), obtaining similar overall Evapotranspiration estimations over forests (both full and mixed), cropland and grassland. Aguirre-García et al., 2021 (and mentioned studies) successfully applied two-source structures to olive groves in arid environments by exploiting satellite information for vegetation and thermal data input into the model. Many studies have focused on the integration of satellite observations in order to obtain more accurate ET estimations, such as D'Urso et al. (2021), who explored the possible improvements in ET estimation in a complex area such as a vineyard by employing a thermal-based data fusion approach.

However, only recently the inter-ET partitioning between plant and soil contributions is being explored. X. Li et al., 2019 have proposed an improved parametrizations of the aerodynamic resistances (alternatively, the conductances) of soil and canopy, linking their relative weight to the transpiration fraction (T/ET). Improved aerodynamic conductances are also at the base of the STIC model Mallick et al., 2015, which has provided internally-partitioned Latent Heat components and reliable evapotranspiration estimates in different ecosystems such as the conterminous US (Bhattarai et al., 2018) and Australia (Mallick et al., 2018). Both Aouade et al. (2020) and Aron et al. (2020) have made use of either isotope tracing or sap flow observations (or both), which require a considerably heavy data-collecting effort. On the other hand, a common measurement of an EC station is CO_2 concentration, which has been used in ET partition by Zahn et al. (2022) with positive results. An extensive use of these methodologies could replicate at EC measurement level what we showed with the lysimeter in this Chapter.

The overall ET errors from FEST-2-EWB, shown in this Chapter, are fairly aligned with those of the prevailing literature. However, its underlying structure preserving SM dynamics and allowing a full time simulation independent of LST data (either measured directly or from satellite) availability makes it a powerful option for vast and long-term agricultural monitoring via hydrological simulation. Furthermore, information about partitioned ET is still being discussed across the literature. In this sense, the positive results from the lysimeter activity are encouraging towards a fruitful employment of two-source modelling schemes in optimizing irrigation water use, in particular for heterogeneous crops.

Chapter 8

FEST-AeroT

In this chapter, the possible integration of aerodynamic temperature within the FEST-EWB hydrological model is discussed, following the scheme outlined in Section 2.6. Section outlines an analysis of possible formulations for the aerodynamic resistance from eddy covariance data, obtaining different possible values for T_{AERO} (Section 8.2), whose variability is filtered through different environmental (meteorological and vegetation) parameters (Section 8.3). Once a specific aerodynamic resistance is selected, the consequent aerodynamic temperatures have been integrated in the hydrological model as additional direct input, in order to analyse the effect of perfect temperature modelling over Latent Heat estimation (Section 8.4). Finally, a way to parametrize T_{AERO} against surface temperature is validated (Section 8.5) to obtain a continuous temperature simulation within the model framework, whose results are shown in Section 8.6.

8.1 Aerodynamic Resistance sensitivity analysis

The first step is a sensitivity analysis on the aerodynamic resistance, a very delicate term of the Sensible Heat equation, and in turn of the aerodynamic resistance. Its parametrization follows the main assumption of logarithmic behaviour of the wind profile and its more or less turbulent interaction with the surface roughness elements (mainly, vegetation). Data from five distinct EC station datasets - Montichiari (MON), Landriano (LAN) and Livraga (LIV) in maize fields in the North of Italy and Foggia-Incoronata (FIN) and Foggia-Onoranza (FON) in tomato fields in the South of Italy - have been used for this analysis: following Equation 2.38, Air Temperature and Sensible Heat measurements were employed with the different Resistance parametrizations detailed in Table 2.2 to obtain the correspondent aerodynamic temperature. The results from all the parametrizations have been compared to those from the Simplified Thom (ST) parametrization, which is the one used in the FEST-EWB model. In Figure 8.1, for the example of the Montichiari case study, two plots are shown for each parametrization, coupling its results with those from ST, both in terms of aerodynamic resistance (blue scatter plots) and temperature (red scatter plots). In terms of resistances, some extremely different behaviours can be traced: some show quasi-linear distributions, quite close to the 1:1 line (and thus to ST values), such as Yang and Xie formulations. Another group is made up of the Full Thom (FT), Verma, Mahrt-Ek and Viney formulations, which show marked resistance underestimations with respect to ST. The scatter plot is almost flat, suggesting a considerable relevance of the instability components which differentiate ST from

these other parametrizations. Finally, a more chaotic group is composed of Choudhury and Hatfield parametrizations, which offer poorly-aligned results and a less clear possible relation to ST estimates. The transition to the aerodynamic temperature (red) scatter plots, performed by plugging the newly obtained aerodynamic resistances into Eq. 2.38, is mediated by the contemporary Sensible Heat and Air Temperature measurements, meaning that the apparent relationships visible for the resistances do not necessarily hold for the temperatures. Indeed, this is the case for the Full Thom, Verma, Mahrt-Ek and Viney group, whose aerodynamic temperatures seem to be fairly aligned to those estimated through ST for the lower values (generally, less than 50°C), before showing a progressively clearer underestimation as temperatures increase. This suggestion that highest temperatures are associated with the most unstable conditions is consistent with the concept of convective atmosphere mixing which enhances turbulent heat exchanges between surface and lower atmosphere. The parametrizations most similar to ST (Yang and Xie) retain their linear distribution also for the aerodynamic temperature, as do the more chaotic formulations (Choudhury and Hatfield).

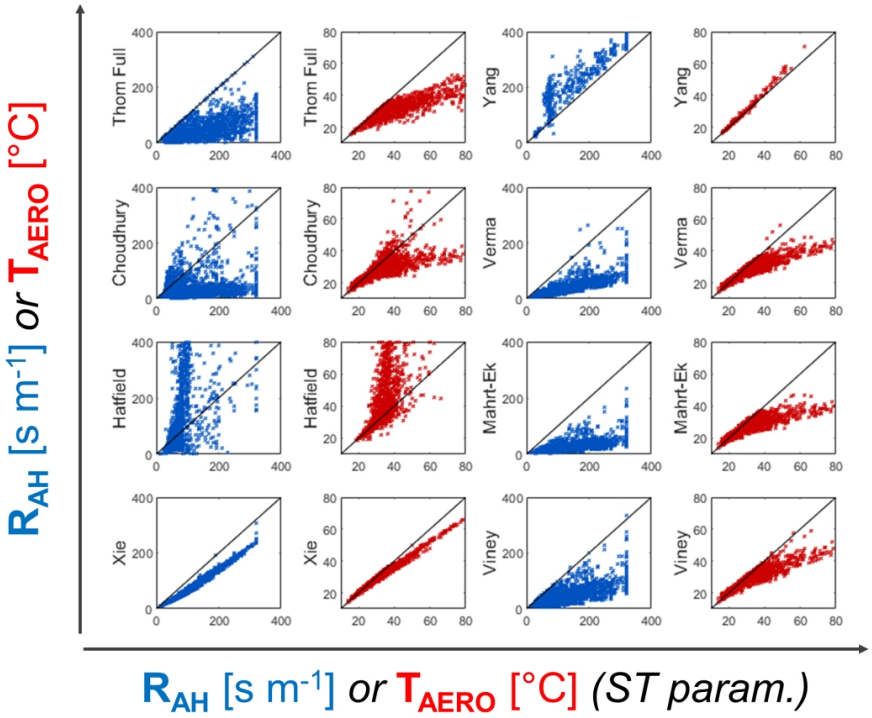

Figure 8.1: Comparison by scatterplots between other parametrizations and ST, in terms of aerodynamic resistance (blue) and temperature (red). Data from the Montichiari EC station.

In Table 8.1, all the parametrizations tested over the Montichiari case are detailed in terms of necessary parameters and statistical indexes of their comparison with the Simplified Thom. In the first part of the table, for each formula are detailed, in order: if the knowledge of the wind shear velocity (u^*) is required, if the formula has empirically-calibrated parameters and if the formula

employs the Richardson number. This last information is relevant because, in all these formulae, the R_I parameter (when present) is present in negative form and under square root (Table 2.2). This means that real values from these parametrizations can be obtained only when surface temperature is higher than air temperature, which somehow limits the range of application of that particular formula. Indeed, the last parameter in the first part of the Table is its employing rate (ω), which identifies the relative amount of the raw data that were employable from the given formula. This number can be seen as an operation-oriented indicator, providing an empirical estimation of how likely that specific parametrization can be employable over a generic EC dataset. High employing rates are registered for ST and Full Thom, while among the others smaller values are found, mainly related to the use of the Richardson number (which precludes the use for surface temperatures lower than the corresponding air temperatures) and empirically-calibrated parameters (with a less marked effect). In the second part of Table 8.1, some statistical adaptation indexes of each formula (as compared to ST estimations) are provided, with the average absolute relative error (RE), the Root-Mean Square Difference (RMSD), the Pearson correlation (ρ) and the Taylor score (Taylor, 2001). While Pearson correlations are generally high (mostly above 0.75), non-negligible differences are found, although mostly within ±10% in terms of RE (generally around 5-6°C in terms of RMSD). Overall, the ST parametrization seems to be the most reliable, provided its width of application (with the highest employing rate) and low data requirements.

Table 8.1: Information and comparison statistics for the investigated R_{AH} parametrizations

Parametrizations		ST	Thom	Yang	Choudhury	Verma	Hatfield	Mahrt-Ek	Xie	Viney
Params.	u^*		X	X						
	Emp.		X	X	X		X			X
	R_I	No	No	Yes	Yes	Yes	Yes	Yes	Yes	Yes
	ω	98%	96%	16%	72%	69%	24%	66%	67%	66%
ST Comparison	RE		-11%	2%	-7%	-8%	17%	-9%	-4%	-7%
	RMSD		6.9°C	1.1°C	6.2°C	5.2°C	11.1°C	5.9°C	2.2°C	4.8°C
	ρ		.88	.99	.76	.90	.59	.85	.99	.92
	TS		60	99	72	71	40	62	95	76

8.2 T_{AERO}-LST across the case studies

The aerodynamic temperatures obtained from the 9 parametrizations are shown in Figure 8.2 for the maize field of Montichiari, contrasted with the corresponding radiometric temperatures. For each density plot, LST is displayed on the horizontal axis, whereas T_{AERO} on the vertical axis and different patterns can be detected. Most formulae provide a data cluster around the 1:1 line, meaning that in most situations the temperatures are hardly distinguishable, as also testified by the interpolation line, almost always juxtaposed T_{AERO} the 1:1 line. However, a general trend can be identified, in which low LST values correspond to even lower T_{AERO}, while high LST values are associated to even higher T_{AERO}.

These findings are similar to those obtained for the other maize fields (shown in Appendix C), but slightly differ from those for the FIN data, relative to a tomato field (Fig. 8.3), in which a distinguishable underestimation of LST with respect to T_{AERO} is visible, with interpolations slopes more in the region of 0.5–0.8. This could suggest that, for arid climates and with low SM regimes,

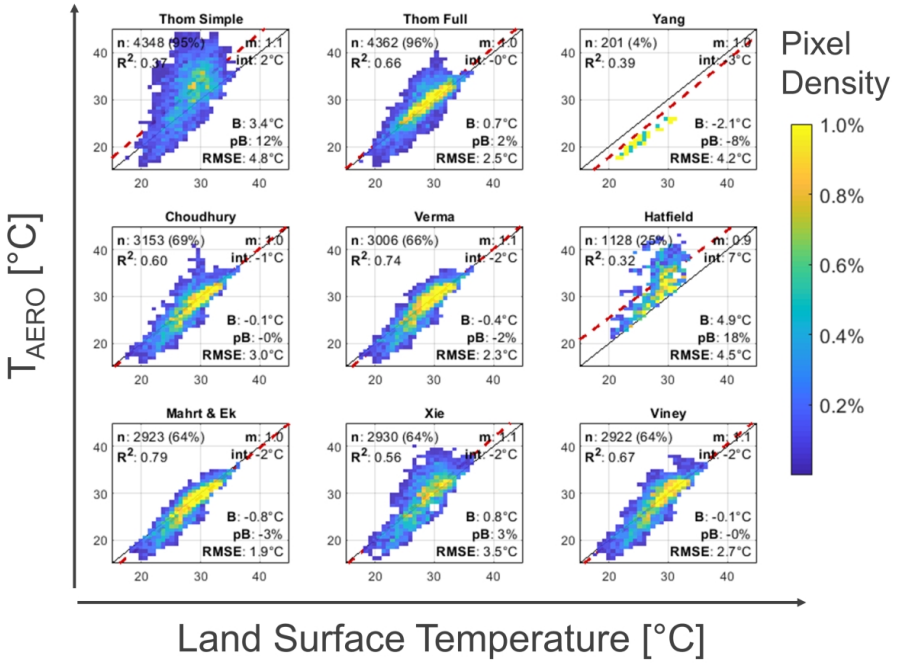

Figure 8.2: T_{AERO} v. LST distributions for the Montichiari data, according to different aerodynamic resistance parametrizations.

Latent Heat could actually be lower than that usually computed employing LST, as differences between the two temperatures reach even values around 10°C. Such high difference suggests that assuming the two temperatures to be equal is not always true and can lead to misinterpretations of energetical fluxes, mainly Sensible Heat (given its direct connection with T_{AERO}) but also, as a result, Latent Heat and, thus, ET.

In the next steps of the analysis, the integration of T_{AERO} within FEST-EWB will be explored. In order to achieve this, the analysis will focus on the Simplified Thom formulation, given its long-standing employment in FEST-EWB applications and in order to perform coherent comparisons with versions of the same model neglecting the role of aerodynamic temperature. This choice is justified also by the quite similar T_{AERO} distributions across all parametrizations (Figs. 8.2 and 8.3) and the ST usage simplicity and low input data requirements.

8.3 T_{AERO}-LST dependency on environment

In order to identify any possible major determinant in the T_{AERO}-LST relations shown in Figures 8.2 and 8.3, a comparison has been performed between any given temperature difference and its relative boundary conditions, both meteorological and vegetation-related. In particular, an analysis in terms of wind speed, air temperature, incoming shortwave solar radiation (S_{IN}), Vapour Pressure Deficit (VPD), vegetation fraction (f_V) and height (H_V), soil moisture (SM) and Latent Heat (L) was performed. In Figure 8.4, the results for the Montichiari data are shown (the other maize

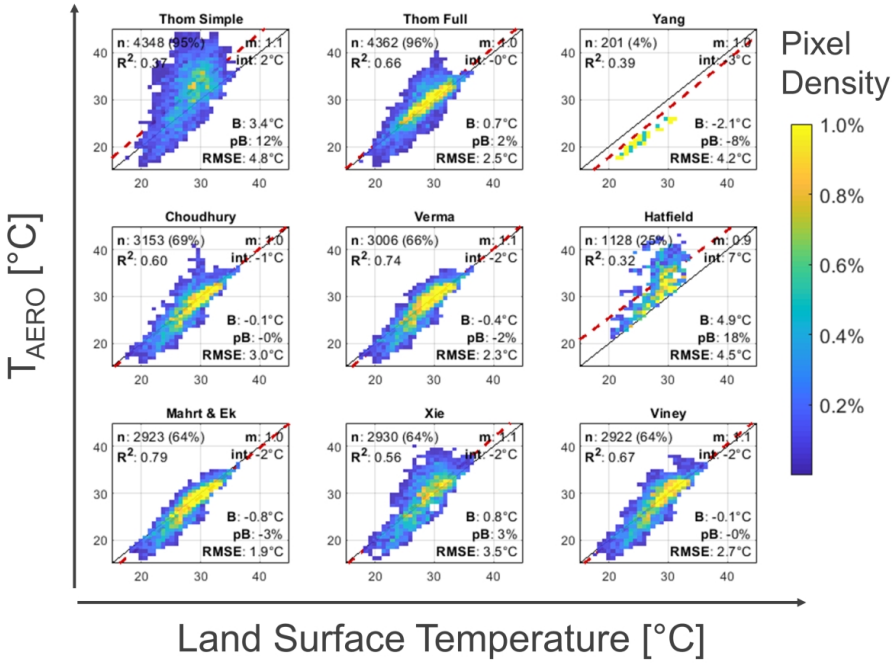

Figure 8.3: T_{AERO} v. LST distributions for the Foggia-Incoronata data, according to different aerodynamic resistance parametrizations.

case studies are detailed in Appendix C). The general trend is that non-meteorological variables (vegetation height and fraction and soil moisture) seem to have low impact on the T_{AERO}-LST difference, with slopes close to 0 and less than 1% variance explained (R^2<0.01). Meteorological variables, on the other hand, show non-negligible links with the temperature difference, reaching R^2 values as high as 0.47 (for S_{IN}), quite in line with what found by Kustas et al. (2007) and Mahrt and Vickers (2004). VPD and Air temperature also show good impacts on the temperature differences, while wind intensity seems to have a "funnel"-shaped influence, with low wind speeds associated with widely-dispersed (T_{AERO}-LST) data and higher values providing less divergent temperatures. This "converging" behaviour could be explained by the fact that higher winds increase air mixing and shift the main driver of heat exchange towards turbulence, rather than convection. Wind speeds lower than 1 m/s are excluded from the analysis as, in such conditions, the conditions are generally too stable for EC measurements to be meaningful. The Foggia-Incoronata data (shown in Figure 8.5) displays some points of contact with the maize data: meteorological variables (except wind) again play a more important role than soil/vegetation parameters, and wind dependency again shows the "funnel" effect already seen in Figure 8.4. However, for all meteorological parameters, the dependency sign results inverted, with lower and lower aerodynamic temperatures with increasing variables. This is consistent with the high-temperature underestimation described in Figure 8.3 and may be linked to the higher surface temperatures found in Southern Italy (36.1°C on average for the FIN test case, against 28.1°C for the MON case).

In the following Table 8.2, the determination coefficients for all case studies are provided. The

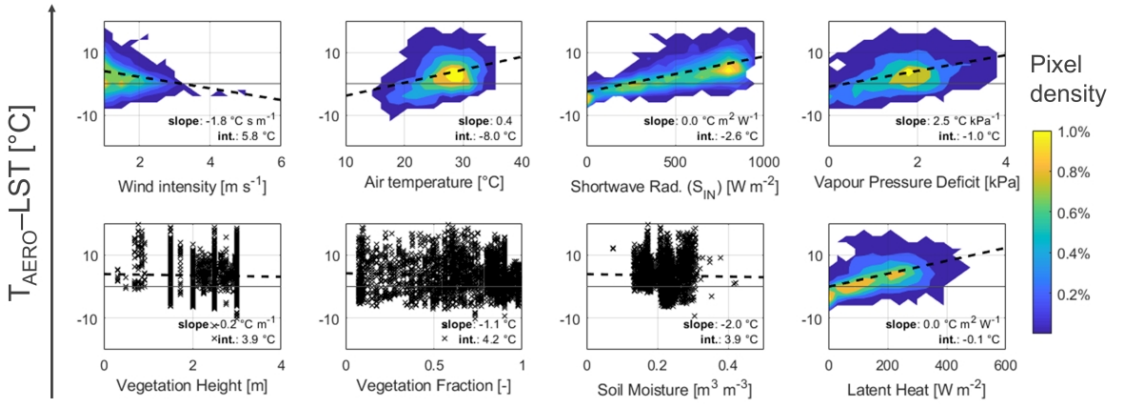

Figure 8.4: Temperature divergence v. environmental parameters, data from the Montichiari (MON) EC tower.

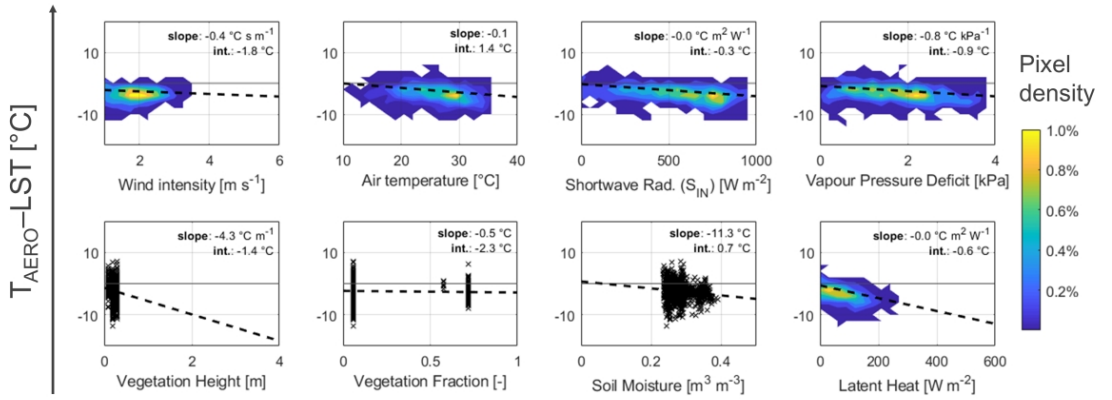

Figure 8.5: Temperature divergence v. environmental parameters, data from the Foggia-Incoronata (FIN) EC tower.

low incidence of non-meteorological variables is confirmed across all case studies, with the highest R^2 reached by Livraga at a mere 0.04. S_{IN} is confirmed as an important variable by another high R^2 value (0.46 in Foggia-Incoronata), although it seems less relevant in for Livraga and Foggia-Onoranza (0.11 and 0.13, respectively) and practically immaterial in Landriano (<0.01). Latent Heat also demonstrates a certain relevance, with a peak R^2 value of 0.61 for Foggia-Onoranza and high values in both Montichiari and Foggia-Incoronata. Generally, a trend can be identified for the southern, more arid, tomato-related case study: wind effect seems negligible (although wind intensities here are much higher than in the north of Italy), while air temperature, S_{IN} and VPD all seem to play an important role. The three northern case studies, on the other hand, show a sketchier scenario, with a uniformity of behaviour shown only in the dependency on wind intensity.

Table 8.2: Correlation statistics between temperature divergences and environmental parameters

	MON	LAN	LIV	FIN	FON
Wind Intensity	0.04	0.05	0.05	<0.01	0.01
Air Temperature	0.12	0.02	<0.01	0.07	0.07
S_{IN}	0.47	<0.01	0.11	0.46	0.13
VPD	0.18	0.05	<0.01	0.08	0.09
Vegetation Height	<0.01	<0.01	0.03	<0.01	0.01
Vegetation Fraction	<0.01	<0.01	0.04	<0.01	<0.01
Soil Moisture	<0.01	<0.01	<0.01	0.02	0.02
Latent Heat	0.25	0.06	<0.01	0.22	0.61

As a final comparison, the seasonal average temperature divergences for all case studies have been contrasted with each season Aridity Index (AI). This parameter is defined as the ratio of rainfall (P) to (potential) Evapotranspiration (PET), and is commonly used to evaluate natural water budget. The comparison is shown in the left-hand plot of Figure 8.6. A certain alignment is visible across the different AIs spanned by the case studies, which results further enhanced if only daytime (close to midday) temperature divergences are factored in the comparison (right-hand plot). It is also interesting to identify the area around which the temperature divergence shifts sign: the 0.4–0.45 range is strikingly close to 0.5, he threshold AI value conventionally assumed to distinguish semi-arid from dry subhumid areas.

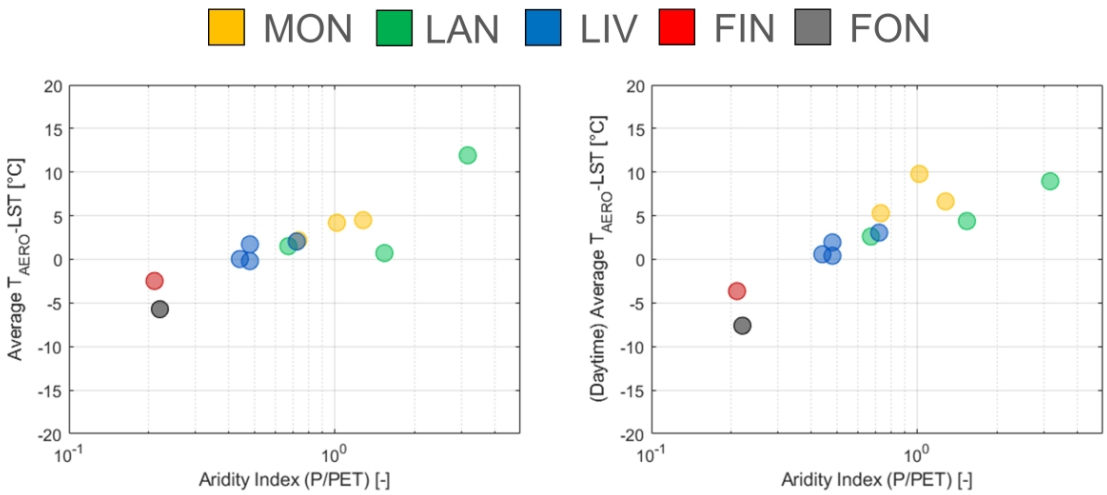

Figure 8.6: Seasonal temperature divergence v. Aridity Index

8.4 Integrating T_{AERO} into hydrological modelling

In a first instance, the integration of T_{AERO} within FEST-EWB requires a deliberately excessive assumption. In the two tentative models that have been developed (Section 2.6.2), T_{AERO} (com-

puted in Section 8.2) was used by the model as an input variable, when available. Obviously, these models represent some kind of "theoretically optimal frontier", representing a perfect Sensible Heat modelling result, and have been developed to identify the consequences of a flawless T_{AERO} integration into the model over Latent Heat. This helps to set a boundary within which the final version of the model enclosing T_{AERO} is expected to perform. The two models have been tested over the Montichiari case study together with the classical FEST-EWB model, for the three-year period of available data (2016 through 2018).

The modelling findings are shown in Figure 8.7, where the scatterplots for the three major energetical fluxes are shown for the three modelling approaches. All compared data are related to the instances in which T_{AERO} measurements are available and thus can be injected in the two new models. In the first column, the Sensible Heat data is shown. By construction, the two T_{AERO}-acquiring models show a perfect interpretation of the flux, so that these first plots only serve to show the general interpretation of the flux in LST-dependent formulations. Latent Heat data (middle row) show a quite dispersed distribution from the Test Model 2, while both the Test Model 1 and the classical FEST-EWB seem to provide good representations of the measured flux. Finally, Net Radiation data (right-hand column) show a minor dispersion of the Test Model 2 data and, generally, a similar clustering of all three models.

The results are recapped in the simplified form of Taylor plots in Figure 8.8, for Latent Heat and Net Radiation alone. The more erratic distributions from Test Model 2 are quite evident here, and non-negligible although minor improvements can be seen between the classical FEST-EWB model and the Test Model 1. The first finding can be related to theoretical reasons: excluding the atmospheric boundary conditions from the Latent Heat formulation – as is done with the Test Model 2 formulation – can deprive it of a crucial component to the overall flux. From the second result, it can be gathered that a model continuously simulating T_{AERO} and employing it in Sensible Heat computation would provide performances somewhere in between those from the classical, LST-driven formulation and those from the theoretical Sensible Heat perfection.

The same analysis has been performed over year 2016 over the Foggia datasets, with the results from the Incoronata (FIN) and Onoranza (FON) data provided in Figure 8.9. Again, in both scenarios the Test Model 1 provides better estimates of Latent Heat than the Test Model 2, while both are equally efficient in simulating the Net Radiation. The aggregated Taylor plot results (Fig. 8.10) are on the same line as those from the Montichiari case study (Fig. 8.8), although the improvement in Latent Heat estimation can here be appreciated in a much clearer way.

8.5 Parametrizing T_{AERO}

Creating a stable link with LST would enable the aerodynamic temperature to be simulated continuously within FEST-EWB framework. Following in the footsteps of Kustas et al. (2007) and Mahrt and Vickers (2004), in this section the possibility to parametrize T_{AERO} is explored. The empirical relations to be tested have been detailed in Section 2.6.3. Two distinct analyses were performed for the northern Italy and southern Italy case studies, provided their differences both in crop and climate.

8.5.1 Maize case studies

The results for the maize case studies are detailed in Figure 8.11. In the first panel (Fig. 8.11a), the parameter optimization for the Standard Parametrization Formula (SPF) is performed, with the

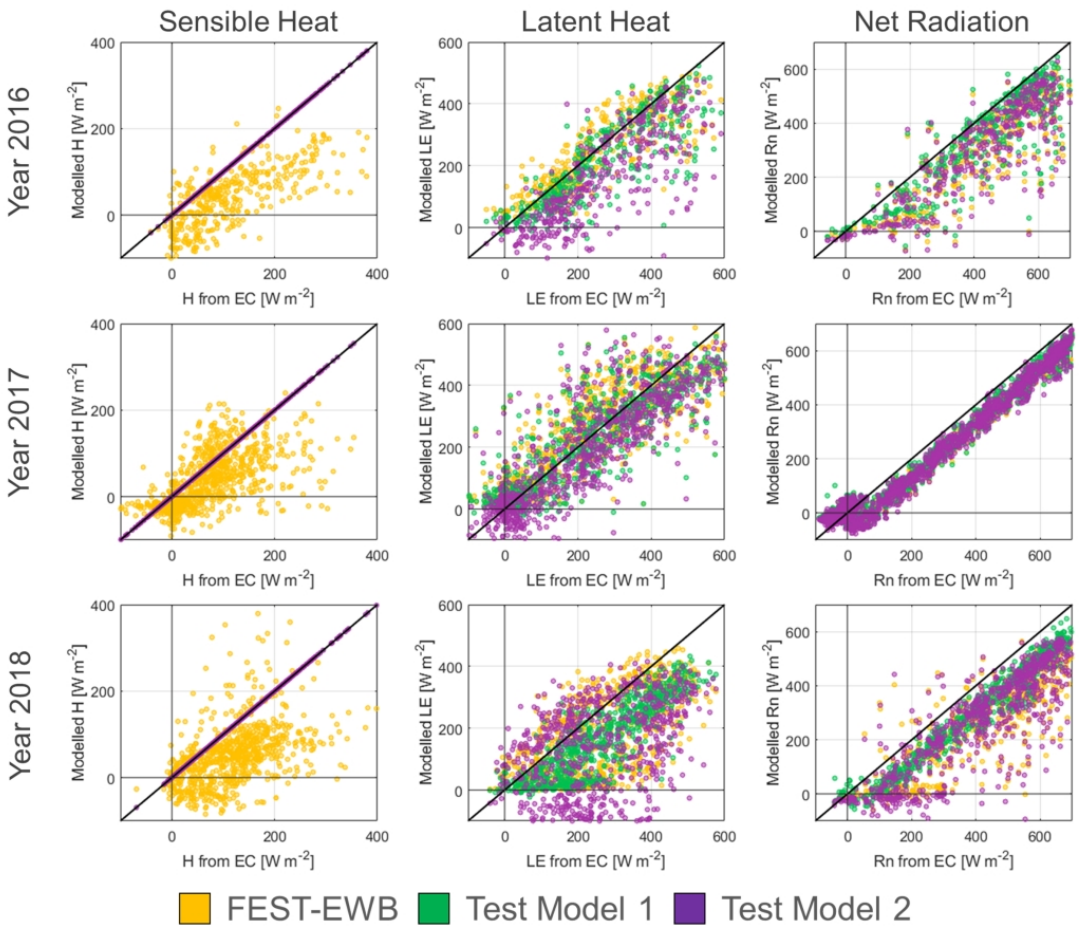

Figure 8.7: Model performances from classic FEST-EWB, Test Model 1 and 2 in terms of Sensible (left-hand column) and Latent (middle column) Heats and Net Radiation (right-hand column). Years 2016–2018 arranged along the rows.

resulting scatterplots for the three different datasets, with further statistical information provided in the following Table 8.3. The data dispersion is small for both Landriano and Livraga (R^2>0.65), but not so much for Montichiari (R^2=0.26) which also has the lowest slope (0.3).

An important observation relates to the C coefficient, which was estimated by both Kustas (arid shrubland) and Mahrt (boreal forest) as quite constant at the value of 0.0087 K m^2 W^{-1}. In these cases, it varies slightly among the datasets but generally is much lower. Similarly, the C_S parameter results quite high with respect to the average proposed by Kustas (850 W m^{-2}), but generally does not make much of a difference at the low C values for which the error is minimized. An insight into the error optimization varying both the C and C_S parameters is provided by Figure 8.12, where the RMSD error between SPF-T_{AERO} and indirectly-measured-T_{AERO} is mapped for all the maize case studies. A positive result is that the global shape of the RMSD dominion is similar across all

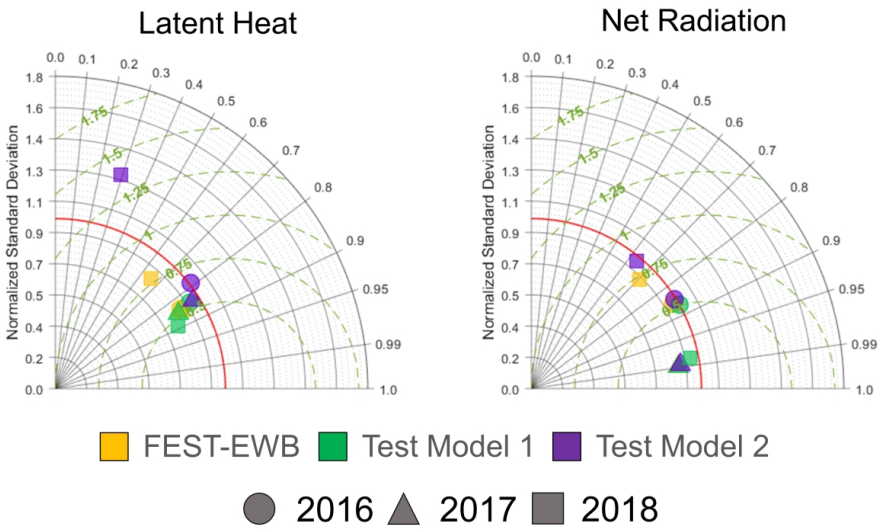

Figure 8.8: Taylor plots for Latent Heat (a) and Net Radiation (b) modelling for the MON data.

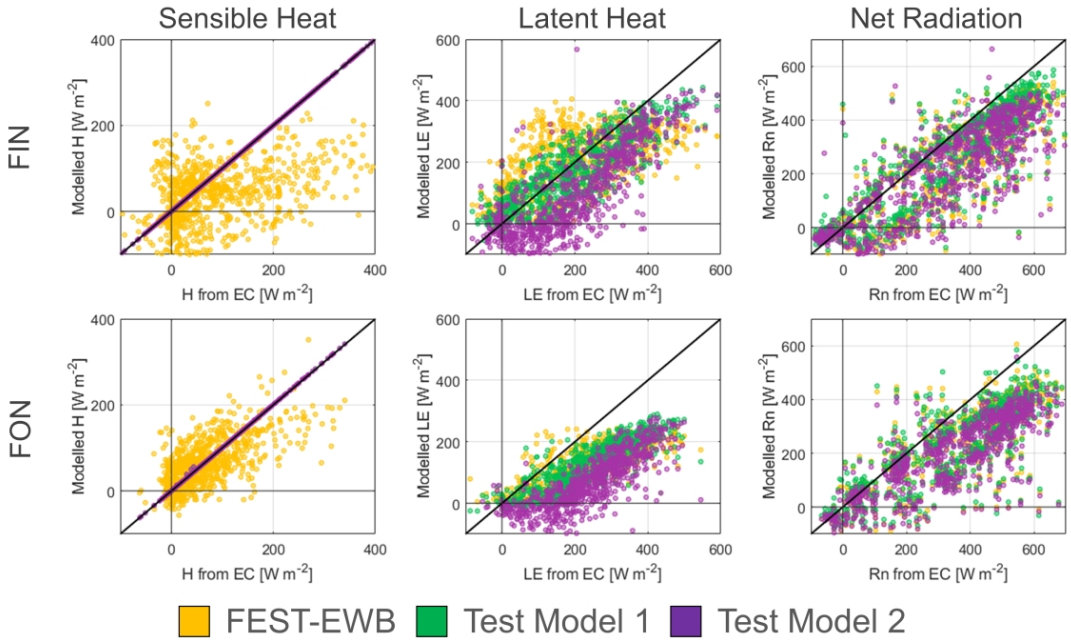

Figure 8.9: Model performances from classic FEST-EWB, Test Model 1 and 2 in terms of Sensible (left-hand column) and Latent (middle column) Heats and Net Radiation (right-hand column). FIN and FON data arranged along the rows.

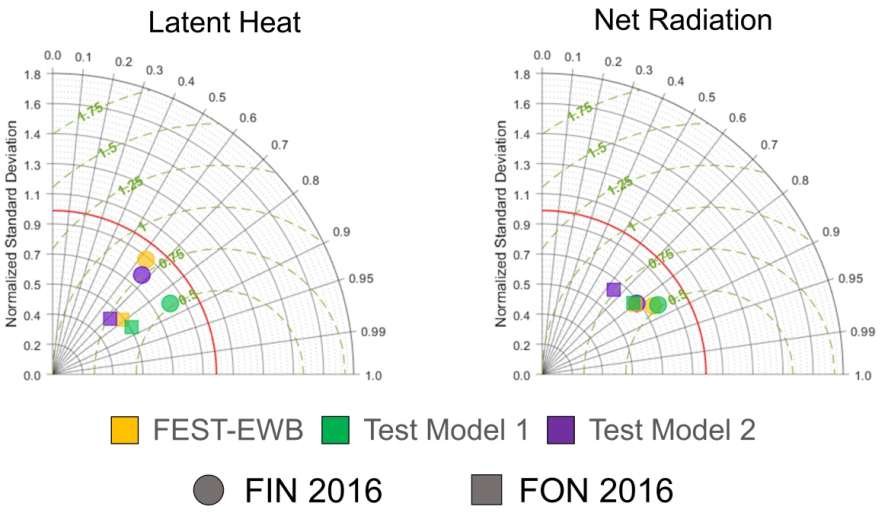

Figure 8.10: Taylor plots for Latent Heat (a) and Net Radiation (b) modelling for the FIN and FON data.

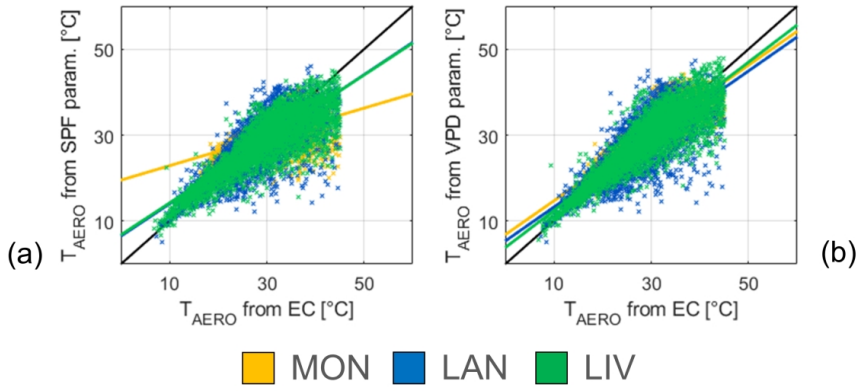

Figure 8.11: Aerodynamic Temperature parametrization with SPF (a) and VPD (b) for the MON, LAN and LIV case studies.

case studies, even though these are not very close to each other (Livraga and Landriano are 30 km apart, while Montichiari is around 80 km far from Livraga). This suggests that crop and climate factors are the main factors defining T_{AERO}.

Figure 8.11b, together with the statistical recap in the right-hand part of Table 8.3, detail the parametrization optimization for the VPD formulation. In this case, the C value increases, getting closer to Kustas' own constant, while the C_S is critically lower (as low as 0 for Landriano), suggesting a minor role of LAI in this new configuration. The VPD weight (α) provides mixed results, being both positive and negative among the three test cases. However, it generally seems

Table 8.3: Parametrization coefficients and statistics for the maize case studies

		SPF			VPD		
		MON	LAN	LIV	MON	LAN	LIV
Params.	C [°C m^2 W^{-1}]	0.0023	0.0005	0.0005	0.0122	0.0046	0.0054
	C_S [W m^{-2}]	1000	1000	1000	200	0	80
	α	n/a	n/a	n/a	-0.25	1	0.75
Stats.	Sample	3932	6482	9060	3932	6482	9060
	ρ	0.51	0.80	0.89	0.85	0.82	0.91
	R^2	0.26	0.65	0.78	0.71	0.66	0.84
	Slope	0.3	0.8	0.7	0.8	0.8	0.9
	Intercept [°C]	19.5	6.5	6.8	6.8	5.4	3.8
	RMSD [°C]	5.24	3.96	3.38	3.08	3.91	2.90

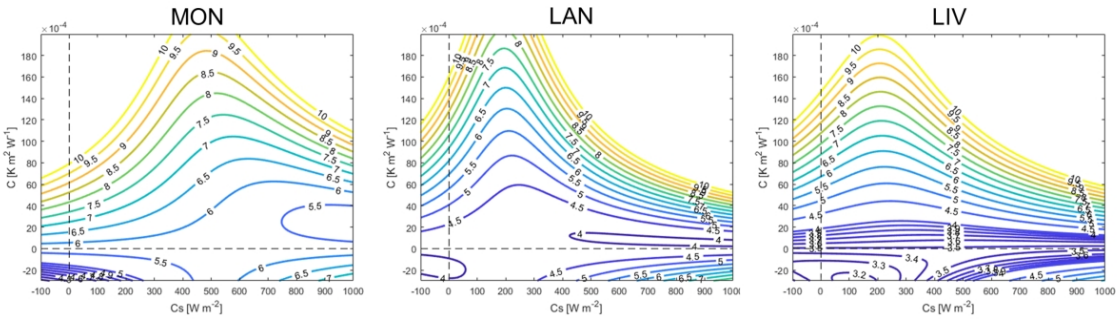

Figure 8.12: SPF parametrization RMSD isolines for varying C and C_S values for the MON (a), LAN (b) and LIV (c) data.

to have an important role in T_{AERO} parametrization. In Figure 8.13, the same plots as in Figure 8.12 are provided, except that the three degrees of freedom in this analysis and the bidimensional possibilities of paper printing require that only two out of three parameters can be shown in full. Two representative C_S values have been chosen (200 W m^{-2} and 850 W m^{-2}) to show the parametrization RMSD variability with C and α. For any given value of C_S, low errors seem to be associated with close-to-zero values of α, which yields the optimization triplets shown in Table 8.3.

Finally, the last rows of Table 8.4 provide an useful information in terms of validation of the present parameter sets. In these rows, for any given formula, the RMSD over each dataset is provided when employing that formula with the parameters calibrated over another dataset. The parameter similarities between Landriano and Livraga mean that the error increase when adopting the other datasets parameters is small, while the differences between Montichiari and the other two (in particular with the VPD formulation) mean that a bigger error would be registered over that dataset. Generally, it seems that the SPF formula is able to identify quite stable parameters across all the case studies, but the VPD formula, although more site-specific, achieves much lower errors.

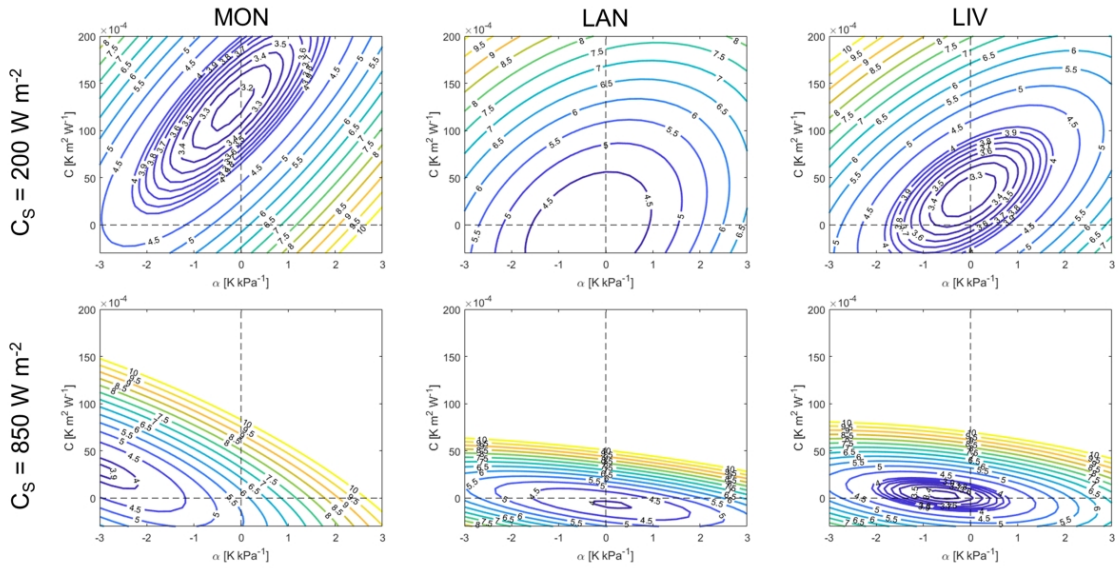

Figure 8.13: VPD parametrization RMSD isolines for varying C and α values for the MON (left-hand column), LAN (middle column) and LIV (right-hand column) data. Ancillary C_S values associated to each row.

Table 8.4: Dataset parametrizations validation (maize)

		Standard formula			VPD formula		
		Using parameters from...					
		MON	LAN	LIV	CHI	LAN	LIV
Error	MON	3.08	4.93	4.93	5.24	5.54	5.54
on	LAN	5.88	3.91	4.06	5.27	3.96	3.96
dataset...	LIV	4.84	2.97	2.90	4.94	3.38	3.38

8.5.2 Tomato case studies

The same analysis as above is replicated over the Foggia-Incoronata and Foggia-Onoranza data from the corresponding tomato fields in the Capitanata Irrigation Consortium. Figure Ta displays the scatterplots relative to the calibration of the SPF, with the relative information summed up in the first part of Table 8.5. For these case studies, the parameter calibration has provided null C_S values for the SPF, suggesting a negligible if not totally ineffective impact of LAI over the temperature difference, and (almost) null C values for the VPD, meaning that aerodynamic temperature, parametrized with the VPD formulation constraints, is less influenced by both incoming radiation and LAI with respect to VPD. In this case, the main take-away is that the VPD formulation does not improve on SPF results, as witnessed by the higher RMSD values (+0.77°C for FIN and +0.09°C for FON), whereas, for the maize case studies (Table 8.3), the novel formulation improved the RMSD across all sites.

Further information on the SPF calibration is provided by the following Figure 8.15, where the

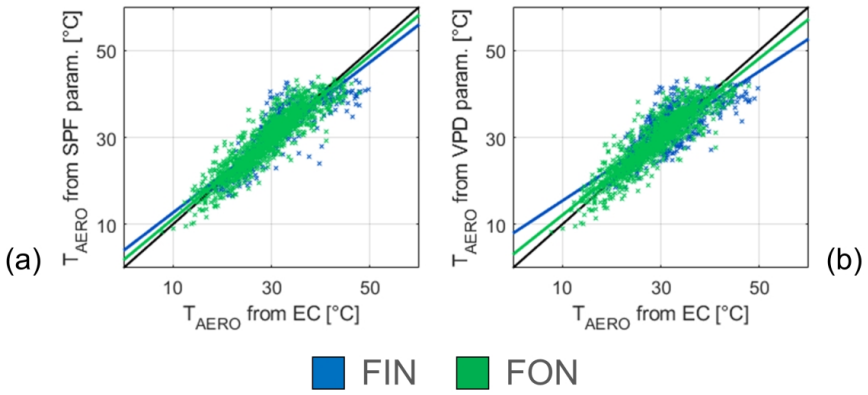

Figure 8.14: Aerodynamic temperature parametrization with SPF (a) and VPD (b) for FIN and FON data.

Table 8.5: Parametrization coefficients and statistics for the tomato case studies

		SPF		VPD		VPD*	
		FIN	FON	FIN	FON	FIN	FON
Params.	C [°C m^2 W^{-1}]	0.0102	0.0043	0.0002	0.0000	-0.0095	0.0035
	C_S [W m^{-2}]	0	0	5000	703	0	0
	α [°C kPa^{-1}]	n/a	n/a	+1.58	+1.19	+0.25	+0.25
Statistics	Sample	726	1623	726	1623	726	1623
	ρ	0.87	0.91	0.79	0.91	0.87	0.91
	R^2	0.77	0.84	0.63	0.82	0.76	0.84
	Slope	0.9	0.9	0.7	0.9	0.8	0.9
	Intercept [°C]	4.0	1.8	7.9	3.1	4.6	2.1
	RMSD [°C]	2.99	2.51	3.76	2.60	2.99	2.49

RMSD mapping is provided for a wide range of C–C_S couples. Low points in error evaluation can be found generally around the C_S=0 vertical line, with optimal values potentially in the negative C_S region, bet generally with low values of the parameter, confirming the lesser importance of LAI in this case study.

In the Figure 8.14b and in the second part of Table 8.5 the parameters and statistics for the VPD formula calibration are shown. In both, the particularly low values for the optimal C coefficient, as opposed to the non-negligible α, suggest that the influence of both incoming radiation and LAI is quite lower than that of VPD. However, one main result is that the inversion of the sign for the C coefficient and the introduction of VPD do not improve the error estimates from the SPF. Instead, moderate increases in RMSD are registered both for Incoronata (+0.77°C) and Onoranza (+0.09°C) data, while for the maize case studies (Table 8.3) the novel formulation had improved the RMSD across all sites. A modified VPD formulation is tested (named "VPD*"), allowing negative values of the C coefficient (alike to the SPF) but adding the VPD parameter. The results, shown in the third part of Table 8.5, identify performances equal to SPF for Foggia-Incoronata and only slightly better

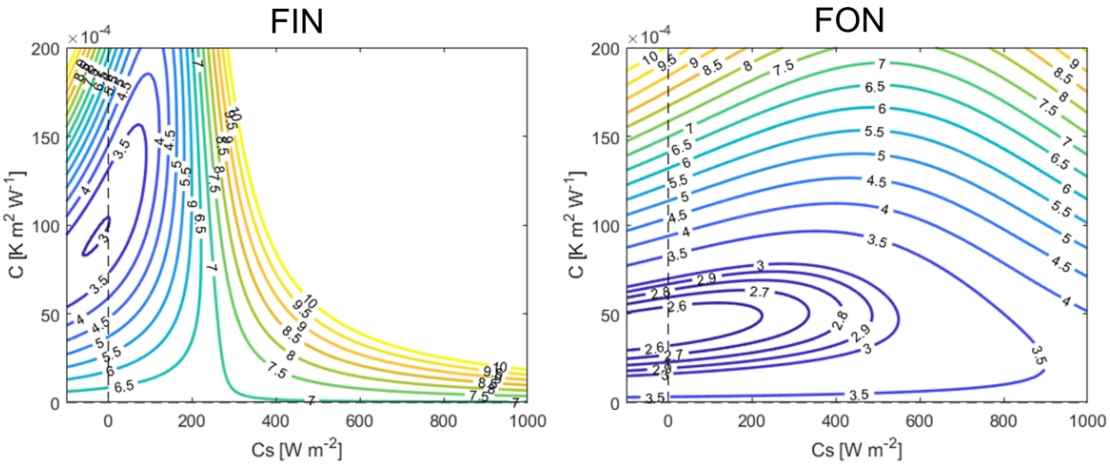

Figure 8.15: SFP parametrization RMSD isolines for varying C and C_S values for the FIN (a) and FON (b) data.

for Foggia-Onoranza (-0.02°C). Overall, this suggests that, for these cases studies, solar radiation is the main parameter that determines aerodynamic temperature divergence from the radiometric. In a form akin to that of Figure 8.13, the RMSD distribution for the VPD formulation, across different values of α and C, is mapped for two reference values of the C_S coefficient (200 and 850 W m^{-2}) in Figure 8.16. The original VPD formulation is generally referred to the C¿0 semi-space, while the modified version (VPD*) encompasses also the negative C values.

8.6 Aerodynamic Temperature continuous modelling

In this final section, a continuous FEST-EWB modelling of aerodynamic temperature has been enforced, employing the VPD parametrization validated in the previous section. The results have been compared with both the classical FEST-EWB model and the Test Model 1, the "theoretical optimum" model from Section 2.6.2, for both maize (Montichiari) and tomato (Foggia-Incoronata and Foggia-Onoranza) case studies. The Test Model 2 has been discarded from the comparison, given its lower-quality results.

8.6.1 Maize case study

Embedding the VPD parametrization (Eq. 2.46) full-time within the FEST-EWB model, the aerodynamic temperature is simulated based on the model's own RET, as opposed to the "optimal" case seen before with the actual radiometric temperature (Fig. 8.11). To provide a complete insight, the modelled aerodynamic temperature is contrasted with its indirectly-measured counterpart in Figure 8.17. Comparing this result with the original FEST-EWB model, T_{RAD}-based parametrizations in Figure 8.11, the main take-away is that, after modelling, a good parametrization is retained, with a close-to-unity interpolation slope and a modest increase in RMSD.

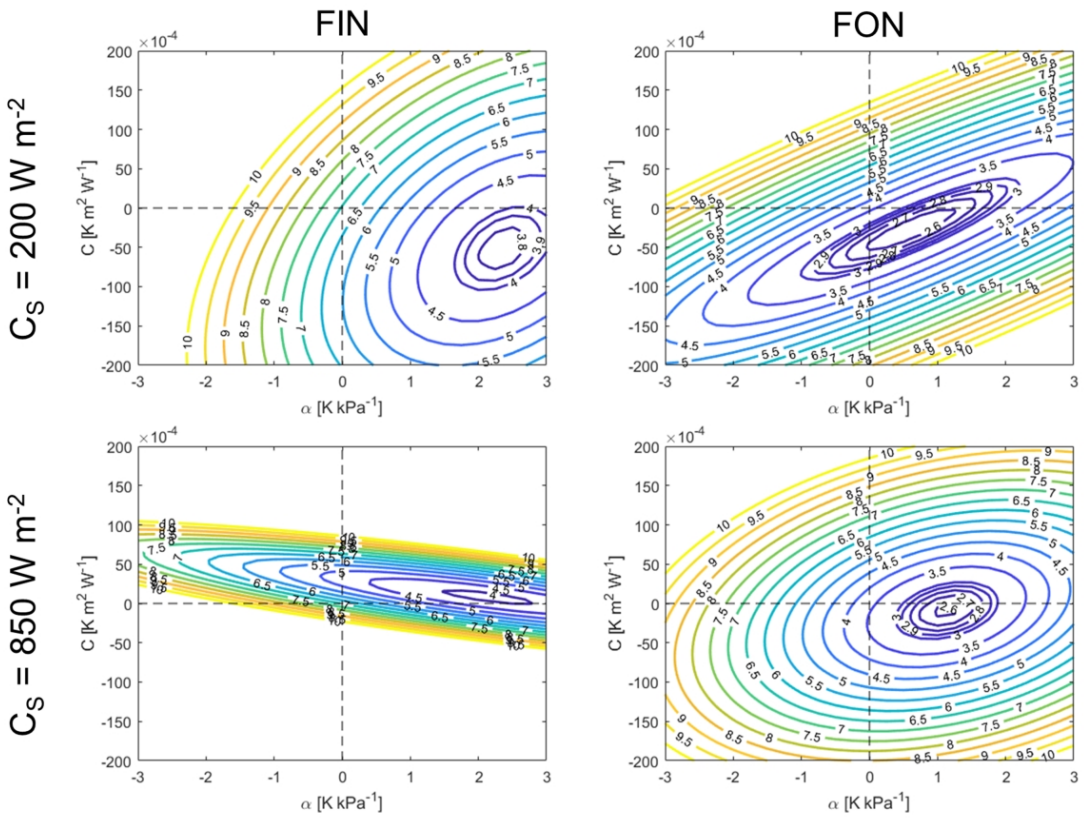

Figure 8.16: VPD parametrization RMSD isolines for varying C and α values for the FIN (left-hand column) and FON (right-hand column) data. Ancillary C_S values associated to each row.

The modelled turbulent fluxes are shown in Figure 8.18. In Sensible Heat modelling, the T$_{\text{AERO}}$-integrated FEST-EWB improves the estimates from the parent model, with higher interpolation slopes (on average over the three years, 0.48 for classic FEST-EWB and 0.75 for FEST-AeroT) and R^2 values (0.37 and 0.40, respectively). Latent Heat modelling shows quite close results across all three models, both in terms of slope (on average, 0.68 for FEST-EWB, 0.74 for Test Model 1 And 0.57 for FEST-AeroT) and RMSE (respectively 85.7 W m^{-2}, 72.5 W m^{-2} and 71.4 W m^{-2}). Finally, little to no difference is detectable at Net Radiation level, as testified by the global Taylor plots provided in Figure 8.19.

8.6.2 Tomato case studies

The same procedure as in the previous section is replicated over the Foggia-Incoronata and Foggia-Onoranza case studies. In this case, provided the analyses shown in Section 8.5.2, the SPF is chosen for the continuous simulation instead of the VPD parametrization, as it guarantees lower errors on measured Land Surface Temperature. The temperature comparison with the modelled Representative Equilibrium Temperature is provided in Figure 8.20. For the Montichiari case study,

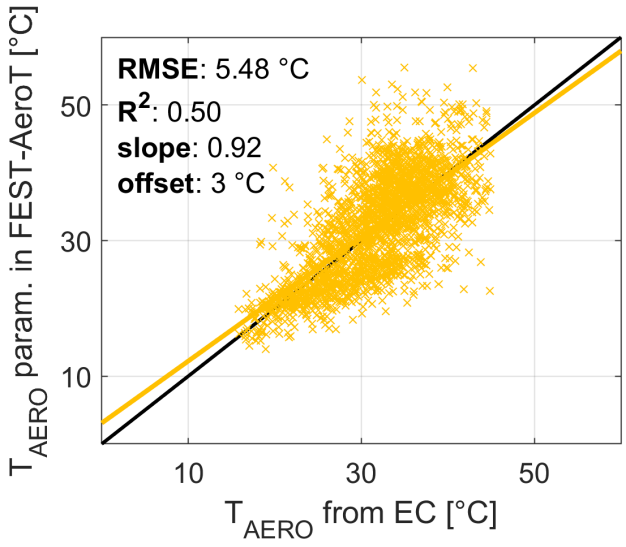

Figure 8.17: Aerodynamic temperature parametrization with RET (MON)

a worsening of +2.4°C in terms of RMSD was recorded after model application (Fig. 8.17), whereas in this scenario worse adaptations are registered (+3.5°C for the Foggia-Incoronata case and +4.3°C for the Foggia-Onoranza one, as opposed to the T_{RAD}-computed RMSD).

In Figure 8.21, the comparison of the modelled fluxes is provided for both tomato cases. Generally, FON result (lower row) seem better than their FIN counterpart (higher row), with close similarities both to the original FEST-EWB simulations and the Test Model 1 including the measured T_{AERO}. In particular, the T_{AERO} underestimation seen in Figure 8.20a could be strictly linked with these worse results, especially for the Sensible Heat ones (Fig. 8.21a) as T_{AERO} values lower than Air Temperature can cause the many negative Sensible Heat values. It is particularly worth noticing how these uncertainties would have been quite unexpected if one were to look only at the *a priori* parametrization calibration, where the FIN data had performed quite positively (Fig. 8.20a), with no underestimation to be detected and a contained global RMSD (2.99°C). FON data, on the other hand, offer a globally positive parametrization and model performance, with good estimations. The Taylor plots (Fig. 8.22) sum up the models performance, highlighting the mixed results over the FIN case study and the better ones on the FON data.

8.7 Final take-aways

This chapter has detailed the findings obtained in the exploration of the aerodynamic temperature and its possible role in hydrological modelling. The main objective has been a full-time integration of this parameter in the FEST-EWB model, where its bearing on the improvement of Latent Heat estimation could be tested in a setting preserving SM dynamics and able to work even in absence of satellite information of LST. In order to achieve this, successive steps have been taken, analysing the reliability of T_{AERO} estimates, its dependency on boundary parameters, its raw impact on Latent Heat estimates in modelling and a possible parametrization on LST for continuous estimation.

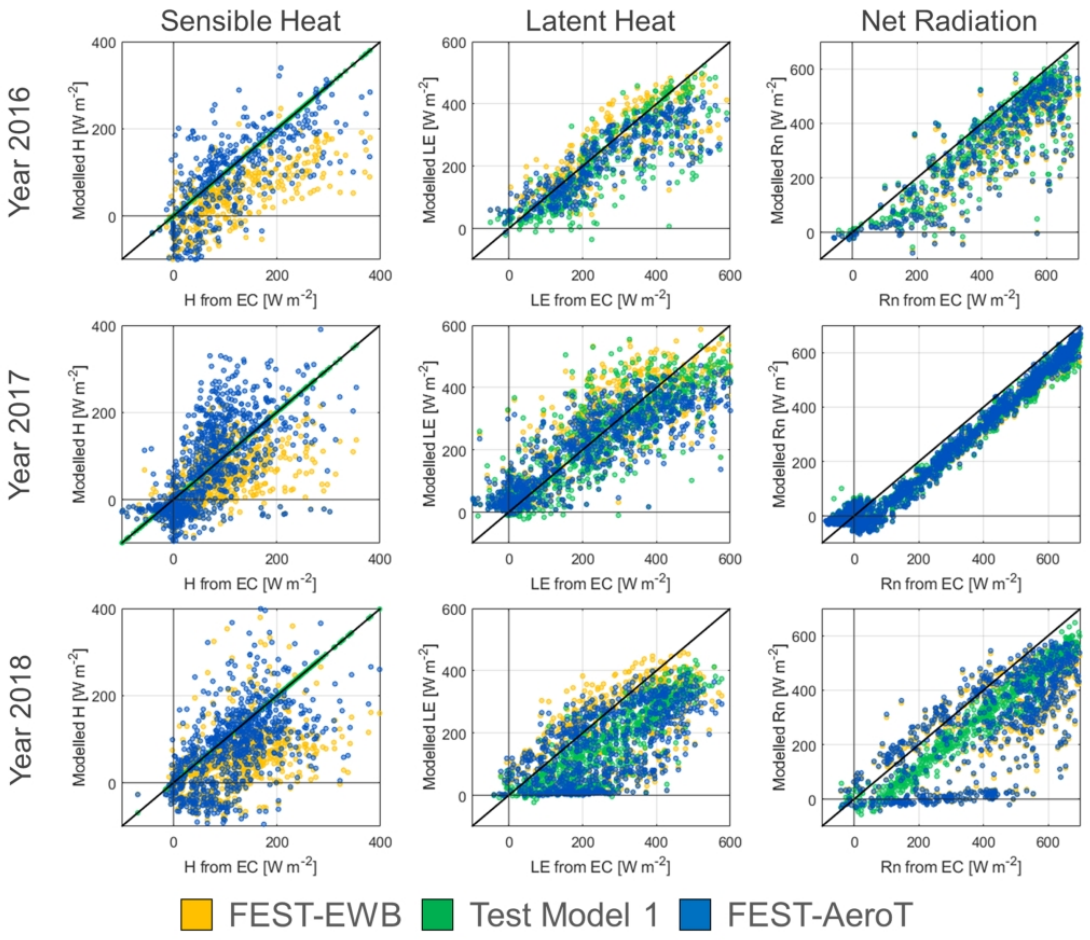

Figure 8.18: Model performances from classic FEST-EWB, Test Model 1 and FEST-AeroT in terms of Sensible (left-hand column) and Latent (middle column) Heats and Net Radiation (right-hand column). Years 2016–2018 arranged along the rows.

In a first part, the retrieval complexity of this parameter is explored by showing how many different possible values can be obtained in the same boundary conditions from different parametrizations of the aerodynamic resistance. The obtained results are quite compatible with those from similar studies (S. Liu et al., 2007): although some coarse groups can be traced across the various parametrizations, a considerable variety is detected among the resistances. This allows to detail how ephemeral and leaden with uncertainty the T_{AERO} physical variable is. Across the analysed case studies, similar general trends of the T_{AERO}-LST comparison could be detected when preserving the general boundary conditions (climate and crop), although the specific temperature distributions result not too similar. When analysing the Capitanata data, relative to an arid climate and a tomato crop, the general trend seemed to shift towards an underlying T_{AERO} underestimation of LST, suggesting that coarse climatic drivers may be one major factor in impacting the T_{AERO}-LST

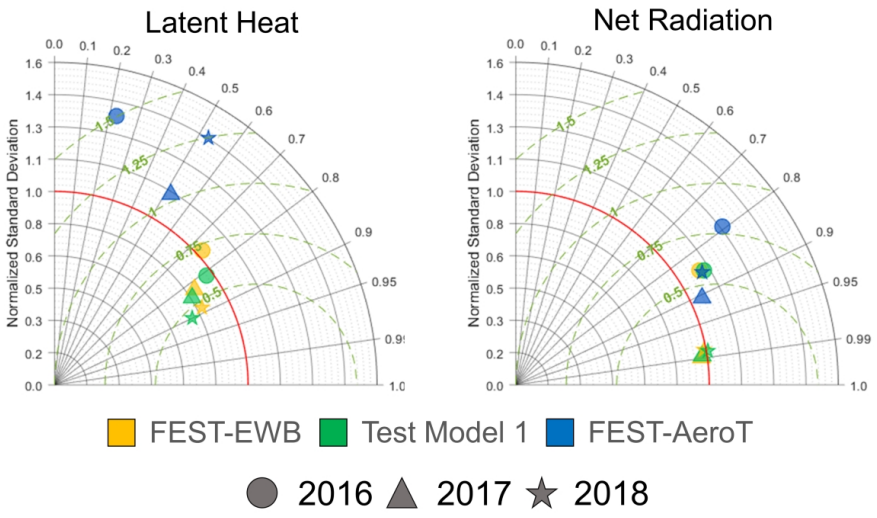

Figure 8.19: Taylor plots for Latent Heat (a) and Net Radiation (b) modelling for the MON data.

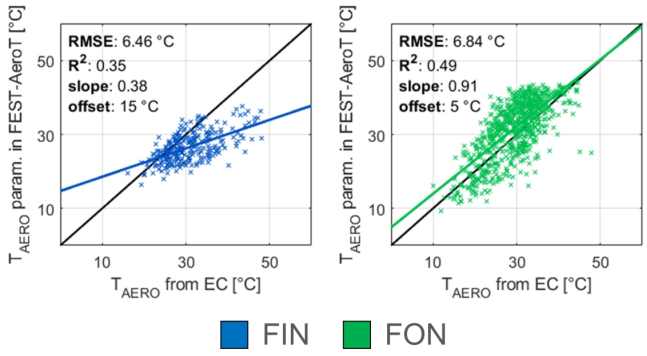

Figure 8.20: Aerodynamic temperature parametrization with RET (FIN and FON)

temperature divergence. This is consistent with the findings from Kustas et al. (2007), which analysed data from an arid shrubland and found radiometric temperatures progressively higher than their aerodynamic counterparts with increasing solar radiation and soil aridity. The temperature divergence range they computed sometimes exceeds 10-15°C, which is consistent with our results in comparable environmental conditions. These results are also consistent with the high divergences found by Chehbouni et al. (1996) and by Sun et al. (1999). The maize datasets, on the other hand, placed in a cooler climate and with abundance of water, showed results much more similar to those of Mahrt and Vickers (2004), who obtained more uncertain temperature divergences (oscillating some degrees around 0°C) in a boreal forest setting.

The theme of the environmental factors affecting the temperature divergence has been explored further in a sensitivity analysis, conducted by factoring in different bio-meteorological indicators.

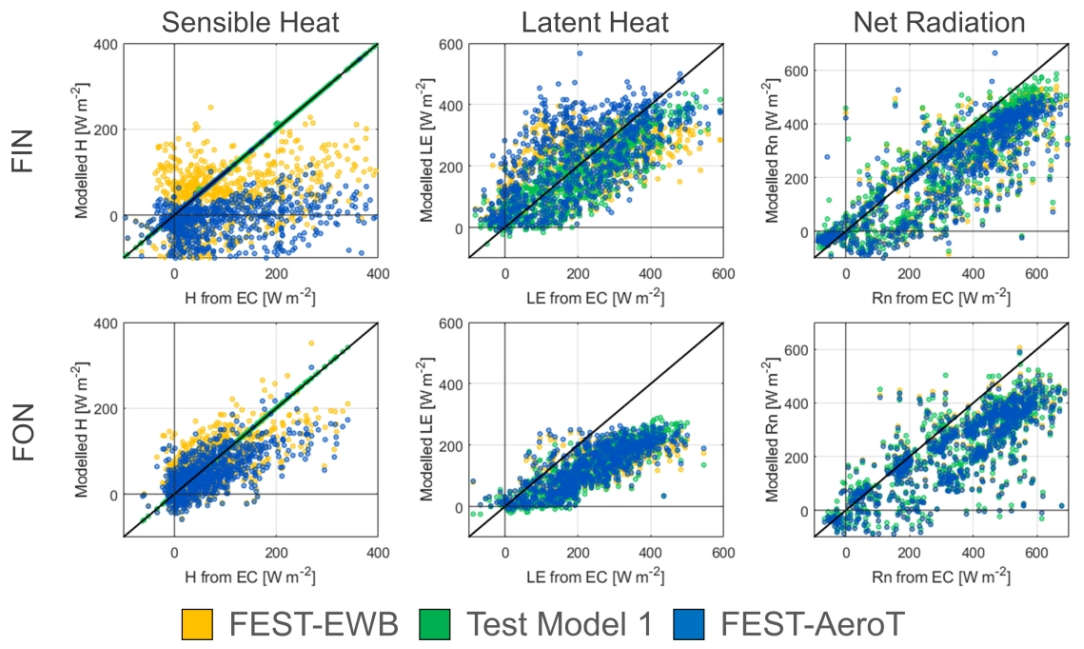

Figure 8.21: Model performances from classic FEST-EWB, Test Model 1 and FEST-AeroT in terms of Sensible (left-hand column) and Latent (middle column) Heats and Net Radiation (right-hand column). Data from the FIN and FON test cases arranged with the rows

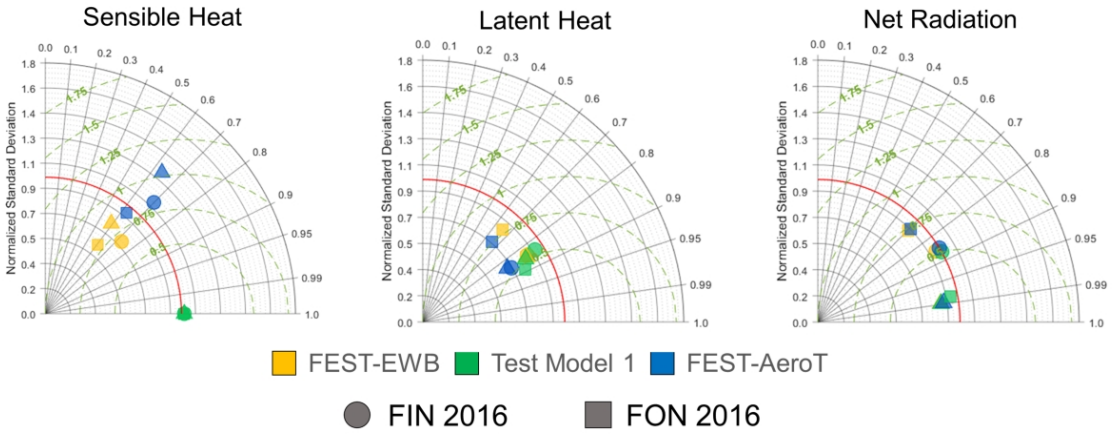

Figure 8.22: Taylor plots for Sensible (a) and Latent (b) Heats and Net Radiation (c), modelled for the FIN and FON data

Some of them (incoming shortwave solar radiation and, in general, meteorological parameters) were found to possess some kind of influence over the divergence, while others (mostly vegetation

parameters) had practically no influence at all. The results are again quite consistent with those of Kustas (2007), who conducted a similar analysis. On the other hand, Mahrt and Vickers (2004) found a potentially non-influent role of soil moisture over temperature divergence. The results obtained for the Capitanata case studies, showing some connection with the soil moisture state, as opposed to those obtained in the Northern Italy maize case studies (which share their non-arid environment with Mahrt and Vickers' dataset), suggest that Soil Moisture may play a role only for water-limited scenarios.

In the second part, the aerodynamic temperature is integrated into FEST-EWB hydrological modelling. Firstly, T_{AERO} data were acquired, when available, into the model realizing a perfect "simulation" of the Sensible Heat. This had the target of setting a sort of "theoretical frontier", representing the possible gains associated with a perfect model result. While Net Radiation estimation was substantially stable, Latent Heat estimation showed some improvements from the simple FEST-EWB model, in particular in the arid Capitanata scenario. Among a model employing T_{AERO} only in Sensible Heat and another explicating also its role in Latent Heat, the latter showed far worse results than the former, probably due to the exclusion of atmospheric boundary conditions in the Latent Heat formulation, necessary to highlight the role of T_{AERO}. At this point, two possible parametrizations have been analysed, in order to firmly link T_{AERO} with the surface temperature and use it continuously during model runs. The use of these parametrizations into the model provided an autonomous new model, FEST-AeroT, able to simulate T_{AERO} at all times. Results were generally mixed, on both the maize and tomato data. Minor improvements were detected in terms of Sensible Heat, with respect to the classic FEST-EWB simulations, whereas more detectable improvements were found in the Montichiari case study for Latent Heat, with opposing performances over the two Capitanata sites. No major differences were overall detected for Net Radiation. These findings are only partially similar to those of Chávez and Neale, 2003, who found that the use of radiometric instead of aerodynamic temperature in Sensible Heat modelling generated a direct estimation error of -17%±50%. They also found that this error could propagate into Latent Heat modelling to an estimation error of +6.4%±30%, which could influence heavily the computed ET. However, in a successive study (Chávez et al., 2010), they found much more lenient estimation errors (+2.8%±6.5% for Sensible Heat and +1%3% for Latent Heat) much more in line with the results here detailed. This adds to the incredible performance variability of models incorporating T_{AERO}, already shown across all this Chapter. Another interesting work by Colaizzi et al. (2004) shows results coming from lysimeter-weighed alfalfa, cotton and sorghum, retrieving similar adaptation statistics to those obtained in this Chapter.

Overall, although the T_{AERO}-LST divergence is measurably non-negligible, the dynamics and determinants at the heart of it remain unclear, without any one definite behaviour across different case studies. This level of uncertainty is probably one reason why plugging T_{AERO} in well-established hydrological modelling structures such as FEST-EWB produces mixed results, with no clear and major improvement in energy fluxes estimation.

Part IV

Final conclusions

Chapter 9

Conclusions

THE object of this thesis work has been the improvement of satellite-based hydrological modelling in agricultural applications. This has been done through a series of activities, covering a wide variety of inter-connected themes all linked to spatial heterogeneity and data source multiplicity: (i) physical consistency of satellite observations of Surface Soil Moisture (SSM) with observed rainfall and irrigation inputs; (ii) suitability of high-density sensor networks against operative satellite data; (iii) the impact of spatial resolution over a model's performance in a heterogeneous context; (iv) the possibility to sharpen hydrological modelling by enriching the modelling of heterogeneous scenarios; (v) questioning the validity of a common modelling assumption for evapotranspiration modelling. The following conclusions are a summary of those presented at the end of Chapters 4 through 8.

9.1 Hydrological consistency of coarse-resolution satellite SSM

In Chapter 4, the **consistency analysis of satellite SSM datasets** was performed, starting from the necessity of employing them in agricultural applications, such as irrigation scheduling. Are they truly reliable? In order to answer this question, on-ground precipitation and irrigation observations have been contrasted with 9 different satellite datasets, ranging in terms of spatial resolution, source and baseline assumptions, developing a hydrological consistency algorithm. The algorithm is able to count how many times satellite SSM retrievals are consistent with the knowledge of water inputs in the area, be them natural precipitation or artificial irrigation. The results are quite underwhelming, with most datasets providing physically consistent SSM information barely 60% of the time. This finding is not altogether new in the scientific literature, although in this thesis it has been complemented with other information. Performances are generally better during the irrigation season, when factoring in the artificial inputs allows to explain more of the satellite SSM variability. This may suggest that untraced irrigation volumes in the (officially) non-irrigation period play a major role in SSM distribution. Retrieval technology seems to play a role in dataset performance, with new-generation L-band products (barely influenced by vegetation and able to penetrate deeper into the soil than older C-band products) providing the best results. Surprisingly, spatial resolution does not seem to be a factor, at least at the coarse resolutions available at the moment (ranging from 1 km up to 40 km), and the same holds for the year-round rainfall depth. Finally, datasets with higher data density are associated with a more stable outcome, although not necessarily a better one. Overall, the main finding is that no soil moisture product among the

tested ones shows a systematic and definitive hydrological coherence with the rainfall and irrigation data.

9.2 Dense ground sensor network accuracy against high-resolution satellite data

In Chapter 5, the focus shifted towards **other** (not only SSM) **satellite data**, trying to determine whether they are more reliable for providing water-related information and how they fare when **contrasted with a high-density sensor network** in a greatly heterogeneous agricultural area. Comparison in terms of radiation (between the sensors and a professional station) has provided good results. In terms of temperature, air temperature both from the sensors and the professional station has been compared with thermal infrared satellite information of surface temperature. The sensor closeness to the ground has been highlighted by a higher similarity with the surface temperature satellite data. Leaf Area Index (LAI) estimations can be retrieved by the radiation dampening recorded from shadowed and illuminated sensors and are a direct function of the fields destination use. As opposed to the available SSM products (without further elaboration, at best at 1 km scale), LAI data can be obtained from satellite at much higher resolutions (30 m), more compatible with the reference scale of the crop fields. Finally, the sensor network has confirmed the low feasibility of employing satellite SSM data in irrigation schemes, as the on-ground variability is lost at their scales. However, using on-ground sensors alone would require heavy maintenance costs (even for low-cost sensors as those used in this thesis work) and data quality uncertainty. A proper merging of on-ground information and satellite data seems a good solution for improving irrigation management and agricultural monitoring activities.

9.3 Modelled ET fluxes accuracy for heterogeneous conditions and Aerodynamic Temperature impact

At this point in the analysis, it is clear that no measured data is exempt of uncertainties, which grow with the complexity of the natural processes involved and the heterogeneity of the surrounding environment. The physical soundness of modelling structures can provide useful information for agricultural management by filling in the gaps of measured data (when absent) and complementing their meaning with the robustness inherited from physical principles and years of diversified applications. For these reasons, the second part of the analysis has focused on the FEST-EWB distributed energy-water balance model. Its ability to compute continuously in time the SM dynamics and perform simulations even in absence of Land Surface Temperature (LST) data (required only for calibration purposes) makes it extremely suited to agricultural applications, where the time scales of required irrigations and the spatial scales of complex, heterogeneous crops are not easily matched by the satellite retrievals of the required information.

In Chapter 6, the attention has been on the **model dependency on scale** when working on a complex and heterogeneous agricultural setting, such as a vineyard. The main case study was a Sicilian vineyard, where very-high resolution (1.7 m) data was available from dedicated flights. Multiple spatial resolutions have been explored, both by directly running the model at that resolution and by directly aggregating the highest resolution model results obtained at 1.7 m. The target was to discuss the model accuracy when fed with coarser resolution data (much more easy to

obtain, and with a much higher frequency) against the highest-resolution benchmark. The answer was positive, since a lower-than-one-third estimation error on Evapotranspiration (ET, chosen as a "talking variable" for its great importance in agricultural applications) was found, compared to ≈10% errors from the (benchmark) aggregated model outputs.

Chapter 7 was devoted to intra-pixel dynamics in heterogeneous scenarios. As testified by many works in the literature, the energetical balances of the soil and vegetation fractions of a pixel are quite different, as can be gauged also in their temperature difference (higher for the soil). The structure itself of the model is thus called into question, as assuming one single surface temperature for an heterogeneous pixel (as is common practice for single-source models) is clearly a source of error. To this end, a **two-source version of FEST-EWB (FEST-2-EWB) has been developed**, separating the energy balances for the two components of any given pixel, all the while retaining the SM-preserving structure, which allows the FEST-EWB model to simulate independently of satellite data availability. The ultimate end was to demonstrate that, by constraining ET to a global pixel temperature, caused the model to overestimate the Transpiration (T) component directly linked to plant activity. On the other hand, a two-source model was expected to provide more reliable Transpiration estimates. The new model was tested over a dedicated innovative laboratory setting where the controlled conditions allowed us to extract the Transpiration component from the total ET, thus obtaining a reliable estimate. The FEST-2-EWB model, provided global performances similar to FEST-EWB in terms of surface temperature, soil moisture and global ET, managed to portray quite closely the extracted Transpiration, where the classic FEST-EWB model produced a consistent overestimation. A similar comparison was also performed in two open field cases, obtaining comparable results, except this time no partitioned T estimates were available to confirm the finding.

Finally, Chapter 8 was focused on a theoretical dilemma regarding the physical accuracy of the modelled evapotranspiration. It is (widely) common practice to use **Radiometric Temperature** in the Sensible Heat formulation, **instead of** its (theoretically correct) counterpart, the **Aerodynamic Temperature**. This Chapter investigates the soundness of this assumption and its effects over ET estimates and modelling errors. A considerable dataset of EC measurements in two main locations (water-abundant, Northern Italy maize fields and quasi-arid, water-deficient Southern Italy tomato fields) was used to derive aerodynamic temperature and compare it with its radiometric counterpart. The result was striking, confirming some findings in the literature, with temperature differences as high as 15-20°C between the two. However, these high differences are not necessarily associated to major model estimation errors. Integrating the aerodynamic temperature into the model infrastructure showed that, given the complex processes behind it, the necessity of parametrizing it with a few (non-sufficient) bio-meteorological parameters provided only small gains in terms of Sensible and Latent Heat estimation. These findings, similar to others in the literature, suggest that the gains in reinstating the aerodynamic temperature to its rightful place may be balanced by the losses in our incomplete knowledge of the processes behind it.

Technological progress needs to be employed to address the increasing Water and Food Security necessities. The work done in this Doctoral Thesis has been aimed precisely at that end, trying to tackle some common simplifying assumptions in the use of satellite data and hydrological modelling, in order to improve current results in agricultural monitoring.

Part V

Appendices

Appendix A

HCI complete results

In the following, some results of the HCI algorithm for the Capitanata and Chiese case studies will be detailed in full.

A.1 Capitanata

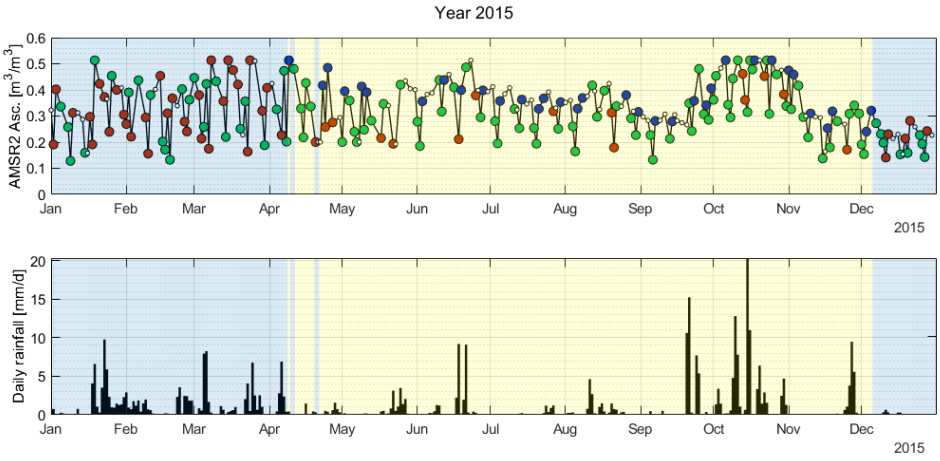

Figure A.1: AMSR2 Asc. (2015)

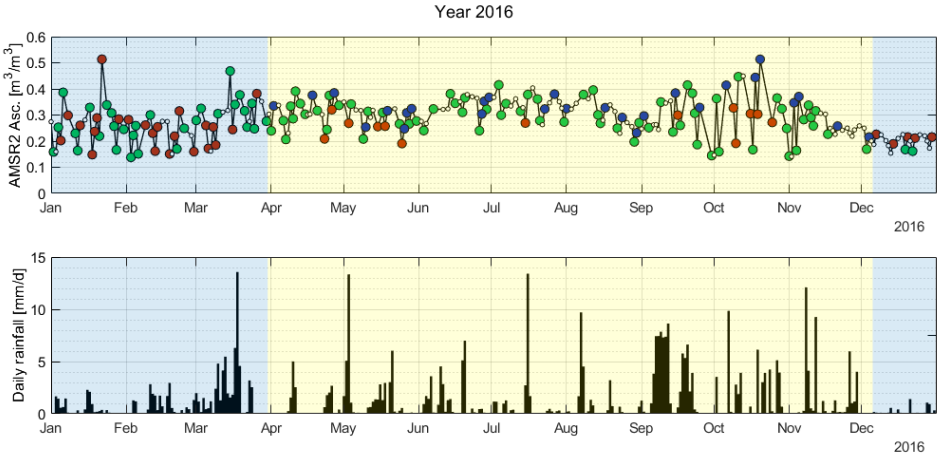

Figure A.2: AMSR2 Asc. (2016)

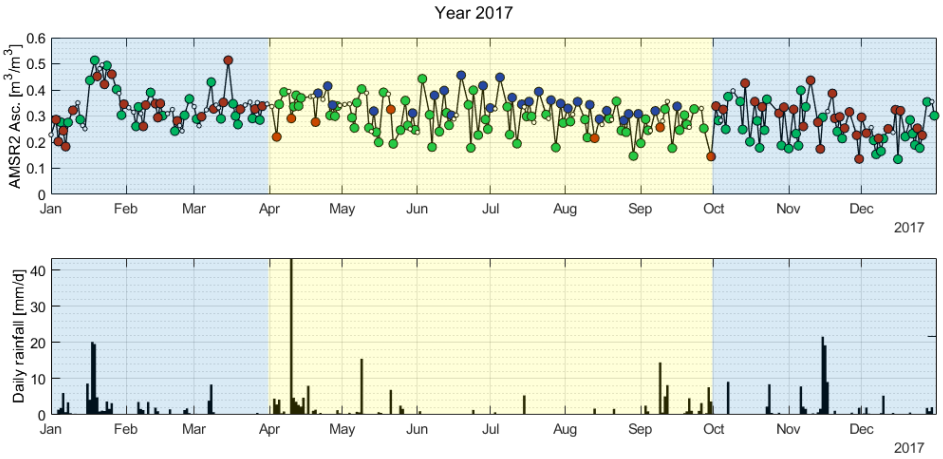

Figure A.3: AMSR2 Asc. (2017)

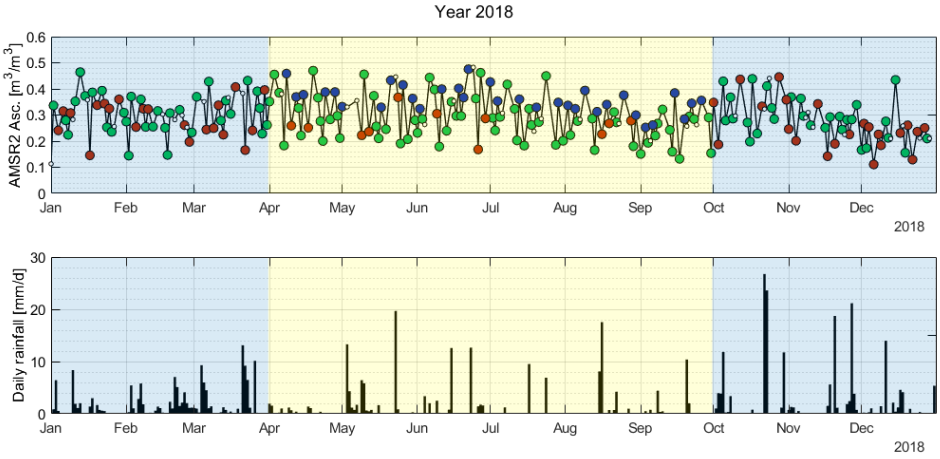

Figure A.4: AMSR2 Asc. (2018)

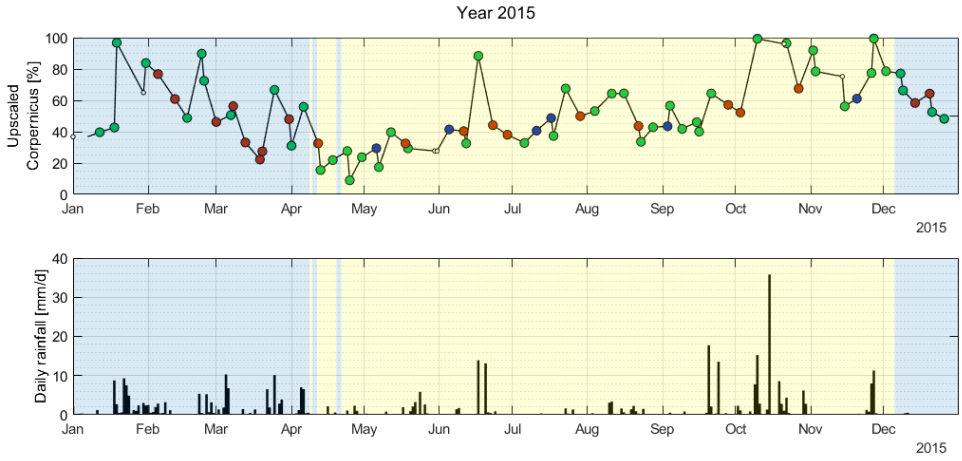

Figure A.5: Copernicus Upscaled (2015)

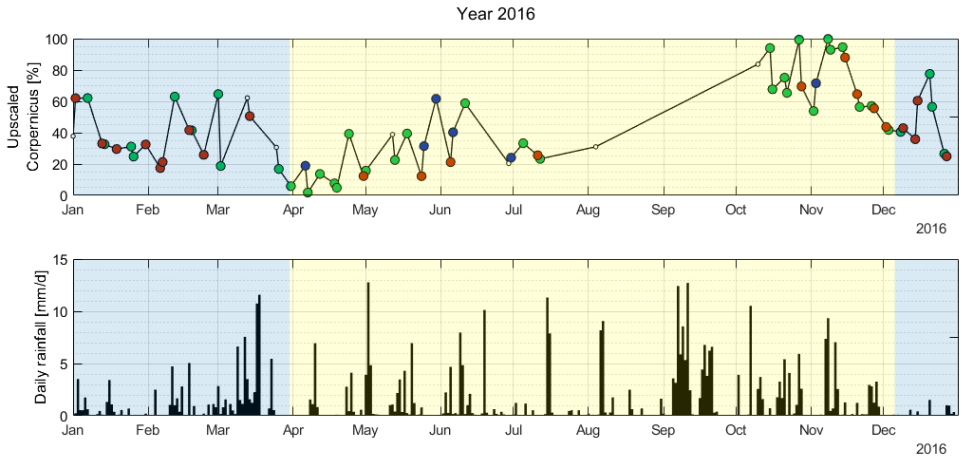

Figure A.6: Copernicus Upscaled (2016)

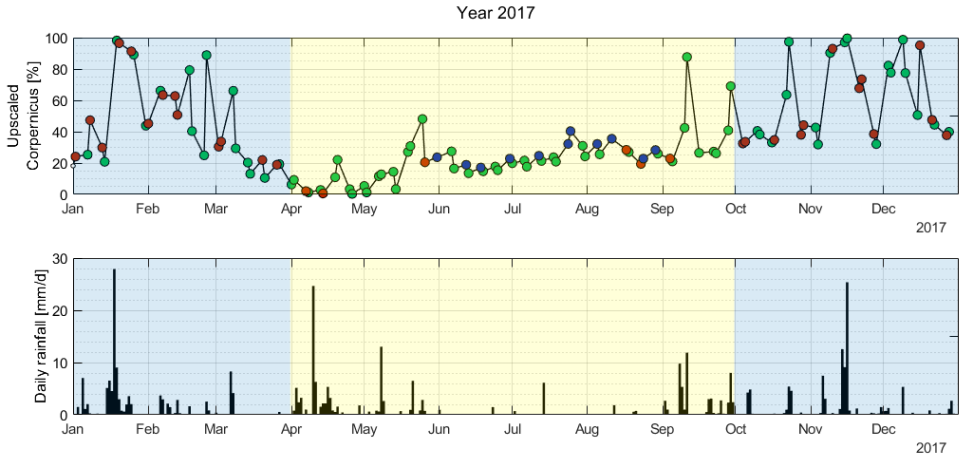

Figure A.7: Copernicus Upscaled (2017)

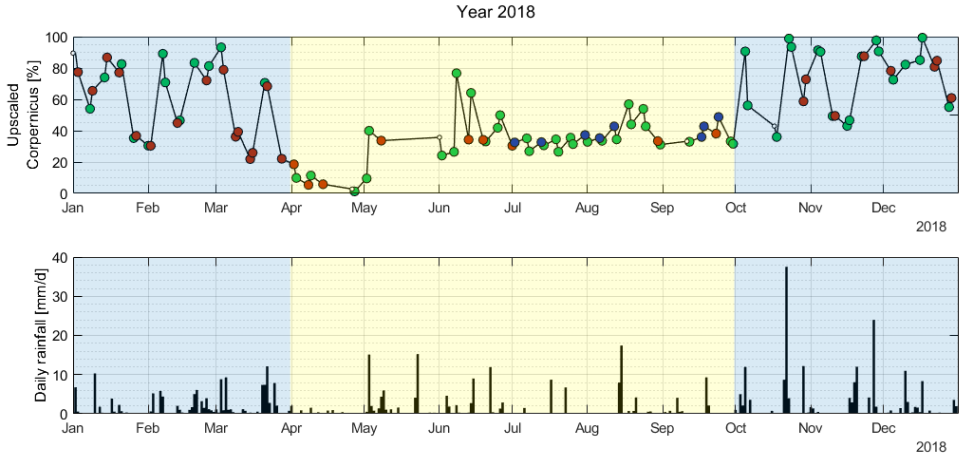

Figure A.8: Copernicus Upscaled (2018)

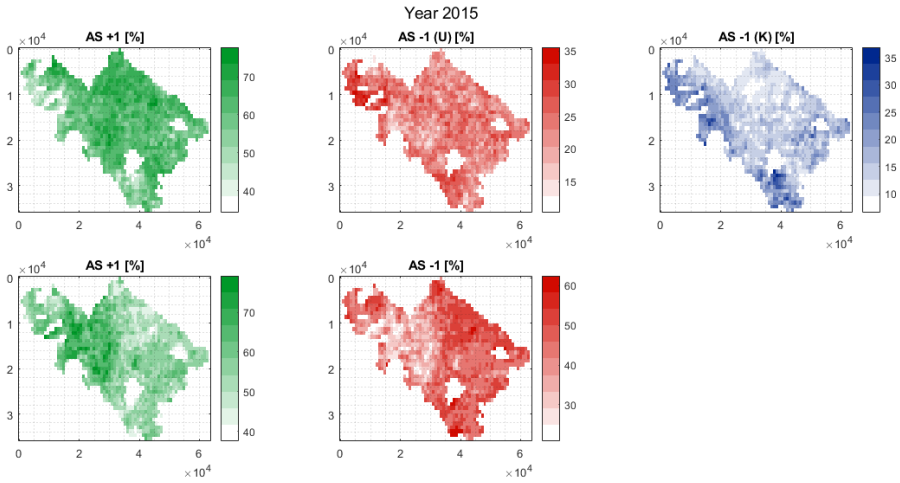

Figure A.9: Copernicus (2015)

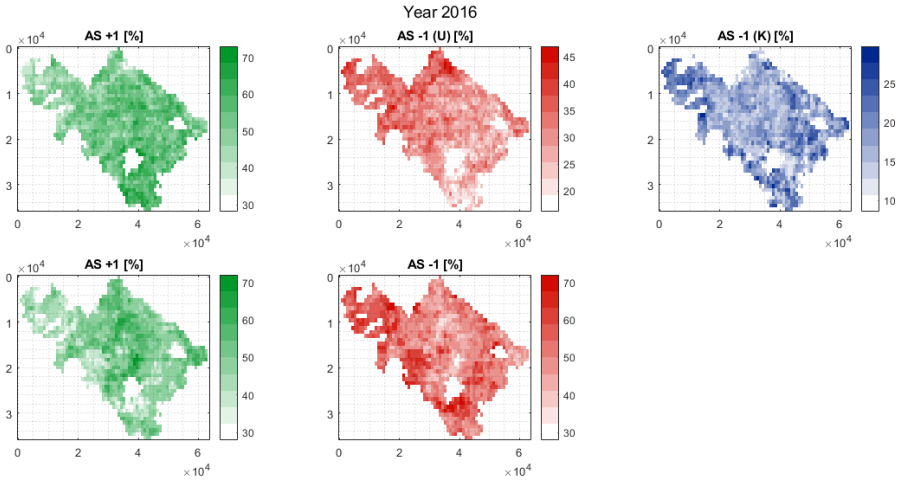

Figure A.10: Copernicus (2016)

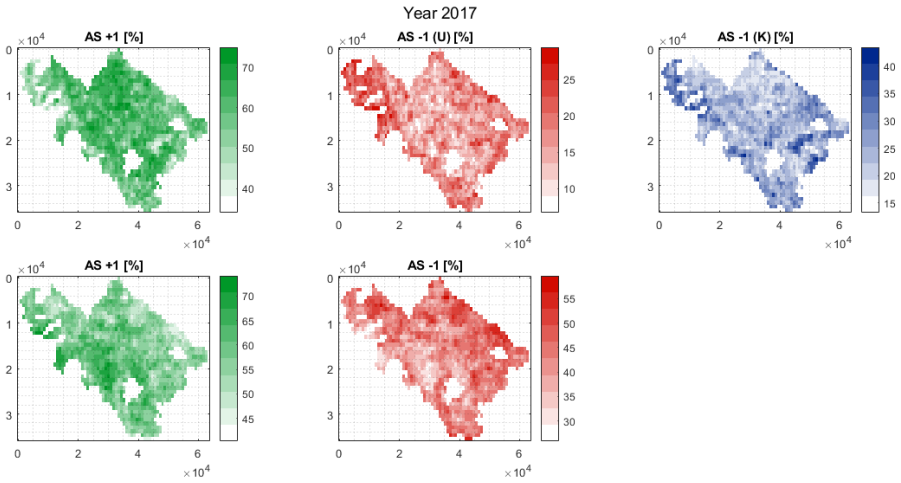

Figure A.11: Copernicus (2017)

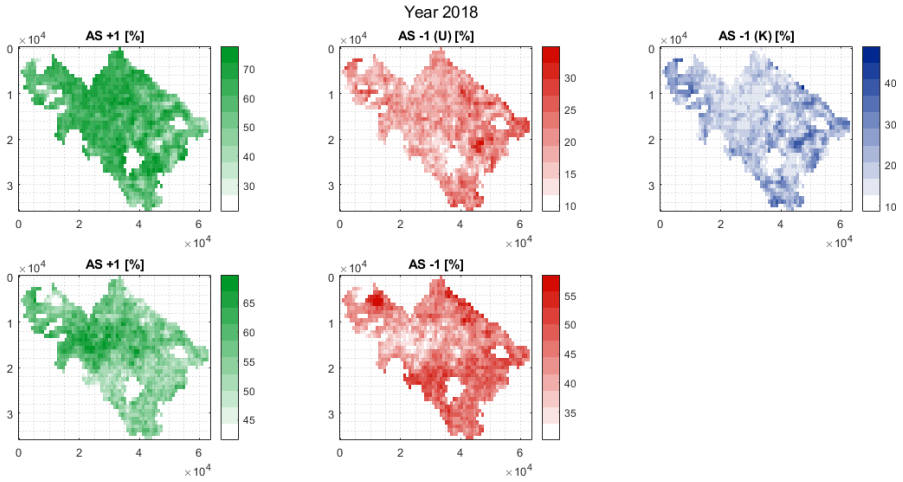

Figure A.12: Copernicus (2018)

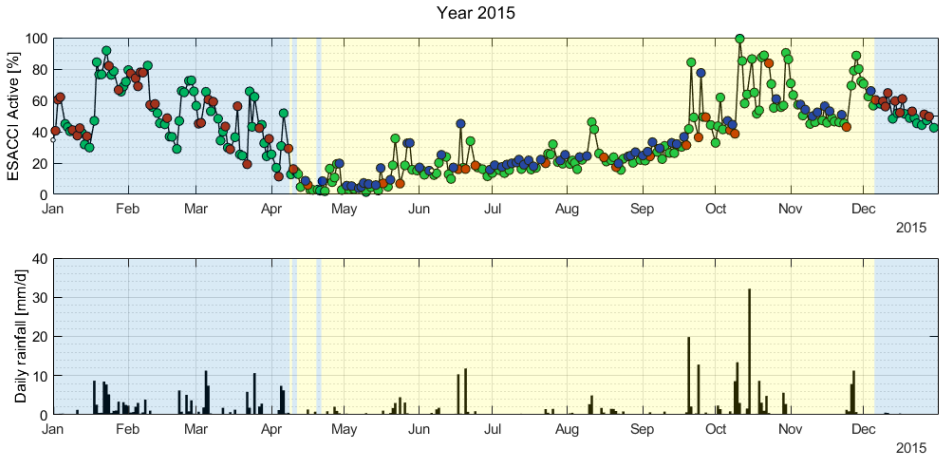

Figure A.13: ESA-CCI Active (2015)

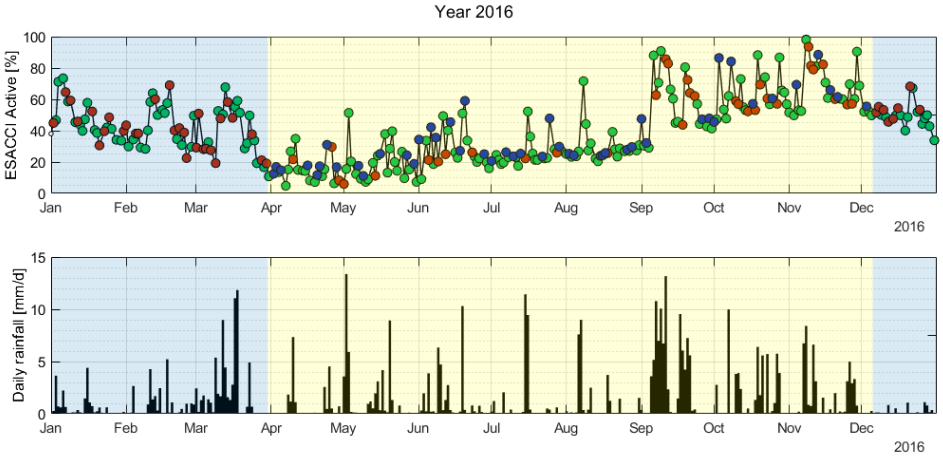

Figure A.14: ESA-CCI Active (2016)

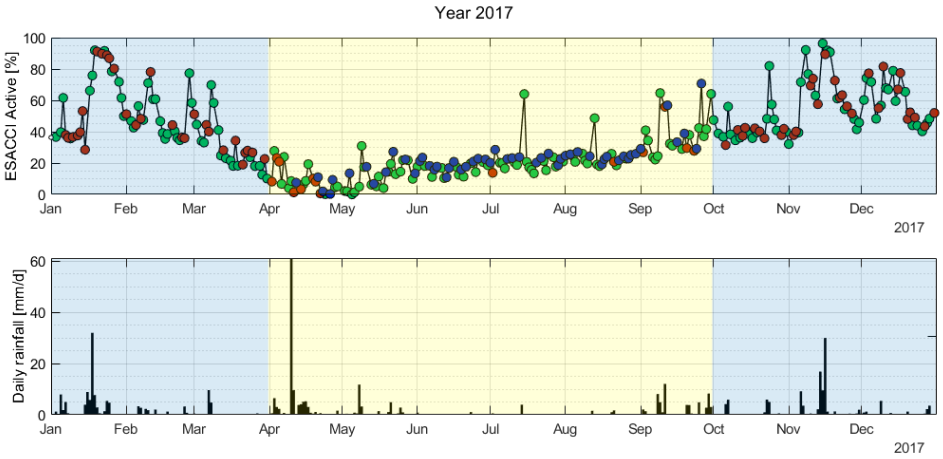

Figure A.15: ESA-CCI Active (2017)

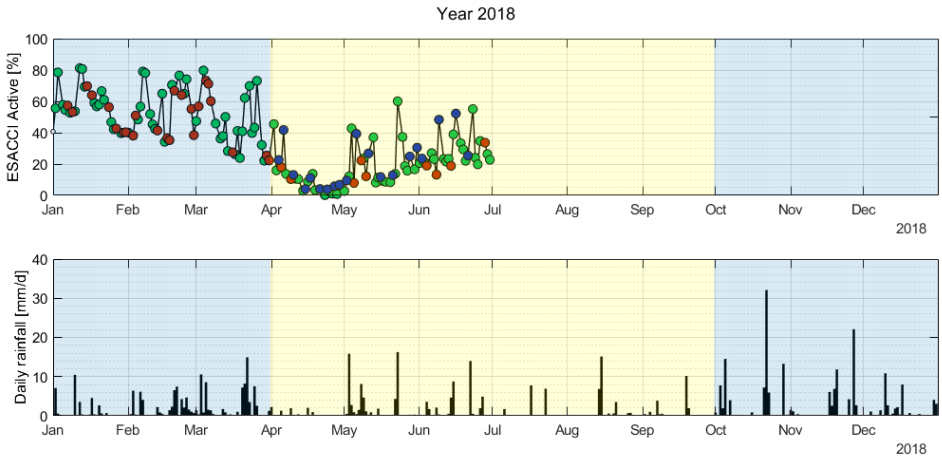

Figure A.16: ESA-CCI Active (2018)

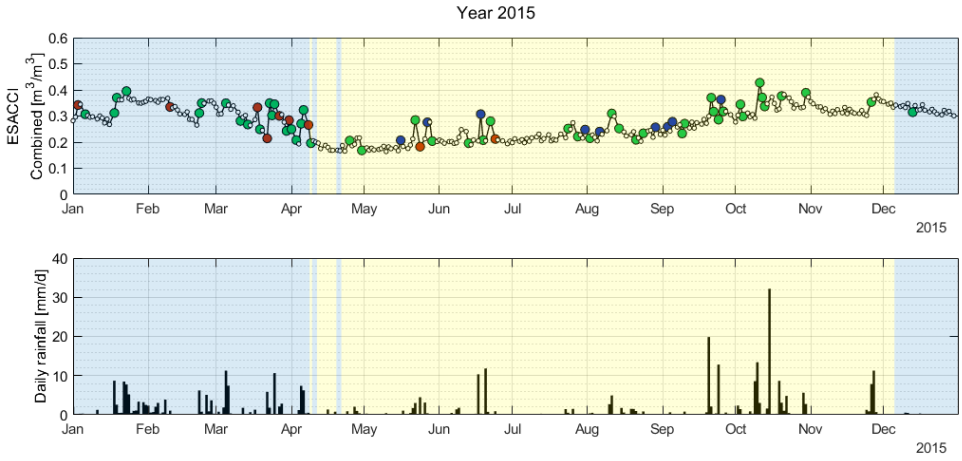

Figure A.17: ESA-CCI Combined (2015)

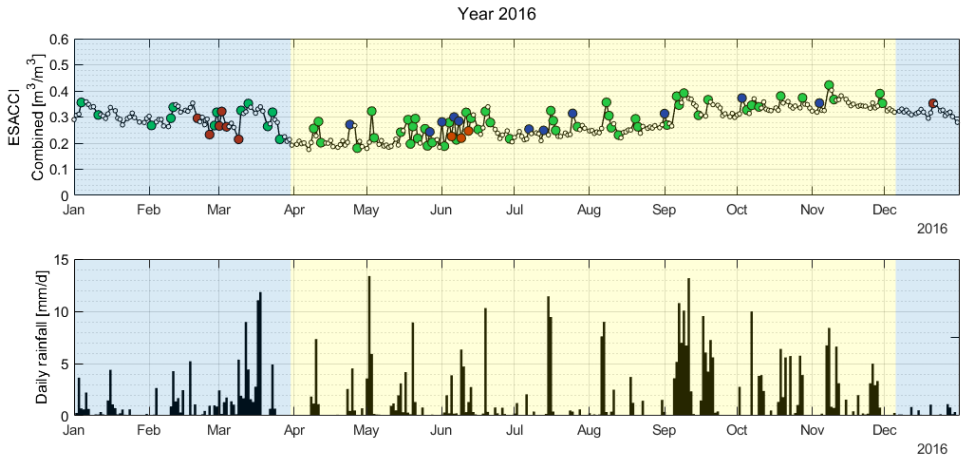

Figure A.18: ESA-CCI Combined (2016)

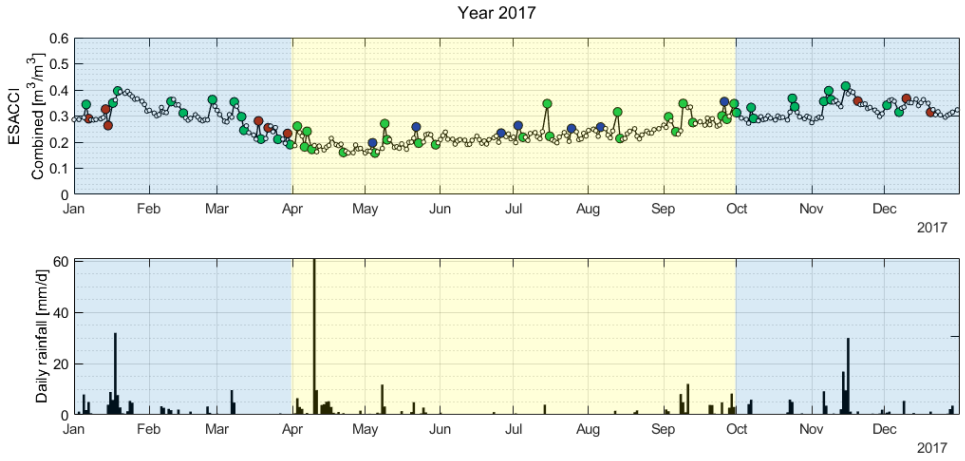

Figure A.19: ESA-CCI Combined (2017)

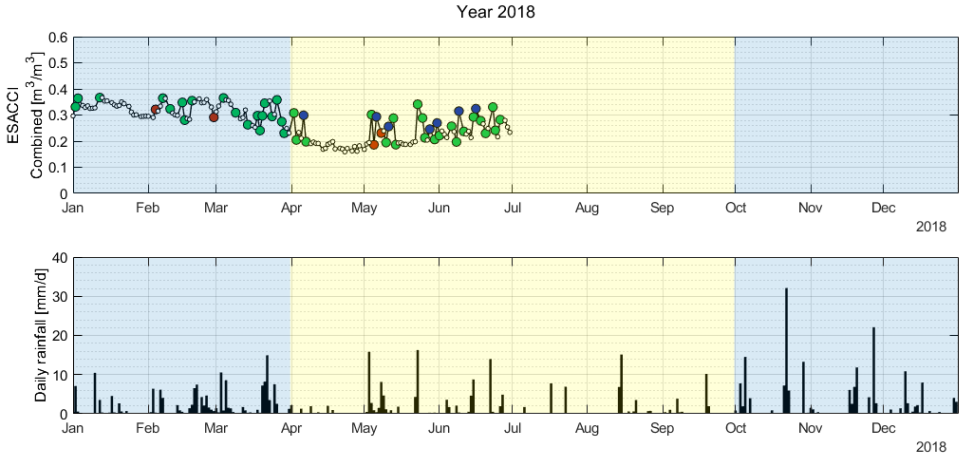

Figure A.20: ESA-CCI Combined (2018)

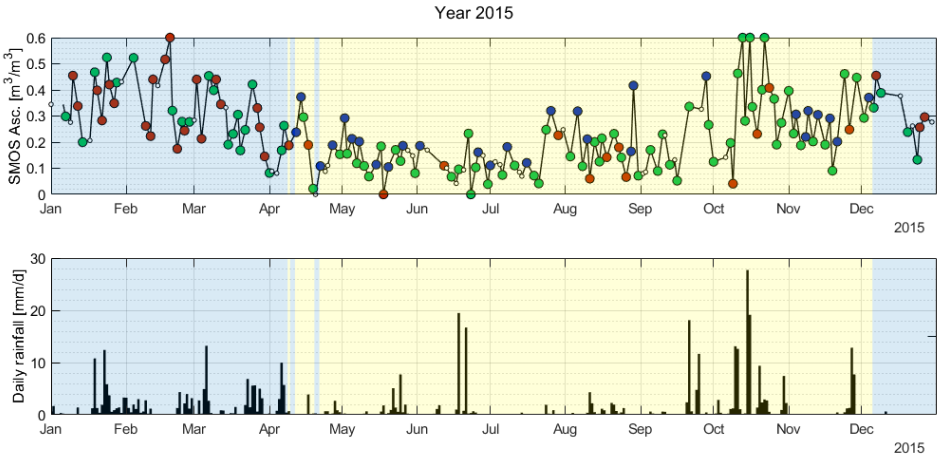

Figure A.21: SMOS Asc. (2015)

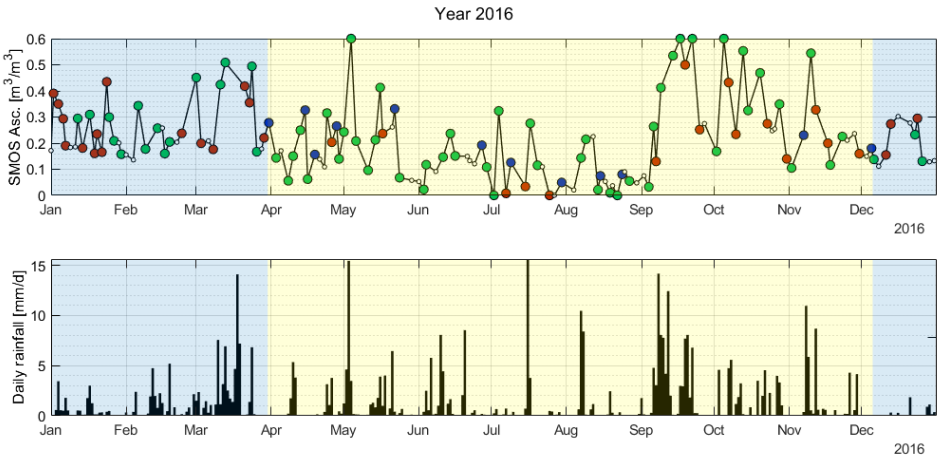

Figure A.22: SMOS Asc. (2016)

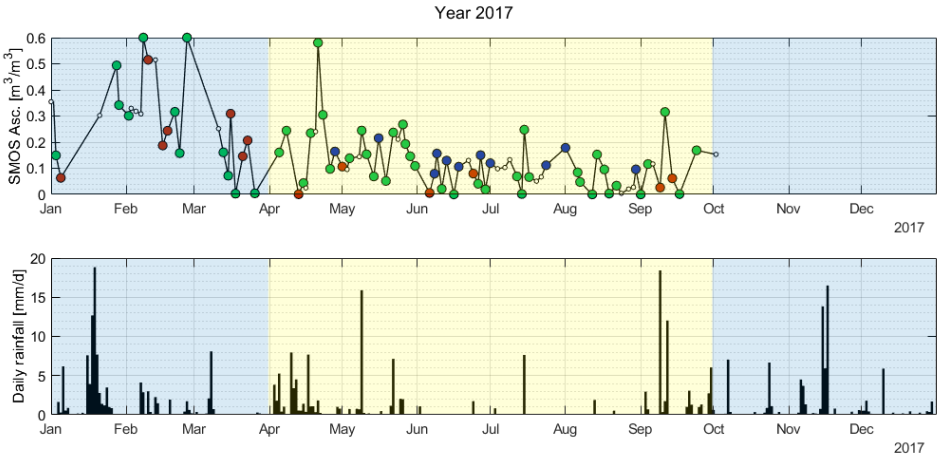

Figure A.23: SMOS Asc. (2017)

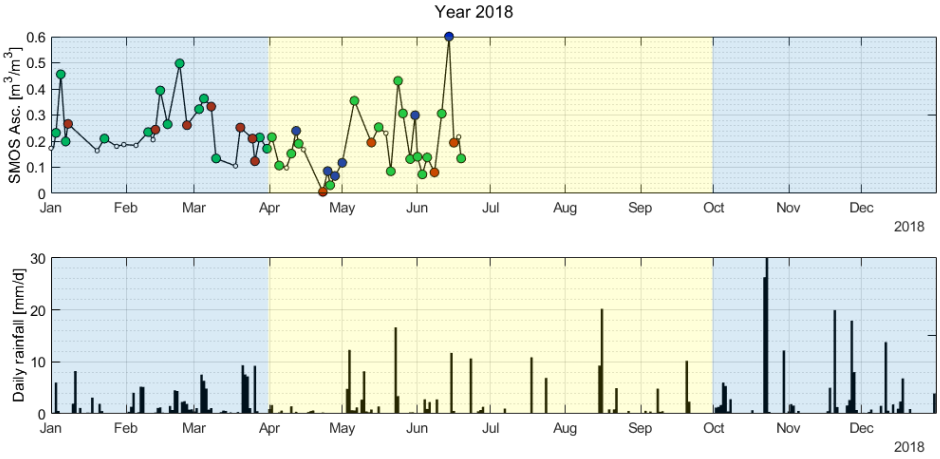

Figure A.24: SMOS Asc. (2018)

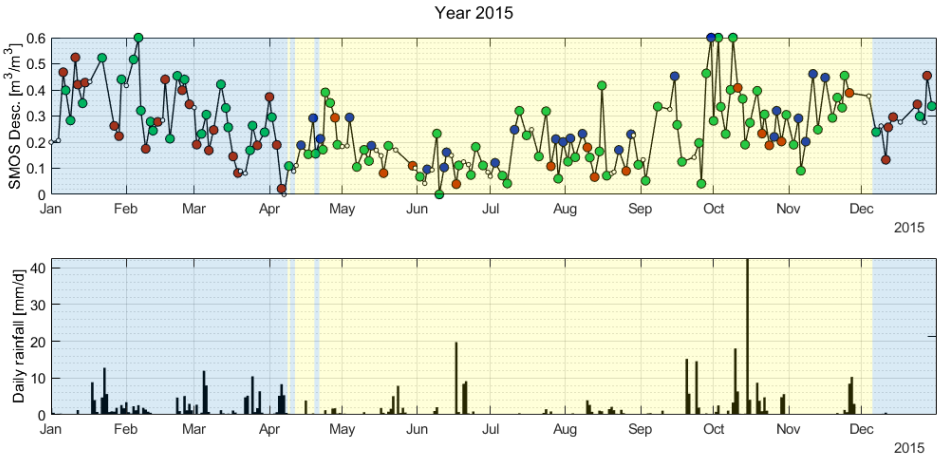

Figure A.25: SMOS Desc. (2015)

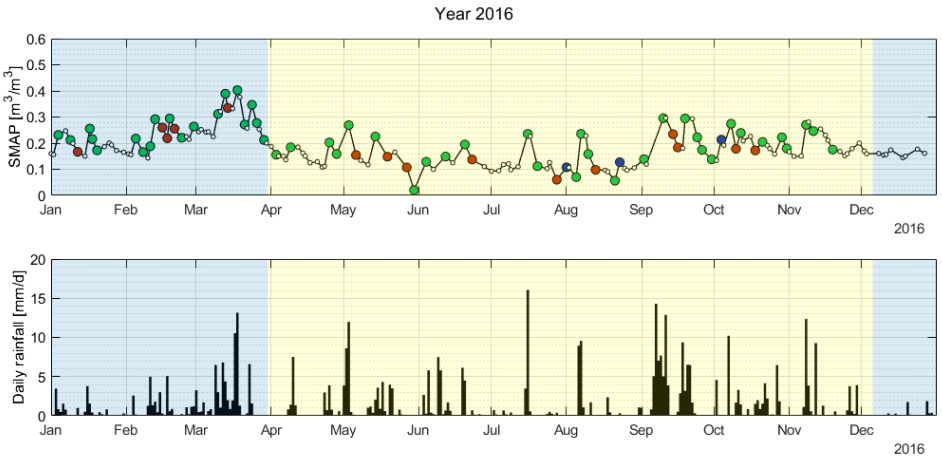

Figure A.26: SMOS Desc. (2016)

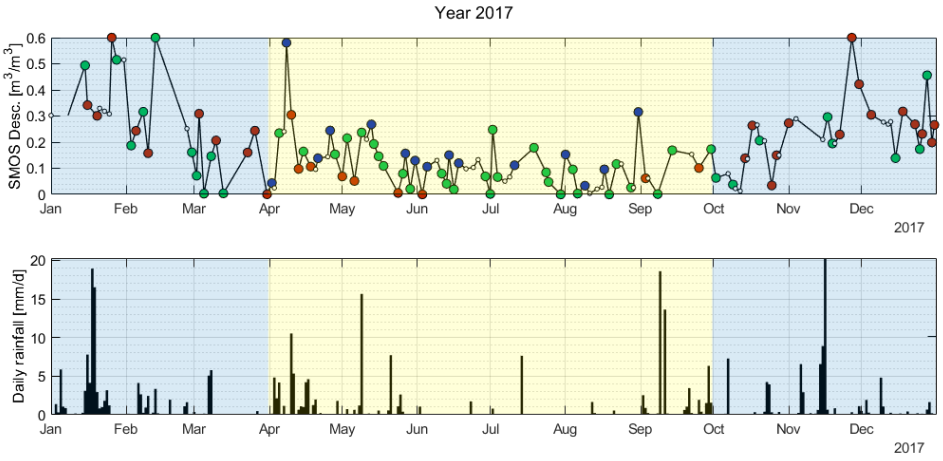

Figure A.27: SMOS Desc. (2017)

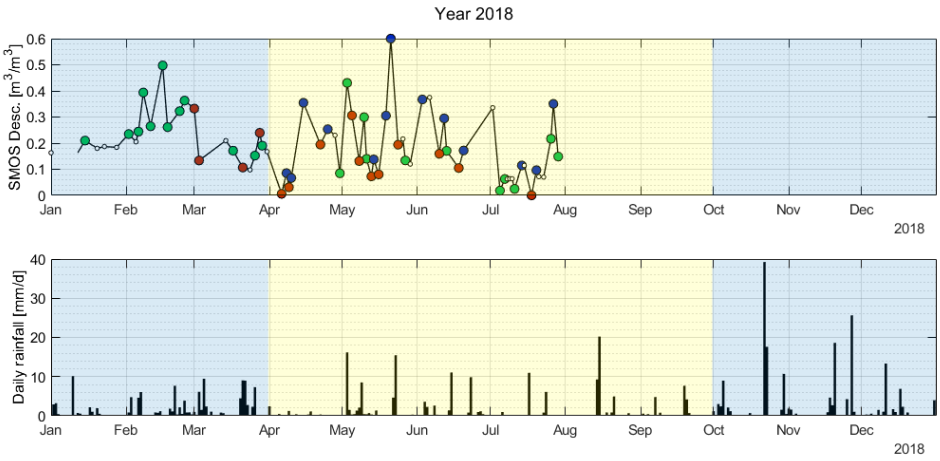

Figure A.28: SMOS Desc. (2018)

A.2 Chiese

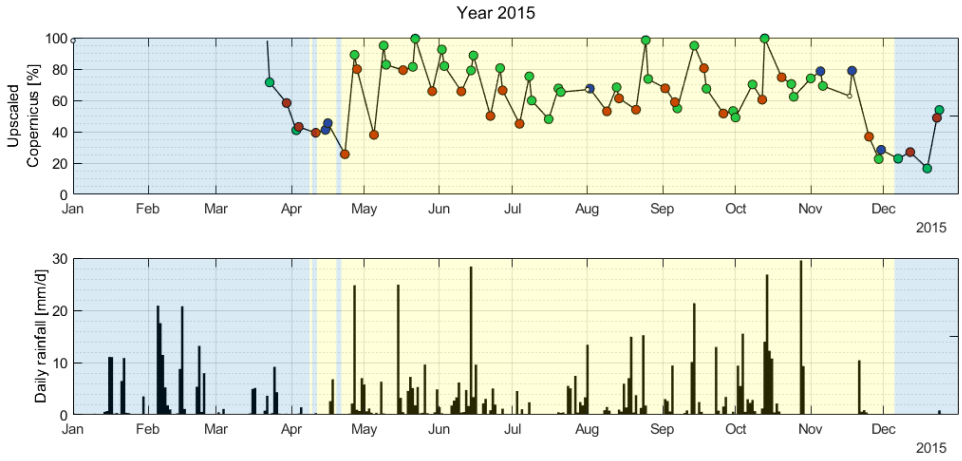

Figure A.29: Upscaled Copernicus (2015)

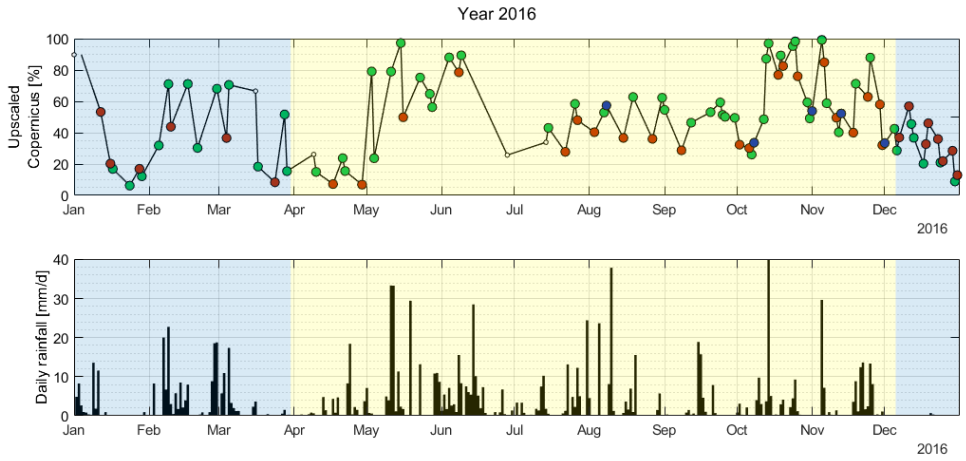

Figure A.30: Upscaled Copernicus (2016)

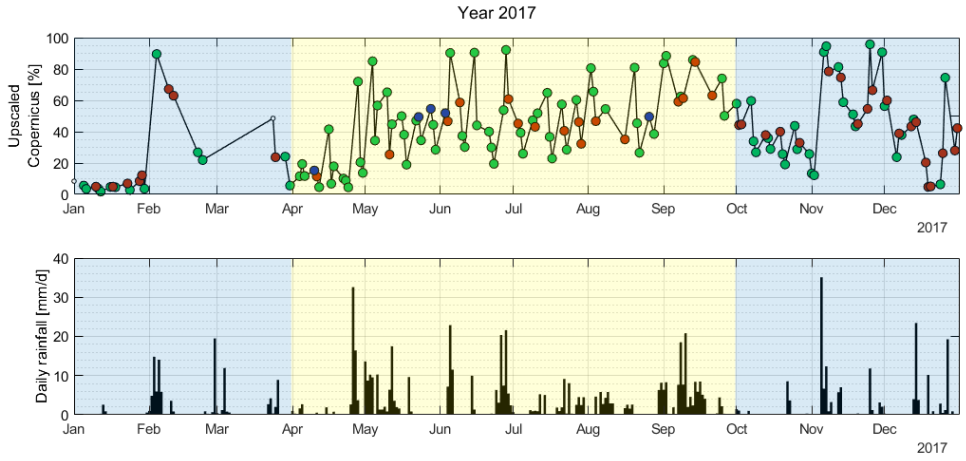

Figure A.31: Upscaled Copernicus (2017)

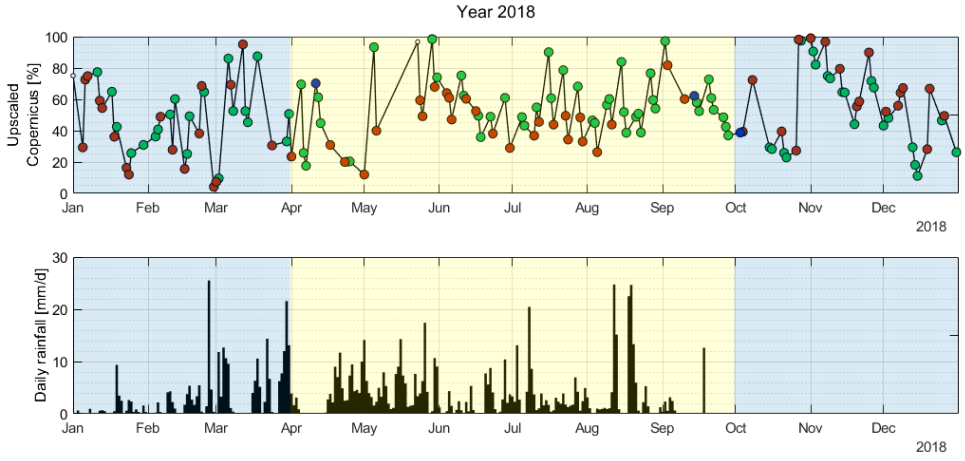

Figure A.32: Upscaled Copernicus (2018)

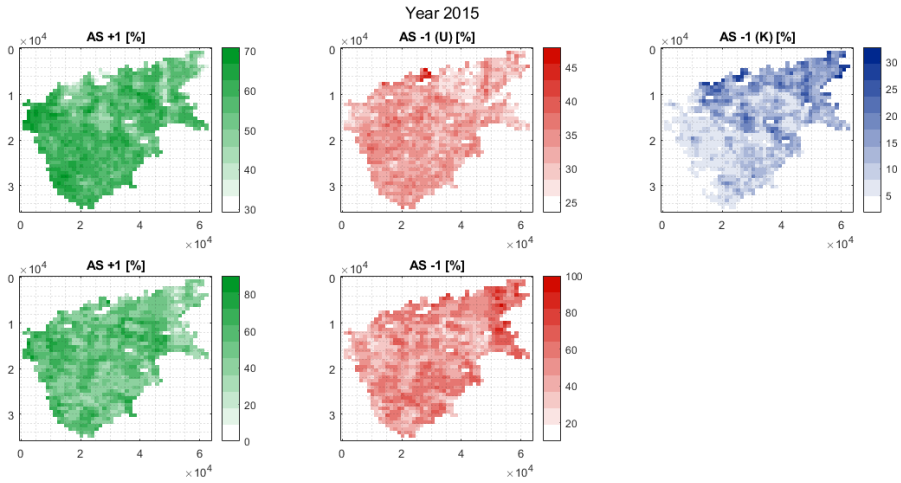

Figure A.33: Copernicus (2015)

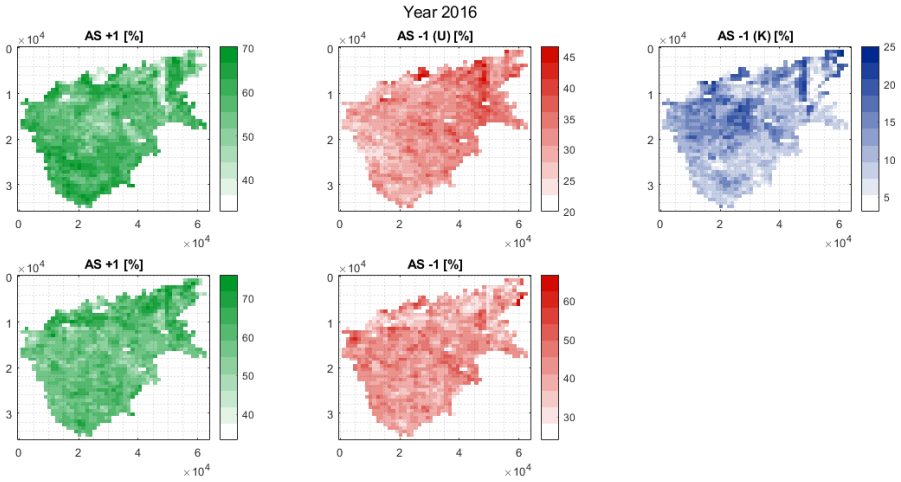

Figure A.34: Copernicus (2016)

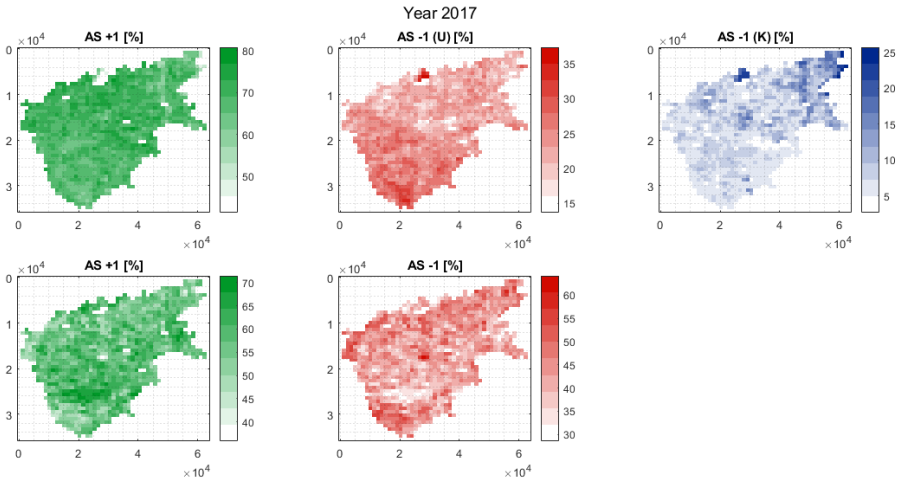

Figure A.35: Copernicus (2017)

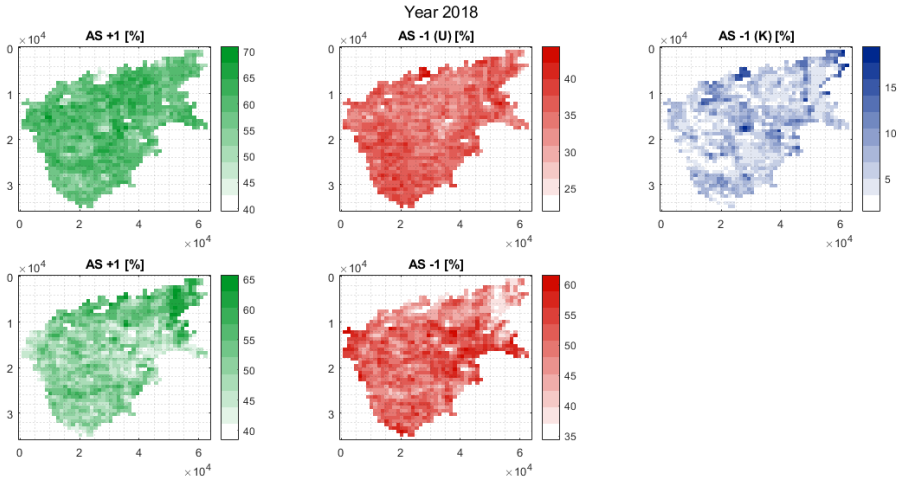

Figure A.36: Copernicus (2018)

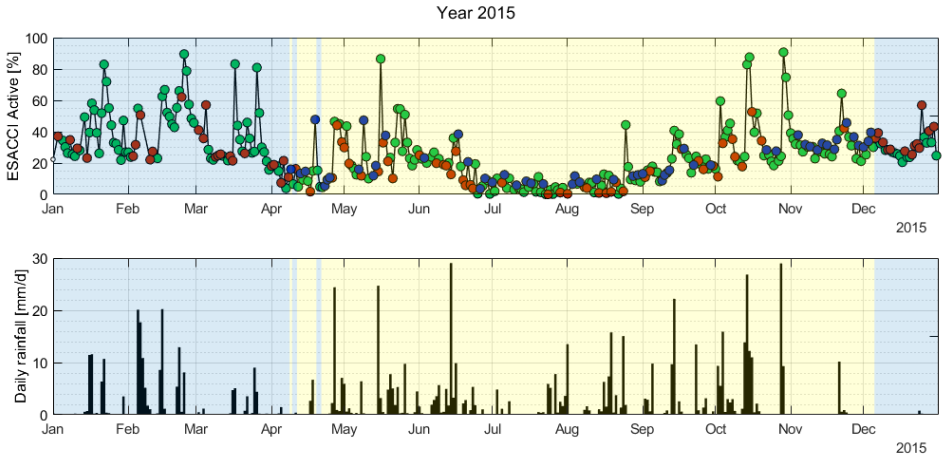

Figure A.37: ESA-CCI Active (2015)

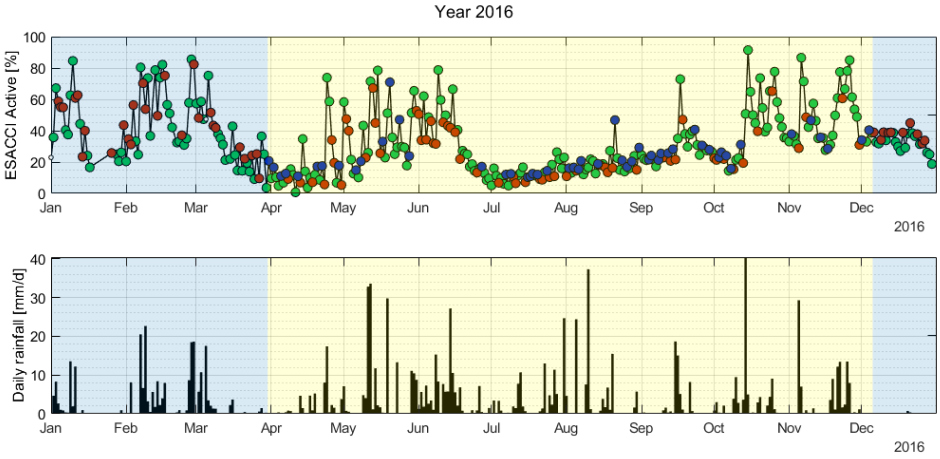

Figure A.38: ESA-CCI Active (2016)

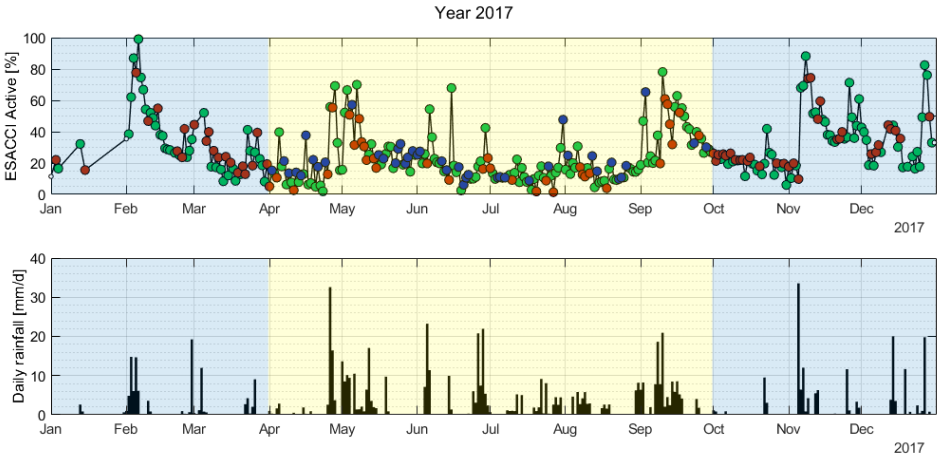

Figure A.39: ESA-CCI Active (2017)

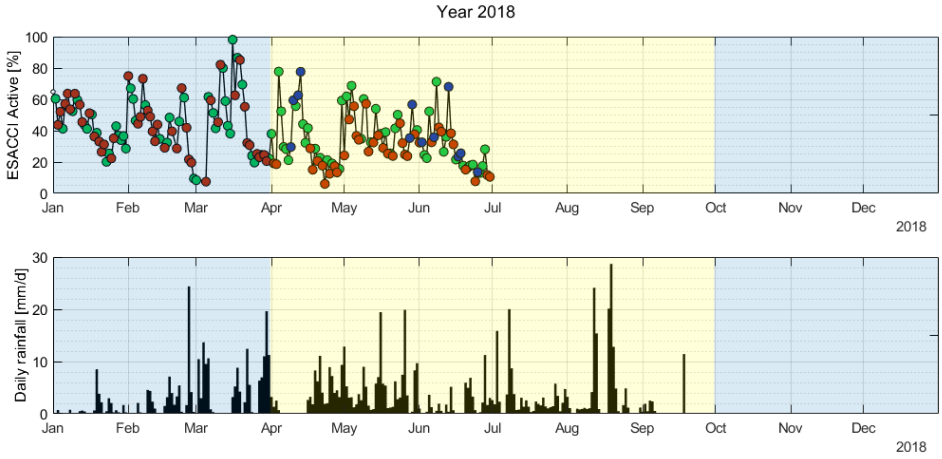

Figure A.40: ESA-CCI Active (2018)

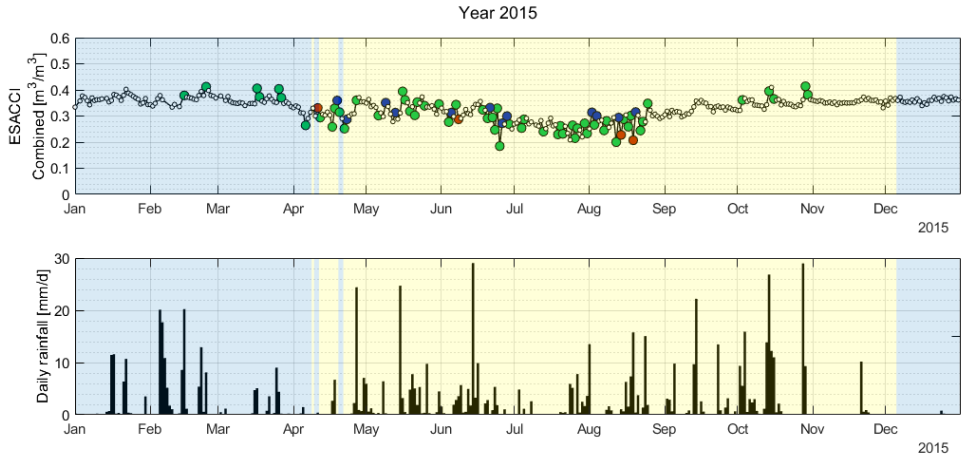

Figure A.41: ESA-CCI Combined (2015)

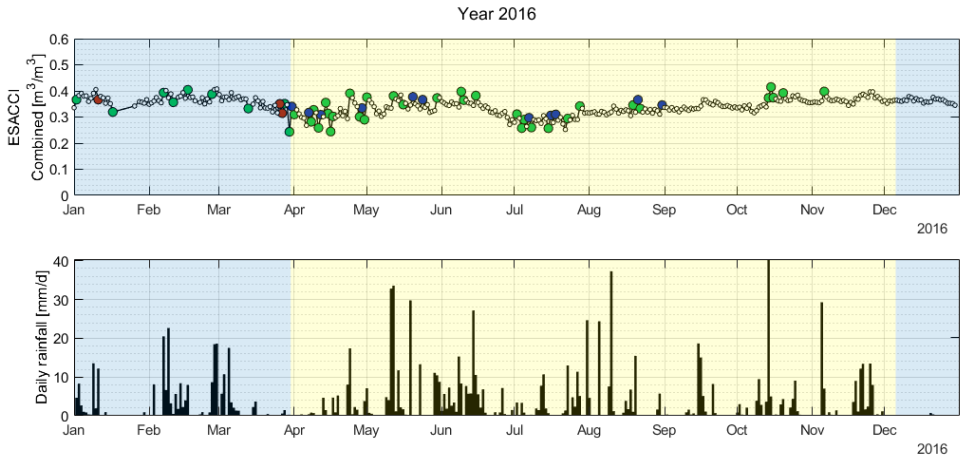

Figure A.42: ESA-CCI Combined (2016)

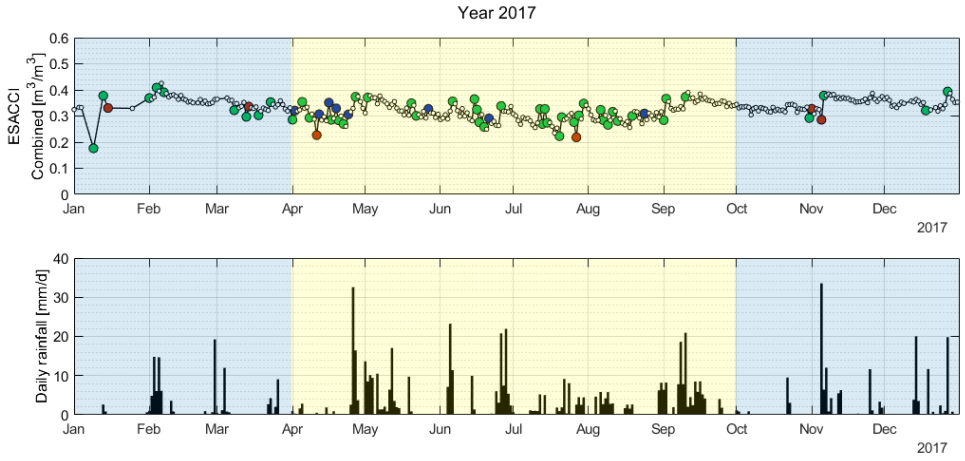

Figure A.43: ESA-CCI Combined (2017)

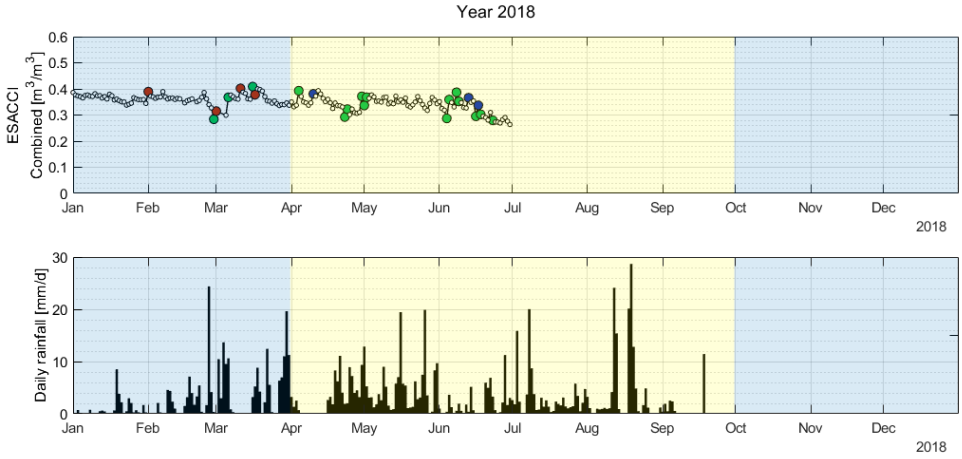

Figure A.44: ESA-CCI Combined (2018)

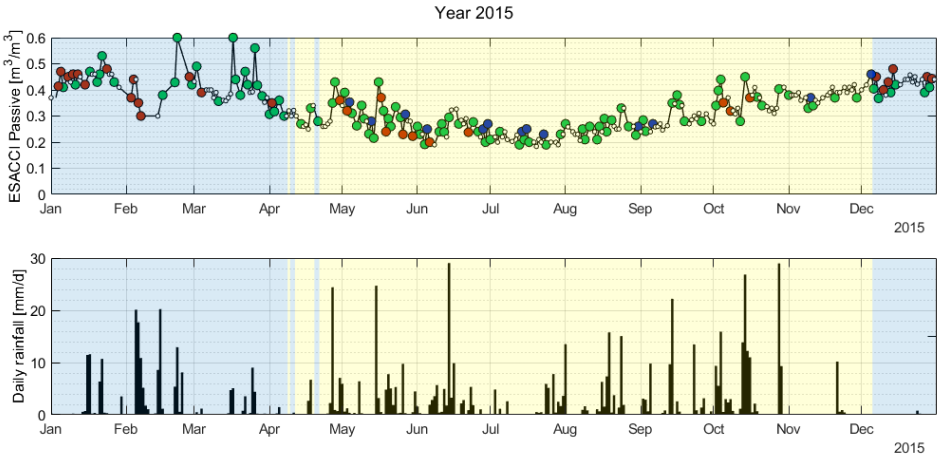

Figure A.45: ESA-CCI Passive (2015)

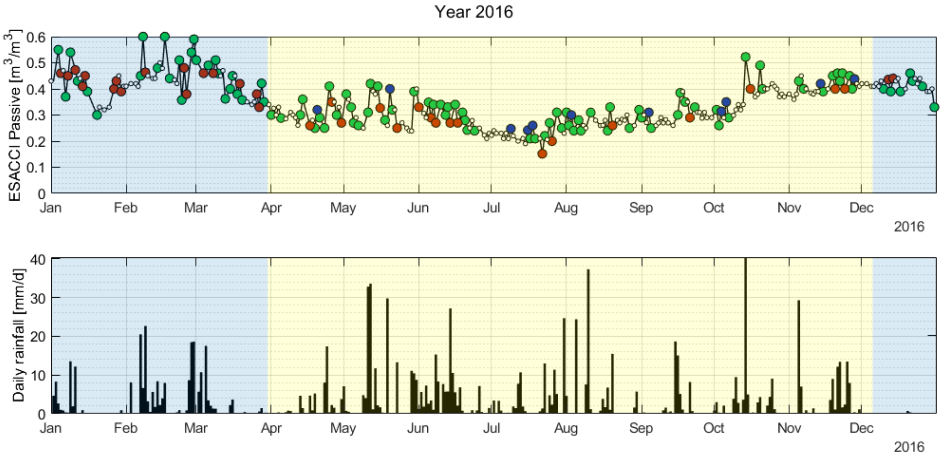

Figure A.46: ESA-CCI Passive (2016)

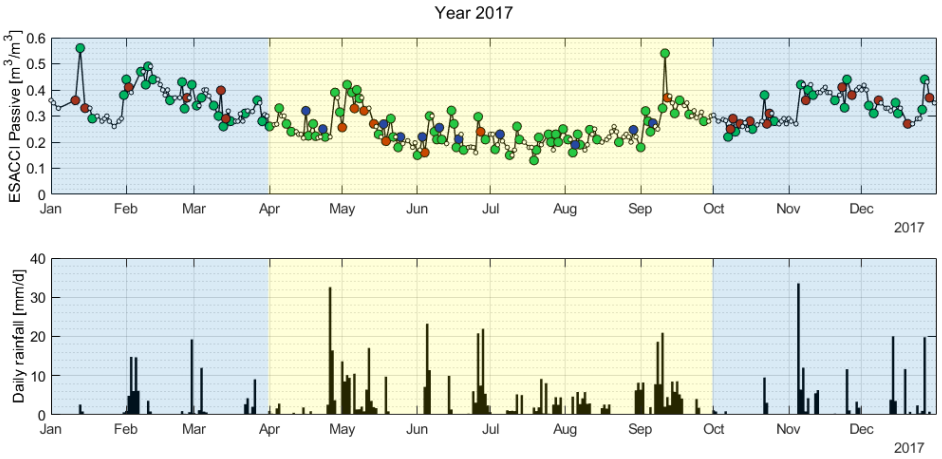

Figure A.47: ESA-CCI Passive (2017)

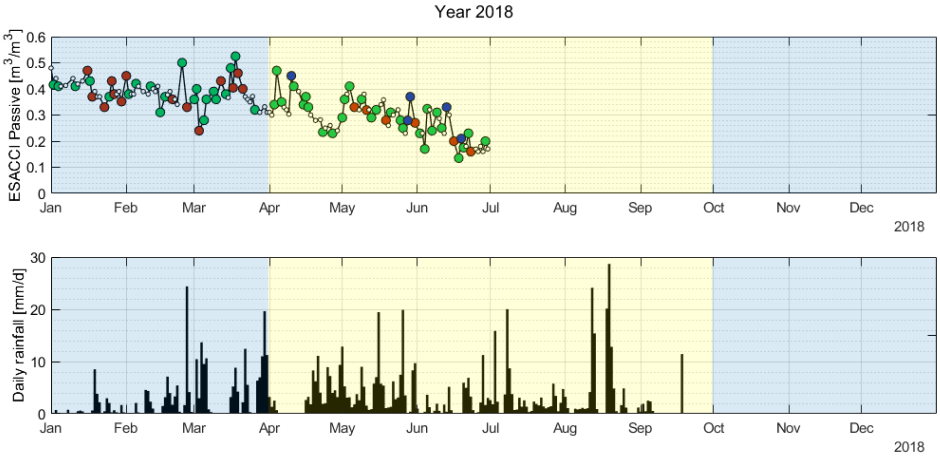

Figure A.48: ESA-CCI Passive (2018)

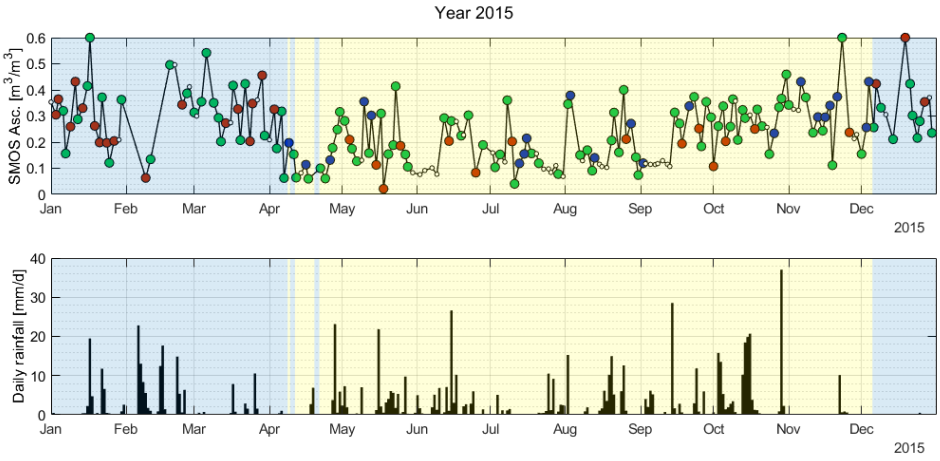

Figure A.49: SMOS Ascending (2015)

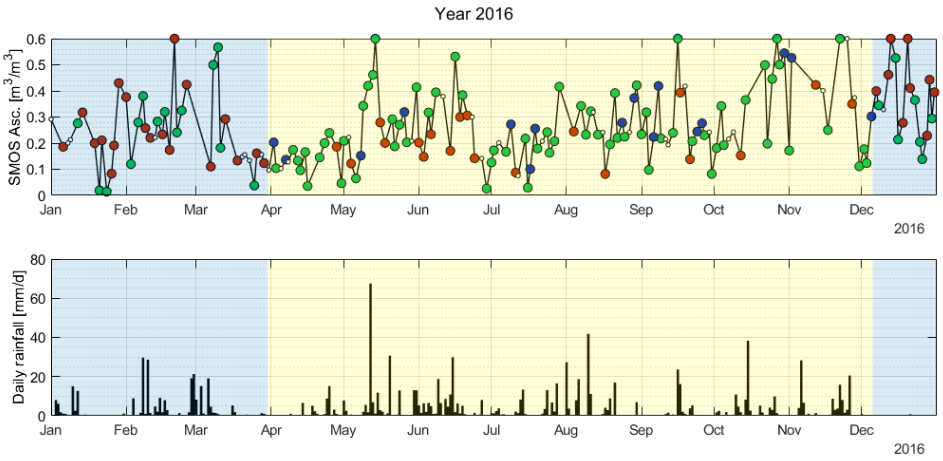

Figure A.50: SMOS Ascending (2016)

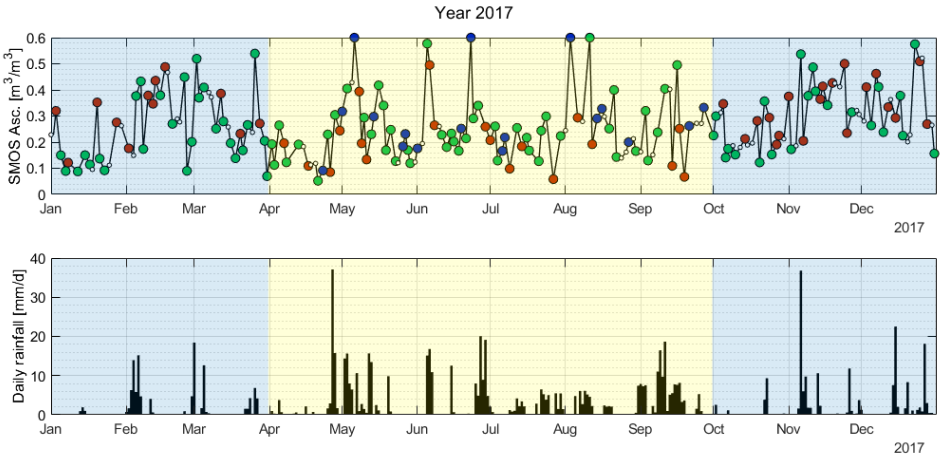

Figure A.51: SMOS Ascending (2017)

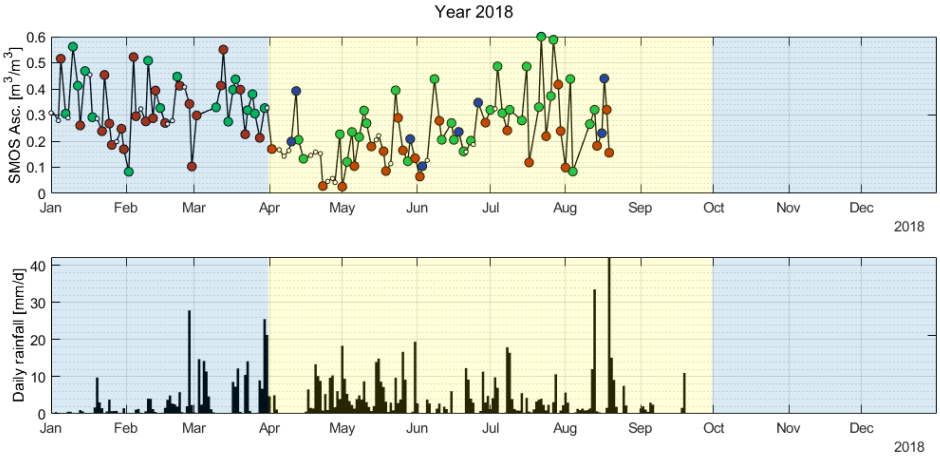

Figure A.52: SMOS Ascending (2018)

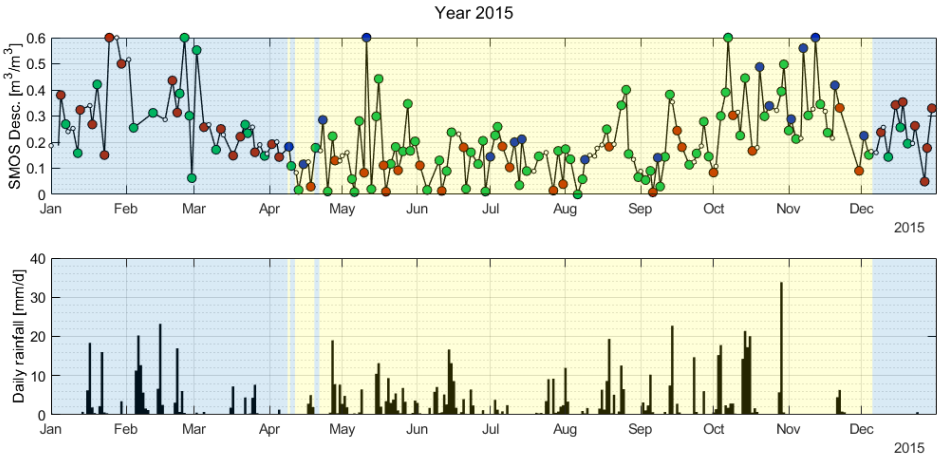

Figure A.53: SMOS Descending (2015)

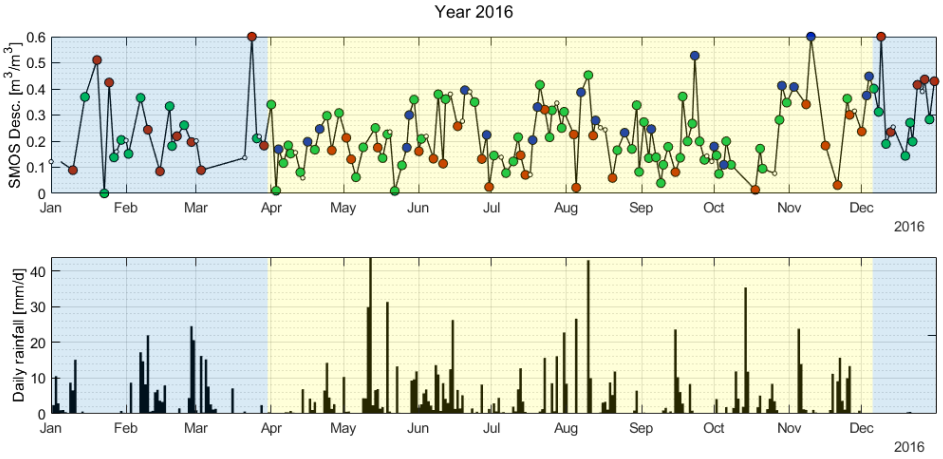

Figure A.54: SMOS Descending (2016)

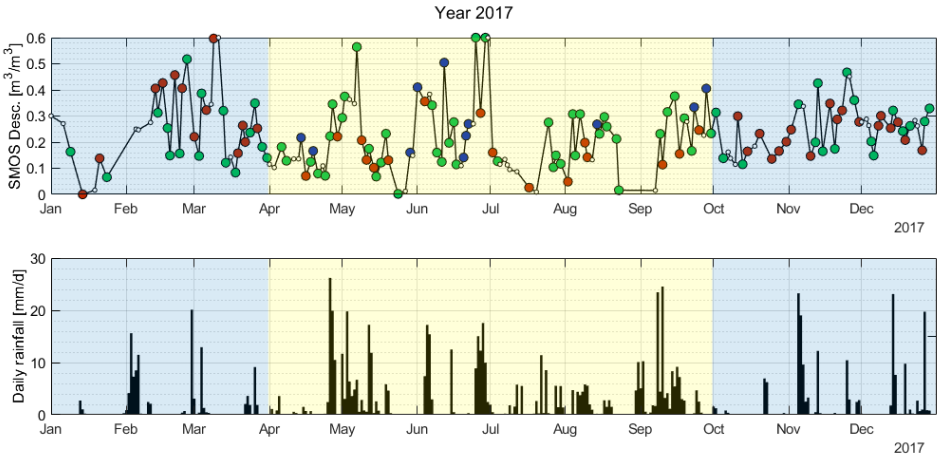

Figure A.55: SMOS Descending (2017)

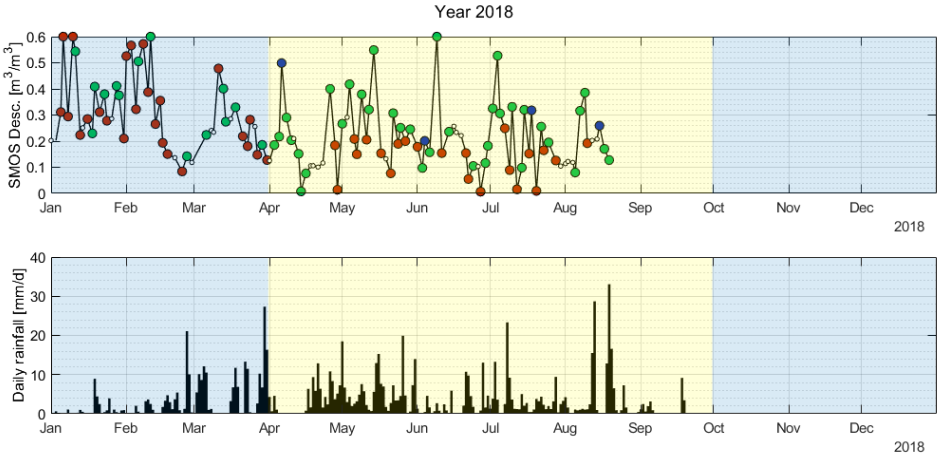

Figure A.56: SMOS Descending (2018)

Appendix B

SSM between Parrot sensors and Satellite

B.1 Foggia Incoronata area

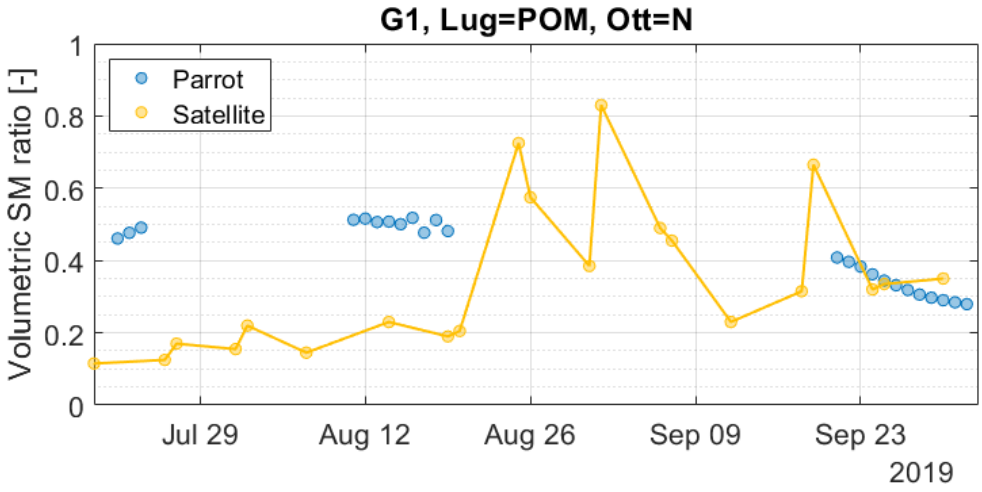

Figure B.1: Sensor G1 Surface Soil Moisture

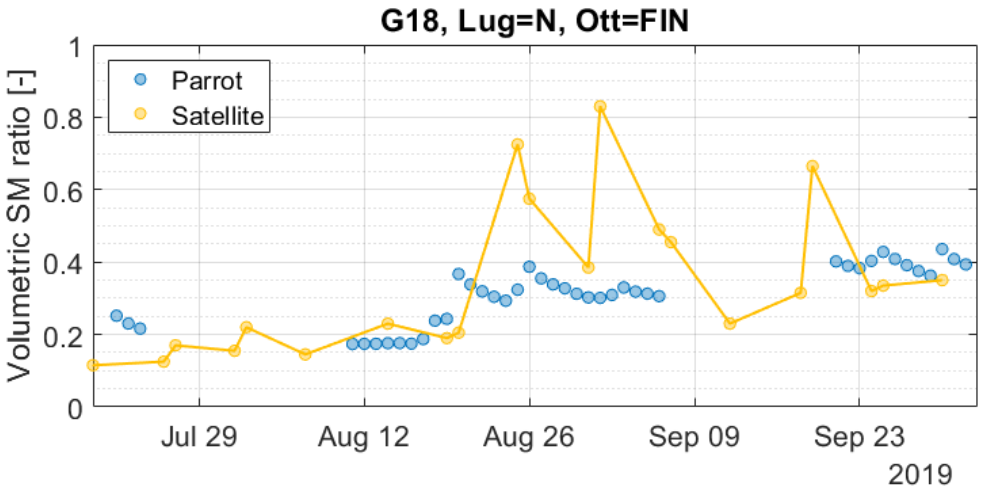

Figure B.2: Sensor G18 Surface Soil Moisture

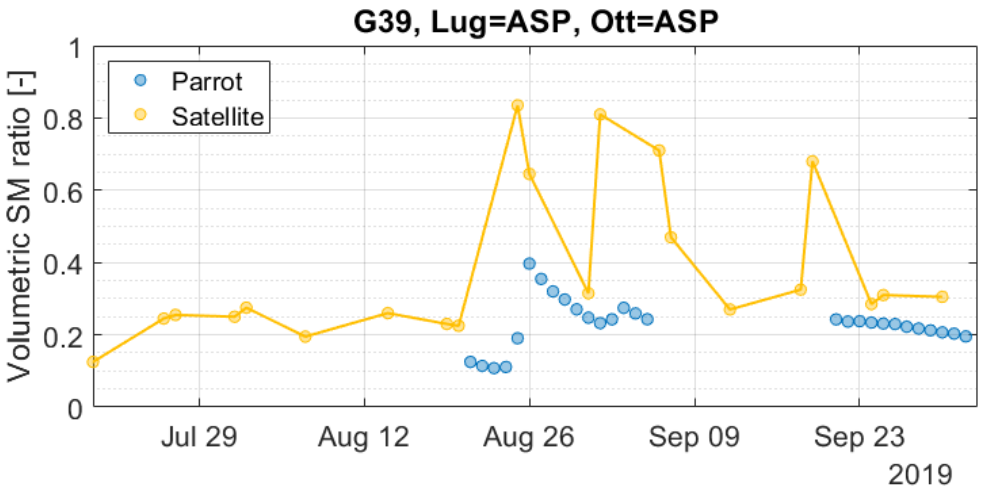

Figure B.3: Sensor G39 Surface Soil Moisture

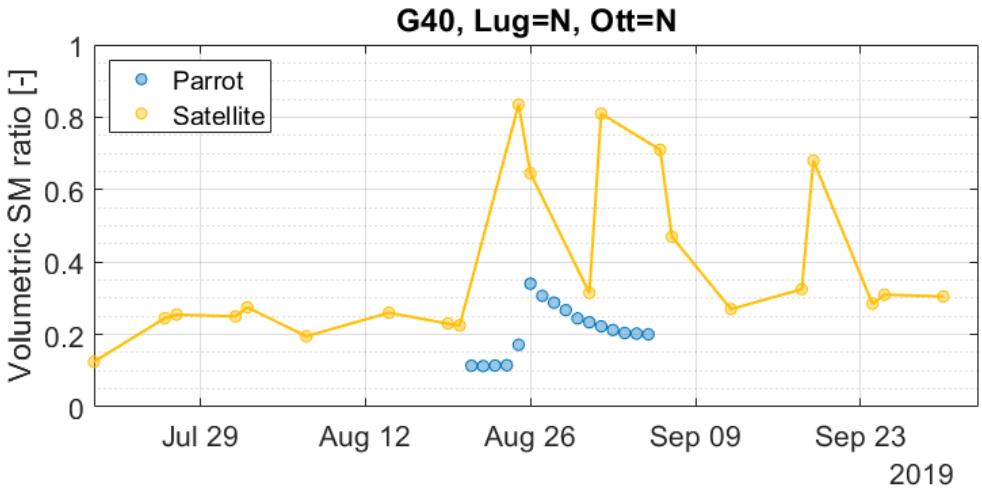

Figure B.4: Sensor G40 Surface Soil Moisture

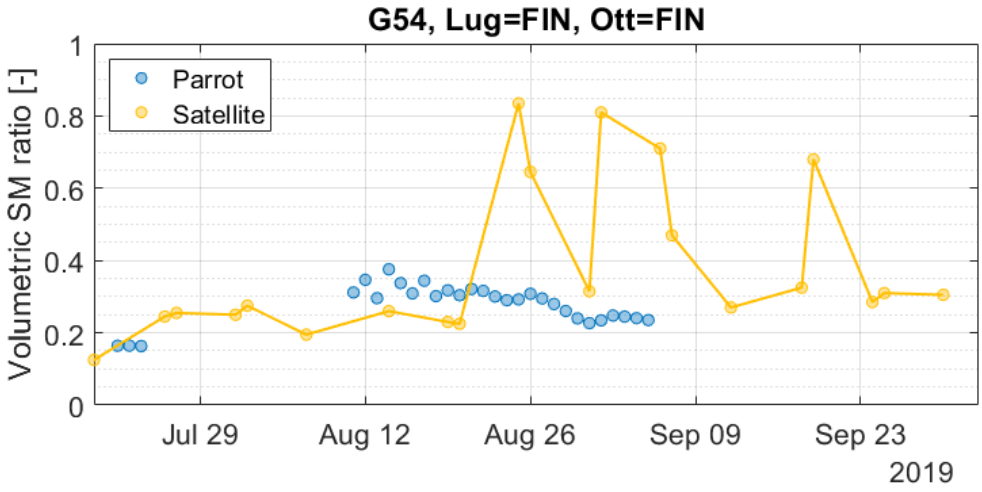

Figure B.5: Sensor G54 Surface Soil Moisture

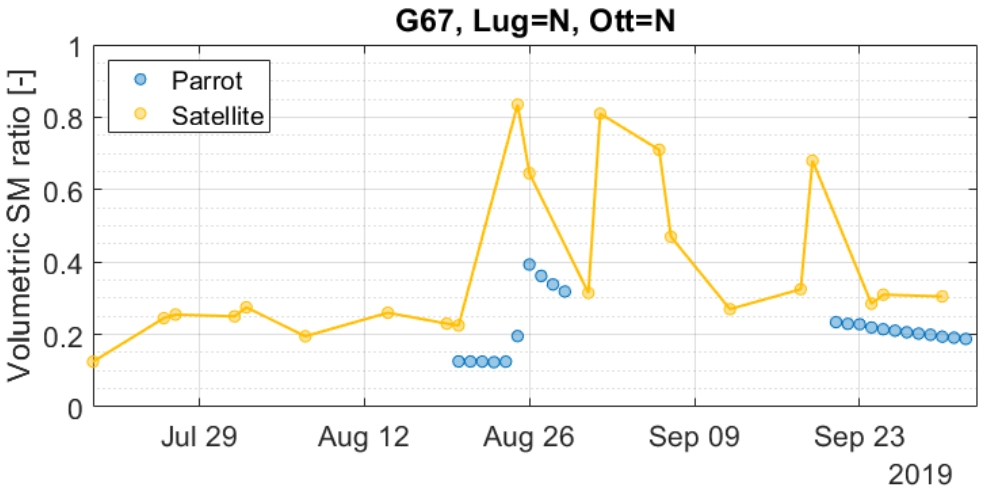

Figure B.6: Sensor G67 Surface Soil Moisture

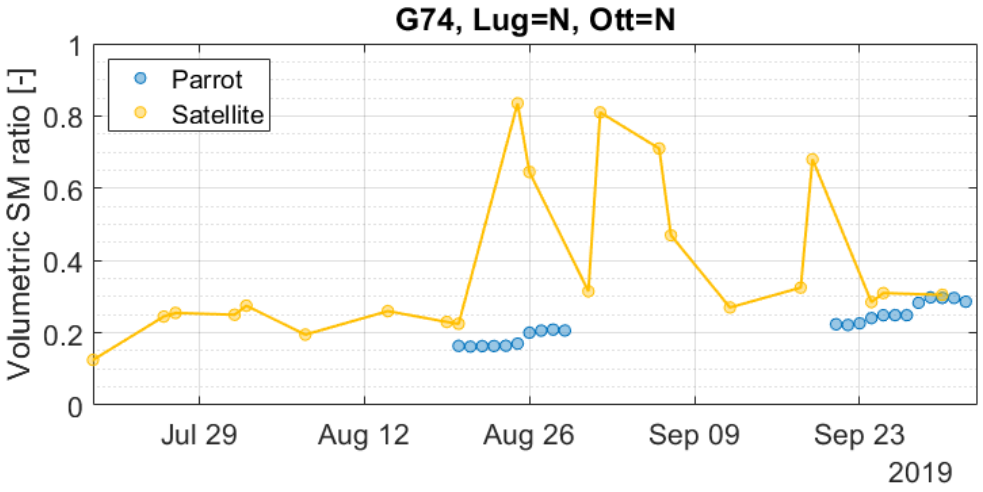

Figure B.7: Sensor G74 Surface Soil Moisture

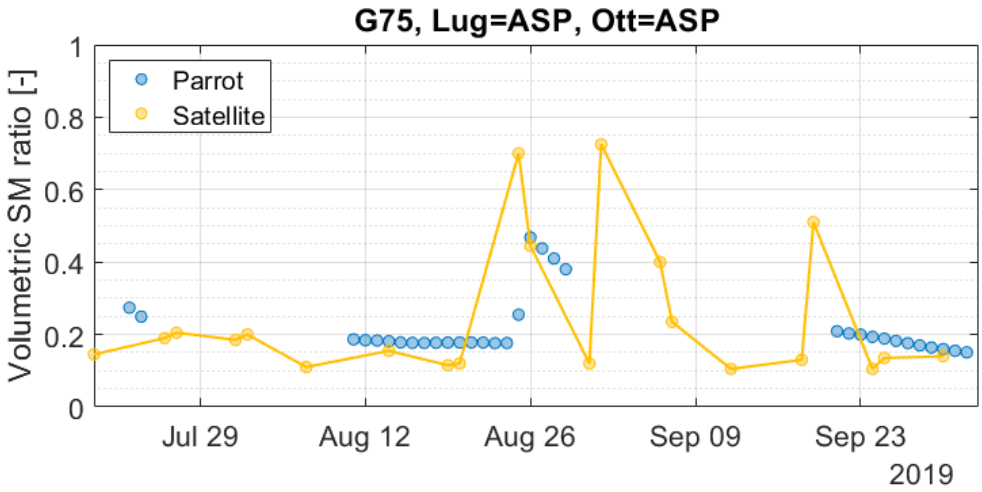

Figure B.8: Sensor G75 Surface Soil Moisture

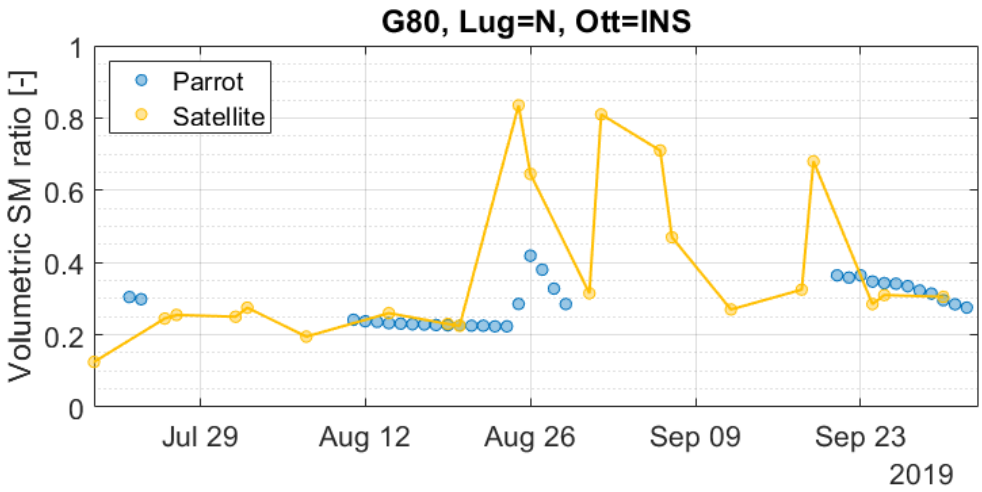

Figure B.9: Sensor G80 Surface Soil Moisture

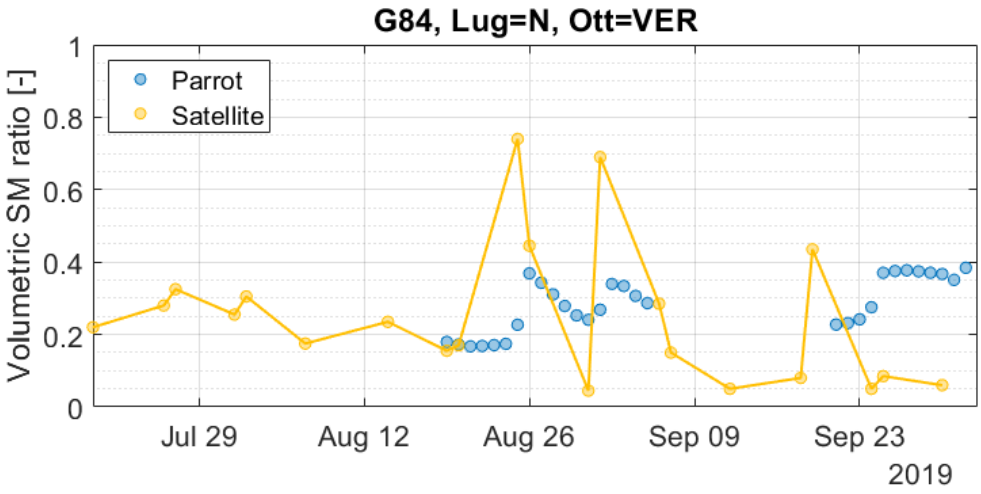

Figure B.10: Sensor G84 Surface Soil Moisture

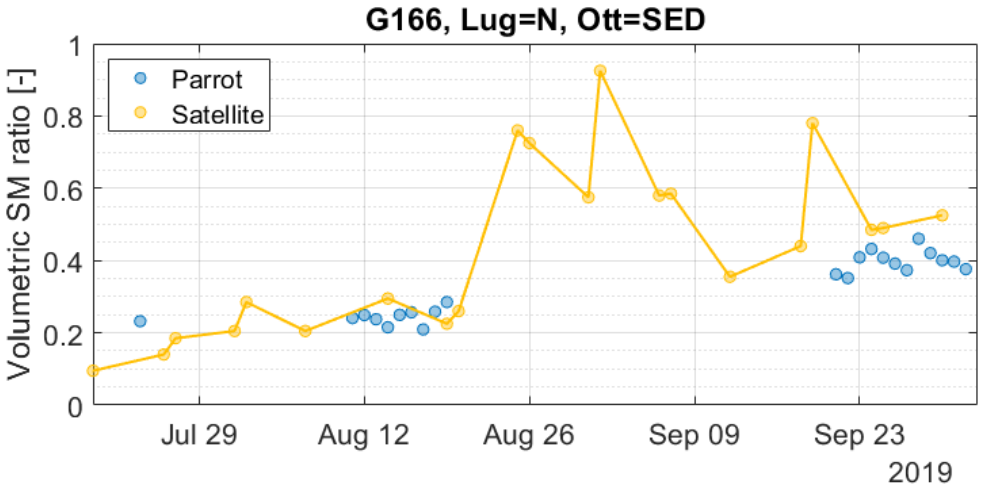

Figure B.11: Sensor G166 Surface Soil Moisture

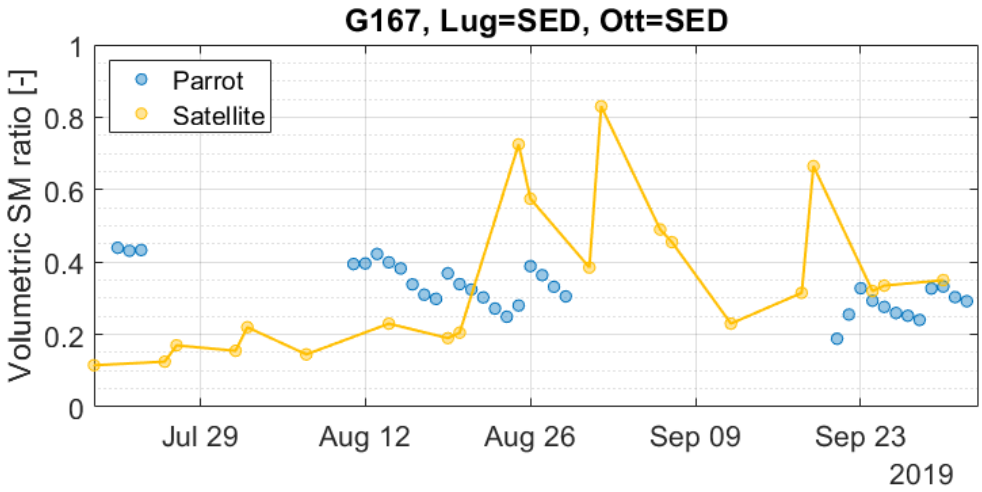

Figure B.12: Sensor G167 Surface Soil Moisture

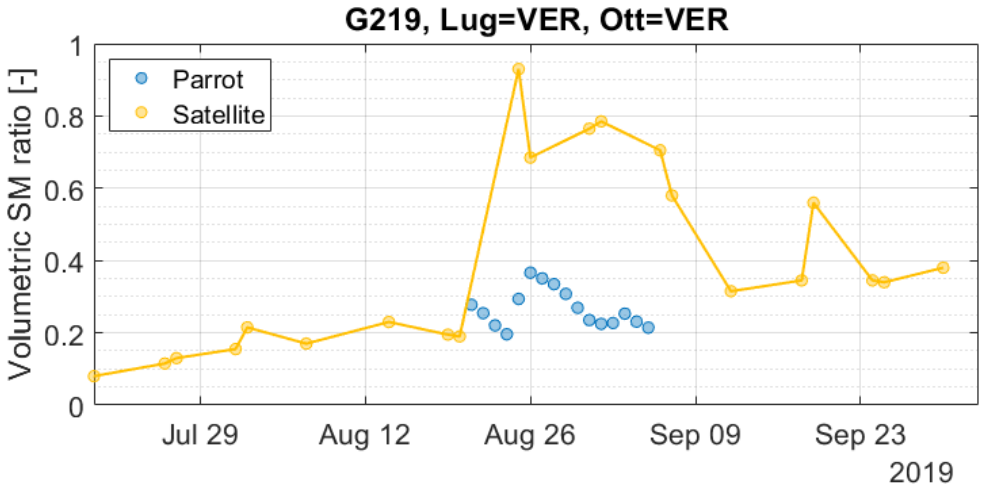

Figure B.13: Sensor G219 Surface Soil Moisture

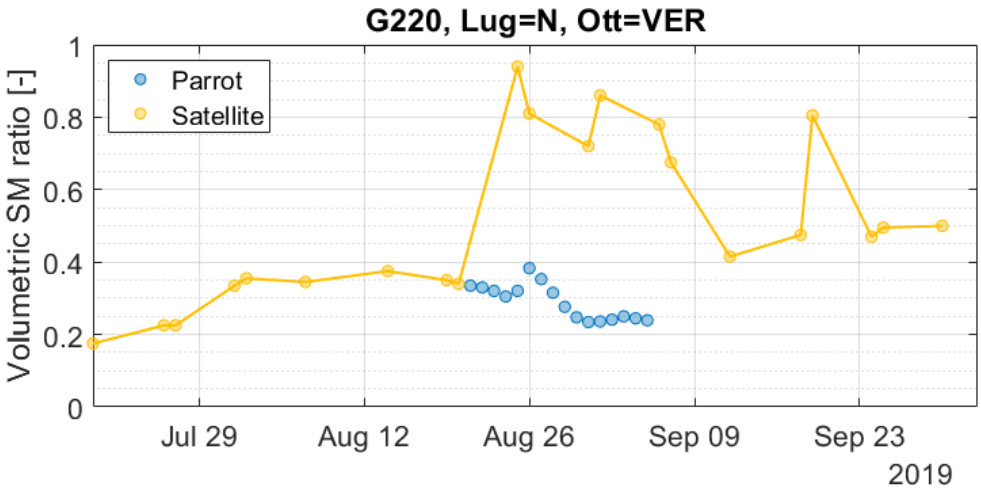

Figure B.14: Sensor G220 Surface Soil Moisture

B.2 Foggia Onoranza area

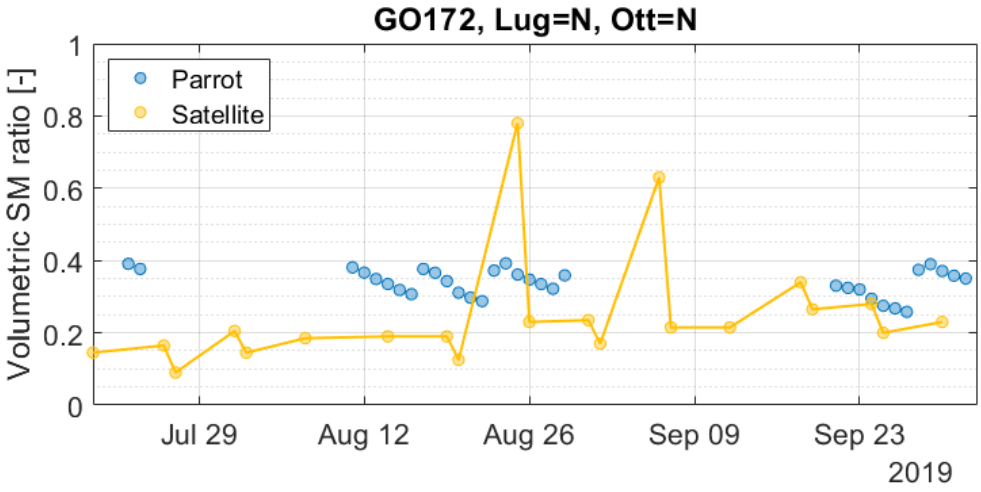

Figure B.15: Sensor GO172 Surface Soil Moisture

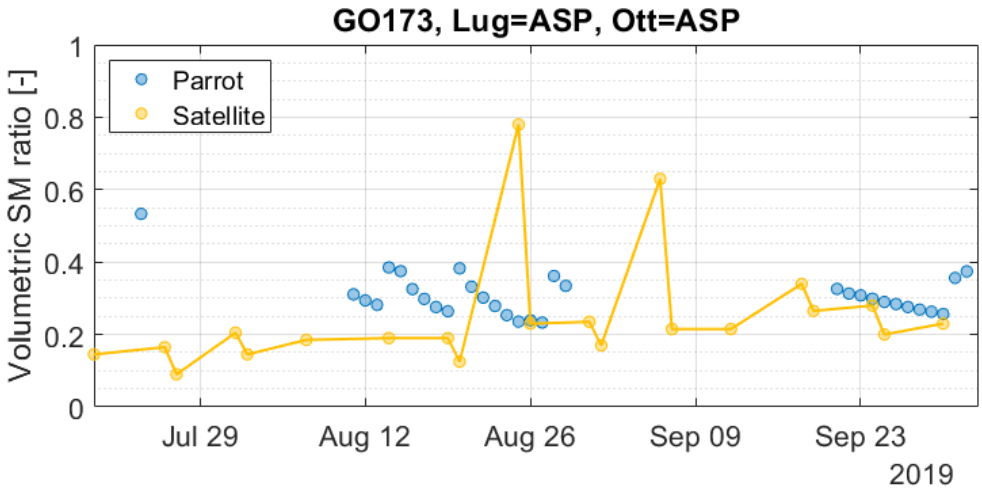

Figure B.16: Sensor GO173 Surface Soil Moisture

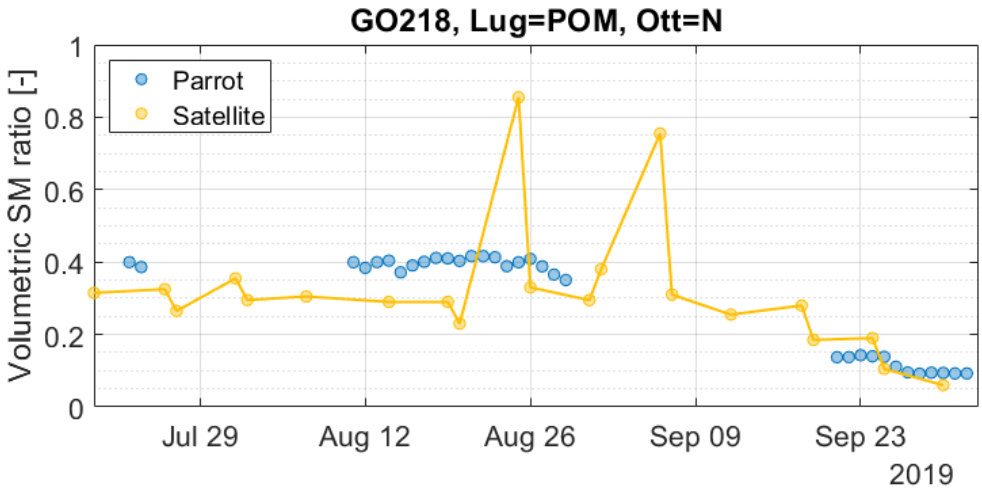

Figure B.17: Sensor GO218 Surface Soil Moisture

Appendix C

Aerodynamic Temperature ancillary results

C.1 R_{AH} and T_{AERO} comparison with ST results

In the following images, the scatter-plot comparisons between ST-retrieved R_{AH} and T_{AERO} and the corresponding values from other parametrizations are shown for the other case studies.

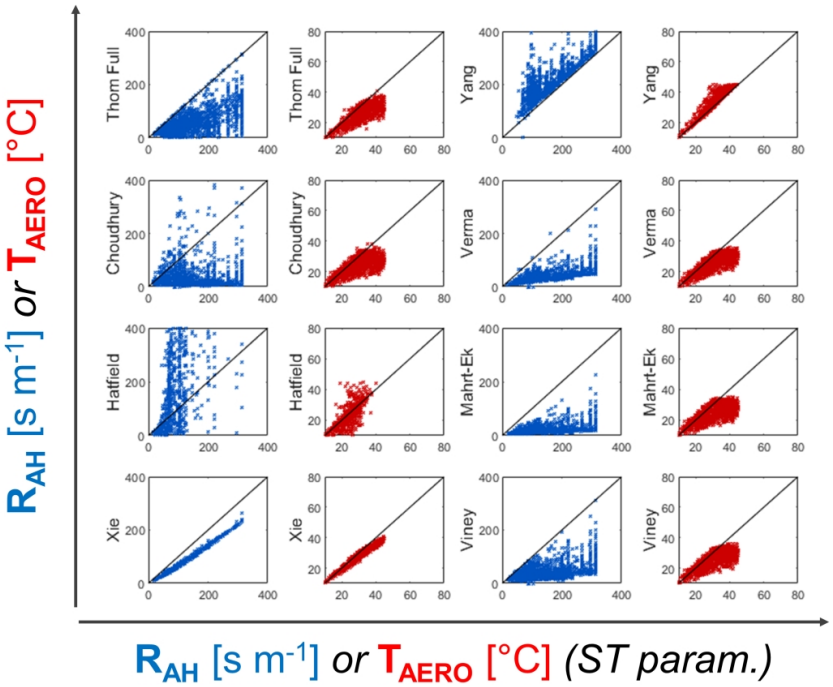

Figure C.1: Comparison by scatterplots between other parametrizations and ST, in terms of aerodynamic resistance (blue) and temperature (red). Data from the Landriano EC station

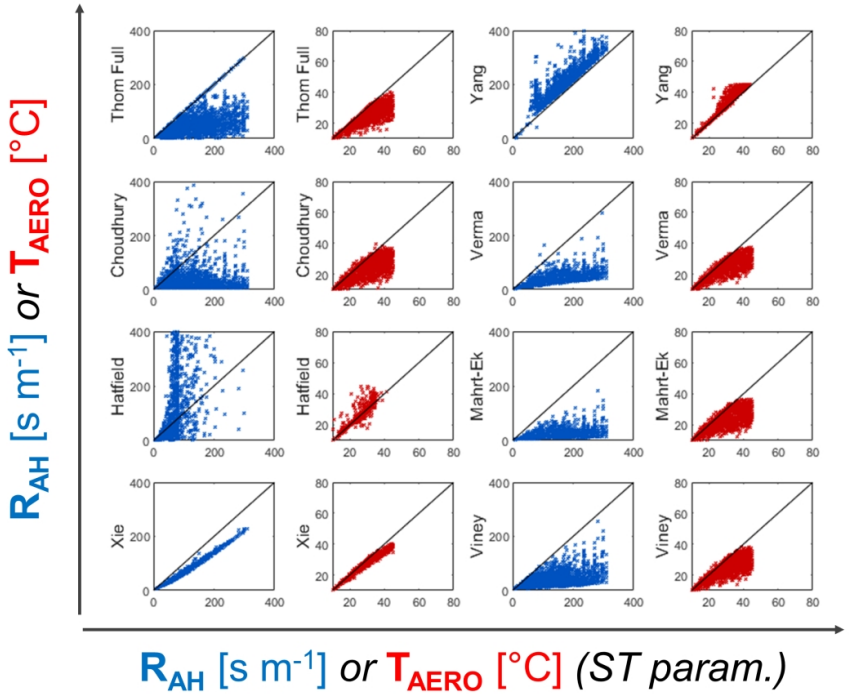

Figure C.2: Comparison by scatterplots between other parametrizations and ST, in terms of aerodynamic resistance (blue) and temperature (red). Data from the Livraga EC station

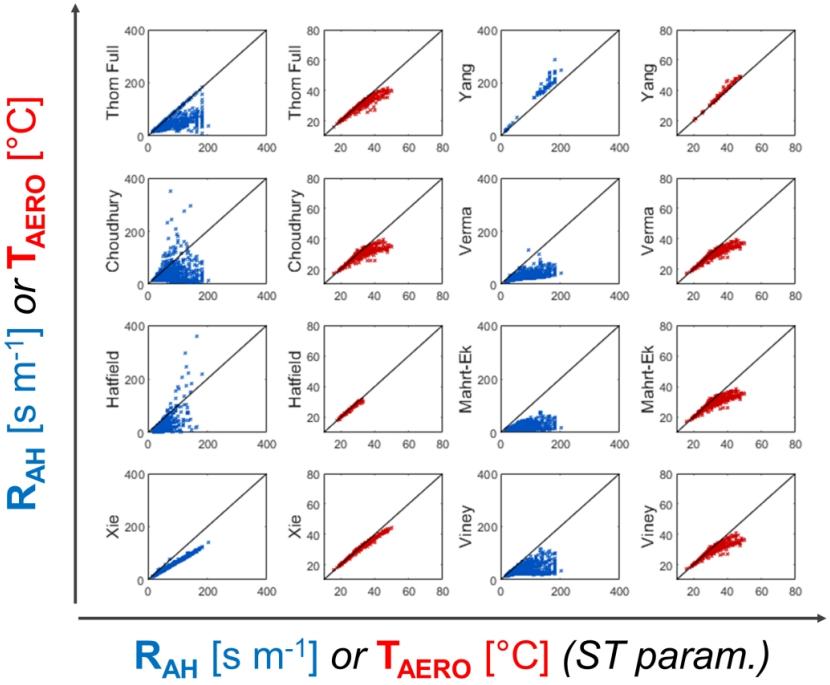

Figure C.3: Comparison by scatterplots between other parametrizations and ST, in terms of aerodynamic resistance (blue) and temperature (red). Data from the Foggia-Incoronata EC station

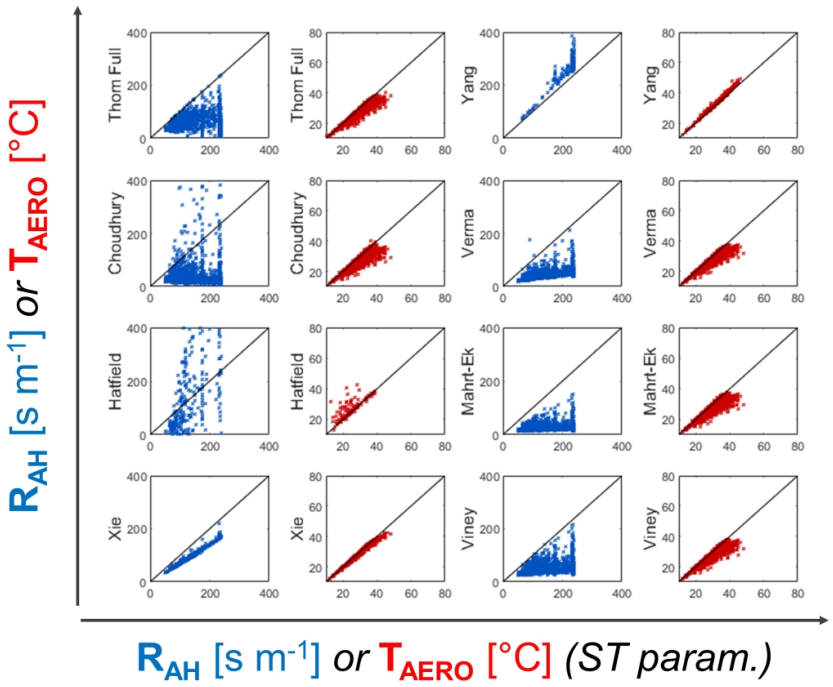

Figure C.4: Comparison by scatterplots between other parametrizations and ST, in terms of aerodynamic resistance (blue) and temperature (red). Data from the Foggia-Onoranza EC station

C.2 T_{AERO} v. Surface Temperature (LAN and LIV)

The T_{AERO} results for the Landriano and Livraga datasets are shown in the images below, opposed to the contemporary surface temperature measurements.

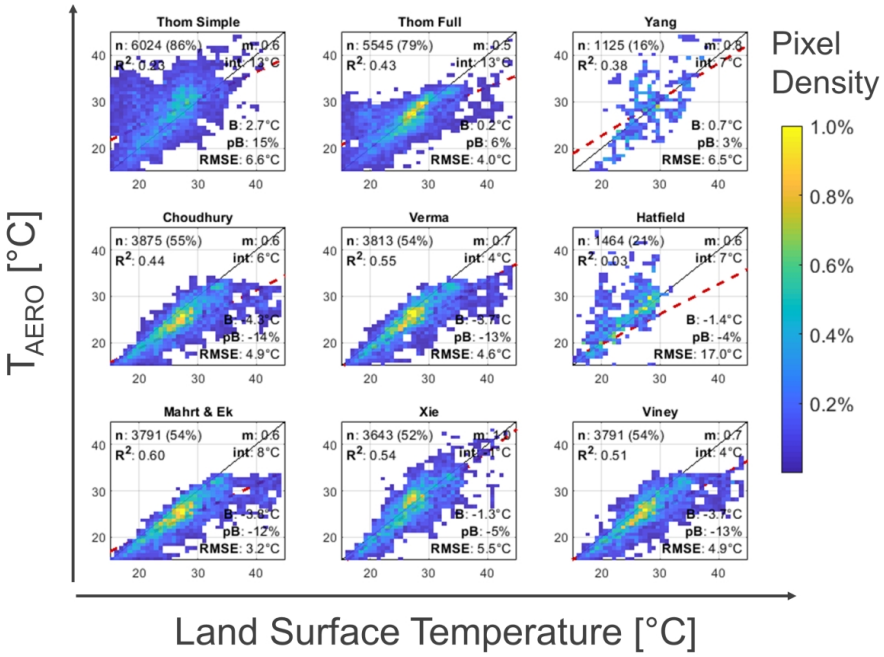

Figure C.5: Aerodynamic temperature comparisons for the Landriano test case

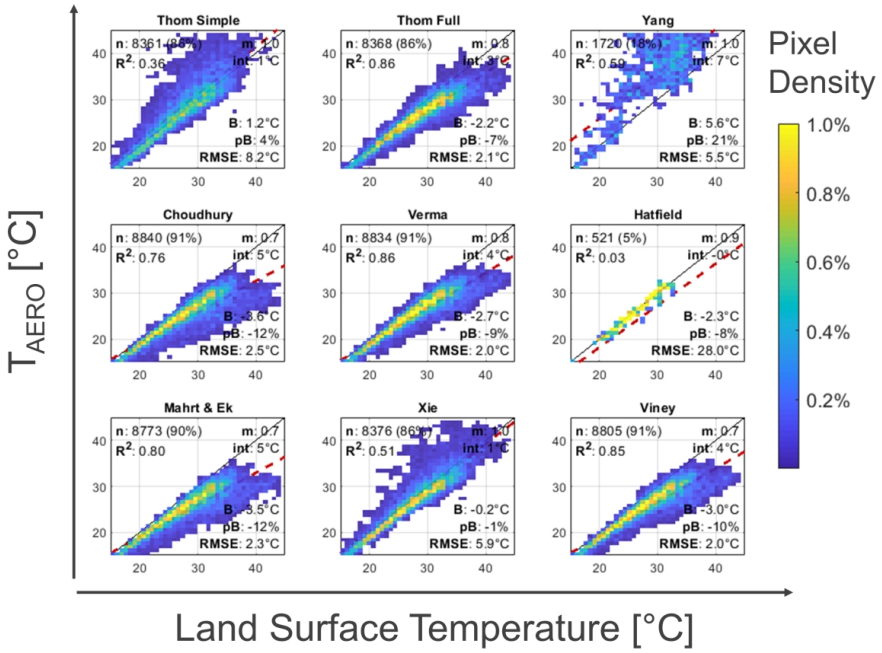

Figure C.6: Aerodynamic temperature comparisons for the Livraga test case

C.3 T_{AERO}–LST v. environmental parameters

The impact of environmental parameters over the temperature divergence in LAN, LIV and FON data is shown in the images below.

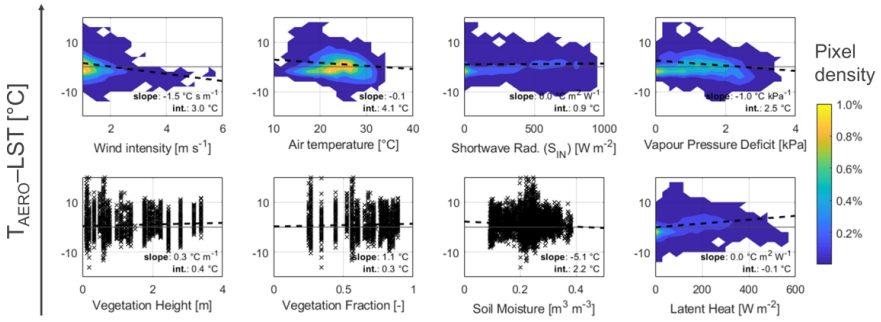

Figure C.7: T_{AERO}–LST v. environmental parametrs for the Landriano test case

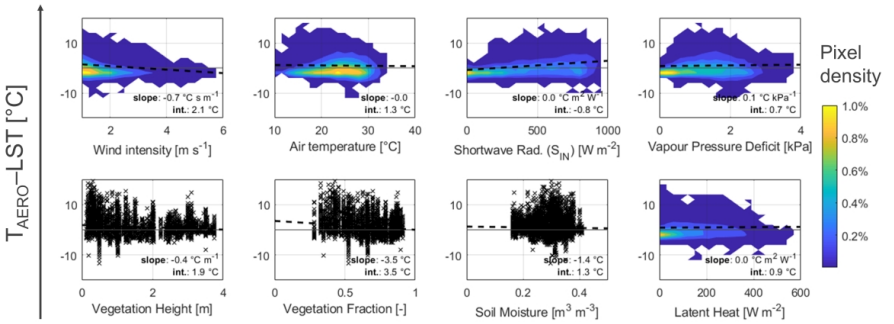

Figure C.8: T_{AERO}–LST v. environmental parametrs for the Livraga test case

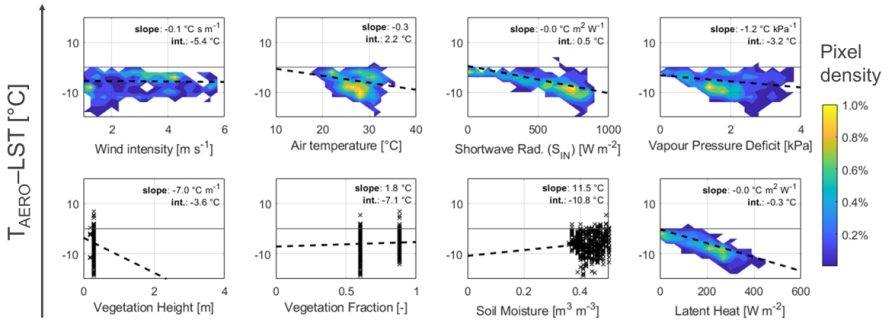

Figure C.9: T_{AERO}–LST v. environmental parametrs for the Foggia-Onoranza test case

Bibliography

Aguirre-García, S. D., Aranda-Barranco, S., Nieto, H., Serrano-Ortiz, P., Sánchez-Cañete, E. P., & Guerrero-Rascado, J. L. (2021). Modelling actual evapotranspiration using a two source energy balance model with sentinel imagery in herbaceous-free and herbaceous-cover mediterranean olive orchards. *Agricultural and Forest Meteorology*, *311*, 108692. https://doi.org/10.1016/J.AGRFORMET.2021.108692

Al Bitar, A., Mialon, A., Kerr, Y. H., Cabot, F., Richaume, P., Jacquette, E., Quesney, A., Mahmoodi, A., Tarot, S., Parrens, M., Al-Yaari, A., Pellarin, T., Rodriguez-Fernandez, N., & Wigneron, J.-P. (2017). The global smos level 3 daily soil moisture and brightness temperature maps. *Earth System Science Data*, *9*, 293–315. https://doi.org/10.5194/essd-9-293-2017

Allen, R. G., Pereira, L. S., Raes, D., & Smith, M. (1998). *Crop evapotranspiration - guidelines for computing crop water requirements - fao irrigation and drainage paper 56*. FAO - Food and Agriculture Organization of the United Nations.

Anderson, M., Neale, C., Li, F., Norman, J., Kustas, W., Jayanthi, H., & Chavez, J. (2004). Upscaling ground observations of vegetation water content, canopy height, and leaf area index during smex02 using aircraft and landsat imagery. *Remote Sensing of Environment*, *92*, 447–464. https://doi.org/10.1016/j.rse.2004.03.019

Aouade, G., Jarlan, L., Ezzahar, J., Er-Raki, S., Napoly, A., Benkaddour, A., Khabba, S., Boulet, G., Garrigues, S., Chehbouni, A., & Boone, A. (2020). Evapotranspiration partition using the multiple energy balance version of the isba-a-gs land surface model over two irrigated crops in a semi-arid mediterranean region (marrakech, morocco). *Hydrology and Earth System Sciences*, *24*, 3789–3814. https://doi.org/10.5194/hess-24-3789-2020

Aron, P. G., Poulsen, C. J., Fiorella, R. P., Matheny, A. M., & Veverica, T. J. (2020). An isotopic approach to partition evapotranspiration in a mixed deciduous forest. *Ecohydrology*, *13*. https://doi.org/10.1002/eco.2229

Bastiaanssen, W., Menenti, M., Feddes, R., & Holtslag, A. (1998). A remote sensing surface energy balance algorithm for land (sebal). 1. formulation. *Journal of Hydrology*, *212-213*, 198–212. https://doi.org/10.1016/S0022-1694(98)00253-4

Bastola, S., & Misra, V. (2014). Evaluation of dynamically downscaled reanalysis precipitation data for hydrological application. *Hydrological Processes*, *28*, 1989–2002. https://doi.org/10.1002/hyp.9734

Bauer-Marschallinger, B., Freeman, V., Cao, S., Paulik, C., Schaufler, S., Stachl, T., Modanesi, S., Massari, C., Ciabatta, L., Brocca, L., & Wagner, W. (2019). Toward global soil moisture monitoring with sentinel-1: Harnessing assets and overcoming obstacles. *IEEE Transactions on Geoscience and Remote Sensing*, *57*, 520–539. https://doi.org/10.1109/TGRS.2018.2858004

Bauer-Marschallinger, B., Paulik, C., Hochstöger, S., Mistelbauer, T., Modanesi, S., Ciabatta, L., Massari, C., Brocca, L., & Wagner, W. (2018). Soil moisture from fusion of scatterometer and sar: Closing the scale gap with temporal filtering. *Remote Sensing*, *10*, 1030. https://doi.org/10.3390/rs10071030

Beck, H. E., Zimmermann, N. E., McVicar, T. R., Vergopolan, N., Berg, A., & Wood, E. F. (2018). Present and future köppen-geiger climate classification maps at 1-km resolution. *Scientific Data*, *5*, 180214. https://doi.org/10.1038/sdata.2018.214

Berg, P., Donnelly, C., & Gustafsson, D. (2018). Near-real-time adjusted reanalysis forcing data for hydrology. *Hydrology and Earth System Sciences*, *22*, 989–1000. https://doi.org/10.5194/hess-22-989-2018

Bhattarai, N., Mallick, K., Brunsell, N. A., Sun, G., & Jain, M. (2018). Regional evapotranspiration from an image-based implementation of the surface temperature initiated closure (stic1.2) model and its validation across an aridity gradient in the conterminous us. *Hydrology and Earth System Sciences*, *22*, 2311–2341. https://doi.org/10.5194/hess-22-2311-2018

Bian, Z., Cao, B., Li, H., Du, Y., Song, L., Fan, W., Xiao, Q., & Liu, Q. (2017). A robust inversion algorithm for surface leaf and soil temperatures using the vegetation clumping index. *Remote Sensing*, *9*, 780. https://doi.org/10.3390/rs9080780

Blöschl, G., & Sivapalan, M. (1995). Scale issues in hydrological modelling: A review. *Hydrological Processes*, *9*, 251–290. https://doi.org/10.1002/hyp.3360090305

Bogena, H., Herbst, M., Huisman, J., Rosenbaum, U., Weuthen, A., & Vereecken, H. (2010). Potential of wireless sensor networks for measuring soil water content variability. *Vadose Zone Journal*, *9*, 1002–1013. https://doi.org/10.2136/vzj2009.0173

Boulet, G., Olioso, A., Ceschia, E., Marloie, O., Coudert, B., Rivalland, V., Chirouze, J., & Chehbouni, G. (2012). An empirical expression to relate aerodynamic and surface temperatures for use within single-source energy balance models. *Agricultural and Forest Meteorology*, *161*, 148–155. https://doi.org/10.1016/j.agrformet.2012.03.008

Breda, N. J. J. (2003). Ground-based measurements of leaf area index: A review of methods, instruments and current controversies. *Journal of Experimental Botany*, *54*, 2403–2417. https://doi.org/10.1093/jxb/erg263

Brocca, L., Hasenauer, S., Lacava, T., Melone, F., Moramarco, T., Wagner, W., Dorigo, W., Matgen, P., Martínez-Fernández, J., Llorens, P., Latron, J., Martin, C., & Bittelli, M. (2011). Soil moisture estimation through ascat and amsr-e sensors: An intercomparison and validation study across europe. *Remote Sensing of Environment*, *115*, 3390–3408. https://doi.org/10.1016/j.rse.2011.08.003

Brooks, R. H., & Corey, A. T. (1964). Hydrology paper no. 3. *Hydraulic properties of porous media*.

Cammalleri, C., Anderson, M. C., Ciraolo, G., D'Urso, G., Kustas, W. P., Loggia, G. L., & Minacapilli, M. (2010). The impact of in-canopy wind profile formulations on heat flux estimation in an open orchard using the remote sensing-based two-source model. *Hydrology and Earth System Sciences*, *14*, 2643–2659. https://doi.org/10.5194/hess-14-2643-2010

Cammalleri, C., Anderson, M., Ciraolo, G., D'Urso, G., Kustas, W., Loggia, G. L., & Minacapilli, M. (2012). Applications of a remote sensing-based two-source energy balance algorithm for mapping surface fluxes without in situ air temperature observations. *Remote Sensing of Environment*, *124*, 502–515. https://doi.org/10.1016/j.rse.2012.06.009

Campbell, G., & Norman, J. (1998). *An introduction to environmental biophysics*. Springer.

Ceppi, A., Ravazzani, G., Salandin, A., Rabuffetti, D., Montani, A., Borgonovo, E., & Mancini, M. (2013). Effects of temperature on flood forecasting: Analysis of an operative case study in

alpine basins. *Natural Hazards and Earth System Sciences*, *13*, 1051–1062. https://doi.org/10.5194/nhess-13-1051-2013

Chávez, J. L., Howell, T. A., Gowda, P. H., Copeland, K. S., & Prueger, J. H. (2010). Surface aerodynamic temperature modeling over rainfed cotton. *Transactions of the ASABE*, *53*, 759–767. https://doi.org/10.13031/2013.30081

Chávez, J. L., & Neale, C. M. U. (2003). Validating airborne multispectral remotely sensed heat fluxes with ground energy balance tower and heat flux source area (footprint) functions. *2003, Las Vegas, NV July 27-30, 2003*. https://doi.org/10.13031/2013.15014

Chehbouni, A. (1996). Examination of the difference between radiative and aerodynamic surface temperatures over sparsely vegetated surfaces. *Remote Sensing of Environment*, *58*, 177–186. https://doi.org/10.1016/S0034-4257(96)00037-5

Chen, F., Crow, W. T., Bindlish, R., Colliander, A., Burgin, M. S., Asanuma, J., & Aida, K. (2018). Global-scale evaluation of smap, smos and ascat soil moisture products using triple collocation. *Remote Sensing of Environment*, *214*, 1–13. https://doi.org/10.1016/j.rse.2018.05.008

Choudhury, B., Reginato, R., & Idso, S. (1986). An analysis of infrared temperature observations over wheat and calculation of latent heat flux. *Agricultural and Forest Meteorology*, *37*, 75–88. https://doi.org/10.1016/0168-1923(86)90029-8

Ciraolo, G., Cammalleri, C., Capodici, F., D'Urso, G., & Maltese, A. (2012). Mapping evapotranspiration on vineyards: A comparison between penman-monteith and energy balance approaches for operational purposes. In C. M. U. Neale & A. Maltese (Eds.). https://doi.org/10.1117/12.974967

Colaizzi, P., Agam, N., Tolk, J., Evett, S., Howell, T., Gowda, P., O'Shaughnessy, S., Kustas, W., & Anderson, M. (2014). Two-source energy balance model to calculate e, t, and et: Comparison of priestley-taylor and penman-monteith formulations and two time scaling methods. *Transactions of the ASABE*, 479–498. https://doi.org/10.13031/trans.57.10423

Colaizzi, P. D., Evett, S. R., Howell, T. A., & Tolk, J. A. (2004). Comparison of aerodynamic and radiometric surface temperature using precision weighing lysimeters. In W. Gao & D. R. Shaw (Eds.). https://doi.org/10.1117/12.559503

Colaizzi, P. D., Kustas, W. P., Anderson, M. C., Agam, N., Tolk, J. A., Evett, S. R., Howell, T. A., Gowda, P. H., & O'Shaughnessy, S. A. (2012). Two-source energy balance model estimates of evapotranspiration using component and composite surface temperatures. *Advances in Water Resources*, *50*, 134–151. https://doi.org/10.1016/j.advwatres.2012.06.004

Corbari, C., & Mancini, M. (2014a). Intercomparison across scales between remotely-sensed land surface temperature and representative equilibrium temperature from a distributed energy water balance model. *Hydrological Sciences Journal*, *59*, 1830–1843. https://doi.org/10.1080/02626667.2014.946418

Corbari, C., Ravazzani, G., Ceppi, A., & Mancini, M. (2013). Multi-pixel calibration of a distributed energy water balance model using satellite data of land surface temperature and eddy covariance data. *Procedia Environmental Sciences*, *19*, 285–292. https://doi.org/10.1016/j.proenv.2013.06.033

Corbari, C., Ravazzani, G., Martinelli, J., & Mancini, M. (2009). Elevation based correction of snow coverage retrieved from satellite images to improve model calibration. *Hydrology and Earth System Sciences*, *13*, 639–649. https://doi.org/10.5194/hess-13-639-2009

Corbari, C., Jovanovic, D. S., Nardella, L., Sobrino, J., & Mancini, M. (2020). Evapotranspiration estimates at high spatial and temporal resolutions from an energy–water balance model

and satellite data in the capitanata irrigation consortium. *Remote Sensing*, *12*, 4083. https://doi.org/10.3390/rs12244083

Corbari, C., & Mancini, M. (2014b). Calibration and validation of a distributed energy–water balance model using satellite data of land surface temperature and ground discharge measurements. *Journal of Hydrometeorology*, *15*, 376–392. https://doi.org/10.1175/JHM-D-12-0173.1

Corbari, C., Masseroni, D., & Mancini, M. (2012). Effetto delle correzioni dei dati misurati da stazioni eddy covariance sulla stima dei flussi evapotraspirativi. *Italian Journal of Agrometeorology*.

Corbari, C., Ravazzani, G., & Mancini, M. (2011). A distributed thermodynamic model for energy and mass balance computation: Fest-ewb. *Hydrological Processes*, *25*, 1443–1452. https://doi.org/10.1002/hyp.7910

Corbari, C., Salerno, R., Ceppi, A., Telesca, V., & Mancini, M. (2019). Smart irrigation forecast using satellite landsat data and meteo-hydrological modeling. *Agricultural Water Management*, *212*, 283–294. https://doi.org/10.1016/j.agwat.2018.09.005

Corbari, C., Timmermans, W., & Andreu, A. (2015). Intercomparison of surface energy fluxes estimates from the fest-ewb and tseb models over the heterogeneous reflex 2012 site (barrax, spain). *Acta Geophysica*, *63*, 1609–1638. https://doi.org/10.2478/s11600-014-0258-x

Cracknell, A. P. (2018). The development of remote sensing in the last 40 years. *International Journal of Remote Sensing*, *39*, 8387–8427. https://doi.org/10.1080/01431161.2018.1550919

Cui, C., Xu, J., Zeng, J., Chen, K.-S., Bai, X., Lu, H., Chen, Q., & Zhao, T. (2017). Soil moisture mapping from satellites: An intercomparison of smap, smos, fy3b, amsr2, and esa cci over two dense network regions at different spatial scales. *Remote Sensing*, *10*, 33. https://doi.org/10.3390/rs10010033

Czapla-Myers, J., McCorkel, J., Anderson, N., Thome, K., Biggar, S., Helder, D., Aaron, D., Leigh, L., & Mishra, N. (2015). The ground-based absolute radiometric calibration of landsat 8 oli. *Remote Sensing*, *7*, 600–626. https://doi.org/10.3390/rs70100600

Dai, A., Trenberth, K. E., & Karl, T. R. (1999). Effects of clouds, soil moisture, precipitation, and water vapor on diurnal temperature range. *Journal of Climate*, *12*, 2451–2473. https://doi.org/10.1175/1520-0442(1999)012⟨2451:EOCSMP⟩2.0.CO;2

de Jeu, R., & Owe, M. (2008). *Amsr2/gcom-w1 surface soil moisture (lprm) l3 1 day 10 km x 10 km descending v001 (*$lprm_amsr2_ds_doilm3$*)*.

DiStasio Jr., R. J., & Resmini, R. G. (2010). Atmospheric compensation of thermal infrared hyperspectral imagery with the emissive empirical line method and the in-scene atmospheric compensation algorithms: A comparison. In S. S. Shen & P. E. Lewis (Eds.). https://doi.org/10.1117/12.849898

Dorigo, W., Himmelbauer, I., Aberer, D., Schremmer, L., Petrakovic, I., Zappa, L., Preimesberger, W., Xaver, A., Annor, F., Ardö, J., Baldocchi, D., Bitelli, M., Blöschl, G., Bogena, H., Brocca, L., Calvet, J.-C., Camarero, J. J., Capello, G., Choi, M., ... Sabia, R. (2021). The international soil moisture network: Serving earth system science for over a decade. *Hydrology and Earth System Sciences*, *25*, 5749–5804. https://doi.org/10.5194/hess-25-5749-2021

Dorigo, W., Wagner, W., Albergel, C., Albrecht, F., Balsamo, G., Brocca, L., Chung, D., Ertl, M., Forkel, M., Gruber, A., Haas, E., Hamer, P. D., Hirschi, M., Ikonen, J., de Jeu, R., Kidd, R., Lahoz, W., Liu, Y. Y., Miralles, D., ... Lecomte, P. (2017). Esa cci soil moisture

for improved earth system understanding: State-of-the art and future directions. *Remote Sensing of Environment*, *203*, 185–215. https://doi.org/10.1016/j.rse.2017.07.001

Dubovik, O., Schuster, G. L., Xu, F., Hu, Y., Bösch, H., Landgraf, J., & Li, Z. (2021). Grand challenges in satellite remote sensing. *Frontiers in Remote Sensing*, *2*. https://doi.org/10.3389/frsen.2021.619818

D'Urso, G., Bolognesi, S. F., Kustas, W. P., Knipper, K. R., Anderson, M. C., Alsina, M. M., Hain, C. R., Alfieri, J. G., Prueger, J. H., Gao, F., McKee, L. G., Michele, C. D., McElrone, A. J., Bambach, N., Sanchez, L., & Belfiore, O. R. (2021). Determining evapotranspiration by using combination equation models with sentinel-2 data and comparison with thermal-based energy balance in a california irrigated vineyard. *Remote Sensing*, *13*, 3720. https://doi.org/10.3390/rs13183720

El Hajj, M., Baghdadi, N., Zribi, M., Rodríguez-Fernández, N., Wigneron, J., Al-Yaari, A., Bitar, A. A., Albergel, C., & Calvet, J.-C. (2018). Evaluation of smos, smap, ascat and sentinel-1 soil moisture products at sites in southwestern france. *Remote Sensing*, *10*, 569. https://doi.org/10.3390/rs10040569

Entekhabi, D., Njoku, E. G., O'Neill, P. E., Kellogg, K. H., Crow, W. T., Edelstein, W. N., Entin, J. K., Goodman, S. D., Jackson, T. J., Johnson, J., Kimball, J., Piepmeier, J. R., Koster, R. D., Martin, N., McDonald, K. C., Moghaddam, M., Moran, S., Reichle, R., Shi, J. C., ... Zyl, J. V. (2010). The soil moisture active passive (smap) mission. *Proceedings of the IEEE*, *98*, 704–716. https://doi.org/10.1109/JPROC.2010.2043918

Ershadi, A., McCabe, M., Evans, J., & Walker, J. (2013). Effects of spatial aggregation on the multi-scale estimation of evapotranspiration. *Remote Sensing of Environment*, *131*, 51–62. https://doi.org/10.1016/j.rse.2012.12.007

Facchi, A., Gharsallah, O., Corbari, C., Masseroni, D., Mancini, M., & Gandolfi, C. (2013). Determination of maize crop coefficients in humid climate regime using the eddy covariance technique. *Agricultural Water Management*, *130*, 131–141. https://doi.org/10.1016/j.agwat.2013.08.014

Foken, T., Wimmer, F., Mauder, M., Thomas, C., & Liebethal, C. (2006). Some aspects of the energy balance closure problem. *Atmospheric Chemistry and Physics*, *6*, 4395–4402. https://doi.org/10.5194/acp-6-4395-2006

Foken, T. (2006). 50 years of the monin–obukhov similarity theory. *Boundary-Layer Meteorology*, *119*, 431–447. https://doi.org/10.1007/s10546-006-9048-6

Foster, T., Gonçalves, I. Z., Campos, I., Neale, C. M. U., & Brozović, N. (2019). Assessing landscape scale heterogeneity in irrigation water use with remote sensing and ¡i¿in situ¡/i¿ monitoring. *Environmental Research Letters*, *14*, 024004. https://doi.org/10.1088/1748-9326/aaf2be

Gao, B. C. (1996). Ndwi—a normalized difference water index for remote sensing of vegetation liquid water from space. *Remote Sensing of Environment*, *58*, 257–266. https://doi.org/10.1016/S0034-4257(96)00067-3

Giacomelli, A., Bacchiega, U., Troch, P. A., & Mancini, M. (1995). Evaluation of surface soil moisture distribution by means of sar remote sensing techniques and conceptual hydrological modelling. *Journal of Hydrology*, *166*, 445–459. https://doi.org/10.1016/0022-1694(94)05100-C

Gonzalez-Dugo, M., Neale, C., Mateos, L., Kustas, W., Prueger, J., Anderson, M., & Li, F. (2009). A comparison of operational remote sensing-based models for estimating crop evapotranspiration. *Agricultural and Forest Meteorology*, *149*, 1843–1853. https://doi.org/10.1016/j.agrformet.2009.06.012

Grayson, R., & Blöschl, G. (2000). *Spatial patterns in catchment hydrology: Observations and modelling*. Cambridge University Press.

Gruber, A., Su, C.-H., Zwieback, S., Crow, W., Dorigo, W., & Wagner, W. (2016). Recent advances in (soil moisture) triple collocation analysis. *International Journal of Applied Earth Observation and Geoinformation*, *45*, 200–211. https://doi.org/10.1016/j.jag.2015.09.002

Gruber, A., Dorigo, W. A., Crow, W., & Wagner, W. (2017). Triple collocation-based merging of satellite soil moisture retrievals. *IEEE Transactions on Geoscience and Remote Sensing*, *55*, 6780–6792. https://doi.org/10.1109/TGRS.2017.2734070

Gruber, A., Scanlon, T., van der Schalie, R., Wagner, W., & Dorigo, W. (2019). Evolution of the esa cci soil moisture climate data records and their underlying merging methodology. *Earth System Science Data*, *11*, 717–739. https://doi.org/10.5194/essd-11-717-2019

Gutman, G., & Ignatov, A. (1998). The derivation of the green vegetation fraction from noaa/avhrr data for use in numerical weather prediction models. *International Journal of Remote Sensing*, *19*, 1533–1543. https://doi.org/10.1080/014311698215333

Hank, T., Bach, H., & Mauser, W. (2015). Using a remote sensing-supported hydro-agroecological model for field-scale simulation of heterogeneous crop growth and yield: Application for wheat in central europe. *Remote Sensing*, *7*, 3934–3965. https://doi.org/10.3390/rs70403934

Hatfield, J., Perrier, A., & Jackson, R. (1983). *Estimation of evapotranspiration at one time-of-day using remotely sensed surface temperatures*. https://doi.org/10.1016/B978-0-444-42214-9.50030-2

Heinemann, S., Siegmann, B., Thonfeld, F., Muro, J., Jedmowski, C., Kemna, A., Kraska, T., Muller, O., Schultz, J., Udelhoven, T., Wilke, N., & Rascher, U. (2020). Land surface temperature retrieval for agricultural areas using a novel uav platform equipped with a thermal infrared and multispectral sensor. *Remote Sensing*, *12*, 1075. https://doi.org/10.3390/rs12071075

Hoefsloot, P., Kayitakire, F., & Duveiller, G. (2012). *Combining crop models and remote sensing for yield prediction - concepts, applications and challenges for heterogeneous, smallholder environments*. Joint Research Centre, Institute for Environment and Sustainability.

Hsieh, C.-I., Katul, G., & Chi, T.-w. (2000). An approximate analytical model for footprint estimation of scalar fluxes in thermally stratified atmospheric flows. *Advances in Water Resources*, *23*, 765–772. https://doi.org/10.1016/S0309-1708(99)00042-1

Huang, J., Gómez-Dans, J. L., Huang, H., Ma, H., Wu, Q., Lewis, P. E., Liang, S., Chen, Z., Xue, J.-H., Wu, Y., Zhao, F., Wang, J., & Xie, X. (2019). Assimilation of remote sensing into crop growth models: Current status and perspectives. *Agricultural and Forest Meteorology*, *276-277*, 107609. https://doi.org/10.1016/j.agrformet.2019.06.008

Huete, A. (1988). A soil-adjusted vegetation index (savi). *Remote Sensing of Environment*, *25*, 295–309. https://doi.org/10.1016/0034-4257(88)90106-X

Hunt, E. R., & Rock, B. N. (1989). Detection of changes in leaf water content using near- and middle-infrared reflectances. *Remote Sensing of Environment*, *30*, 43–54. https://doi.org/10.1016/0034-4257(89)90046-1

Hunt, J. (1998). Lewis fry richardson and his contributions to mathematics, meteorology and models of conflict. *Annual Review of Fluid Mechanics*, *30*, xiii–xxxvi. https://doi.org/10.1146/annurev.fluid.30.1.0

Jackson, T. J., Cosh, M. H., Bindlish, R., Starks, P. J., Bosch, D. D., Seyfried, M., Goodrich, D. C., Moran, M. S., & Du, J. (2010). Validation of advanced microwave scanning radiometer soil

moisture products. *IEEE Transactions on Geoscience and Remote Sensing*, *48*, 4256–4272. https://doi.org/10.1109/TGRS.2010.2051035

Jarvis, P. (1976). He interpretation of the variations in leaf water potential and stomatal conductance found in canopies in the field. *Philosophical Transactions of the Royal Society of London. Series B, Biological Sciences*, *273*, 593–610.

Jimenez-Munoz, J. C., Sobrino, J. A., Skokovic, D., Mattar, C., & Cristobal, J. (2014). Land surface temperature retrieval methods from landsat-8 thermal infrared sensor data. *IEEE Geoscience and Remote Sensing Letters*, *11*, 1840–1843. https://doi.org/10.1109/LGRS.2014.2312032

Jolivot, A., Lebourgeois, V., Leroux, L., Ameline, M., Andriamanga, V., Bellón, B., Castets, M., Crespin-Boucaud, A., Defourny, P., Diaz, S., Dieye, M., Dupuy, S., Ferraz, R., Gaetano, R., Gely, M., Jahel, C., Kabore, B., Lelong, C., le Maire, G., … Bégué, A. (2021). Harmonized in situ datasets for agricultural land use mapping and monitoring in tropical countries. *Earth System Science Data*, *13*, 5951–5967. https://doi.org/10.5194/essd-13-5951-2021

Joshi, N., Baumann, M., Ehammer, A., Fensholt, R., Grogan, K., Hostert, P., Jepsen, M., Kuemmerle, T., Meyfroidt, P., Mitchard, E., Reiche, J., Ryan, C., & Waske, B. (2016). A review of the application of optical and radar remote sensing data fusion to land use mapping and monitoring. *Remote Sensing*, *8*, 70. https://doi.org/10.3390/rs8010070

Karpouzli, E., & Malthus, T. (2003). The empirical line method for the atmospheric correction of ikonos imagery. *International Journal of Remote Sensing*, *24*, 1143–1150. https://doi.org/10.1080/0143116021000026779

Kendall, M. G. (1938). A new measure of rank correlation. *Biometrika*, *30*, 81. https://doi.org/10.2307/2332226

Kerr, Y. H., Waldteufel, P., Wigneron, J.-P., Delwart, S., Cabot, F., Boutin, J., Escorihuela, M.-J., Font, J., Reul, N., Gruhier, C., Juglea, S. E., Drinkwater, M. R., Hahne, A., Martín-Neira, M., & Mecklenburg, S. (2010). The smos mission: New tool for monitoring key elements ofthe global water cycle. *Proceedings of the IEEE*, *98*, 666–687. https://doi.org/10.1109/JPROC.2010.2043032

Kerr, Y., Al-Yaari, A., Rodriguez-Fernandez, N., Parrens, M., Molero, B., Leroux, D., Bircher, S., Mahmoodi, A., Mialon, A., Richaume, P., Delwart, S., Bitar, A. A., Pellarin, T., Bindlish, R., Jackson, T., Rüdiger, C., Waldteufel, P., Mecklenburg, S., & Wigneron, J.-P. (2016). Overview of smos performance in terms of global soil moisture monitoring after six years in operation. *Remote Sensing of Environment*, *180*, 40–63. https://doi.org/10.1016/j.rse.2016.02.042

Khan, M. S., Baik, J., & Choi, M. (2021). A physical-based two-source evapotranspiration model with monin–obukhov similarity theory. *GIScience Remote Sensing*, *58*, 88–119. https://doi.org/10.1080/15481603.2020.1857625

Kustas, W., Li, F., Jackson, T., Prueger, J., MacPherson, J., & Wolde, M. (2004). Effects of remote sensing pixel resolution on modeled energy flux variability of croplands in iowa. *Remote Sensing of Environment*, *92*, 535–547. https://doi.org/10.1016/j.rse.2004.02.020

Kustas, W., & Anderson, M. (2009). Advances in thermal infrared remote sensing for land surface modeling. *Agricultural and Forest Meteorology*, *149*, 2071–2081. https://doi.org/10.1016/j.agrformet.2009.05.016

Kustas, W. P., & Norman, J. M. (1999). Evaluation of soil and vegetation heat flux predictions using a simple two-source model with radiometric temperatures for partial canopy cover. *Agricultural and Forest Meteorology*, *94*, 13–29. https://doi.org/10.1016/S0168-1923(99)00005-2

Kustas, W., Anderson, M., Norman, J., & Li, F. (2007). Utility of radiometric–aerodynamic temperature relations for heat flux estimation. *Boundary-Layer Meteorology*, *122*, 167–187. https://doi.org/10.1007/s10546-006-9093-1

Kutílek, M., & Nielsen, D. R. (1994). *Soil hydrology*. Catena-Verlag.

Li, F., Kustas, W. P., Anderson, M. C., Prueger, J. H., & Scott, R. L. (2008). Effect of remote sensing spatial resolution on interpreting tower-based flux observations. *Remote Sensing of Environment*, *112*, 337–349. https://doi.org/10.1016/j.rse.2006.11.032

Li, X., Gentine, P., Lin, C., Zhou, S., Sun, Z., Zheng, Y., Liu, J., & Zheng, C. (2019). A simple and objective method to partition evapotranspiration into transpiration and evaporation at eddy-covariance sites. *Agricultural and Forest Meteorology*, *265*, 171–182. https://doi.org/10.1016/j.agrformet.2018.11.017

Li, Y., Kustas, W. P., Huang, C., Nieto, H., Haghighi, E., Anderson, M. C., Domingo, F., Garcia, M., & Scott, R. L. (2019). Evaluating soil resistance formulations in thermal-based two-source energy balance (tseb) model: Implications for heterogeneous semiarid and arid regions. *Water Resources Research*, *55*, 1059–1078. https://doi.org/10.1029/2018WR022981

Liang, S. (2000). Numerical experiments on the spatial scaling of land surface albedo and leaf area index. *Remote Sensing Reviews*, *19*, 225–242. https://doi.org/10.1080/02757250009532420

Liu, S., Lu, L., Mao, D., & Jia, L. (2007). Evaluating parameterizations of aerodynamic resistance to heat transfer using field measurements. *Hydrology and Earth System Sciences*, *11*, 769–783. https://doi.org/10.5194/hess-11-769-2007

Liu, Y., Dorigo, W., Parinussa, R., de Jeu, R., Wagner, W., McCabe, M., Evans, J., & van Dijk, A. (2012). Trend-preserving blending of passive and active microwave soil moisture retrievals. *Remote Sensing of Environment*, *123*, 280–297. https://doi.org/10.1016/j.rse.2012.03.014

Lundstrom, D. R., & Stegman, E. C. (1988). *Irrigation scheduling by the checkbook method*.

Mahrt, L., & Ek, M. (1984). The influence of atmospheric stability on potential evaporation. *Journal of Climate and Applied Meteorology*, *23*, 222–234. https://doi.org/10.1175/1520-0450(1984)023⟨0222:TIOASO⟩2.0.CO;2

Mahrt, L., & Vickers, D. (2004). Bulk formulation of the surface heat flux. *Boundary-Layer Meteorology*, *110*, 357–379. https://doi.org/10.1023/B:BOUN.0000007244.42320.1e

Mallick, K., Boegh, E., Trebs, I., Alfieri, J. G., Kustas, W. P., Prueger, J. H., Niyogi, D., Das, N., Drewry, D. T., Hoffmann, L., & Jarvis, A. J. (2015). Reintroducing radiometric surface temperature into the penman-monteith formulation. *Water Resources Research*, *51*, 6214–6243. https://doi.org/10.1002/2014WR016106

Mallick, K., Toivonen, E., Trebs, I., Boegh, E., Cleverly, J., Eamus, D., Koivusalo, H., Drewry, D., Arndt, S. K., Griebel, A., Beringer, J., & Garcia, M. (2018). Bridging thermal infrared sensing and physically-based evapotranspiration modeling: From theoretical implementation to validation across an aridity gradient in australian ecosystems. *Water Resources Research*, *54*, 3409–3435. https://doi.org/10.1029/2017WR021357

Maltese, A., Cammalleri, C., Capodici, F., Ciraolo, G., Colletti, F., Loggia, G. L., & Santangelo, T. (2011). Comparing actual evapotranspiration and plant water potential on a vineyard. In C. M. U. Neale & A. Maltese (Eds.). https://doi.org/10.1117/12.899070

Mancini, M. (1990). *La modellazione distribuita della risposta idrologica: Effetti della variabilità spaziale e della scala di rappresentazione del fenomeno dell'assorbimento*. Politecnico di Milano.

Mantovani, F. F. (2016). *Misure in laboratorio e modellistica numerica dell'umidità del suolo e dei processi del ciclo idrologico: Il lisimetro*. Politecnico di Milano.

Marcial-Pablo, M., Gonzalez-Sanchez, A., Jimenez-Jimenez, S. I., Ontiveros-Capurata, R. E., & Ojeda-Bustamante, W. (2019). Estimation of vegetation fraction using rgb and multispectral images from uav. *International Journal of Remote Sensing*, *40*, 420–438. https://doi.org/10.1080/01431161.2018.1528017

Masseroni, D., Corbari, C., & Mancini, M. (2014). Validation of theoretical footprint models using experimental measurements of turbulent fluxes over maize fields in po valley. *Environmental Earth Sciences*, *72*, 1213–1225. https://doi.org/10.1007/s12665-013-3040-5

McCabe, M. F., Ershadi, A., Jimenez, C., Miralles, D. G., Michel, D., & Wood, E. F. (2016). The gewex landflux project: Evaluation of model evaporation using tower-based and globally gridded forcing data. *Geoscientific Model Development*, *9*, 283–305. https://doi.org/10.5194/gmd-9-283-2016

McCabe, M., Wood, E., Wójcik, R., Pan, M., Sheffield, J., Gao, H., & Su, H. (2008). Hydrological consistency using multi-sensor remote sensing data for water and energy cycle studies. *Remote Sensing of Environment*, *112*, 430–444. https://doi.org/10.1016/j.rse.2007.03.027

McCumber, M. C., & Pielke, R. A. (1981). Simulation of the effects of surface fluxes of heat and moisture in a mesoscale numerical model: 1. soil layer. *Journal of Geophysical Research*, *86*, 9929. https://doi.org/10.1029/JC086iC10p09929

Meng, X., Li, R., Luan, L., Lyu, S., Zhang, T., Ao, Y., Han, B., Zhao, L., & Ma, Y. (2018). Detecting hydrological consistency between soil moisture and precipitation and changes of soil moisture in summer over the tibetan plateau. *Climate Dynamics*, *51*, 4157–4168. https://doi.org/10.1007/s00382-017-3646-5

Meyers, T. P., & Hollinger, S. E. (2004). An assessment of storage terms in the surface energy balance of maize and soybean. *Agricultural and Forest Meteorology*, *125*(1), 105–115. https://doi.org/10.1016/j.agrformet.2004.03.001

Michael, P. R., Johnston, D. E., & Moreno, W. (2020). A conversion guide: Solar irradiance and lux illuminance. *Journal of Measurements in Engineering*, *8*, 153–166. https://doi.org/10.21595/jme.2020.21667

Mikhail, E., Bethel, J., & McGlone, J. (2001). *Modern photogrammetry*. Wiley Sons.

Mishra, A. K., & Coulibaly, P. (2009). Developments in hydrometric network design: A review. *Reviews of Geophysics*, *47*, RG2001. https://doi.org/10.1029/2007RG000243

Molero, B., Leroux, D. J., Richaume, P., Kerr, Y. H., Merlin, O., Cosh, M. H., & Bindlish, R. (2018). Multi-timescale analysis of the spatial representativeness of in situ soil moisture data within satellite footprints. *Journal of Geophysical Research: Atmospheres*, *123*, 3–21. https://doi.org/10.1002/2017JD027478

Monin, A., & Obukhov, A. (1954). Osnovnye zakonomernosti turbulentnogo peremeshivanija v prizemnom sloe atmosfery (basic laws of turbulent mixing in the atmosphere near the ground). *Trudy geofiz. inst. AN SSSR*, *24*, 163–187.

Monteith, J. (1965). Evaporation and environment. *Symposia of the Society for Experimental Biology*, *19*, 205–234.

Naeimi, V., Scipal, K., Bartalis, Z., Hasenauer, S., & Wagner, W. (2009). An improved soil moisture retrieval algorithm for ers and metop scatterometer observations. *IEEE Transactions on Geoscience and Remote Sensing*, *47*, 1999–2013. https://doi.org/10.1109/TGRS.2008.2011617

Nieto, H., Kustas, W. P., Torres-Rúa, A., Alfieri, J. G., Gao, F., Anderson, M. C., White, W. A., Song, L., del Mar Alsina, M., Prueger, J. H., McKee, M., Elarab, M., & McKee, L. G. (2019). Evaluation of tseb turbulent fluxes using different methods for the retrieval of

soil and canopy component temperatures from uav thermal and multispectral imagery. *Irrigation Science*, *37*, 389–406. https://doi.org/10.1007/s00271-018-0585-9

Nilson, T. (1971). A theoretical analysis of the frequency of gaps in plant stands. *Agricultural Meteorology*, *8*, 25–38. https://doi.org/10.1016/0002-1571(71)90092-6

Njoku, E., & Chan, S. (2006). Vegetation and surface roughness effects on amsr-e land observations. *Remote Sensing of Environment*, *100*, 190–199. https://doi.org/10.1016/j.rse.2005.10.017

Norman, J., Kustas, W., & Humes, K. (1995). Source approach for estimating soil and vegetation energy fluxes in observations of directional radiometric surface temperature. *Agricultural and Forest Meteorology*, *77*, 263–293. https://doi.org/10.1016/0168-1923(95)02265-Y

Ochoa-Tocachi, B. F., Buytaert, W., Antiporta, J., Acosta, L., Bardales, J. D., Célleri, R., Crespo, P., Fuentes, P., Gil-Ríos, J., Guallpa, M., Llerena, C., Olaya, D., Pardo, P., Rojas, G., Villacís, M., Villazón, M., Viñas, P., & Bièvre, B. D. (2018). High-resolution hydrometeorological data from a network of headwater catchments in the tropical andes. *Scientific Data*, *5*, 180080. https://doi.org/10.1038/sdata.2018.80

Ochsner, T. E., Cosh, M. H., Cuenca, R. H., Dorigo, W. A., Draper, C. S., Hagimoto, Y., Kerr, Y. H., Larson, K. M., Njoku, E. G., Small, E. E., & Zreda, M. (2013). State of the art in large-scale soil moisture monitoring. *Soil Science Society of America Journal*, *77*, 1888–1919. https://doi.org/10.2136/sssaj2013.03.0093

Paciolla, N., Corbari, C., Bitar, A. A., Kerr, Y., & Mancini, M. (2020). Irrigation and precipitation hydrological consistency with smos, smap, esa-cci, copernicus ssm1km, and amsr-2 remotely sensed soil moisture products. *Remote Sensing*, *12*, 3737. https://doi.org/10.3390/rs12223737

Paciolla, N., Corbari, C., Hu, G., Zheng, C., Menenti, M., Jia, L., & Mancini, M. (2021). Evapotranspiration estimates from an energy-water-balance model calibrated on satellite land surface temperature over the heihe basin. *Journal of Arid Environments*, *188*, 104466. https://doi.org/10.1016/j.jaridenv.2021.104466

Paciolla, N., Corbari, C., Maltese, A., Ciraolo, G., & Mancini, M. (2021). Proximal-sensing-powered modelling of energy-water fluxes in a vineyard: A spatial resolution analysis. *Remote Sensing*, *13*, 4699. https://doi.org/10.3390/rs13224699

Parlange, J.-Y., Steenhuis, T., Haverkamp, R., Barry, D., Culligan, P., Hogarth, W., Parlange, M., Ross, P., & Stagnitti, F. (1999). *Soil properties and water movement* (M. B. Parlange & J. W. Hopmans, Eds.).

Pearson, K. (1896). Vii. mathematical contributions to the theory of evolution.—iii. regression, heredity, and panmixia. *Philosophical Transactions of the Royal Society of London. Series A, Containing Papers of a Mathematical or Physical Character*, *187*, 253–318. https://doi.org/10.1098/rsta.1896.0007

Penman, H. (1948). Natural evaporation from open water, bare soil and grass. *Proceedings of the Royal Society of London. Series A. Mathematical and Physical Sciences*, *193*, 120–145. https://doi.org/10.1098/rspa.1948.0037

Piles, M., Sanchez, N., Vall-llossera, M., Camps, A., Martinez-Fernandez, J., Martinez, J., & Gonzalez-Gambau, V. (2014). A downscaling approach for smos land observations: Evaluation of high-resolution soil moisture maps over the iberian peninsula. *IEEE Journal of Selected Topics in Applied Earth Observations and Remote Sensing*, *7*, 3845–3857. https://doi.org/10.1109/JSTARS.2014.2325398

Priestley, C. H. B., & Taylor, R. J. (1972). On the assessment of surface heat flux and evaporation using large-scale parameters. *Monthly Weather Review*, *100*, 81–92. https://doi.org/10.1175/1520-0493(1972)100⟨0081:OTAOSH⟩2.3.CO;2

Qiu, J., Crow, W. T., Wagner, W., & Zhao, T. (2019). Effect of vegetation index choice on soil moisture retrievals via the synergistic use of synthetic aperture radar and optical remote sensing. *International Journal of Applied Earth Observation and Geoinformation*, *80*, 47–57. https://doi.org/10.1016/j.jag.2019.03.015

Quintana-Seguí, P., Barella-Ortiz, A., Regueiro-Sanfiz, S., & Miguez-Macho, G. (2020). The utility of land-surface model simulations to provide drought information in a water management context using global and local forcing datasets. *Water Resources Management*, *34*, 2135–2156. https://doi.org/10.1007/s11269-018-2160-9

Ravazzani, G., Corbari, C., Ceppi, A., Feki, M., Mancini, M., Ferrari, F., Gianfreda, R., Colombo, R., Ginocchi, M., Meucci, S., Vecchi, D. D., Dell'Acqua, F., & Ober, G. (2017). From (cyber)space to ground: New technologies for smart farming. *Hydrology Research*, *48*, 656–672. https://doi.org/10.2166/nh.2016.112

Rozzoni, L. (2017). *Irrigazione parsimoniosa e produttività delle colture tramite modellistica ed esperimenti in campo e laboratorio*. Politecnico di Milano.

Sedlar, J., & Hock, R. (2009). Testing longwave radiation parameterizations under clear and overcast skies at storglaciären, sweden. *The Cryosphere*, *3*, 75–84. https://doi.org/10.5194/tc-3-75-2009

Sehler, R., Li, J., Reager, J., & Ye, H. (2019). Investigating relationship between soil moisture and precipitation globally using remote sensing observations. *Journal of Contemporary Water Research Education*, *168*, 106–118. https://doi.org/10.1111/j.1936-704X.2019.03324.x

Shanmugapriya, P., Rathika, S., Ramesh, T., & Janaki, P. (2019). Applications of remote sensing in agriculture - a review. *International Journal of Current Microbiology and Applied Sciences*, *8*, 2270–2283. https://doi.org/10.20546/ijcmas.2019.801.238

Sharma, V., Kilic, A., & Irmak, S. (2016). Impact of scale/resolution on evapotranspiration from landsat and modis images. *Water Resources Research*, *52*, 1800–1819. https://doi.org/10.1002/2015WR017772

Sishodia, R. P., Ray, R. L., & Singh, S. K. (2020). Applications of remote sensing in precision agriculture: A review. *Remote Sensing*, *12*, 3136. https://doi.org/10.3390/rs12193136

Skokovic, D. (2017). *Calibration and validation of thermal infrared remote sensing sensors and land/sea surface temperature algorithms over the iberian peninsula*. Universidad de Valencia.

Skokovic, D., Sobrino, J. A., & Jimenez-Munoz, J. C. (2017). Vicarious calibration of the landsat 7 thermal infrared band and lst algorithm validation of the etm+ instrument using three global atmospheric profiles. *IEEE Transactions on Geoscience and Remote Sensing*, *55*, 1804–1811. https://doi.org/10.1109/TGRS.2016.2633810

Sliney, D. H. (2007). Radiometric quantities and units used in photobiology and photochemistry: Recommendations of the commission internationale de l'eclairage (international commission on illumination). *Photochemistry and Photobiology*, *83*, 425–432. https://doi.org/10.1562/2006-11-14-RA-1081

Sobrino, J. A., Jimenez-Munoz, J. C., Soria, G., Romaguera, M., Guanter, L., Moreno, J., Plaza, A., & Martinez, P. (2008). Land surface emissivity retrieval from different vnir and tir sensors. *IEEE Transactions on Geoscience and Remote Sensing*, *46*, 316–327. https://doi.org/10.1109/TGRS.2007.904834

Su, Z. (2002). The surface energy balance system (sebs) for estimation of turbulent heat fluxes. *Hydrology and Earth System Sciences*, *6*, 85–100. https://doi.org/10.5194/hess-6-85-2002

Sun, J., Massman, W., & Grantz, D. A. (1999). Aerodynamic variables in the bulk formulation of turbulent fluxes. *Boundary-Layer Meteorology*, *91*, 109–125. https://doi.org/10.1023/A:1001838832436

Taylor, K. E. (2001). Summarizing multiple aspects of model performance in a single diagram. *Journal of Geophysical Research: Atmospheres*, *106*, 7183–7192. https://doi.org/10.1029/2000JD900719

Thom, A. S. (1975). *Vegetation and the atmosphere* (J. Monteith, Ed.).

Thornthwaite, C. W., & Holzman, B. (1939). The determination of evaporation from land and water surfaces. *Monthly Weather Review*, *67*, 4–11. https://doi.org/10.1175/1520-0493(1939)67⟨4:TDOEFL⟩2.0.CO;2

Timmermans, W. J., van der Tol, C., Timmermans, J., Ucer, M., Chen, X., Alonso, L., Moreno, J., Carrara, A., Lopez, R., de la Cruz Tercero, F., Corcoles, H. L., de Miguel, E., Sanchez, J. A. G., Pérez, I., Franch, B., Munoz, J.-C. J., Skokovic, D., Sobrino, J., Soria, G., … Su, Z. ((2015). An overview of the regional experiments for land-atmosphere exchanges 2012 (reflex 2012) campaign. *Acta Geophysica*, *63*, 1465–1484. https://doi.org/10.2478/s11600-014-0254-1

Twine, T. E., Kustas, W. P., Norman, J. M., Cook, D. R., Houser, P. R., Meyers, T. P., Prueger, J. H., Starks, P. J., & Wesely, M. L. (2000). Correcting eddy-covariance flux underestimates over a grassland. *Agricultural and Forest Meteorology*, *103*, 279–300. https://doi.org/10.1016/S0168-1923(00)00123-4

Ulaby, F., Moore, M., & Fung, A. (1982). *Microwave remote sensing, active and passive* (Vol. 2). Artech House.

Verhoef, A., Bruin, H. A. R. D., & Hurk, B. J. J. M. V. D. (1997). Some practical notes on the parameter kb ¡sup¿1¡/sup¿ for sparse vegetation. *Journal of Applied Meteorology*, *36*, 560–572. https://doi.org/10.1175/1520-0450(1997)036⟨0560:SPNOTP⟩2.0.CO;2

Verma, S., Rosenberg, N., Blad, B., & Baradas, M. (1976). Resistance-energy balance method for predicting evapotranspiration: Determination of boundary layer resistance and evaluation of error effects. *Agronomy Journal*, *68*, 776–782.

Vermote, E. F., Saleous, N. E., Justice, C. O., Kaufman, Y. J., Privette, J. L., Remer, L., Roger, J. C., & Tanré, D. (1997). Atmospheric correction of visible to middle-infrared eos-modis data over land surfaces: Background, operational algorithm and validation. *Journal of Geophysical Research: Atmospheres*, *102*, 17131–17141. https://doi.org/10.1029/97JD00201

Viney, N. R. (1991). An empirical expression for aerodynamic resistance in the unstable boundary layer. *Boundary-Layer Meteorology*, *56*, 381–393. https://doi.org/10.1007/BF00119213

Wanders, N., Karssenberg, D., Bierkens, M., Parinussa, R., de Jeu, R., van Dam, J., & de Jong, S. (2012). Observation uncertainty of satellite soil moisture products determined with physically-based modeling. *Remote Sensing of Environment*, *127*, 341–356. https://doi.org/10.1016/J.RSE.2012.09.004

Watson, D. J. (1947). Comparative physiological studies on the growth of field crops: I. variation in net assimilation rate and leaf area between species and varieties, and within and between years. *Annals of Botany*, *11*, 41–76. https://doi.org/10.1093/oxfordjournals.aob.a083148

Woods, M., Ajates, R., Gulari, N., Burton, V. J., van der Velden, N. K., & Hemment, D. (2019). *Grow observatory: Mission outcomes*. https://doi.org/10.20933/100001130

Xaver, A., Zappa, L., Rab, G., Pfeil, I., Vreugdenhil, M., Hemment, D., & Dorigo, W. A. (2020). Evaluating the suitability of the consumer low-cost parrot flower power soil moisture sensor for scientific environmental applications. *Geoscientific Instrumentation, Methods and Data Systems*, *9*, 117–139. https://doi.org/10.5194/gi-9-117-2020

Xie, X. (1988). An improved energy balance-aerodynamic resistance model used estimation of evapotranspiration on the wheat field. *Acta Meteorologica Sinica*, *1*, 102–106.

Yang, K., Tamai, N., & Koike, T. (2001). Analytical solution of surface layer similarity equations. *Journal of Applied Meteorology*, *40*, 1647–1653. https://doi.org/10.1175/1520-0450(2001)040⟨1647:ASOSLS⟩2.0.CO;2

Zahn, E., Bou-Zeid, E., Good, S., Katul, G. G., Thomas, C. K., Ghannam, K., Smith, J. A., Chamecki, M., Dias, N. L., Fuentes, J. D., Alfieri, J. G., Kwon, H., Caylor, K., Gao, Z., Soderberg, K., Bambach, N. E., Hipps, L. E., Prueger, J. H., & Kustas, W. P. (2022). Direct partitioning of eddy-covariance water and carbon dioxide fluxes into ground and plant components [Submitted]. *Agricultural Forest Meteorology*.

Zappa, L., Forkel, M., Xaver, A., & Dorigo, W. (2019). Deriving field scale soil moisture from satellite observations and ground measurements in a hilly agricultural region. *Remote Sensing*, *11*, 2596. https://doi.org/10.3390/rs11222596